STUDIES ON ACTIVE SYSTEMS

By

AMIR SHEE

PHYS07201504008

Institute of Physics, Bhubaneswar

A thesis submitted to the

Board of Studies in Physical Sciences

In partial fulfillment of requirements

for the Degree of

DOCTOR OF PHILOSOPHY

of

HOMI BHABHA NATIONAL INSTITUTE

August, 2021

Homi Bhabha National Institute

Recommendations of the Viva Voce Committee

As members of the Viva Voce Committee, we certify that we have read the dissertation prepared by AMIR SHEE entitled "STUDIES ON ACTIVE SYSTEMS" and recommend that it may be accepted as fulfilling the dissertation requirement for the Degree of Doctor of Philosophy.

Chairman - Prof. Sudipta Mukherji Date: October 6, 2021

S. Mukherji.

Guide /Convener - Prof. Debasish Chaudhuri Date: October 6, 2021

Debasish Chaudhuri

Examiner - Prof. Dibyendu Das Date: October 6, 2021

Dibyendu Das

Member 1 - Prof. Goutam Tripathy Date: October 6, 2021

G. Tripathy

Member 2 - Prof. Saptarshi Mandal Date: October 6, 2021

Saptarshi Mandal

Member 3 - Prof. Kirtiman Ghosh Date: October 6, 2021

Kirtiman Ghosh.

Final approval and acceptance of this thesis is contingent upon the candidate's submission of the final copies of the dissertation to HBNI.

I/We hereby certify that I/we have read this thesis prepared under my/our direction and recommend that it may be accepted as fulfilling the thesis requirement.

Date : October 6, 2021

Place : Bhubaneswar

Debasish Chaudhuri

Prof. Debasish Chaudhuri

Guide

STATEMENT BY AUTHOR

This dissertation has been submitted in partial fulfillment of requirements for an advanced degree at Homi Bhabha National Institute (HBNI) and is deposited in the Library to be made available to borrowers under rules of the HBNI.

Brief quotations from this dissertation are allowable without special permission, provided that accurate acknowledgement of source is made. Requests for permission for extended quotation from or reproduction of this manuscript in whole or in part may be granted by the Competent Authority of HBNI when in his or her judgment the proposed use of the material is in the interests of scholarship. In all other instances, however, permission must be obtained from the author.

Shee

Amir Shee

DECLARATION

I, hereby declare that the investigation presented in the thesis has been carried out by me. The work is original and has not been submitted earlier as a whole or in part for a degree / diploma at this or any other Institution / University.

Shee

Amir Shee

List of Publications arising from the thesis

Journal

1. ‘‘Active Brownian particles: mapping to equilibrium polymers and exact computation of moments”, **Amir Shee**, Abhishek Dhar and Debasish Chaudhuri, *Soft Matter*, **2020**, 16, 4776-4787.

2. ‘‘Semiflexible polymer in a gliding assay: reentrant transition, role of turnover and activity”, **Amir Shee**, Nisha Gupta, Abhishek Chaudhuri and Debasish Chaudhuri, *Soft Matter*, **2021**, 17, 2120-2131.

3. ‘‘Filament-motor protein system under loading: instability and limit cycle oscillations”, **Amir Shee**, Subhadip Ghosh and Debasish Chaudhuri, *Soft Materials*, DOI: 1539445X.2021.1887221, **2021**.

Preprint

1. ‘‘Active Brownian motion with speed fluctuations in arbitrary dimensions: exact calculation of moments and dynamical crossover”, **Amir Shee** and Debasish Chaudhuri, *arXiv:2108.12228*, **2021**.

Conferences

1. Participated in “EMBO lecture course: Experimental and Theoretical approaches to cell mechanics”, RRI and NCBS, Bangalore, India, April 23-May 6, 2017. Presented a poster on ‘Pattern formation in active fluids switching between active and passive fraction’.

2. Participated in “Soft Matter Young Investigator Meet (SMYIM-2018)”, Shimla, India; 23-25 May, 2018. Presented a poster on ‘Pattern formation and dynamics in active fluids’.

3. Participated in “Indian Statistical Physics Community Meeting (ISPCM-2019)”, ICTS, Bangalore; 14-16 February, 2019. Presented a poster on ‘Pattern

formation in active fluids having deformation dependent turnover’.

4. Participated in the meeting named “ Thirsting for Theoretical Biology (ONLINE) ”, ICTS Bangalore, India, 11-22 January, 2021.

Shee

Amir Shee

ACKNOWLEDGEMENTS

First of all, I express my sincere gratitude to my supervisor, Dr. Debasish Chaudhuri, for suggesting this new topic and all the insightful discussions we had during these years. I like to thank my doctoral committee: Prof. Sudipta Mukherji, Dr. Goutam Tripathy, Dr. Saptarshi Mandal, Dr. Kirtiman Ghosh, their encouragement, insightful comments, and questions. My gratitude goes to Prof. Abhishek Dhar for the collaboration, discussions on work presented in Chapter 2 of this thesis, and my visit to ICTS, Bangalore. I would also thank Dr. Vijaykumar Krishnamurthy and Dr. Arghya Das for discussions during my ICTS visit. I would also like to thank Dr. Abhishek Chaudhuri for the collaboration and all the fruitful discussions. I thank Dr. Nisha Gupta for the collaboration work presented in Chapter 6. I also thank Dr. Subhadip Ghosh and V.N.S Pradeep for the collaboration and discussions on work presented in Chapter 5. I like to thank Dr. Biplab Bhattacherjee, Dr. Priyo Shankar Pal, Dr. Pinaki Swain, Dr. Amit Kumar, Chitrak Karan, and Arpan Sinha for all these years of fun, teas, coffees, discussion on work, and friendship. I have also benefitted from all the people I met during the schools and the conferences I have attended.

All the simulation results presented were supported in part by the SAMKHYA: High-Performance Computing Facility provided by the Institute of Physics(IOPB), Bhubaneswar, India. I acknowledge Homi Bhabha National Institute, India, and the Department of Atomic Energy, Government of India for academic support and the research fellowship.

I thank my friends Atanu Maity, Mukaddar Sk., Dibyendu Rana, Dilruba Hasina, Alapan Dutta, and Purbasha Sarangi and all the fun we have had in the last five years. Finally, I would like to acknowledge with sincere gratitude the love and support of my family. They all kept me going. It would not have been possible without them.

Amir Shee

CONTENTS

SUMMARY vii

LIST OF FIGURES xxv

LIST OF TABLES xxvi

CHAPTER 1 INTRODUCTION 1

CHAPTER 2 ACTIVE BROWNIAN PARTICLE (ABP) 7

2.1 Introduction 7

2.2 Definition of the model 10

2.3 Exact mapping to equilibrium polymer model 12

2.3.1 Comparisons between ABP dynamics and mapped polymer simulations 14

2.3.2 How far from extensible semi-flexible polymer is mapped polymer(or ABP) ? 18

2.4 Exact computation of moments for ABP 19

2.5 Orientation correlation and average displacement 21

2.5.1 Orientation correlation 21

2.5.2 Displacement 22

2.6 Quadratic order moment and displacement fluctuation 23

  2.6.1 Quadratic order moment 23

  2.6.2 Displacement fluctuation 25

2.7 Components of displacement fluctuation 26

2.8 Quartic order moment 29

2.9 End- to- end distribution with chain length 32

2.10 Differentiation of ABP with active Ornstein-Uhlenbeck process(AOUP) 35

  2.10.1 AOUP model and calculation of moments 35

  2.10.2 Comparision with ABP 36

  2.10.3 Kurtosis : deviation from Gaussian process 36

2.11 Conclusions 39

CHAPTER 3 ACTIVE BROWNIAN PARTICLE: FLUCTUATION IN THE SPEED 41

3.1 Introduction 41

3.2 Model 43

3.3 Calculation of moments from Fokker-Planck equation 46

3.4 Active speed 47

  3.4.1 Mean speed 47

  3.4.2 Speed fluctuation 48

3.5 Correlation functions 49

3.6 Displacement 50

  3.6.1 Position-orientation cross-correlation: $\langle \hat{\boldsymbol{u}} \cdot \mathbf{r} \rangle$ 51

  3.6.2 Mean squared displacement 52

3.6.3 Displacement fluctuation 68

3.6.4 Components of displacement fluctuation 72

3.7 Fourth order moments and kurtosis 77

3.7.1 Fourth moment of speed 77

3.7.2 Fourth moment of displacement 78

3.7.3 Persistent motion 81

3.7.4 Kurtosis: deviation from Gaussian process 83

3.8 Conclusions 85

3.9 Appendix 86

3.9.1 Autocorrelation of active speed 86

3.9.2 Steady state probability distribution of speed and its cumulative distribution 88

CHAPTER 4 ACTIVE BROWNIAN PARTICLE: ACTIVE SPEED ASSOCIATE WITH AN ADDITIVE GAUSSIAN NOISE 91

4.1 Introduction 91

4.2 Model 92

4.2.1 Fokker-Planck equation 93

4.3 Mean squared displacement and displacement fluctuation 94

4.4 Components of displacement fluctuation 98

4.5 Displacement distribution 103

4.6 Fourth moment and kurtosis 105

4.7 Conclusions 111

CHAPTER 5 FILAMENT-MOTOR PROTEINS SYSTEM UNDER LOADING . . . 113
5.1 Introduction . . . 113
5.2 Model . . . 115
5.3 Mean field theory . . . 117
5.3.1 Constant loading . . . 119
5.3.2 Elastic loading . . . 120
5.4 Fokker-Planck approach to mean field . . . 126
5.5 Stochastic simulation . . . 130
5.6 Conclusions . . . 132
CHAPTER 6 SEMIFLEXIBLE FILAMENT IN A GLIDING ASSAY . . . 134
6.1 Introduction . . . 134
6.2 Model and simulation . . . 137
6.2.1 Model . . . 137
6.2.2 Simulation . . . 139
6.3 Spiral formation, rotation and breaking . . . 140
6.4 First order phase transition : open chain to spiral . . . 142
6.5 Phase diagram : reentrant transition . . . 144
6.6 Turn number fluctuations . . . 146
6.7 Size and shape . . . 149
6.7.1 End- to- end separation . . . 149
6.7.2 Effective persistence length . . . 151

6.7.3 Radius of gyration tensor 152

6.8 Dynamics 153

6.8.1 Dynamics of turning number 154

6.8.2 Dynamics of size, shape, and orientation 155

6.8.3 Time scales 156

6.9 Conclusions 159

6.10 Appendix 161

6.10.1 Equilibrium persistence 161

6.10.2 Correlation time in smoothened polymer 162

CHAPTER 7 PATTERN FORMATION IN ACTIVE FLUIDS: UNIFORM AND STRESS-DEPENDENT TURNOVER 163

7.1 Introduction 163

7.2 Hydrodynamic description of model 165

7.3 Dimensionless equations and linear stability analysis 167

7.3.1 Dimensionless equations 167

7.3.2 Linear stability analysis 168

7.4 Uniform turnover 169

7.4.1 In the absence of pressure 169

7.4.2 In the presence of pressure 173

7.5 Stress-dependent turnover 175

7.6 Conclusions 179

7.7 Appendix 180

7.7.1 Implicit-Explicit (IMEX) Scheme: MCNAB method 180

CHAPTER 8 CONTRACTILE ACTIVE FLUIDS WITH STRAIN-RATE-DEPENDENT TURNOVER 182

8.1 Introduction 182

8.2 Model 183

8.3 Linear Stability Analysis 185

8.4 Phase diagram 189

8.5 Conclusions 195

8.6 Appendix 195

8.6.1 Physical parameters 195

CHAPTER 9 DISCUSSIONS 197

REFERENCES 208

SUMMARY

In this thesis we study active matter systems using analytical and numerical approaches. Active matter consists of self-propelled components, converting stored or ambient energy into systematic movement [1–3]. They are driven out of equilibrium through the consumption and dissipation of energy by each of these active units, violating the detailed balance condition and the equilibrium fluctuation-dissipation relation. Examples of such systems are abound in nature, covering multiple length scales, from motor proteins, cytoskeleton, motile cells, growing tissues to birds and animals [2, 4–7].

Despite tremendous progress in the knowledge of collective properties of active matter, the dynamical properties of non-interacting active particles are not yet fully understood. Recent studies indicate how even a single active particle can display qualitatively rich physics [8–14]. We develop an exact mapping of the path probabilities of the active Brownian particles (ABP) in the presence of thermal bath to configurational properties of *extensible* semiflexible polymers. Using a Laplace transform of the governing Fokker-Planck equation of the active Brownian particle motion, we describe a direct method to derive exact expressions for all the moments of the relevant dynamical variables in arbitrary dimensions. The ABPs described above does not incorporate the possible stochasticity in the generation of active speed. To study its influence, we first consider a stochastic speed generation following an active Ornstein-Uhlenbeck process [15]. To explore the competition between various time scales in the dynamics, we extend the Laplace transform of Fokker-Planck equations to calculate exact time-dependent moments of dynamical variables in arbitrary dimensions. We also consider a second model of active speed fluctuations due to stochastic chemical processes generating the active speed [16] and explore its dynamical behavior in arbitrary dimensions. The displacement distribution function in two-dimensions displays crossovers from Gaussian to bimodal to a non-Gaussian unimodal behavior with increasing time. At longer times, the distribution returns to the Gaussian behavior via another intermediate bimodal structure.

Next we consider the dynamics of cytoskeleton from two perspectives. The gliding motion of cytoskeleton filaments on a motor protein assay has been used extensively in experiments to study dynamics of cytoskeletal filaments outside living cells [17–21]. We begin by investigating the dynamics of a rigid filament in a motor protein assay in one dimension. We model motor proteins as active harmonic linkers with their tails immobilized on a substrate. Their heads attach to the filament stochastically to extend along it in a polar fashion. Thus, it exerts a force on the filament before detaching. The rate of extension and detachment are load-dependent. Under elastic loading, we find the emergence of stable limit cycle oscillations of the filament via a supercritical Hopf bifurcation with a change in activity and the number of motor proteins. Numerical simulations of the system for a large number of motor proteins show good agreement with the mean-field predictions. We further investigate conformational dynamics of semiflexible cytoskeletal filaments in a gliding assay. The conformations of the filament undergo a first-order phase transition from open-chain to spiral. They show a reentrant transition behavior in both the active extension and turnover, defined as the ratio of attachment-detachment rates. The size and shape of the polymer change non-monotonically along the phase transition, and the relevant autocorrelation functions display a double-exponential decay.

Finally, we consider the actomyosin cytoskeleton [22] within a coarse-grained field-theoretic description. The actomyosin is known to show active contractility and flows over a long time scale [23, 24]. We use a two component active fluid model undergoing advection-diffusion and turnover. We consider the turnover rates to be constant, stress dependent, and strain-rate dependent. In strain-rate dependent turnover, the local extension (compression) increases (decreases) the active to passive transformation favoring the passive (active) state. Depending on the bare on-rate and Péclet number characterizing the active contractility, the system shows a homogeneous steady-state and spatial pattern formation in the presence or absence of a steady-state flow. The steady-state patterns show two different possibilities – one in which the maxima of active and passive densities co-appear in space; on the other, they segregate spatially.

In summary, we investigate active systems: from active particles to semiflexible filaments driven by the activity of molecular motors to a two-component active fluid model of cytoskeletal complex.

LIST OF FIGURES

1.1 (color online) Example of a spherical active particle: a Janus swimmer with different surface property at two hemispheres. This shows decomposition of hydrogen peroxide on the platinum-covered hemisphere (black) to generate motion (green arrow). The figure is adapted from Ref. [25]. 2

1.2 (color online) Schemetic representation of cytoskeletal filaments and motor proteins. (A) Microtubule and actin filament: microtubule polymerized from tubulin dimers and actin filament polymerized from globular actin monomers. (B) Kinesin motors move on microtubules hydrolyzing ATP. Myosin-II motor proteins move along F-actins hydrolyzing ATP. (C) An gliding assay of motor proteins consisting of kinesins and myosins adhered to a cover slip. Microtubules and F-actins are added to the chamber where they bind to the motor proteins and get propelled actively. The methylcellulose is added to keep the F-actin and microtubules crowded to the surface. The figure is adapted from Ref. [26]. 4

1.3 (color online) Components of the eukaryotic cell. The actin filaments are shown in red, microtubules in green, and the nuclei in blue. The figure is adapted from Wikipedia https://www.wikipedia.org/ . . 5

2.1 (color online) Schematic representation of active Brownian particle. The velocity of ABP is $v_0\hat{\boldsymbol{u}}$ where v_0 is the speed of the particle with heading direction along $\hat{\boldsymbol{u}} = (u_1, u_2, ..., u_d)$ in d-dimension. 10

2.2 (color online) Typical ABP trajectory. The blue point shows the initial starting point with heading dircetion along x-axis. Direct simulation of equation of motion (2.1), (2.2) in two dimension with parameters $D = 1$, $D_r = 1$, and $v_0 = 130$. 11

2.3 (color online) Typical configurations of (a) the polymer mapping of the ABP model (Eq. (2.8)), (b) the related worm-like-chain (Eq. (2.9)), (c) the related Gaussian polymer under a directed external force (Eq. (2.10)), and (d) the related extensible semiflexible chain (Eq. (2.13)). The thick (red) line in (a) shows the worm-like-chain conformation that the Gaussian polymer denoted by the beads and springs tries to align with. The configurations are plotted with chain length $L = 15\,\sigma$, persistence length $\ell_p = 4.28\,\sigma$, spring constant $A = 30.0\,\sigma^{-1}$ in (a) and (d), and $A = 1.0\,\sigma^{-1}$ in (c) . Note that A does not play any role in deciding the conformation in (b). 13

2.4 (color online) Comparison between probability distributions of ABP displacement (solid lines) and end-to-end separation of polymers (points): Here $v_0 = 1.8\,\sigma/\tau_u$ and $D = 0.02\,\sigma^2/\tau_u$ are held constant. In all the simulations, the first step in the ABP model, and the bond orientation of one end of the polymer are held fixed along the x-direction. The bimodal distributions corresponding to $D_r\tau_u = 0.02\,(\square)$, $0.03\,(\triangle)$, $0.05\,(\diamond)$, $0.1\,(\circ)$, $0.2\,(\triangledown)$. Inset: The same comparisons at $D_r\tau_u = 0.08\,(\diamond)$, $0.09\,(\triangledown)$, $0.1\,(\circ)$, $0.11\,(\square)$, $0.12\,(\triangle)$. 14

2.5 (color online) Comparison between probability distributions of ABP displacement (solid lines) and end-to-end separation of polymers (points): We keep $v_o = 1.8\,\sigma/\tau_u$, $D_r = 0.1\,\tau_u^{-1}$ for ABP constant, and show the mapping of ABP to polymer for $D\tau_u/\sigma^2 = 0.02\,(\circ)$, $0.5\,(\square)$, $2\,(\triangle)$. Inset: The loss of bimodality magnified. 16

2.6 (color online) Comparison between probability distributions of ABP displacement (solid lines) and end-to-end separation of polymers (points): We kept $D = 1.0\,\sigma^2/\tau_u$ and $D_r = 1.0\tau_u^{-1}$ constant and varied v_0 keeping $v_0\tau$ constant. The data denotes $v_0\tau_u/\sigma = 10\,(\triangledown)$, $20\,(\circ)$, $40\,(\diamond)$, $100\,(\triangle)$. 17

2.7 (color online) Comparison between the ABP model and the extensible semiflexible chain (ESC). We keep parameters $v_0 = 1.8\,\sigma/\tau_u$, $D_r = 0.1\,\tau_u^{-1}$ constant. The lines show results from the ABP model at $D\tau_u/\sigma^2 = 0.02$ (red), 0.5 (green), 2 (blue). Points denote results for ESC at the corresponding $A\sigma = 45$ (red $\circ$), 1.8 (green $\square$), 0.45 (blue $\triangle$). Inset: magnified view highlights difference between the results of the two models. 18

2.8 (color online) (a) Orientational correlation $\langle \hat{\boldsymbol{u}}(t) \cdot \hat{\boldsymbol{u}}(0) \rangle$, and (b) the displacement $\langle r_{\parallel} \rangle$ along the initial orientation $\hat{\boldsymbol{u}}_0$ of the ABP are shown as a function of time t in 2d. Here $D = 1.0\,\sigma^2/\tau_u$, and $v_0 = 1.0\,\sigma/\tau_u$ are held constant, and we use $D_r\tau_u = 0.1(\square)$, $0.2(\circ)$. The results of numerical simulations are shown by points, and analytic predictions by dashed lines. In this figure, and all other figures presented in this section, the length and time axes are expressed in units of $\bar{\ell} = \sqrt{D/D_r}$ and $\tau_r = 1/D_r$, respectively. The dashed line in (a) shows $\langle \hat{\boldsymbol{u}}(t) \cdot \hat{\boldsymbol{u}}(0) \rangle = e^{-t}$ in the semi-log plot, and in (b) shows $\langle r_{\parallel} \rangle / \lambda = (1 - e^{-t})$ with $\lambda = v_0/\sqrt{DD_r}$. 22

2.9 (color online) Time dependence of ratios $\langle r^2 \rangle / t$ and $\langle \delta r^2 \rangle / t$ in two dimension. $D_r = 1.0\,\tau_u^{-1}$, $v_0 = 10\,\sigma/\tau_u$ are held constant. The results of numerical simulation at $D\tau_u/\sigma^2 = 0.1(\diamond)$, $1(\circ)$, $100(\square)$ are shown by points denoted in the two figures. Dashed lines show plots of $\langle \mathbf{r}^2 \rangle$ and $\langle \delta \mathbf{r}^2 \rangle$ present in Eqs. (2.23) and (2.25) respectively. For individual curves, arrows denote $t_I = (2d/\lambda^2)\tau_r$, $t_{II} = [3/(d-1)]\tau_r$ in (a), and $t_I = [3d/(d-1)]^{1/2}\tau_r$ and $t_{II} = [4/3(d-1)]\tau_r$ in (b), with $d = 2$. 25

2.10 (color online) The plots of $\langle \delta r_{\parallel}^2 \rangle$ and $\langle \delta \mathbf{r}_{\perp}^2 \rangle$ as a function of time t in two dimension. $D_r = 1.0\,\tau_u^{-1}$, $D = 1.0\,\sigma^2/\tau_u$ are held constant. The data for $v_0\tau_u/\sigma = 1\,(\square)$, $130\,(\circ)$ are shown in the two figures. The dashed lines show plots of $\langle \delta r_{\parallel}^2 \rangle$ and $\langle \delta \mathbf{r}_{\perp}^2 \rangle$ obtained from Eq. (2.36) and (2.37). For the expressions of $t_{I,II}^{\parallel}$ and $t_{I,II}^{\perp}$, see the discussion after Eq. (2.38). The solid lines in the figures denote the intermediate scaling. 28

2.11 (color online) Evolution of the ratio $\langle r^4 \rangle / t^2$ with time in 2d. $D_r = 1.0\,\tau_u^{-1}$ and $D = 1.0\,\sigma^2/\tau_u$ are held constant. The points denote simulation results, and the dashed lines denote analytic prediction in Eq. (2.41). (a) $v_0 = 3\,\sigma/\tau_u$ shows two crossovers at $t_I = 0.22\,\tau_r$, $t_{II} = 4.36\,\tau_r$, (b) $v_0 = 10\,\sigma/\tau_u$ shows three crossovers at crossover times $t_I \approx 0.02\,\tau_r$, $t_{II} = 0.17\,\tau_r$ and $t_{III} = 1.45\,\tau_r$. The black solid lines in the two curves indicate the intermediate scaling behaviors. 31

2.12 (color online) The displacement distributions at $D_r = 1.0\,\tau_u^{-1}$, $v_0 = 10\,\sigma/\tau_u$ and $D = 0.1\,\sigma^2/\tau_u$ over different time-segments indicated by the $v_0 t$ values shown in the figures. The persistence length of the mapped polymer $\ell_p = 10^3\bar{\ell}$. The length of trajectories considered are $L = 0.1\,\bar{\ell}\,(a), 1.0\,\bar{\ell}\,(b), 10\,\bar{\ell}\,(c), \ldots, 10^4\bar{\ell}\,(f)$. 33

2.13 (color online) The 2d displacement distributions $p(\tilde{x}, \tilde{y})$ at $D_r = 1.0\,\tau_u^{-1}$, $v_0 = 10.0\,\sigma/\tau_u$ and $D = 0.1\,\sigma^2/\tau_u$ over different time segments τ, presented as heat maps. The length of trajectories considered are $L = v_0\tau = 0.1\,\bar{\ell}\,(a), 1.0\,\bar{\ell}\,(b), 10\,\bar{\ell}\,(c), \ldots, 10^4\bar{\ell}\,(f)$. 34

2.14 (color online) The change in distributions $p(\tilde{r})$ $[(a)-(c)]$ and $p(\tilde{x},\tilde{y})$ $[(d)-(f)]$ at $D_r = 1.0\,\tau_u^{-1}$, $v_0 = 10.0\,\sigma/\tau_u$ and $D = 0.1\,\sigma^2/\tau_u$ for different contour lengths $L = v_0\tau$ in the regime of bimodality. The persistence length $\ell_p = 10^3\bar{\ell}$. The length of trajectories considered are $L = 3\ell_p\,[(a),(d)]\,3.5\ell_p\,[(b),(e)]$, $4\ell_p\,[(c),(f)]$. 34

2.15 (color online) Deviation from Gaussian nature in terms of $\mathcal{K}$ is shown as a function of time t expressed in units of $\tau_r = 1/D_r$. The translational diffusion $D = 1.0\,\sigma^2/\tau_u$ is held constant. (a) Plot with $D_r = 1.0\,\tau_u^{-1}$ for $v_0\,\tau_u/\sigma = 0,\ 1,\ 3,\ 10$. (b) Plot at $v_0 = 10\,\sigma/\tau_u$ for $D_r\tau_u = 1,\ 5,\ 10,\ 20$. 38

3.1 (color online) Typical ABP trajectories in two-dimensions (2d) over a duration $t = 100\,\tau_r$ are shown in the absence (a) and (b) presence of external drive: (a) Persistent motion at $\tilde{\boldsymbol{F}}_0 = 0$, (b) Directed persistent motion at $\tilde{\boldsymbol{F}}_0 = 5\,\hat{r}$ with $\hat{r} = \hat{x}+\hat{y}$ in cartesian coordinates. The plots use $Pe = 20$, $\tilde{D}_v = 1$, and $\tilde{\gamma}_v = 1$. The blue point with arrow in each plot shows starting position and orientation of the ABP. In these plots we used the initial active speed $v_1 = \bar{v}Pe$ and heading direction $\hat{\boldsymbol{u}}_0 = \hat{x}$ along the x-axis. 45

3.2 (color online) Speed fluctuation $\langle \delta v^2 \rangle$ as a function of time t/τ_r at $\tilde{D}_v = 1$ and $\tilde{\gamma}_v = 1$ in 2d for $Pe = 0.1(\circ)$, $1(\triangledown)$, $10(\diamond)$. The points are simulation results and the solid line is a plot of Eq. (3.8). . . . 48

3.3 (color online) Displacement in the initial orientation $\langle r_\parallel \rangle$ as a function of time t at $D_v\tau_r/\bar{v}^2 = 1$ and $\gamma_v\tau_r = 1$ in 2d for $Pe \equiv v_0/\bar{v} = 0.1(\circ)$, $5(\triangledown)$, $20(\diamond)$. The points denote simulation results, and lines depict $\langle r_\parallel \rangle = \langle \mathbf{r} \rangle \cdot \hat{\boldsymbol{u}}_0$ using Eq. (3.14). (a) Displacements for the persistent ABP in the absence of external force, $\mu\boldsymbol{F}_0/\bar{v} = 0$. (b) Displacements in the presence of external force, $\mu\boldsymbol{F}_0/\bar{v} = \hat{r}$. The initial speed and heading directions are chosen to be $v_1 = v_0$ and $\hat{\boldsymbol{u}}_0 = \hat{x}$, respectively. 50

3.4 (color online) The position-orientation cross-correlation $\langle \hat{\boldsymbol{u}} \cdot \mathbf{r} \rangle$ as a function of time t at $D_v\tau_r/\bar{v}^2 = 1$ and $\gamma_v\tau_r = 1$ in 2d for $Pe = 1$, 0.1, 0.01. The lines depict Eq. (3.16) with the initial speed $v_1 = v_0$ and heading direction $\hat{\boldsymbol{u}}_0 = \hat{x}$. In the presence of external drive $\mu\boldsymbol{F}_0/\bar{v} = \hat{r}$, the cross correlation varies non-monotonically to finally saturate to $\langle \hat{\boldsymbol{u}} \cdot \mathbf{r} \rangle/\bar{\ell} = Pe$ in $d = 2$. The maxima for each Pe value appear at time points $t_m/\tau_r = 1 + Pe$. 53

3.5 (color online) Time dependence of $\langle \mathbf{r}^2 \rangle / t$ in 2d, in the absence of external force. The slow and fast relaxations of active speed are considered in (a, b) $\gamma_v \tau_r \ll 1$, and (c, d) $\gamma_v \tau_r \gg 1$, respectively. The points denote simulation results, the solid lines depict Eq. (3.23) with $d = 2$, and the dashed lines depict Eq. (3.25). Parameter values used in (a, b): $\gamma_v \tau_r = 5 \times 10^{-4}$, $D_v \tau_r / \bar{v}^2 = 2.5$ with $Pe \equiv v_0 / \bar{v} = 22.36$ (a) and 1.12 (b). Parameter values used in (c, d): $\gamma_v \tau_r = 5 \times 10^2$, $D_v \tau_r / \bar{v}^2 = 10^7$ with $Pe \equiv v_0 / \bar{v} = 20$ (c) and 1 (d). Initial conditions are chosen such as the active speed speed $v_1 / \bar{v} = Pe$ and the heading direction $\hat{\boldsymbol{u}}_0 = \hat{x}$ is along the x-axis. 58

3.6 (color online) Persistent motion. Mean squared displacement $\langle \mathbf{r}^2 \rangle$ as in Eq. (3.23) as a function of time t in two dimension, $d = 2$. (a) Parameters used are $\tilde{\gamma_v} = \gamma_v \tau_r = 5 \times 10^{-4}$, $\tilde{D_v} = D_v \tau_r / \bar{v}^2 = 2.5$ with $Pe = v_0 / \bar{v} = 22.36$ (solid line), 1.12 (dashed line). The solid line shows four crossover with crossover times $t_I / \tau_r = 0.008$, $t_{II} / \tau_r = 3.03$, $t_{III} / \tau_r = 202.8$ and $t_{IV} / \tau_r = 2200$. The dashed line shows two crossovers: : a diffusive-ballistic crossover at $t_I^* / \tau_r = 0.8$ and a ballistic-diffusive crossover at $t_{IV} / \tau_r = 2000$. (b) Parameters used are $\tilde{\gamma_v} = \gamma_v \tau_r = 2 \times 10^3$, $\tilde{D_v} = D_v \tau_r / \bar{v}^2 = 10^{11}$, with $Pe = v_0 / \bar{v} = 2 \times 10^3$ (solid line), 10 (dashed line). The solid line shows five crossover with crossover times $t_I / \tau_r = 10^{-6}$, $t_{II} / \tau_r = 6 \times 10^{-5}$, $t'_{III} / \tau_r = 8.6 \times 10^{-4}$ and $t'_{IV} / \tau_r = 1.25 \times 10^{-2}$, and $t_V = 2.02$. The dashed line shows two crossovers with crossover times $t^*_{II} / \tau_r = 7.75 \times 10^{-6}$ and $t'_{III} / \tau_r = 8.6 \times 10^{-4}$. Initial activity: speed $v_1 / \bar{v} = Pe$ and orientation along x-axis, $\hat{\boldsymbol{u}}_0 = \hat{x}$. 60

3.7 (color online) Directed persistent motion. Mean squared displacements $\langle \mathbf{r}^2 \rangle$ as in Eq. (3.31) are depicted as a function of time t for directed persistent motion with speed fluctuation in 2d. The initial condition is set by speed $v_1 / \bar{v} = Pe$ and heading direction $\hat{\boldsymbol{u}}_0 = \hat{x}$. (a) Parameters used are $\tilde{\gamma_v} = \gamma_v \tau_r = 5 \times 10^{-4}$, $\tilde{D_v} = D_v \tau_r / \bar{v}^2 = 2.5$, and $\tilde{\boldsymbol{F}}_0 = \mu \boldsymbol{F}_0 / \bar{v} = 2.2 \times 10^{-2}\ \hat{r}$ with $\hat{r} = \hat{x} + \hat{y}$, active speed $Pe = v_0 / \bar{v} = 22.36$ (solid line) and 1.12 (dashed line). The solid line exhibits five crossovers with crossover times $t_I / \tau_r = 8 \times 10^{-3}$, $t_{II} / \tau_r = 3.03$, $t_{III} / \tau_r = 202.9$ and $t_{IV} / \tau_r = 2199$, and $t_V / \tau_r = 1.1 \times 10^7$. The dashed line shows three crossovers with crossover times $t_I^* / \tau_r = 0.8$, $t_{IV} / \tau_r = 2 \times 10^3$, $t_V / \tau_r = 10^7$. (b) Parameters used are $\tilde{\gamma_v} = \gamma_v \tau_r = 2 \times 10^3$, $\tilde{D_v} = D_v \tau_r / \bar{v}^2 = 10^{11}$, and $\tilde{\boldsymbol{F}}_0 = \mu \boldsymbol{F}_0 / \bar{v} = 10^2\ \hat{r}$, active speed $Pe = v_0 / \bar{v} = 2 \times 10^3$ (solid line) and 10 (dashed line). The solid line exhibits six crossover with crossover times $t_I / \tau_r = 10^{-6}$, $t_{II} / \tau_r = 6 \times 10^{-5}$, $t_{III} / \tau_r = 0.0016$ and $t_{IV} / \tau_r = 0.0225$, $t_V / \tau_r = 2.02$, and $t_{VI} / \tau_r = 4 \times 10^2$. The dashed line shows three crossovers with crossover times $t^*_{II} / \tau_r = 7.7 \times 10^{-6}$, $t'_{III} / \tau_r = 9 \times 10^{-4}$, $t_V / \tau_r = 2.5$. 65

3.8 (color online) Displacement fluctuations $\langle \delta \mathbf{r}^2 \rangle$ in Eq. (3.38) as a function of time t in $d = 2$. (a) Parameters used are $\tilde{\gamma_v} = \gamma_v \tau_r = 5 \times 10^{-4}$, $\tilde{\gamma_v} = D_v \tau_r / \bar{v}^2 = 2.5$ with active speed $Pe = v_0/\bar{v} = 22.36$ (solid line), 1.12 (dashed line). The solid line shows four crossovers with crossover times $t_I/\tau_r = 0.008$, $t_{II}/\tau_r = 3.03$, $t_{III}/\tau_r = 202.8$ and $t_{IV}/\tau_r = 2.2 \times 10^3$. The dashed line shows two crossovers with crossover times $t_I^*/\tau_r = 0.8$ and $t_{IV}/\tau_r = 2 \times 10^3$. ($b$) Parameters used are $\tilde{\gamma_v} = \gamma_v \tau_r = 2 \times 10^3$, $\tilde{D_v} = D_v \tau_r / \bar{v}^2 = 10^{11}$ with $Pe = v_0/\bar{v} = 2 \times 10^3$ (solid line), 10 (dashed line). The solid line exhibits four crossovers with crossover times $t_I/\tau_r = 8 \times 10^{-6}$, $t_{II}/\tau_r = 7 \times 10^{-4}$, $t'_{III}/\tau_r = 1.4 \times 10^{-1}$ and $t'_{IV}/\tau_r = 1.7$. The dashed line shows two crossovers with crossover times $t_I/\tau_r = 8 \times 10^{-6}$, $t_{II}/\tau_r = 7 \times 10^{-4}$. 69

3.9 (color online) Components of displacement fluctuation, (a, c) $\langle \delta r_{\parallel}^2 \rangle$ and (b, d) $\langle \delta \mathbf{r}_{\perp}^2 \rangle$ as a function of time t in 2d. (a, b) $\tilde{\gamma_v} = \gamma_v \tau_r = 5 \times 10^{-4}$, $\tilde{D_v} = D_v \tau_r / \bar{v}^2 = 2.5$ with $Pe = v_0/\bar{v} = 22.36$ (solid line), 1.12 (dashed line). (c, d) $\tilde{\gamma_v} = \gamma_v \tau_r = 2 \times 10^3$, $\tilde{D_v} = D_v \tau_r / \bar{v}^2 = 10^{11}$ with $Pe = v_0/\bar{v} = 2 \times 10^3$ (solid line), 10 (dashed line). The inset in Figure (c) (zoomed in view of the shaded region in main figure) shows a sub-diffusive behavior in the parallel component of displacement fluctuation over an intermediate time regime. 76

3.10 (color online) Persistent motion: Plots of $\langle \mathbf{r}^4 \rangle$ (a, b) and Kurtosis $(\mathcal{K})$ (c, d) as a function of time in two dimensions. (a, c) Parameter values used are $\tilde{\gamma_v} = \gamma_v \tau_r = 10^2$, $\tilde{D_v} = D_v \tau_r / \bar{v}^2 = 4 \times 10^4$, and $Pe = v_0/\bar{v} = 7.07$. (b, d) Parameter values used are $\tilde{\gamma_v} = \gamma_v \tau_r = 5 \times 10^{-2}$, $\tilde{D_v} = D_v \tau_r / \bar{v}^2 = 0.25$, and $Pe = v_0/\bar{v} = 3.54$. The points denote simulation results averaged over 10^6 independent trajectories. The solid lines depict analytic results obtained from the inverse Laplace transform of Eq. (3.47). The orange line in (c, d) corresponds to zero kurtosis. Initial conditions used are speed $v_1/\bar{v} = Pe$ and orientation $\hat{\boldsymbol{u}}_0 = \hat{x}$. 83

3.11 (color online) Directed persistent motion: (a) $\langle \mathbf{r}^4 \rangle$ and (b) Kurtosis $\mathcal{K}$ as a function of time in 2d at $\tilde{\gamma_v} = \gamma_v \tau_r = 0.5$, $\tilde{D_v} = D_v \tau_r / \bar{v}^2 = 1$, $Pe = v_0/\bar{v} = 1$, and $\tilde{\boldsymbol{F}}_0 = \mu \boldsymbol{F}_0 / \bar{v} = 0.01\ \hat{r}$. The solid line in ($a$) and ($b$) correspond to the inverse Laplace transform of Eq. (3.47). The dashed line in (a) corresponds to the long-time scaling in Eq. (3.51). The dashed line in (b) is corresponds to $\mathcal{K} = 0$. The initial conditions used are the speed $v_1/\bar{v} = Pe$ and the heading direction $\hat{\boldsymbol{u}}_0 = \hat{x}$. . 84

3.12 (color online) Active speed autocorrelation $\langle \delta v(\tau) \delta v(0) \rangle$ as a function of time τ at $\tilde{D_v} = D_v \tau_r / \bar{v}^2 = 1$, $Pe \equiv v_0/\bar{v} = 1$ for $\tilde{\gamma_v} = \gamma_v \tau_r = 10(\circ)$, $1(\triangle)$, $0.01(\diamond)$. The points denote simulation results and the lines correspond to the function $\exp(-\gamma_v \tau)$ calculated in Eq. (3.60). Here $\langle \delta v(\tau) \delta v(0) \rangle = \langle \delta v(\tau) \delta v(0) \rangle / \langle \delta v^2(0) \rangle$ with $\langle \delta v^2(0) \rangle = D_v / \gamma_v$. . . . 88

3.13 (color online) Cumulative distribution function $F(v_m)$ in Eq. (3.65) as a function of v_m at $D_v\tau_r/\bar{v}^2 = 1$. (a) $Pe = 0, 1, 5$ and $\gamma_v\tau_r = 1$. (b) $\gamma_v\tau_r = 0.1, 1, 10$ and $Pe = 1$. 89

4.1 (color online) Time dependence of (a) $\langle \mathbf{r}^2\rangle$ in Eq. (4.9) and (b) $\langle \delta\mathbf{r}^2\rangle$ in Eq. (4.13) in $d = 2$ for $Pe = v_0/\bar{v} = 1$ (dashed line), 100 (solid line) with $\tilde{D}_{\rm a} = D_{\rm ac}\tau_r/\bar{\ell}^2 = 1$. The crossover times for $Pe = 100$ are (a) $t_I \approx 6 \times 10^{-4}$ and $t_{II} \approx 3$ and (b) $t_I = 0.03$ and $t_{II} \approx 4/3$. . . 95

4.2 (color online) Comparision of $\langle \mathbf{r}^2\rangle$ in Eq. (4.9) (solid line) with $\langle \mathbf{r}^2\rangle$ in Eq. (4.10) (dashed line) in two dimensions. Parameter values used are $Pe = v_0/\bar{v} = 1$ (green solid line), 100 (red solid line) with $\tilde{D}_{\rm a} = D_{\rm ac}\tau_r/\bar{\ell}^2 = 1$. We used the conversion of the parameters $(D_v\tau_r/\bar{v}^2)/(\gamma_v^2\tau_r^2) = D_{\rm ac}\tau_r/\bar{\ell}^2$ with $D_v\tau_r/\bar{v}^2 = 0.1$ (a) and 10^6 (b). . 97

4.3 (color online) Components of displacement fluctuation in two dimensions for low activity ($Pe^2 \leq \tilde{D}_{\rm a}$). Points denote simulations results and lines depict analytical predictions. The components of displacement fluctuations $\langle \delta r_{\|}^2\rangle$ (○, red) and $\langle \delta\mathbf{r}_{\perp}^2\rangle$ (△, blue) correspond to Eq. (4.18) and Eq. (4.19) respectively. The parameter values used for (a) $\tilde{D}_{\rm a} = D_{\rm ac}\tau_r/\bar{\ell}^2 = 1$ and $Pe = v_0\tau_r/\bar{\ell} = 0.1$, (b) $\tilde{D}_{\rm a} = D_{\rm ac}\tau_r/\bar{\ell}^2 = 1$ and $Pe = v_0\tau_r/\bar{\ell} = 1$, (c) $\tilde{D}_{\rm a} = D_{\rm ac}\tau_r/\bar{\ell}^2 = 10^3$ and $Pe = v_0\tau_r/\bar{\ell} = 31.62$. The parallel component shows subdiffusive behavior as the condition $Pe^2 \leq \tilde{D}_{\rm a}$ holds. (c) The crossover timescales are $t_I^{\perp}/\tau_r = 10^{-3}$, and $t_{II}^{\perp}/\tau_r = 1$. 100

4.4 (color online) Components of displacement fluctuation in $d = 2$ for high activity $Pe^2 > \tilde{D}_{\rm a}$. The points denote numerical simulations and the lines denote theory. The parallel (○, red) and perpendicular (△, blue) components of displacement fluctuation correspond to Eq. (4.18) and Eq. (4.19) respectively. The parameter values used are (a) $\tilde{D}_{\rm a} = D_{\rm ac}\tau_r/\bar{\ell}^2 = 1$, $Pe = v_0\tau_r/\bar{\ell} = 10^2$ and (b) $\tilde{D}_{\rm a} = D_{\rm ac}\tau_r/\bar{\ell}^2 = 10^5$ and $Pe = v_0\tau_r/\bar{\ell} = 1.58 \times 10^4$. In (a), the crossover times are denoted by $t_I^{\|}/\tau_r = 0.11$, $t_{II}^{\|}/\tau_r = 0.71$, $t_I^{\perp}/\tau_r = 1.7 \times 10^{-2}$, and $t_{II}^{\perp}/\tau_r = 0.8$. In (b), the crossover times are denoted by $t_I^{\|}/\tau_r = 0.13$, $t_{II}^{\|}/\tau_r = 0.71$, $t_I^{\perp}/\tau_r = 10^{-5}$, $t_{II}^{\perp}/\tau_r = 1.2 \times 10^{-3}$, and $t_{III}^{\perp}/\tau_r = 0.8$. 102

4.5 (color online) Probability distribution of displacement $2\pi p(\tilde{r})$ at $Pe = v_0\tau_r/\bar{\ell} = 31.6$ and $\tilde{D}_{\rm ac} = D_{\rm ac}\tau_r/\bar{\ell}^2 = 10$ over different time-segments expressed as $L = v_0 t/\bar{\ell} = 0.32$ (a), 0.63 (b), 3.16 (c), 31.62 (d), 126.49 (e), and 316.23 (f). Here $\tilde{r} = r/L$. 104

4.6 (color online) (a) Fourth moment and (b) kurtosis of displacement as a function of time in $d = 2$ at $\tilde{D}_{\rm a} = 1$. Points denote numerical simulations and lines denoted theory. (a) Two crossovers at $Pe = 0.1$ (red ∘): $\langle \mathbf{r}^4 \rangle \sim t^2$ to $\sim t^\alpha$ with $\alpha < 2$ to $\sim t^2$. Three crossovers at $Pe = 0.3$ (green △): $\langle \mathbf{r}^4 \rangle \sim t^2$ to $\sim t^\alpha$ with $\alpha < 2$ to $\sim t^\alpha$ with $\alpha > 2$ to a final $\sim t^2$. (c) Kurtosis as a function of time corresponding to (a). (b) Kurtosis as a function of time corresponding to $Pe = 0.1$ (red solid line) and $Pe = 0.3$ (green dashed line). 108

4.7 (color online) (a) Fourth moment and (b) kurtosis of displacement as a function of time in $d = 2$ at $\tilde{D}_{\rm a} = 1$. (a) Two crossovers at $Pe = v_0\tau_r/\bar{\ell} = 4$ (▽) at $t_I \approx 0.17$ and $t_{II} \approx 6.38$. Three crossovers at $Pe = v_0\tau_r/\bar{\ell} = 10$ (◇) at $t_I \approx 0.027$, $t_{II} \approx 0.32$, and $t_{III} \approx 1.42$. (b) Kurtosis as a function of time at $Pe = 4$ (solid line) and $Pe = 10$ (dashed line). 109

4.8 (color online) Deviation from Gaussian nature: A heat map of kurtosis $\mathcal{K}$ for different Pe and time t in $d = 2$ at $\tilde{D}_{\rm a} = 1$. 110

5.1 (color online) Schematic diagram of the model where a motile MT filament is attached with a harmonic trap of stiffness constant K_T. When attached, kinesin walks along the filament towards right with a velocity v_m, pulling the filament towards left. Figure is adapted from Subhadip Ghosh's thesis. 116

5.2 (color online) Phase diagram under constant loading in $\tilde{v}_0 - \tilde{f}_d$ plane shown using the heat map of the quantity q defined in Eq. (5.6). We use parameter values typical of a microtubule- kinesin system, $\tilde{k}_m = 450\,(k_m = 1.7\,{\rm pN/nm})$, $\tilde{f}_s = 60$, $\tilde{\omega} = 20$ and use $N = 5$ number of MPs. The color-box shows the mapping of q-values to the color code. The light blue (yellow) region denotes unstable (stable) phase under perturbation. 120

5.3 Phase diagram for filament in MP assay under elastic loading in $N - \tilde{\omega}$ plane, with $\tilde{k}_m = 450$, $\tilde{v}_0 = 24.24$, $\tilde{f}_s = 60$, $\tilde{f}_d = 19.2$, $\tilde{K}_T = 83$ kept fixed. The lines denote the linear stability phase boundaries between linearly stable (s), stable spiral (ss), unstable spiral (us), and linearly unstable (u) phases. The points denoted by △ and ○ indicate decaying oscillations and limit cycle oscillations, respectively, corresponding to the full non-linear dynamics in Eq. (5.4). Phase diagram for filament in MP assay under harmonic trap in $\tilde{v}_0 - \tilde{f}_d$ plane, keeping $\tilde{k}_m = 450$, $\tilde{\omega} = 20$, $\tilde{f}_s = 60$, $N = 5$ and $\tilde{K}_T = 83$ fixed. 124

5.4 The linear stability phase boundary between the stable spiral (blue: ss) and unstable spiral (yellow: us) phase in the plane of elastic loading stiffness K_T and MP number N is shown using the heat map of $C - AB$ in Eq. (5.10). The color box shows the mapping for the values of the function. Parameters used correspond to kinesin-microtubule assay, keeping $\tilde{k}_m = 450$, $\tilde{\omega} = 20$, $\tilde{f}_s = 60$, $\tilde{f}_d = 19.2$, $\tilde{v}_0 = 24.24$ fixed. The points denoted by $\triangle$ and $\bigcirc$ indicate decaying oscillations (ss) and stable limit cycle oscillations (us), respectively, corresponding to the full non-linear dynamics shown in Eq. (5.4). Here we express K_T in units of pN/nm. 125

5.5 (color online) (a, b) Kymographs show the time evolution of the probability distributions of MPs with extension $\tilde{y}$: (a) in the attached state (P_a), and (b) in the detached state (P_d). The color-box describes the values of probability distributions. The relaxation dynamics are determined by dimensionless diffusion constants $\tilde{D}_a = 15.6$, $\tilde{D}_d = 17.4$, and the relaxation rate $\tilde{\nu} = 80$. Other parameter values used are $\tilde{v}_0 = 50$, $\tilde{f}_d = 4$, $\tilde{k}_m = 4.57$, $\tilde{\omega} = 5$, $\tilde{f}_s = 14.29$, $N = 160$ and $\tilde{K}_T = 4.57$. (c) Phase diagram for harmonically trapped microtubule-kinesin assay in $\tilde{v}_0$-$\tilde{f}_d$ plane, at fixed $\tilde{k}_m = 4.57$, $\tilde{\omega} = 5$, $\tilde{f}_s = 14.29$, $N = 160$ and $\tilde{K}_T = 4.57$. The points denote the two phases characterized by decaying oscillations ($\triangle$) and stable limit cycle oscillations ($\bigcirc$) obtained from numerical simulations. The solid black line identifies the boundary of supercritical Hopf-bifurcation predicted by Eq. (5.10). (d, e) Dynamics corresponding to open $\circ$. (d) Time series of $\tilde{x}$ (solid line) and $\tilde{n}_m$ (dashed line). (e) Unstable limit cycle corresponding to time series of growing oscillation in (d). (f, g) Dynamics corresponding to open $\triangle$. (d) Time series of $\tilde{x}$ (solid line) and $\tilde{n}_m$ (dashed line). (e) Stable limit cycle corresponding to time series of decaying oscillation in (f). 128

5.6 (color online) Schematic representation of Microtubule-kinesin motors. Motile microtubule filament attaches with a harmonic trap of stiffness constant K_T. The attached active kinesin represent in blue head walks along the filament towards the right with a velocity v_m, pulling the filament towards the left. Pluronic F-127 used for surface blocking. 130

5.7 (color online) Time evolutions of (a) microtubule displacement $\tilde{x}(\tau)$, and (b) mean kinsein extension $\tilde{y}(\tau)$. (c) A parametric plot of $\tilde{x}(\tau)$ and $\tilde{y}(\tau)$ shows stable limit cycle. (d) Correlation function of microtubule displacement $C_{\tilde{x}}(\tau)$ in the time-periodic steady state. The red (green) lines in all these figures correspond to numerical simulations (solutions to the Fokker-Planck based mean field equations). We used $\tilde{v}_0 = 50$, $\tilde{f}_d = 4$. All other parameter values are the same as in Fig. (5.5)(c). 131

6.1 (color online) A schematic diagram of the system showing a polymer floating on the motility assay. The *tails* of MPs are attached irreversibly on a square grid. The *head* domains can attach to the filament, when any segment of it comes within the capture radius. The active extension of the attached *head* along the filament generates force in the opposite direction. The MP *stalk* is modeled as a harmonic spring. 138

6.2 (color online) Time evolution of the turning number ψ_N at $Pe = 10^5$ and the ratio $\omega_{\mathrm{on}}/\omega_0 = 1$. Time t is expressed in the unit of τ. The plot shows stochastic switching between three states, an open state with $\psi_N \approx 0$, and two spiral states with $\psi_N \approx \pm 3$. Representative polymer configurations corresponding to the three states are shown at three time instances indicated by arrows. 141

6.3 (color online) Typical configurations of the (a) formation and (b) breaking of the spiral at $Pe = 10^5$ and the ratio $\omega_{\mathrm{on}}/\omega_0 = 1$. Time t is expressed in the unit of τ. The solid point indicate the head of the spiral. 141

6.4 (color online) Typical configurations of the rotation of the spiral at $Pe = 10^5$ and the ratio $\omega_{\mathrm{on}}/\omega_0 = 1$. Time t is expressed in the unit of τ. The solid point indicate the head of the spiral. 142

6.5 (color online) (a) Probability distribution functions of turn number $p(\psi_N)$ for different $Pe = \tilde{Pe} \times 10^5$ where values of $\tilde{Pe}$ are denoted in the figure legend, at a fixed ratio $\omega_{on}/\omega_0 = 1$. The triple- maxima characterize the coexistence in transition from open chains to spirals. The dependence of the stable (global) (red ○) and metastable (blue ◇) maxima of $p(\psi_N)$ are shown as a function of Pe at $\omega_{\mathrm{on}}/\omega_0 = 1$ in (b), and as a function of $\omega_{\mathrm{on}}/\omega_0$ at $Pe = 1.39 \times 10^5$ in (c). In (b), the green lines show the plot of $\pm(|u_4|/2u_6)^{1/2}$, and the grey lines show the plot of $\pm(u_2/2u_4)^{1/2}$, where u_2, u_4 and u_6 are defined by Eq. (6.6). 143

6.6 (color online) Phase diagram calculated from probability distribution of turn number $p(\psi_N)$. The data points denoted by green △ denotes a stable open chain state, in the complete absence of spirals. The blue □ points denote stable open chains in the presence of metastable spirals. The red ○ denotes stable spirals coexisting with metastable open chains. The boundaries between □ and ○ denote the binodals where open chains and spirals are equally probable. The solid line capturing one such phase boundary is a plot of the function $\omega_{\mathrm{on}}/\omega_0 = \alpha/(Pe - \alpha)$ where $\alpha = 3.67 \times 10^4$ (see Section-(6.6)). 145

6.7 (color online) (a) The steady state turning number fluctuation $\langle\psi_N^2\rangle$ as a function of Pe at different values of $\omega_{\rm on}/\omega_0$ ratios denoted in the figure legend. (b) Approximate data collapse of different plots in (a) by using scale factors $\mathcal{A}$, $\mathcal{B}$. Inset: The dependence of $\mathcal{A}$ and $\mathcal{B}$ on $q=\omega_{\rm on}/\omega_0$. The solid line $\Omega_f = 1.42\,q/(0.52+q)$ shows a fit to the data for $\mathcal{A}$. The dotted line shows a fit $(0.37+q)/1.41\,q$ to the data for $\mathcal{B}$ in the regime $q>0.3$. The dash- dotted line is a plot of $1/\Omega_f$. Comparison of time series of ψ_N for bond lengths $r_0 = 1.0\sigma$ (red), 0.75σ (blue) and 0.5σ (green) are shown at $Pe = 3.97\times10^4$ (c) and $Pe = 3.97\times10^5$ (d). Time t is expressed in the unit of τ. The data for $r_0 = 0.75\,\sigma$ and $0.5\,\sigma$ are shifted upwards by 8 and 16 for better visibility. (e) Kurtosis $\mathcal{K}_{\psi_N}$ of turning number ψ_N plotted at $\omega_{\rm on}/\omega_0 = 0.2,\ 1.0,\ 20$ with data shown by the same symbols as in (a). The open □ and ○ denote data at $\omega_{\rm on}/\omega_0 = 1.0$ for $r_0 = 0.75\,\sigma$ and $0.5\,\sigma$ respectively. 146

6.8 (color online) (a) End-to-end distribution functions $2\pi p(\tilde{r}_e)$ for $Pe = \tilde{Pe}\times10^5$ with $\tilde{Pe}$ values shown in the figure legend, at a fixed $\omega_{\rm on}/\omega_0 = 1$. ($b$) Mean squared end- to- end separation $\langle\tilde{r}_e^2\rangle$ as a function of Pe for $\omega_{on}/\omega_0 = 0.5\,(\triangledown),\ 1\,(\triangle),\ 5\,(\square),\ 10\,(\diamond),\ 20\,(\bigcirc)$. Error bars are smaller than the symbol size. The lines through data are guides to eye. 150

6.9 (color online) Persistence length. (a) Tangent-tangent correlation function for $Pe\times10^{-5} = 0(\square),\ 0.99(\bigcirc),\ 1.98(\triangle)$ and $\omega_{on}/\omega_0 = 1$. The points denote the simulation results, and the solid lines represent the fitting functions $\exp(-\tilde{s}/\tilde{l}_p)$. ($b$) Variation of the effective persistence length $\tilde{l}_p$ with Pe at $\omega_{\rm on}/\omega_0 = 0.5\,(\triangledown),\ 1\,(\triangle),\ 5\,(\square),\ 10\,(\diamond),\ 20\,(\bigcirc)$. The lines through data are guides to eye. At equilibrium, the chain has persistence length $\tilde{l}_p \approx 0.3$, close to the values at $Pe = 0$. 151

6.10 (color online) Probability distributions of the eignevalues (a) $\tilde{\lambda}_+$, and (b) $\tilde{\lambda}_-$, (c) size $\tilde{R}_g^2$, and (d) shape $\tilde{R}_s^2$ are shown. All the distribution functions are obtained at $\omega_{\rm on}/\omega_0 = 1$, and the different graphs in (a)–(d) correspond to the $Pe = \tilde{Pe}\times10^5$ with $\tilde{Pe}$- values indicated in the legend of (a). 152

6.11 (color online) Radius of Gyration. Fig. (a), (b) shows the variation of size $\langle\tilde{R}_g^2\rangle$ and shape $\langle\tilde{R}_s^2\rangle$ with standard error as a function of Pe at different $\omega_{on}/\omega_0 = 0.5$ (brown $\triangledown$), 1 (pink $\triangle$) 5 (green $\square$), 10 (blue $\diamond$), 20 (red $\bigcirc$) respectively. 153

6.12 (color online) Two time autocorrelation function $C_{\psi_N}(t) = \langle\psi_N(t)\psi_N(0)\rangle/\langle\psi_N^2(0)\rangle$ evaluated at different $Pe = \tilde{Pe}\times10^5$ with $\tilde{Pe}$ shown in the figure-legend keeping the on- off ratio $\omega_{\rm on}/\omega_0 = 1$ constant. Time t is expressed in the unit of τ. 154

6.13 (color online) Two- time correlation functions of (a) R_g^2, and (b) R_s^2 at various $Pe = \tilde{P}e \times 10^5$ with $\tilde{P}e$-values indicated in the legend, keeping $\omega_{\text{on}}/\omega_0 = 1$ fixed. Time t is expressed in the unit of τ. The points are same as in Fig. (6.12) 155

6.14 (color online) Two- time correlation functions of eigen- vector $\hat{\boldsymbol{u}}$ at various $Pe = \tilde{P}e \times 10^5$ with $\tilde{P}e$-values indicated in the legend, keeping $\omega_{\text{on}}/\omega_0 = 1$ fixed. Time t is expressed in the unit of τ. The points are same as in Fig. (6.12) 156

6.15 (color online) (a) Variation of correlation time τ_c (in the unit of τ) with Pe at $\omega_{\text{on}}/\omega_0 = 1$, obtained for ψ_N, R_g^2, R_s^2, and $\hat{\boldsymbol{u}}$. The brown solid line denotes the scaling form $1/Pe^2$. (b) Time scales calculated at $\omega_{\text{on}}/\omega_0 = 1$ using the expressions from the approximate non-conserved dynamics Eq. (6.11). 158

6.16 (color online) Increase in equilibrium persistence length due to reduction of bond length r_0 with respect to the WCA length scale σ. Tangent-tangent correlation functions $\langle \hat{t}(\tilde{s}) \cdot \hat{t}(0) \rangle$ as a function of $\tilde{s} = s/L$ are shown at three values of $r_0/\sigma = 1$, 0.75, 0.5. The lines denote the exponential decay of correlation as $\exp(-\tilde{s}/\tilde{l}_p)$, with corresponding persistence length $\tilde{l}_p$ denoted in the figure legend. Plots for $r_0/\sigma = 0.75$, 0.5 are shifted upwards by 0.2 and 0.4 for better visibility. 161

6.17 (color online) Two time correlation functions of turning number $C_{\psi_N}(t)$ for a smoothened polymer with $r_0/\sigma = 0.75$ calculated at $\omega_{\text{on}}/\omega_0 = 1$ and various activity $Pe = \tilde{P}e \times 10^5$ with $\tilde{P}e$-values denoted in the figure legend. The inset shows a non-monotonic variation of the corresponding correlation times with Pe. 162

7.1 (Color online) Schematic representation of actomyosin complex: Bound state and unbound state. Bound state : Myosin II attached F-actin and Unbound state : Myosin II and F-actin in detached state. The diagram also indicates myosin subunits, and globular actins (G-actin). 165

7.2 (Color online) Two component active fluids system with uniform turnover in the absence of pressure $\xi = 0$. Plot of the maximum eigen value $\lambda_{max} = (tr + \sqrt{\Delta})/2$ of the linear stability matrix in Eq. (7.10) as a function of q with Péclet numbers $Pe = 5.0(\bigcirc)$, $5.5(\triangle)$, $6.0(\diamond)$. Inset: The first zero crossing of maximum eigen value (λ) is shown for $Pe = 2.0(\bigcirc)$, $2.5(\triangle)$, $3.0(\diamond)$. In a system of size $L = 2\pi$, the minimum possible q mode that influences the system is $q = 2\pi/L = 1$. This suggests that the uniform state in such a system at $Pe = 5.0$ will be linearly stable – see the region inside the black dashed line in the main figure covering the region of $\lambda > 0$ and $q \geq 1$. With increasing system size L, smaller q-modes can appear. The parameter values used are $D = 0.1$, $\omega_0 = 1$, $\omega_{on} = 1$, $C_{t0} = 1$. 170

7.3 (Color online) Two component active fluid with uniform turnover in the absence of pressure $\xi = 0$. The system size is $L = 2\pi$. (a) shows a non-uniform pattern of bound concentrations $C_b(x)$. (b) shows a non-uniform pattern of unbound concentrations $C_u(x)$. (c) corresponding to the velocity profile $v(x)$ and (d) represents the active stress $\sigma_a(x)$. The parameter values are $D = 0.1$, $\omega_0 = 1$, $\omega_{on} = 1$, $C_{t0} = 1$ and $Pe = 5.5$. 171

7.4 (Color online) Phase diagram for the two component active fluid with uniform turnover and pressure $\xi = 0$ for system size $L = 2\pi$ in one dimension. The linearly stable (LS) regime represents $\lambda_{max} < 0$ and linearly unstable (LU) regime represents $\lambda_{max} > 0$. The phase boundary corresponds to $\lambda_{max} = 0$ where $\lambda_{max} = (tr + \sqrt{\Delta})/2$ where tr is given by Eq. (7.11) and Δ is given by Eq. (7.12). The points denote results from direct numerical integrations of Eq. (8.5), (8.6), and (8.7). The symbols denote homogeneous steady state ($\bigcirc$) fluid pattern and inhomogeneous pattern formation ($\triangledown$). The growing modes within linearly stability analysis corresponding to the linearly unstable regime (LU) regime stabilizes by the non-linearities in the equations forming steady patterns. The parameter values used are $D = 0.1$, $\omega_0 = 1$, $C_{t0} = 1$. 172

7.5 (Color online) Two component active fluids system with uniform turnover in the presence of pressure $\xi = 1$. Plot of the real part(black solid line) and imaginary part(blue dashed line) of the maximum eigen value $\lambda_{max} = (tr + \sqrt{\Delta})/2 \equiv \lambda_{Re} + i\lambda_{Im}$ of the linear stability matrix Ω in Eq. (7.13) as a function of mode number q. Fig. (a), (b), and (c): $Pe = 15$, $\omega_{on} = 0.001$ (a), 0.011 (b), and 0.021 (c). Fig. (d), (e), and (f): $\omega_{on} = 0.01$, $Pe = 11$ (d), 12 (e), and 13 (f). The parameter values are $D = 0.1$, $\omega_0 = 0.01$, $C_{t0} = 1$. 173

7.6 (Color online) Phase diagram of the two component active fluid with uniform turnover in the presence of pressure $\xi = 1$, for system size $L = 2\pi$ in one dimension. The black solid line corresponds to $tr = 0$ in Eq. (7.14), and the dashed blue line corresponds to $\Delta = 0$ and $tr > 0$ in Eq. (7.15). The regime between these two lines represents the unstable spiral phase. The points denote numerical integrations of Eq. (8.5), (8.6), and (8.7). The symbols denote regimes of homogenous steady state (○), localized pulsation (◇), and inhomogeneous steady state pattern (□). The parameter values used are $D = 0.1$, $\omega_0 = 0.01$, $C_{t0} = 1$. 175

7.7 (Color online) Evolution of the relevant fields (a) $C_b(x,t)$, (b) $C_u(x,t)$, and (c) $v(x,t)$ for the two component active fluid with uniform turnover in the presence of pressure $\xi = 1$. The parameter values are $D = 0.1$, $\omega_0 = 0.01$, $C_{t0} = 1$, $\omega_{\mathrm{on}} = 0.004$, $Pe = 20$ correspond to the localized pulsatory patterns. The initial homogeneous state starts to show pulsations ear $t = 150$. 176

7.8 (Color online) Evolution of the relevant fields (a) $C_b(x,t)$, (b) $C_u(x,t)$, and (c) $v(x,t)$ for the two component active fluid with uniform turnover in the presence of pressure $\xi = 1$. The parameter values $D = 0.1$, $\omega_0 = 0.01$, $C_{t0} = 1$, $\omega_{on} = 0.005$, $Pe = 20$ correspond to stationary pattern formation. The initial homogeneous state starts to form pattern near $t = 100$. 177

7.9 (Color online) Two component active fluids system with stress-dependent turnover in the presence of pressure $\xi = 1$. The steady state solution of bound concentration C_{b0} is shown as a function of ω_{on} and Pe. We numerically solved the self-consistent Eq. (7.16) for parameter values $D = 0.1$, $\alpha = -0.1$ $\omega_0 = 0.01$, $C_{t0} = 1$. 177

7.10 (Color online) Phase diagram of the two component active fluid with stress-dependent turnover in the presence of pressure $\xi = 1$, for system size $L = 2\pi$ in one dimension. The different color shades correspond to predictions of three different states from linear stability analysis: stable spiral (green SS), unstable spiral (red US), linearly unstable (yellow LU). The symbols denote phase behaviors obtained from direct numerical integration of Eq. (8.5), (8.6), and (8.7). The symbols denote regimes of pattern formation (□), localized pulsation (◇), and homogeneous fluid (○). The parameter values used are $D = 0.1$, $\alpha = -0.1$ $\omega_0 = 0.01$, $C_{t0} = 1$. 178

8.1 (Color online) Pulsed contractility in actomyosin. Myosin II *contractility*-induced advection leads to the actomyosin assembly state. Negative feedback via strain-rate from the myosin II reduces (enhances) the off-rate at the center (edges) of the assembly state [27]. 183

8.2 (Color online) Plots of the real (solid line) and imaginary (dashed line) parts of the maximum eigen-value of the linear stability matrix as a function of wave number q for the two component active fluid with strain-rate dependent turnover in one dimension. The parameter values are $D = 0.1$, $\omega_0 = 1$, $\alpha = 10$, $C_{t0} = 1$. (a, b, c) $Pe = 2.75$, $\omega_{on} = 0.25(a)$, $1.00(b)$, $1.75(c)$. (d, e, f) $\omega_{on} = 1.0$, $Pe = 2.0(d)$, $2.5(e)$, $3.0(f)$. 186

8.3 (Color online) Phase diagram in ω_{on}-Pe plane for two component active fluids with strain-rate-dependent turnover in one dimension. The lines correspond to phase boundaries calculated from the linear stability matrix(Ω) represents in Eq. (8.9). The solid black line is the plot of the $tr = 0$. The dashed blue line corresponds to $tr^2 - 4\ det = 0$ with the condition $tr > 0$ and the dashed green line corresponds to $det = 0$ with the condition $tr < 0$. The points denote numerical results: homogenous steady-state (○), moving phase-separated pattern(◇), stationary mixed pattern(▽), and stationary phase-separated pattern(□). The moving pattern is shown in Fig. (8.4). The stationary mixed and phase-separated patterns are shown in Fig. (8.6). The parameter values used in this plot are $L = 2\pi$, $D = 0.1$, $\omega_0 = 1$, $\alpha = 10$, $C_{t0} = 1$. 188

8.4 (Color online) Moving pattern. Kymogrsph shows the time evolution of C_a, C_p and v for two component active fluids with strain-rate-dependent turnover in one dimension. The parameter values are $L = 2\pi$, $D = 0.1$, $\omega_0 = 1$, $\omega_{on} = 0.5$, $Pe = 2.6$, $C_{t0} = 1$. 190

8.5 (Color online) (a) Time evolution of S_b, S_u and S_v for two component active fluids with strain-rate-dependent turnover in one dimension. Here $S_b \equiv S_b - C_{b0}$ and $S_u \equiv S_u - C_{u0}$ where $C_{b0} = \omega_{on} C_{t0}/(\omega_0 + \omega_{on})$ and $C_{u0} = C_{t0} - C_{b0}$. The parameter values are $D = 0.1$, $\omega_0 = 1$, $\omega_{on} = 0.5$, $Pe = 2.6$, $q = 1$, $C_{t0} = 1$. (b) Average flow velocity($|S_v|$) as a function of ω_{on} for Pe =2.75. (c) Average flow velocity($|S_v|$) as a function of Pe for $\omega_{on} = 1$. (b, c) The parameter values are $L = 2\pi$, $D = 0.1$, $\omega_0 = 1$, $C_{t0} = 1$. 192

8.6 (Color online) Kymogrsph shows the time evolution of C_a, C_p and v for two component active fluids with strain-rate-dependent turnover in one dimension with $L = 2\pi$, $D = 0.1$, $\omega_0 = 1$, $C_{t0} = 1$. (a, b, c) Stationary (mixed) pattern. The parameter values are $\omega_{on} = 0.15$, $Pe = 3.5$. (d, e, f) Stationary phase-separated pattern. The parameter values are $\omega_{on} = 0.5$, $Pe = 3$. 193

8.7 (Color online) Time evolution of S_b, S_u and S_v for two component active fluids with strain-rate-dependent turnover in one dimension with $L = 2\pi$, $D = 0.1$, $\omega_0 = 1$, $C_{t0} = 1$. Here $S_b \equiv S_b - C_{b0}$ and $S_u \equiv S_u - C_{u0}$ where $C_{b0} = \omega_{on} C_{t0}/(\omega_0 + \omega_{on})$ and $C_{u0} = C_{t0} - C_{b0}$. The parameter values corresponds to (a) stationary (mixed) pattern with $\omega_{on} = 0.15$ and $Pe = 3.5$ and (b) stationary phase-separated pattern with $\omega_{on} = 0.5$ and $Pe = 3$. 194

LIST OF TABLES

3.1 $\langle \mathbf{r}^2 \rangle$ scaling: characterizing dominance of fluctuation in diffrent regime 62

5.1 Parameters: Two values of v_0 and f_d correspond to ATP concentrations of 5 μM and 2 mM respectively. 118

8.1 We list the physical parameter values used in our analysis. 196

8.2 We estimate various scaled parameter values and ranges using Table-8.1. We list all the scaled parameters here. 196

1

Introduction

Active matter consists of self-propelled elements [2, 3, 24, 28–30]. They consume and dissipate energy at the smallest scale to maintain self-propulsion and produce active stress in the local environment. Such systems remain out of equilibrium, breaking the detailed balance condition and the equilibrium fluctuation-dissipation relation. Biological examples of active matter are abound in nature. They are found across scales, from microscopic molecular motors and cytoskeletal extracts, swimming and gliding bacteria, motile cell cultures to macroscopic bird flocks and animal herds [2]. While the number of artificial self propelled systems remains smaller, their examples are rapidly growing. They include sub-micron sized active colloids, active rollers, vibrated granular rods, and robots [3].

In fabricated active matter, the self propulsion can be achieved following several routes. For example, silica micro-spheres half coated with platinum when immersed in hydrogen peroxide solution self-propels by hydrolyzing H_2O_2. The half-coating in these Janus particles breaks the isotropy allowing them to move in a directed fashion before undergoing reorientation, leading to a ballistic-diffusive crossover in dynamics (Fig. 1.1). The generation of self-propulsion involves stochastic processes, e.g., hydrolysis of hydrogen peroxide in the current example. Such stochasticity can

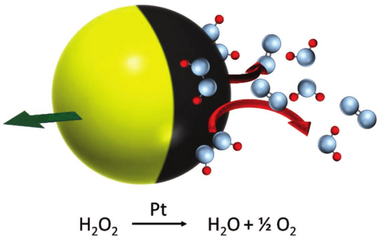

Figure 1.1: (color online) Example of a spherical active particle: a Janus swimmer with different surface property at two hemispheres. This shows decomposition of hydrogen peroxide on the platinum-covered hemisphere (black) to generate motion (green arrow). The figure is adapted from Ref. [25].

lead to important dynamical signatures as will be shown in the first part of this thesis. Another example of artificial self-propelled particle is camphor boats. In a solvent like water they can change the local surface tension by releasing camphor and utilize the change to generate self-propulsion [31, 32]. When vibrated, asymmetric granular rods can perform self-propulsion in a direction determined by the difference in friction between the two ends of the rod [2].

The non-equilibrium system of passive matter is typically driven from outside at the longest scale. Examples are: sheared fluid, where the shear stress or strain are applied from outside on the boundaries of the fluid; heat transport obtained by attaching two heat baths of different temperatures at the two ends of a system. In these examples, clearly, the driving is applied on the system from the largest scales, as opposed to the consumption and dissipation of energy by each individual elements at the smallest scale in active matter.

As has been already mentioned, biological examples of active matter are abundant in nature and found across scales: motor proteins [22, 33–36], cytoskeleton [7, 37–41], cell migration [42–44], bird flocking [45], formation of fish schools [46], etc. The cytoskeleton consists of semiflexible polymers like actin filaments, intermediate filaments and microtubules and associated motor proteins myosin, kinesin, dynein, etc [22, 47, 48]. Their persistence length l_p varies by orders of magnitude, e.g., filamentous actin has $l_p \approx 16\,\mu$m and microtubule has $l_p \approx 1$ mm [26]. The filaments are typically cross-linked to form a network which undergoes turnover [49–

51]. The motor-proteins associated with each kind of filament, e.g., myosin family on filamentous actin and kinesin family on microtubule, can move along them hydrolyzing ATP and can produce active stresses. The motor proteins share a conserved mechano- chemical cycle in which the energy release from ATP hydrolysis is used in motion and force-generation [5, 41, 52, 53]. Motor proteins move along the polar filament in a directed manner, e.g., on microtubules kinesin and dynein move in opposite directions, while kinesin is a plus-end directed motor, dynein moves towards the minus end. This consumption of energy and generation of drive at the shortest length-scale is the characteristic of active matter [2, 29, 54]. The cytoskeleton maintains the size and shape of cells and mediate their deformation and movement [39, 55].

Much of our current understanding of cytoskeletal extract was developed using gliding assay experiments as shown in Fig. (1.2). In such a setup, the tails of motor proteins are irreversibly attached to a substrate. The conjugate filament, e.g., microtubule for kinesin motor proteins, can glide on such an assay as the motor proteins bind to the filament and hydrolyze ATP to generate relative motion. Motion of such a filament under external load, e.g., arising from a harmonic trap can lead to limit cycle oscillations [56–59]. Competition between opposing groups of MPs can lead to spontaneous oscillations in gliding assays [60]. Cytoskeletal filaments driven by motor proteins shows interesting shape changes, e.g., spiral formation [17, 19, 61, 62] and collective gliding and swirling at higher densities [20, 21, 63]. In the second part of this thesis we consider a detailed model of molecular motors driving semiflexible filaments exploring the dynamics and shape changes.

The role of cytoskeleton in cell division is conserved across species. The dynamics and pattern formation in cell motility, cell shape change, cell division is yet to be fully understood. Similar spontaneous oscillations are observed in various contexts in cell biology [64, 65], e.g., sarcomere oscillations, mitotic spindle oscillations, and chromosome oscillations [66–69]. An example of a fluorescently labelled cell with its different components labelled by different colors is shown in Fig. (1.3). The actomyosin cytoskeleton consisting of F-actin network and myosin

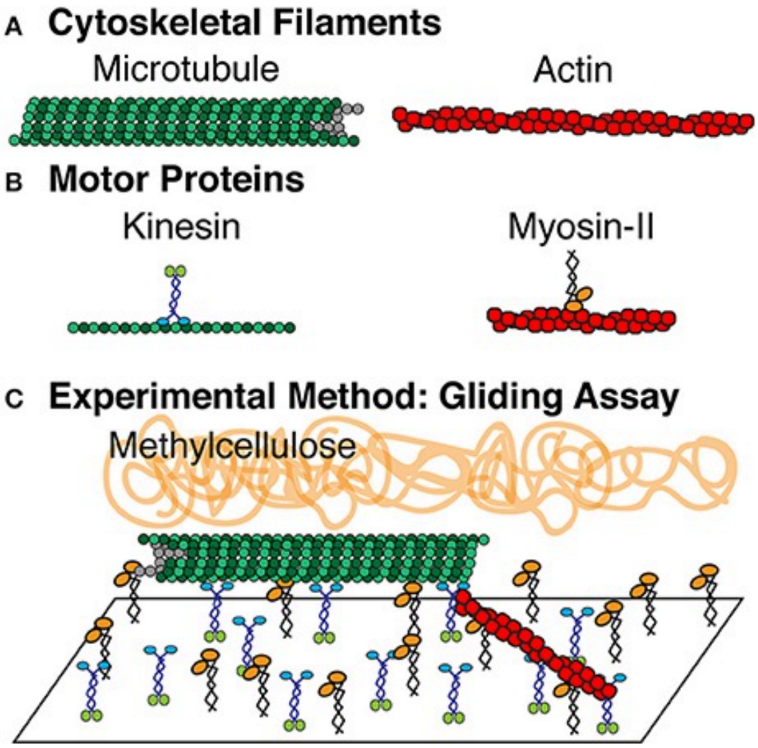

Figure 1.2: (color online) Schemetic representation of cytoskeletal filaments and motor proteins. (A) Microtubule and actin filament: microtubule polymerized from tubulin dimers and actin filament polymerized from globular actin monomers. (B) Kinesin motors move on microtubules hydrolyzing ATP. Myosin-II motor proteins move along F-actins hydrolyzing ATP. (C) An gliding assay of motor proteins consisting of kinesins and myosins adhered to a cover slip. Microtubules and F-actins are added to the chamber where they bind to the motor proteins and get propelled actively. The methylcellulose is added to keep the F-actin and microtubules crowded to the surface. The figure is adapted from Ref. [26].

motor proteins generate local contractile stress. The mechanism powers a wide range of physiological processes, e.g., muscle contraction, cell division, cell migration, and morphogenesis in cells and tissues. The contractile stress generated by myosin II is sensitive to external force and substrate stiffness [39, 70]. The F-actin network reorganizes with time to allow flow. The turnover of myosin association with the network microscopically depend on the load applied on myosins. The continuous cortical flows requires local remodelling of the actomyosin networks [71, 72]. In a coarse-grained level this provides a mechanism to relax the active stress generated on the network. Its role in actomyosin dynamics and pattern formation is not yet fully understood. The actomyosin can be modeled as an active fluid over long

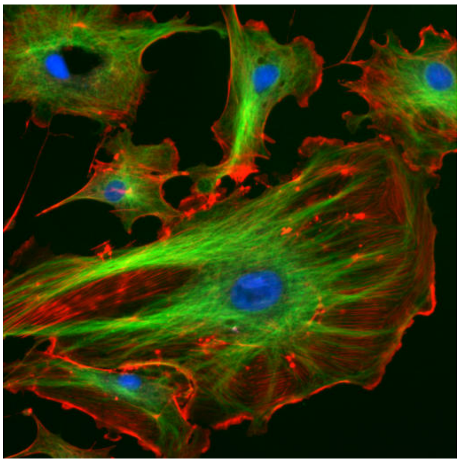

Figure 1.3: (color online) Components of the eukaryotic cell. The actin filaments are shown in red, microtubules in green, and the nuclei in blue. The figure is adapted from Wikipedia https://www.wikipedia.org/

time-scales. The local fluid velocity originates in response to the inhomogeneous contractile stress. It was recognized early on that changes in cellular and tissue morphology is determined by a close coupling between chemical and mechanical processes [73]. The generation of active mechanical forces utilizing ATP and associated active advection can lead to spatial pattern formation in cells [23, 74]. Such pattern formation, spontaneous oscillation, pulsation, propagation of stress waves were observed and studied in several contexts [57, 75–78]. In the last part of this thesis, we consider a simple two-component active hydrodynamic model for actomyosin, allowing for local turnover between active and passive state. We use this model to demonstrate emergence of various pattern forming and dynamical phases.

Outline of the thesis

In this thesis, we focus on active systems. In the first part, we study the dynamics of active Brownian particles (ABP). We propose and utilize a Laplace transform method based on Fokker-Planck equations to derive exact expressions for all possible moments of dynamical variables in arbitrary dimensions. We begin in Chapter-2 by considering ABPs with constant active speed in the presence of orientational diffusion and a thermal bath. We show that an exact mapping of the ABP trajectories to an equilibrium extensible semiflexible polymer is possible. The dynamics shows several ballistic-diffusive crossovers that we analyze in detail. In Chapter-3, and Chapter-4 we consider the impact of speed fluctuations on the dynamics of ABPs, again deriving several exact results. We present direct numerical simulations showing clear agreement with analytic predictions, and to obtain displacement distributions.

In the second part of the thesis, we consider filament- motor protein systems. In Chapter-5, we present a detailed model of a gliding assay of motor proteins and use numerical simulations to study the dynamics of a rigid rod on such an assay. We present detailed phase diagrams and study the impacts of various control parameters, e.g., the number of molecular motors, their active speed, attachment-detachment ratio etc. The behavior of the filament under external directed load and harmonic loading are presented. The numerical results show good agreement with mean field theory in the limit of large number of motor proteins. In Chapter-6 we consider the dynamics of a semiflexible filament on the molecular motor assay. Again we use a direct numerical simulation and compare our results with approximate mean field theory. We observe a re-entrant transition between open chain and spiral configurations.

In the last part of the thesis, we consider the dynamics of actomyosin in the presence of a substrate. We present and use a two-component active fluid model, allowing turnover between the components. In Chapter 7, we consider possibilities of constant turnover and stress-dependent turnover. In Chapter 8, we consider the possibility of a strain-rate dependent turnover. We perform direct numerical integrations of the coupled non-linear fields, and perform linear stability analysis to explore their properties. The two chapters show emergence of various pattern forming phases, pulsating patterns and, in one case, moving patterns.

Finally, in Chapter 9, we summarize our findings and conclude.

2

Active Brownian particle (ABP)

2.1 Introduction

Active particles are entities that can perform dissipative self-propulsion even in the absence of external driving force. Their dynamics violates equilibrium fluctuation-dissipation relation. The energy required for the motion is supplied at the local scale by different processes depending on the situation, e.g., internal energy depot in bacteria, hydrolysis of chemical fuel like ATP for molecular motors, and transverse shaking in active granular matter [1–4, 30, 58]. The direction of active motion is decided by the inbuilt asymmetry of the particles [4], or environment, e.g., as provided by filamentous tracks for molecular motors [58]. The system remains out of equilibrium, detailed balance being broken naturally in self propulsion.

The model of active Brownian particles (ABPs), in which a particle has its own heading direction of self-propulsion, while the heading direction itself performs rotational diffusion, has been used to describe self-propelled colloidal particles [79, 80]. Its behavior becomes equivalent to that of bacterial run and tumble motion in the long time limit [81]. A related model of the active Ornstein-Uhlenbeck process (AOUP) also describes self propulsion and has attracted considerable attention recently, due to its relative simplicity [8, 12, 82].

Despite a tremendous advancement in the knowledge of collective properties of active matter, the dynamics of single active particles is not yet completely understood. Some recent analytic results [8–10, 12–14, 83–90] indicate the qualitatively rich physics that even a single active particle can exhibit. The work in [9, 10] considered free ABP in two dimensions in the presence of thermal noise. Using a Fourier series expansion of the corresponding Fokker-Planck equation they were able to obtain various analytic results for the radial distribution and also some moments. In particular they computed the Kurtosis and pointed out that this could be used to differentiate the ABP from Gaussian models such as the AOUP. The same model was solved exactly in [12] by using a series expansion involving a Fourier basis for the position of the ABP and a Mathieu functions basis for its angular degree of freedom. On the other hand [13, 87] studied ABP without thermal noise and obtained exact results for short time and long time asympotitic properties of the positional distributions and pointed out the presence of anisotropies in short time behaviour.

Remarkably, the Fokker-Planck equation corresponding to the ABP, in the absence of thermal noise, was studied as early as 1952 [91, 92] in the context of understanding the so-called worm-like-chain (WLC) model of semi-flexible polymers. The WLC model is the continuous version of the Kratky-Porod model, which in turn corresponds to a persistent random walker. In fact an exact mapping can be obtained between the trajectories of an ABP and the equilibrium configurations of the semi-flexible polymer and this has been used to understand the equilibrium properties of the polymer [93–95]. On the other hand it is well known that trajectories of passive Brownian particles generate so-called flexible Gaussian polymers [96]. In terms of energetics, the WLC model is one which has only bending energy, while the Gaussian polymer has only stretching energy. It is then natural to ask what the polymer model would be that corresponds to an ABP in the presence of translational thermal noise. One of the aims of the chapter is to explore this connection. A second main objective of the chapter is to point out that the approach of [91] provides an efficient method of computing all moments (of both positional and orientational degrees of freedom) of the ABP (with or without translational thermal noise), in arbitrary dimensions.

In this chapter, we consider free ABPs in d-dimensions, in the presence of translational thermal noise. We summarize here our main results:-

1) We discuss the mapping of the ABP trajectories to the equilibrium polymer configurations. We point out that the polymer model differs from the physical system including both bending and stretching energy and the physical relevance is thus not clear. Nevertheless we illustrate the mapping by comparing results for various dynamical moments and displacement distribution functions of ABPs with the corresponding polymer properties obtained from equilibrium polymer simulations. We show that ABP simulations provide an efficient alternate means of obtaining equilibrium polymer properties that usually require Monte-Carlo or Langevin simulations.

2) We show how arbitrary moments of position and orientation degrees of freedom can be computed exactly by utilizing the Fokker-Planck equation governing the dynamics of ABP, using the approach in [91]. Interesting dynamical crossovers displayed by the moments are analyzed using the exact expressions. The resultant dynamics crosses over from short-time equilibrium diffusion, to intermediate time active ballistic motion, to long time effective diffusion. Short time anisotropies in the distribution, pointed out in [87] are also discussed. As has been pointed out in earlier studies [8, 9], we show that the Kurtosis, which we compute exactly, can be used to distinguish between the ABP and the AOUP models.

The plan of the chapter is as follows. In the Section-2.2, we present the ABP model in the presence of translational diffusion. We demonstrate an exact mapping of path probabilities of trajectories of ABP to configurational properties of equivalent equilibrium polymer model in Section-2.3. In Section-2.4, we present the method to calculate exact moments in any arbitrary dimensions. In Section-2.5, We calculate orientation correlation and average displacement and compare them with the simulation results in two dimensions. In Section-2.6, We calculate quadratic order moment and displacement fluctuation and show the crossovers with crossover

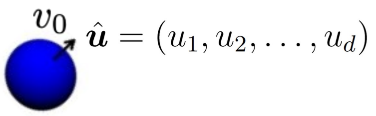

Figure 2.1: (color online) Schematic representation of active Brownian particle. The velocity of ABP is $v_0\hat{\boldsymbol{u}}$ where v_0 is the speed of the particle with heading direction along $\hat{\boldsymbol{u}} = (u_1, u_2, ..., u_d)$ in d-dimension.

timescales. In the similar method, we calculate components of displacement fluctuation in Section-2.7 and quartic order moment in Section-2.8. In Section-2.9, we present a detailed analysis of how the distribution function of displacement of ABP changes with time. In Section-2.10, We calculate an exact generalized Kurtosis to differentiate ABP to active Ornstein-Uhlenbeck particle(AOUP). We conclude in Section-2.11 with a discussion of our main results present in this chapter.

2.2 Definition of the model

The active Brownian particle (ABP) in d-dimensions is described by its position $\mathbf{r} = (r_1, r_2, \ldots, r_d)$ and its orientation $\hat{\boldsymbol{u}} = (u_1, u_2, \ldots, u_d)$ which is a unit vector in d-dimensions. Schematic representation of the particle with velocity $\boldsymbol{v} = v_0\hat{\boldsymbol{u}}$ shows in Fig. (2.1). Here speed of the particle v_0 is constant. Let the infinitesimal increment at time t are denoted by $dr_i = r_i(t+dt) - r_i(t)$ and $du_i = u_i(t+dt) - u_i(t)$. In Ito convention[97, 98], the equation of motion of the ABP is given by

$$dr_i = v_0 u_i \, dt + dB_i^t(t), \tag{2.1}$$

$$du_i = (\delta_{ij} - u_i u_j) \, dB_j^r(t) - (d-1) D_r u_i \, dt, \tag{2.2}$$

where the Gaussian noise terms $\boldsymbol{dB}^t$ and $\boldsymbol{dB}^r$ have mean zero and variances $\langle dB_i^t dB_j^t \rangle = 2D\delta_{ij} \, dt$, $\langle dB_i^r dB_j^r \rangle = 2D_r\delta_{ij} \, dt$ control the translational and rotational diffusions, respectively.

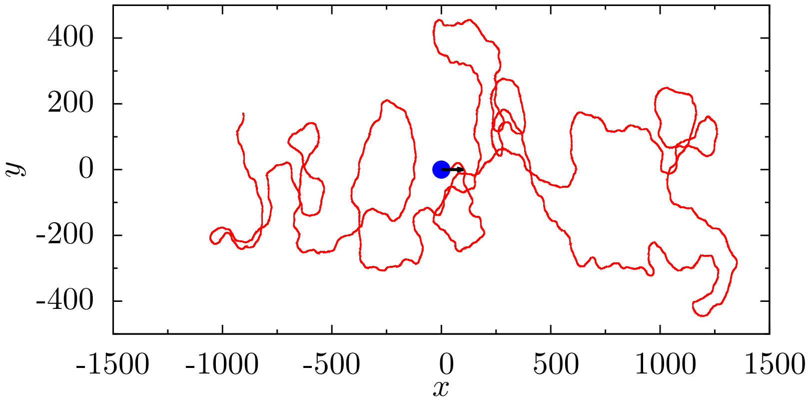

Figure 2.2: (color online) Typical ABP trajectory. The blue point shows the initial starting point with heading dircetion along x-axis. Direct simulation of equation of motion (2.1), (2.2) in two dimension with parameters $D = 1$, $D_r = 1$, and $v_0 = 130$.

Alternatively, we can write the Eq. (2.2) in the Stratonovich form

$$(S) \qquad du_i = (\delta_{ij} - u_i u_j) \circ \eta_j^r dt. \tag{2.3}$$

Eq. (2.1) gives $\langle dr_i \rangle = v_0 u_i dt$ and $\langle dr_i dr_j \rangle = 2D\delta_{ij}\, dt$. The form of Eq. (2.2) ensures the normalization $\hat{\boldsymbol{u}}^2 = 1$ at all times. Eq. (2.2) implies the mean and variance of the orientational fluctuations

$$\langle du_i \rangle = -(d-1) D_r u_i \, dt \tag{2.4}$$

and

$$\langle du_i du_j \rangle = 2D_r(\delta_{ij} - u_i u_j)\, dt. \tag{2.5}$$

These expressions are utilized in deriving the Fokker-Planck equation for this system which is discussed in Section-2.4.

It is straightforward to perform a direct numerical simulation of Eqs. (2.1), (2.2) using the Euler-Maruyama integration scheme to generate trajectories of motion depicted in Fig. (2.2). In the following, we first show how the ABP trajectories can be mapped to an effective polymer model.

2.3 Exact mapping to equilibrium polymer model

The probability distribution of a stochastic trajectory $\{\mathbf{r}(t), \hat{\boldsymbol{u}}(t)\}$, corresponding to the evolution Eqs. (2.1), (2.2) over the time-range $t \in (0, \tau)$, is given by

$$\mathcal{P}[\{\mathbf{r}(t), \hat{\boldsymbol{u}}(t)\}] \propto e^{-\frac{1}{4D}\int_0^\tau dt\left(\frac{\partial \mathbf{r}}{\partial t} - v_0 \hat{\boldsymbol{u}}\right)^2 - \frac{1}{4D_r}\int_0^\tau dt\left(\frac{\partial \hat{\boldsymbol{u}}}{\partial t}\right)^2}. \tag{2.6}$$

Denoting a length segment of the trajectory by $v_0 dt = dl$, one obtains $\partial \mathbf{r}/\partial t = v_0(\partial \mathbf{r}/\partial l)$ and $\partial \hat{\boldsymbol{u}}/\partial t = v_0(\partial \hat{\boldsymbol{u}}/\partial l)$ to get

$$\mathcal{P}[\{\mathbf{r}(l), \hat{\boldsymbol{u}}(l)\}] \propto e^{-\frac{v_0}{4D}\int_0^L dl\left(\frac{\partial \mathbf{r}}{\partial l} - \hat{\boldsymbol{u}}\right)^2 - \frac{v_0}{4D_r}\int_0^L dl\left(\frac{\partial \hat{\boldsymbol{u}}}{\partial l}\right)^2}, \tag{2.7}$$

where $L = v_0 \tau$ is the total length traversed. This action for the path probability distribution can be written as $\mathcal{P}[\{\mathbf{r}(l), \hat{\boldsymbol{u}}(l)\}] \propto e^{-\beta \mathcal{E}}$, where now $\mathcal{E}$ can be interpreted as the energy of a polymer configuration, and given by

$$\beta \mathcal{E} = \frac{A}{2}\int_0^L dl \left(\frac{\partial \mathbf{r}}{\partial l} - \hat{\boldsymbol{u}}(l)\right)^2 + \frac{\kappa}{2}\int_0^L dl \left(\frac{\partial \hat{\boldsymbol{u}}}{\partial l}\right)^2, \tag{2.8}$$

where, $\beta = 1/k_B T$, and we identify $A = v_0/2D$, and $\kappa = v_0/2D_r$. This is the energy cost of a polymer configuration described by $\{\mathbf{r}(l), \hat{\boldsymbol{u}}(l)\}$, where note that $\mathbf{r}(l)$ and $\hat{\boldsymbol{u}}(l)$ are independent fields. In the limit of vanishing translational diffusion ($A \to \infty$), we require $\dot{\mathbf{r}} = v_0 \hat{\boldsymbol{u}}(t)$ and so in this case we can identify $\hat{\boldsymbol{u}}(l) = \partial \mathbf{r}/\partial l$ as the local unit tangent vector on the polymer configuration obeying the constraint $|\partial \mathbf{r}/\partial l|^2 = 1$. Thus, in this limit, the polymer is effectively described by the second term in the energy expression in Eq. (2.8) and this corresponds precisely to the worm-like chain (WLC) model with [93, 96]

$$\beta \mathcal{E} = \frac{\kappa}{2}\int_0^L dl \left(\frac{\partial \hat{\boldsymbol{u}}}{\partial l}\right)^2. \tag{2.9}$$

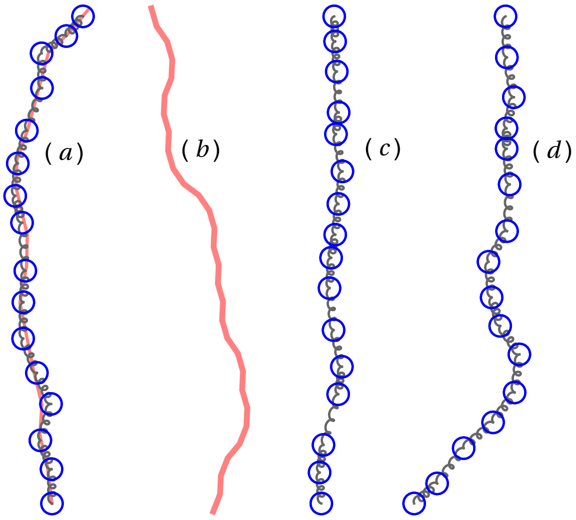

Figure 2.3: (color online) Typical configurations of (a) the polymer mapping of the ABP model (Eq. (2.8)), (b) the related worm-like-chain (Eq. (2.9)), (c) the related Gaussian polymer under a directed external force (Eq. (2.10)), and (d) the related extensible semiflexible chain (Eq. (2.13)). The thick (red) line in (a) shows the worm-like-chain conformation that the Gaussian polymer denoted by the beads and springs tries to align with. The configurations are plotted with chain length $L = 15\,\sigma$, persistence length $\ell_p = 4.28\,\sigma$, spring constant $A = 30.0\,\sigma^{-1}$ in (a) and (d), and $A = 1.0\,\sigma^{-1}$ in (c) . Note that A does not play any role in deciding the conformation in (b).

On the ther hand, the limit $\kappa \to \infty$ requires that $\hat{u}$ be a constant unit vector. Using this input in the first term of Eq. (2.8) leads to the energy functional

$$\beta \mathcal{E} = \frac{A}{2} \int_0^L dl \left(\frac{\partial \mathbf{r}}{\partial l} \right)^2 - A[\mathbf{r}(L) - \mathbf{r}(0)] \cdot \hat{\boldsymbol{u}} \tag{2.10}$$

which corresponds to a Gaussian polymer with a force along the direction $\hat{\boldsymbol{u}}$ [96].

In Fig. (2.3) we show a comparison between (a) a typical configuration of the polymer mapping of the ABP model, (b) its constant bond-length limit of the WLC model, (c) its limit of the Gaussian chain under directed external force for the same parameter values. In Fig. (2.3)(d) we show a related configuration of an extensible semiflexible chain (ESC), discussed in Section-2.3.2.

To extract equilibrium properties of polymers a common strategy is to perform either Monte-Carlo simulations or Langevin dynamics. In the following section we compare results from such simulations with those obtained from simulations of

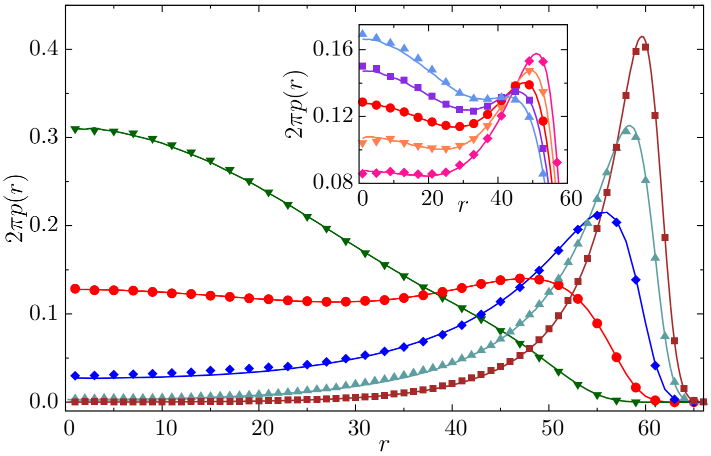

Figure 2.4: (color online) Comparison between probability distributions of ABP displacement (solid lines) and end-to-end separation of polymers (points): Here $v_0 = 1.8\,\sigma/\tau_u$ and $D = 0.02\,\sigma^2/\tau_u$ are held constant. In all the simulations, the first step in the ABP model, and the bond orientation of one end of the polymer are held fixed along the x-direction. The bimodal distributions corresponding to $D_r\tau_u = 0.02\,(\square)$, $0.03\,(\triangle)$, $0.05\,(\diamond)$, $0.1\,(\circ)$, $0.2\,(\triangledown)$. Inset: The same comparisons at $D_r\tau_u = 0.08\,(\diamond)$, $0.09\,(\triangledown)$, $0.1\,(\circ)$, $0.11\,(\square)$, $0.12\,(\triangle)$.

the ABP dynamics, using the exact mapping of polymer configurations and ABP trajectories.

2.3.1 Comparisons between ABP dynamics and mapped polymer simulations

Let us now test the polymer mapping numerically by comparing displacement distributions of the ABP with the end-to-end distributions of the mapped polymer. We present results in two dimensions ($2d$). Replacing the orientation field $\hat{\boldsymbol{u}}(l) = (\cos\theta(l), \sin\theta(l)\,)$, the second term in the expression of energy in Eq. (2.8) simplifies to $\frac{\kappa}{2}\int_0^L dl\left(\frac{\partial\theta}{\partial l}\right)^2$.

After discretization the energy becomes,

$$\beta\mathcal{E} = \sum_{i=1}^{N-1}\frac{A}{2\sigma}\left[\mathbf{b}_i - \sigma\hat{\boldsymbol{u}}_i\right]^2 + \sum_{i=1}^{N-1}\frac{\kappa}{2\sigma}\left[\theta_{i+1} - \theta_i\right]^2, \tag{2.11}$$

where $\mathbf{b}_i = \mathbf{r}_{i+1} - \mathbf{r}_i$ is the bond vector between the i-th and $(i+1)$-th bead, and in the first term the vector $\hat{\boldsymbol{u}}_i = (\cos\theta_i, \sin\theta_i)$. The continuum limit is obtained as $\sigma \to 0$ with $L \equiv v_0\tau = (N-1)\sigma$, A/σ and κ/σ held constant. To perform equilibrium simulations of the polymer, we use the over-damped Langevin equations of motion

$$\begin{aligned} \gamma\,\dot{\mathbf{r}}_i &= -\partial\mathcal{E}/\partial\mathbf{r}_i + \sqrt{2\gamma k_B T}\,\mathbf{F}_i \\ \gamma_r\,\dot{\theta}_i &= -\partial\mathcal{E}/\partial\theta_i + \sqrt{2\gamma_r k_B T}\,\Lambda_i, \end{aligned} \tag{2.12}$$

where $\mathbf{F}_i$ and Λ_i denote uni-deviate Gaussian white noise terms. Here k_BT and σ set the unit of energy and length respectively, and $\tau_u = \gamma\sigma^2/k_BT$ sets the characteristic time over which a bead diffuses over its size σ. In our simulations we choose the Langevin heat bath characterized by an isotropic friction $\gamma = \gamma_r = 1/\tau_u$. The simulations are performed using Euler-Maruyama integration of these equations, with time step $\delta t = 0.001\tau_u$.

We perform polymer simulations with 64 beads, and compare the results with ABP trajectories generated over $L \equiv v_0\tau = 63\sigma$. We obtain the end-to-end distribution function $p(r)$ for the polymer mapping, and compare the results with probability distributions of the particle-displacements obtained from the original ABP model. The distributions are normalized to $\int_0^\infty p(r)\,2\pi r\,dr = 1$. Three parameters in the ABP model, D, D_r and v_0 control the dynamics.

In Fig. (2.4) we fix $v_0 = 1.8\,\sigma/\tau_u$, $D = 0.02\,\sigma^2/\tau_u$ and vary D_r of the ABP that maps to different $\kappa = v_0/2D_r$ of the semiflexible chain, and keeps the bond stiffness $A = v_0/2D$ constant. The semiflexibility of the chain is determined by the rigidity parameter L/ℓ_p, the ratio of polymer length L to persistence length $\ell_p = 2\kappa/(d-1)$. In terms of the ABP model, $L/\ell_p = (d-1)D_r\tau$. Fig. (2.4) shows the distribution functions in the range of $0.7 \lesssim L/\ell_p \lesssim 7$. The inset of Fig. (2.4) focuses on the region of bimodality $2.8 \lesssim L/\ell_p \lesssim 4.2$ recapturing the WLC behavior [93]. The agreement between the two data sets of the ABP model and its polymer mapping is evident from the figure. The relatively large value of $A\,(= v_0/2D = 45\sigma^{-1})$ in the corresponding polymer model, for the parameter choice in Fig. (2.4), ensures

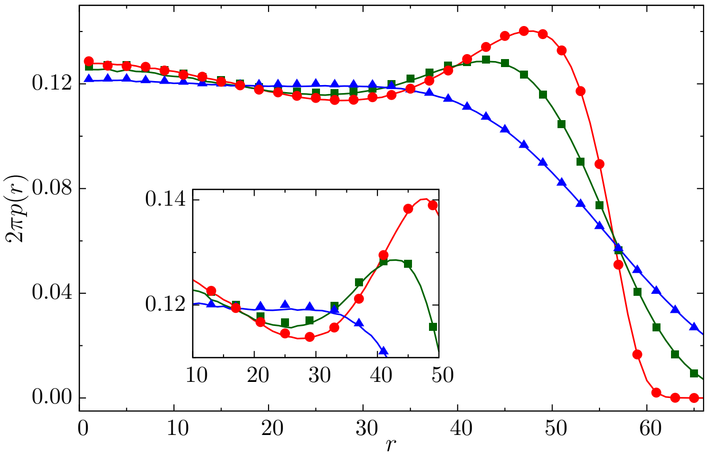

Figure 2.5: (color online) Comparison between probability distributions of ABP displacement (solid lines) and end-to-end separation of polymers (points): We keep $v_o = 1.8\,\sigma/\tau_u$, $D_r = 0.1\,\tau_u^{-1}$ for ABP constant, and show the mapping of ABP to polymer for $D\tau_u/\sigma^2 = 0.02\,(\circ)$, $0.5\,(\square)$, $2\,(\triangle)$. Inset: The loss of bimodality magnified.

small bond length fluctuations (within 7.5%), allowing to recapitulate the behavior of WLC polymer.

The bimodality in the distribution function for the ABP means that some of the trajectories will generate small displacements, while some other will produce large displacements. The corresponding polymer will fluctuate between configurations having low to high end-to-end separation. The free energy $F(r, L) = -k_B T \ln[p(r, L)]$ will show a double minima suggesting a non-monotonic force-extension exemplifying a region of negative response in the Helmholtz ensemble [93].

In Fig. (2.5), we hold $v_0 = 1.8\,\sigma/\tau_u$, $D_r = 0.1\,\tau_u^{-1}$ fixed such that at $D = 0.02\,\sigma^2/\tau_u$ one obtains clean bimodal distribution as in Fig. (2.4). We proceed to increase D and examine the robustness of the bimodality. At larger D, the effective spring constant of the bond lengths $A = v_0/2D$ reduces. Corresponding to $D\tau_u/\sigma^2 = 0.02$, 0.5, 2 one finds two orders of magnitude reduction of spring constant $A\sigma = 45$, 1.8, 0.45 respectively. This allows large bond- length fluctuations. Fig. (2.5) shows clear numerical agreement between the distribution functions obtained from the two models, exemplifying the mapping. Clearly with reducing A first the contrast of the bimodality reduces as the distribution gets flatter, and

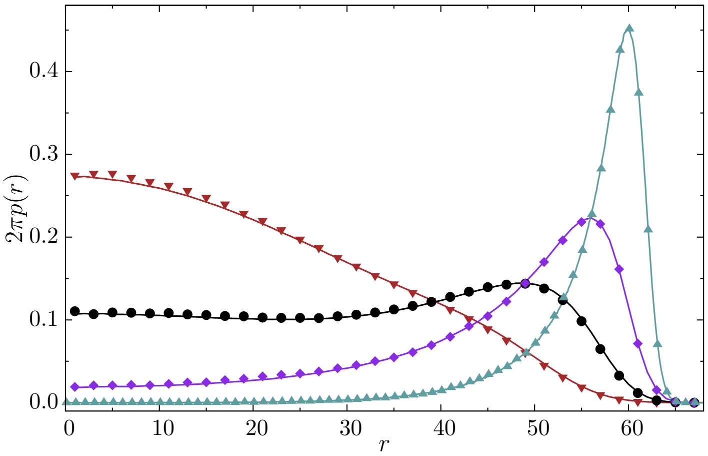

Figure 2.6: (color online) Comparison between probability distributions of ABP displacement (solid lines) and end-to-end separation of polymers (points): We kept $D = 1.0\,\sigma^2/\tau_u$ and $D_r = 1.0\tau_u^{-1}$ constant and varied v_0 keeping $v_0\tau$ constant. The data denotes $v_0\tau_u/\sigma = 10\,(\triangledown)$, $20\,(\circ)$, $40\,(\diamond)$, $100\,(\triangle)$.

finally at $A\sigma = 0.45$ the bimodal structure vanishes.

Finally, in Fig. (2.6) we demonstrate the change in the probability distribution of finite time trajectories of ABP as the propulsion velocity v_0 is varied, keeping $L = v_0\tau$ constant. Here we fix the values of D_r and D. Increasing v_0 increases both $A = v_0/2D$ and $\kappa = v_0/2D_r$ together in the polymer mapping. At small v_0, the chain remains in the flexible Gaussian regime. With increasing v_0 the bond-length fluctuations decrease as the corresponding spring constant A increases. The persistence length ℓ_p increases as well. This leads the chain towards the WLC regime showing the emergence of bimodality near $v_0 = 20\,\sigma/\tau_u$. The comparison of results between the two models show good agreement.

Having established the mapping of the ABP model to the polymer model, the results presented in the following will be interpreted interchangeably. For a fixed v_0, the evolution time τ in ABP will be understood in terms of contour length $L = v_0\tau$.

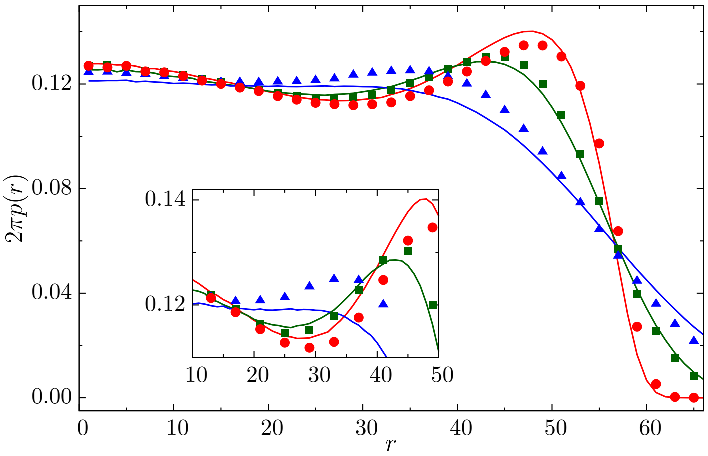

Figure 2.7: (color online) Comparison between the ABP model and the extensible semiflexible chain (ESC). We keep parameters $v_0 = 1.8\,\sigma/\tau_u$, $D_r = 0.1\,\tau_u^{-1}$ constant. The lines show results from the ABP model at $D\tau_u/\sigma^2 = 0.02$ (red), 0.5 (green), 2 (blue). Points denote results for ESC at the corresponding $A\sigma = 45$ (red $\circ$), 1.8 (green $\square$), 0.45 (blue $\triangle$). Inset: magnified view highlights difference between the results of the two models.

2.3.2 How far from extensible semi-flexible polymer is mapped polymer(or ABP) ?

We briefly comment on how the polymer model described by Eq. (2.8) differs from polymers with both bending and stretching energy terms, which we refer to as a extensible semi-flexible chain (ESC). Let us consider a polymer with monomer positions $\mathbf{r}_1, \mathbf{r}_2, \ldots, \mathbf{r}_N$. We define bond vectors $\mathbf{b}_n = \mathbf{r}_{n+1} - \mathbf{r}_n$, for $n = 1, 2, \ldots, N-1$ and let the local tangent $\mathbf{t}_n = \mathbf{b}_n / b_n$, where $b_n = |\mathbf{b}_n|$. Then the following energy describes the ESC with stretching and bending energy terms:

$$\beta\mathcal{E}_{\mathrm{ESC}} = \sum_{n=1}^{N-1} \frac{A}{2\sigma}(b_n - \sigma)^2 + \sum_{n=1}^{N-2} \frac{\kappa}{2\sigma}(\mathbf{t}_{n+1} - \mathbf{t}_n)^2. \tag{2.13}$$

In the continuum limit this gives

$$\begin{aligned}
\beta\mathcal{E}_{\rm ESC} &= \sum_{n=1}^{N-1}\frac{A}{2\sigma}(\mathbf{r}_{n+1}-\mathbf{r}_n-\sigma\mathbf{t}_n)^2+\sum_{n=1}^{N-2}\frac{\kappa}{2\sigma}(\mathbf{t}_{n+1}-\mathbf{t}_n)^2, \\
&= \int_0^N dn\left[\frac{A}{2\sigma}\left(\frac{\partial\mathbf{r}(n)}{\partial n}-b\mathbf{t}(n)\right)^2+\frac{\kappa}{2\sigma}\left(\frac{\partial\mathbf{t}(n)}{\partial n}\right)^2\right], \\
&= \int_0^L dl\left[\frac{A}{2}\left(\frac{\partial\mathbf{r}(l)}{\partial l}-\mathbf{t}(l)\right)^2+\frac{\kappa}{2}\left(\frac{\partial\mathbf{t}(l)}{\partial l}\right)^2\right], \qquad (2.14)
\end{aligned}$$

where a contour segment is denoted by $l = nb$ and the chain length $L = Nb$. This energy has the same form as in Eq. (2.8), however, note that $\mathbf{r}(l)$ and $\mathbf{t}(l)$ are *not independent fields and are related through the equality* $\mathbf{t}(l) = (\partial\mathbf{r}(l)/\partial l)/|\partial\mathbf{r}(l)/\partial l|$. On the other hand, $\mathbf{r}(l)$ and $\mathbf{u}(l)$ in Eq. (2.8) *are independent* fields. Hence, while superficially the two energies in Eq. (2.8) and Eq. (2.14) look identical, the polymer representation of the active particle needs a different physical interpretation. This in fact corresponds to a flexible Gaussian polymer sitting on top of another semiflexible polymer with an inter-polymer interaction that tries to align the two polymers.

In Fig. (2.7) we compare numerical simulation results from the polymer models in Eq. (2.13) and Eq. (2.11). It is clear from the figure that the distributions obtained from the two models are different. The end-to-end separations they predict do not agree, except in the limit of large A. The difference is due to the absence of the constraint $\mathbf{t}(l) = (\partial\mathbf{r}(l)/\partial l)/|\partial\mathbf{r}(l)/\partial l|$, which is an integral part of ESC, in the polymer mapping of ABP. For large spring constant A, the bond length fluctuations become negligible reducing the polymer configurations corresponding to both the models equivalent to the WLC polymer.

2.4 Exact computation of moments for ABP

The probability distribution $P(\mathbf{r},\hat{\boldsymbol{u}},t)$ of the position $\mathbf{r}$ and the active orientation $\hat{\boldsymbol{u}}$, controlling the self-propulsion velocity $\mathbf{v}(t) = v_0\hat{\boldsymbol{u}}(t)$, of the ABP follows the

Fokker-Planck equation

$$\partial_t P(\mathbf{r}, \hat{\boldsymbol{u}}, t) = D\nabla^2 P + D_r \nabla_u^2 P - v_0\, \hat{\boldsymbol{u}} \cdot \nabla P,$$

where ∇^2 is the d-dimensional Laplacian operator, and ∇_u^2 denotes the Laplacian in the $(d-1)$ dimensional orientation space. We note that the spherical Laplacian can be expressed in terms of the cartesian coordiantes $\boldsymbol{y}$ defined through $u_i = y_i/y$ where $y = \mid \boldsymbol{y} \mid$ as $\nabla_u^2 = y^2 \sum_{i=1}^d \partial_{y_i}^2 - [y^2 \partial_y^2 + (d-1) y \partial_y]$. This equation can be derived using the standard procedure of determining the mean and variance of infinitesimal displacements in position $\mathbf{r}(t)$ and orientation $\hat{\boldsymbol{u}}(t)$. We used the *Ito* interpretation of the stochastic dynamics. The first and last terms on the right hand side describe the translational diffusion and active drift respectively. The second term describes orientational diffusion and follows from the result obtained in Eq. (2.5).

Using the Laplace transform $\tilde{P}(\mathbf{r}, \hat{\boldsymbol{u}}, s) = \int_0^\infty dt e^{-st} P(\mathbf{r}, \hat{\boldsymbol{u}}, t)$, the Fokker-Planck equation can be recast in the form,

$$-P(\mathbf{r}, \hat{\boldsymbol{u}}, 0) + s\tilde{P}(\mathbf{r}, \hat{\boldsymbol{u}}, s) = D\nabla^2 \tilde{P} + D_r \nabla_u^2 \tilde{P} - v_0\, \hat{\boldsymbol{u}} \cdot \nabla \tilde{P}.$$

Let us define the mean of an arbitrary observable in the Laplace space by $\langle \psi \rangle_s = \int d\mathbf{r}\, d\hat{\boldsymbol{u}}\, \psi(\mathbf{r}, \hat{\boldsymbol{u}}) \tilde{P}(\mathbf{r}, \hat{\boldsymbol{u}}, s)$. Multiplying the above equation by $\psi(\mathbf{r}, \hat{\boldsymbol{u}})$ and integrating over all possible $(\mathbf{r}, \hat{\boldsymbol{u}})$ we find

$$-\langle \psi \rangle_0 + s\langle \psi \rangle_s = D\langle \nabla^2 \psi \rangle_s + D_r \langle \nabla_u^2 \psi \rangle_s + v_0\, \langle \hat{\boldsymbol{u}} \cdot \nabla \psi \rangle_s, \tag{2.15}$$

where the initial condition sets $\langle \psi \rangle_0 = \int d\mathbf{r}\, d\hat{\boldsymbol{u}}\, \psi(\mathbf{r}, \hat{\boldsymbol{u}}) P(\mathbf{r}, \hat{\boldsymbol{u}}, 0)$. Without any loss of generality, we consider $P(\mathbf{r}, \hat{\boldsymbol{u}}, 0) = \delta(\mathbf{r})\delta(\hat{\boldsymbol{u}} - \hat{\boldsymbol{u}}_0)$. Eq. (2.15) can be utilized to compute all the moments as a function of time. In the following, we illustrate the approach by explicitly deriving some of these moments and using them to analyze the ABP motion (equivalently the polymer model).

2.5 Orientation correlation and average displacement

2.5.1 Orientation correlation

Let us first consider the evolution of velocity $\mathbf{v}(t) = v_0 \hat{\boldsymbol{u}}(t)$. Thus we consider $\psi(\mathbf{r}, \hat{\boldsymbol{u}}) = \hat{\boldsymbol{u}}$. It is easy to see that $\langle \psi \rangle_0 = \hat{\boldsymbol{u}}_0$, $\langle \nabla^2 \psi \rangle_s = 0$, $\langle \hat{\boldsymbol{u}} \cdot \nabla \psi \rangle_s = 0$, and $\nabla_u^2 \hat{\boldsymbol{u}} = -(d-1)\hat{\boldsymbol{u}}$. As a result Eq. (2.15) leads to

$$\langle \hat{\boldsymbol{u}} \rangle_s = \frac{\hat{\boldsymbol{u}}_0}{s + (d-1)D_r},$$

which, after performing inverse Laplace transform gives an exponential decay

$$\langle \hat{\boldsymbol{u}}(t) \rangle = \hat{\boldsymbol{u}}_0 e^{-(d-1)D_r t}. \tag{2.16}$$

From the above derivation, it is easy to see that

$$\langle \hat{\boldsymbol{u}} \cdot \hat{\boldsymbol{u}}_0 \rangle(t) = e^{-(d-1)D_r t}, \tag{2.17}$$

if one considered $\psi(\mathbf{r}, \hat{\boldsymbol{u}}) = \hat{\boldsymbol{u}} \cdot \hat{\boldsymbol{u}}_0$. This shows that the orientational correlation decays with a correlation time $\tau_r = [(d-1)D_r]^{-1}$ in d-dimensions.

The persistence time τ_r sets the unit of time in the problem. Using it along with the translational diffusion constant D, the unit of length can be set by $\bar{\ell} = \sqrt{D/D_r}$ resulting in a unit of velocity $\bar{v} = \bar{\ell}/\tau_r = \sqrt{D D_r}$. The dimension-less activity can be expressed as $\lambda = v_0/\bar{v}$.

In Fig. (2.8)(a) we show simulation results of two-time orientational correlation $\langle \hat{\boldsymbol{u}}(t) \cdot \hat{\boldsymbol{u}}(0) \rangle$, and its comparison with the analytical form e^{-t} where t is expressed in units of $\tau_r = 1/D_r$ in $2d$.

A mapping of the orientational correlation to the tangent-tangent correlation of the WLC model is possible, considering the trajectory length $l = v_0 t$ as a polymer segment of the same length. The correlation $\langle \hat{\boldsymbol{u}}(t) \cdot \hat{\boldsymbol{u}}(0) \rangle = \exp(-t/\tau_r)$ is then

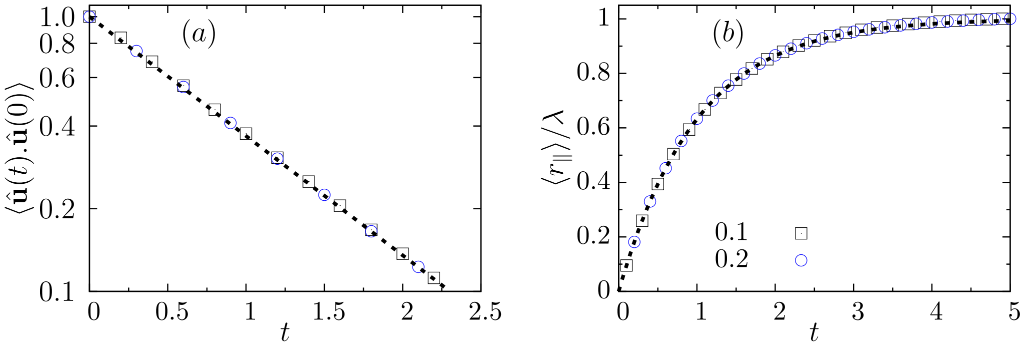

Figure 2.8: (color online) (a) Orientational correlation $\langle \hat{\boldsymbol{u}}(t) \cdot \hat{\boldsymbol{u}}(0) \rangle$, and (b) the displacement $\langle r_{\parallel} \rangle$ along the initial orientation $\hat{\boldsymbol{u}}_0$ of the ABP are shown as a function of time t in 2d. Here $D = 1.0\,\sigma^2/\tau_u$, and $v_0 = 1.0\,\sigma/\tau_u$ are held constant, and we use $D_r\tau_u = 0.1(\square)$, $0.2(\circ)$. The results of numerical simulations are shown by points, and analytic predictions by dashed lines. In this figure, and all other figures presented in this section, the length and time axes are expressed in units of $\bar{\ell} = \sqrt{D/D_r}$ and $\tau_r = 1/D_r$, respectively. The dashed line in (a) shows $\langle \hat{\boldsymbol{u}}(t) \cdot \hat{\boldsymbol{u}}(0) \rangle = e^{-t}$ in the semi-log plot, and in (b) shows $\langle r_{\parallel} \rangle /\lambda = (1 - e^{-t})$ with $\lambda = v_0/\sqrt{DD_r}$.

equivalent to $\langle \hat{\boldsymbol{u}}(l) \cdot \hat{\boldsymbol{u}}(0) \rangle = \exp(-l/\ell_p)$ with $\ell_p = v_0/(d-1)D_r$. This is consistent with the WLC result $\ell_p = 2\kappa/(d-1)$ and the mapping $\kappa = v_0/2D_r$ between the ABP and its corresponding polymer model.

2.5.2 Displacement

Using $\psi = \mathbf{r}$ in Eq. (2.15), along with the result $\langle \hat{\boldsymbol{u}} \rangle_s = \hat{\boldsymbol{u}}_0/(s + (d-1)D_r)$ allows us to obtain

$$\langle \mathbf{r} \rangle_s = \frac{v_0\, \hat{\boldsymbol{u}}_0}{s(s + (d-1)D_r)}, \tag{2.18}$$

which leads to

$$\langle \mathbf{r} \rangle(t) = \frac{v_0\, \hat{\boldsymbol{u}}_0}{(d-1)D_r} \left(1 - e^{-(d-1)D_r\, t}\right). \tag{2.19}$$

Let us define the displacement components along and perpendicular to the initial orientation as

$$\boldsymbol{r}_{\|} = (\mathbf{r}.\hat{\boldsymbol{u}}_0)\hat{\boldsymbol{u}}_0, \quad \mathbf{r}_\perp = \mathbf{r} - \boldsymbol{r}_{\|} \ . \tag{2.20}$$

We then see that the mean displacement along the initial orientation $\langle r_{\|}\rangle = \langle \mathbf{r}\cdot\hat{\boldsymbol{u}}_0\rangle$ grows and saturates to a finite value as $\langle r_{\|}\rangle/\bar{\ell} = \lambda(1 - e^{-t/\tau_r})$, where $\lambda = v_0/\bar{v}$ is the dimensionless parameter controlling activity (see Fig. (2.8)(b)). On the other hand, the average displacement vector perpendicular to $\hat{\boldsymbol{u}}_0$ vanishes $\langle \mathbf{r}_\perp\rangle = 0$.

2.6 Quadratic order moment and displacement fluctuation

2.6.1 Quadratic order moment

Let us now consider $\psi(\mathbf{r},\hat{\boldsymbol{u}}) = \mathbf{r}^2$ and calculate the time dependence of $\langle \mathbf{r}^2\rangle(t)$. It is easy to see that $\langle\psi\rangle_0 = 0$ and $\langle\nabla_u^2\psi\rangle_s = 0$. The average $\langle\nabla^2\mathbf{r}^2\rangle_s = 2d\langle 1\rangle_s$. Note that $\langle 1\rangle_s = \int d\mathbf{r}d\hat{\boldsymbol{u}}\tilde{P} = \int d\mathbf{r}d\hat{\boldsymbol{u}}\int_0^\infty dte^{-st}P = \int_0^\infty dte^{-st}\{d\mathbf{r}d\hat{\boldsymbol{u}}P\} = \int_0^\infty dte^{-st} = 1/s$. Further, $\langle\hat{\boldsymbol{u}}\cdot\nabla\mathbf{r}^2\rangle_s = 2\langle\hat{\boldsymbol{u}}\cdot\mathbf{r}\rangle_s$. Thus Eq. (2.15) leads to $s\langle\mathbf{r}^2\rangle_s = 2dD/s + 2v_0\langle\hat{\boldsymbol{u}}\cdot\mathbf{r}\rangle_s$. To complete the calculation, one needs to evaluate $\langle\hat{\boldsymbol{u}}\cdot\mathbf{r}\rangle_s$ using the same Eq. (2.15). One may proceed like before, utilizing the relation $\nabla_u^2\hat{\boldsymbol{u}} = -(d-1)\hat{\boldsymbol{u}}$, $\langle\hat{\boldsymbol{u}}\cdot\nabla\psi\rangle_s = \langle\hat{\boldsymbol{u}}^2\rangle_s = 1/s$, to get $s\langle\hat{\boldsymbol{u}}\cdot\mathbf{r}\rangle_s = -(d-1)D_r\langle\hat{\boldsymbol{u}}\cdot\mathbf{r}\rangle_s + v_0/s$. This gives

$$\langle\hat{\boldsymbol{u}}\cdot\mathbf{r}\rangle_s = \frac{v_0}{s(s+(d-1)D_r)}, \tag{2.21}$$

which leads to the cross-correlation

$$\langle\hat{\boldsymbol{u}}\cdot\mathbf{r}\rangle = \frac{v_0}{(d-1)D_r}\left(1 - e^{-(d-1)D_r\,t}\right).$$

Plugging the relation from Eq. (2.21) into Eq. (2.15) one finds

$$\langle \mathbf{r}^2 \rangle_s = \frac{2dD}{s^2} + \frac{2v_0^2}{s^2(s+(d-1)D_r)}. \tag{2.22}$$

Performing the inverse Laplace transform, we obtain

$$\langle \mathbf{r}^2 \rangle \; = \; 2d\left(D + \frac{v_0^2}{(d-1)dD_r}\right)t - \frac{2v_0^2}{(d-1)^2 D_r^2}\left(1 - e^{-(d-1)D_r t}\right). \tag{2.23}$$

In the limit of $t \ll \tau_r = 1/(d-1)D_r$, the motion is dominated by the simple translational diffusion, $\langle \mathbf{r}^2 \rangle \approx 2dD\,t$. In the long time limit, the equation gives diffusive scaling $\langle \mathbf{r}^2 \rangle = 2d\,D_{\text{eff}}t$ with the effective diffusion constant in d-dimensions

$$D_{\text{eff}} = D + \frac{v_0^2}{(d-1)dD_r}. \tag{2.24}$$

A series expansion of Eq. (2.23) around $t = 0$ gives

$$\langle \mathbf{r}^2 \rangle = 2dDt + v_0^2 t^2 - \frac{1}{3}v_0^2(d-1)D_r t^3 + \mathcal{O}(t^4).$$

This shows that $\langle \mathbf{r}^2 \rangle$ will crossover from a diffusive $\sim t$ to ballistic $\sim t^2$ scaling at $t_I = (2d/\lambda^2)\tau_r$. This is expected to be followed by another crossover from ballistic to diffusive behavior near $t_{II} \approx [3/(d-1)]\tau_r$. These crossovers along with the estimated crossover-points t_I and t_{II} are shown in Fig. (2.9)(a) for an ABP moving in 2d. The simulation results agree with the above estimates. In the limit of $D = 0$, only a single crossover from $\langle \mathbf{r}^2 \rangle \sim t^2$ to $\langle \mathbf{r}^2 \rangle \sim t$ at $t_{II}D_r \approx 3/(d-1)$ survives.

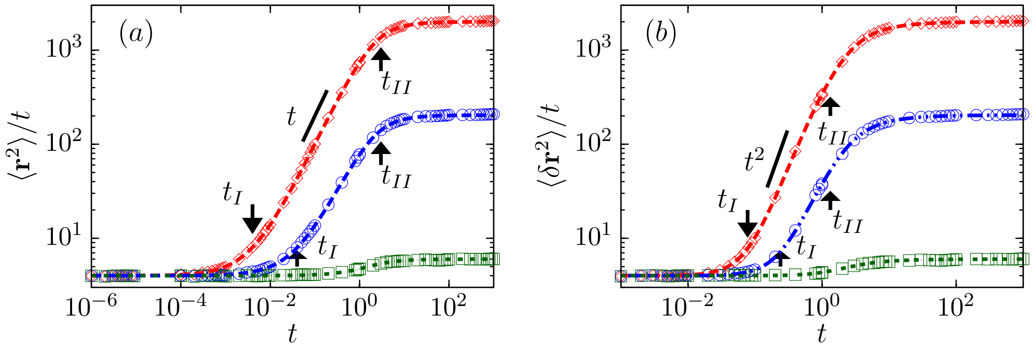

Figure 2.9: (color online) Time dependence of ratios $\langle r^2 \rangle / t$ and $\langle \delta r^2 \rangle / t$ in two dimension. $D_r = 1.0\,\tau_u^{-1}$, $v_0 = 10\,\sigma/\tau_u$ are held constant. The results of numerical simulation at $D\tau_u/\sigma^2 = 0.1(\diamond)$, $1(\circ)$, $100(\square)$ are shown by points denoted in the two figures. Dashed lines show plots of $\langle \mathbf{r}^2 \rangle$ and $\langle \delta\mathbf{r}^2 \rangle$ present in Eqs. (2.23) and (2.25) respectively. For individual curves, arrows denote $t_I = (2d/\lambda^2)\tau_r$, $t_{II} = [3/(d-1)]\tau_r$ in (a), and $t_I = [3d/(d-1)]^{1/2}\tau_r$ and $t_{II} = [4/3(d-1)]\tau_r$ in (b), with $d = 2$.

2.6.2 Displacement fluctuation

Using Eqs. (2.19) and (2.23), one can calculate the fluctuation of the displacement $\langle \delta\mathbf{r}^2 \rangle = \langle \mathbf{r}^2 \rangle - \langle \mathbf{r} \rangle^2$.

$$\langle \delta\mathbf{r}^2 \rangle = 2d \left(D + \frac{v_0^2}{(d-1)dD_r} \right) t - \frac{v_0^2}{(d-1)^2 D_r^2} \left(3 - 4\, e^{-(d-1)D_r\, t} + e^{-2(d-1)D_r t} \right). \tag{2.25}$$

The lines through the simulation results plotted with points in Fig. (2.9)(b) correspond to this relation. In the small time limit it can be expanded to give

$$\langle \delta\mathbf{r}^2 \rangle = 2dDt + \frac{2}{3}(d-1)D_r v_0^2 t^3 - \frac{1}{2}(d-1)^2 D_r^2 v_0^2 t^4 + \mathcal{O}(t^5). \tag{2.26}$$

Thus the mean squared displacement $\langle \delta\mathbf{r}^2 \rangle$ is expected to show crossovers from a diffusive $\sim t$ scaling to $\sim t^3$ scaling at $t_I \approx [3d/(d-1)]^{1/2}\tau_r/\lambda$. This would be followed by another crossover back to diffusive scaling near $t_{II} \approx [4/3(d-1)]\tau_r$. These crossovers obtained from simulations in 2d and their comparison with the above analyses are shown in Fig. (2.9)(b). In the limit of $D = 0$, only a single crossover from $\langle \delta\mathbf{r}^2 \rangle \sim t^3$ to $\langle \mathbf{r}^2 \rangle \sim t$ at $t_{II} \approx [4/3(d-1)]\tau_r$ survives.

The expression for $\langle \mathbf{r}^2 \rangle$ in Eq. (2.23) can easily be mapped to find the expression for the end-to-end separation for WLC model, setting $D = 0$. As before, we use $\kappa = v_0/2D_r$, $l = v_0 t$ to obtain

$$\langle \mathbf{r}^2 \rangle = \frac{4\kappa l}{d-1} - \frac{8\kappa^2(1 - e^{-\frac{(d-1)l}{2\kappa}})}{(d-1)^2}, \tag{2.27}$$

a well known result of the WLC model [93].

2.7 Components of displacement fluctuation

Due to the persistence of motion, the fixing of initial active orientation of the ABP leads to asymmetric displacements, characetrized by $\langle r_\parallel^2 \rangle$ and $\langle \mathbf{r}_\perp^2 \rangle$, where $r_\parallel$ and $\mathbf{r}_\perp \perp \hat{\boldsymbol{u}}_0$ are defined in Eq. (2.20). Without any loss of generality, we assume that the initial orientation of activity $\hat{\boldsymbol{u}}_0$ is in the x-direction, $\hat{\boldsymbol{u}}_0 = \hat{x}$. Using $r_\parallel^2 = x^2$ as ψ in Eq. (2.15), we get

$$s\langle r_\parallel^2 \rangle_s = 2D/s\, + 2v_0 \langle x u_x \rangle_s. \tag{2.28}$$

To proceed, we again consider $\psi = x u_x$ in Eq. (2.15), giving $\langle \psi \rangle_0 = 0$, $\nabla^2 \psi = 0$, $\nabla_u^2 \psi = -(d-1) x u_x$, $\hat{\boldsymbol{u}} \cdot \nabla \psi = u_x^2$, to get $s\langle x u_x \rangle_s = -(d-1) D_r \langle x u_x \rangle_s + v_0 \langle u_x u_x \rangle_s$ leading to

$$\langle x u_x \rangle_s = \frac{v_0}{s + (d-1)D_r} \langle u_x u_x \rangle_s. \tag{2.29}$$

At this stage we need to calculate $\langle u_x^2 \rangle$. Using $\langle u_x^2 \rangle_0 = 1$, $\nabla^2 u_x^2 = 0$, $\langle \nabla_u^2 u_x^2 \rangle_s = -2d\langle u_x^2 \rangle_s + 2/s$, $\hat{\boldsymbol{u}} \cdot \nabla u_x^2 = 0$ in Eq. (2.15) we find

$$\langle u_x u_x \rangle_s = \frac{(s + 2D_r)}{s(s + 2dD_r)}. \tag{2.30}$$

In calculating $\langle \nabla_u^2 u_x^2 \rangle_s$ we used the general relation

$$\nabla_u^2 (u_i u_j) = -2d\, u_i u_j + 2\delta_{ij}. \tag{2.31}$$

To derive this, let us consider $u_i u_j = r_i r_j / r^2$ and $\nabla^2 = \partial_r^2 + (1/r^2)\nabla_u^2$. Note that this Laplacian ∇^2 operates on the active orientation, not on the position vector of the particle. If f is a function of $\hat{\boldsymbol{u}}$ alone, $\nabla^2 f = (1/r^2)\nabla_u^2 f$. It is easy to directly calculate $\nabla^2(r_i r_j/r^2)$ component- wise in cartesian coordinates. The result $\nabla^2(r_i r_j/r^2) = -2d\, r_i r_j/r^4 + (2/r^2)\delta_{ij}$ then leads to Eq. (2.31).

Using Eqs. (2.28), (2.29), and (2.30), we obtain

$$\langle r_\parallel^2 \rangle_s = \frac{2D}{s^2} + \frac{2v_0^2(s+2D_r)}{s^2(s+(d-1)D_r)(s+2dD_r)}. \tag{2.32}$$

Performing inverse Laplace transform one finds

$$\begin{aligned} \langle r_\parallel^2 \rangle &= 2\left(D + \frac{v_0^2}{(d-1)dD_r}\right) t \\ &+ \frac{v_0^2}{D_r^2}\left(\frac{(d-1)e^{-2dD_r t}}{d^2(d+1)} + \frac{2(3-d)e^{-(d-1)D_r t}}{(d-1)^2(d+1)} + \frac{d^2-4d+1}{(d-1)^2 d^2}\right). \end{aligned} \tag{2.33}$$

This can be used to calculate the relative fluctuations $\langle \delta r_\parallel^2 \rangle = \langle r_\parallel^2 \rangle - \langle r_\parallel \rangle^2$ and $\langle \delta \mathbf{r}_\perp^2 \rangle = \langle \mathbf{r}_\perp^2 \rangle = \langle \mathbf{r}^2 - r_\parallel^2 \rangle$, since $\langle \mathbf{r}_\perp \rangle = 0$. They are given by

$$\begin{aligned} \langle \delta r_\parallel^2 \rangle &= 2\left(D + \frac{v_0^2}{(d-1)dD_r}\right) t \\ &+ \frac{v_0^2}{D_r^2}\left(\frac{(d-1)e^{-2dD_r t}}{d^2(d+1)} + \frac{8e^{-(d-1)D_r t}}{(d-1)^2(d+1)} - \frac{e^{-2(d-1)D_r t}}{(d-1)^2} - \frac{4d-1}{(d-1)^2 d^2}\right), \end{aligned} \tag{2.34}$$

$$\begin{aligned} \langle \delta \mathbf{r}_\perp^2 \rangle &= 2(d-1)\left(D + \frac{v_0^2}{(d-1)dD_r}\right) t \\ &+ \frac{v_0^2}{D_r^2}\left(\frac{4e^{-(d-1)D_r t}}{d^2-1} - \frac{(d-1)e^{-2dD_r t}}{d^2(d+1)} - \frac{3d-1}{d^2(d-1)}\right). \end{aligned} \tag{2.35}$$

In two dimensions ($d = 2$) the mean squared displacements of the parallel and

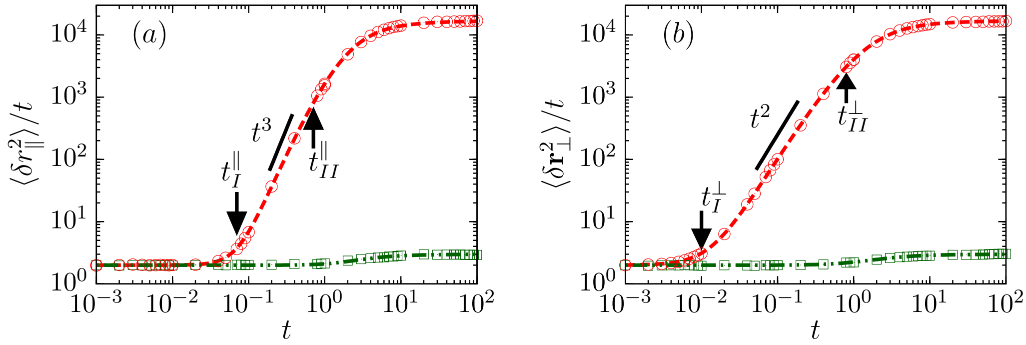

Figure 2.10: (color online) The plots of $\langle\delta r_\parallel^2\rangle$ and $\langle\delta \mathbf{r}_\perp^2\rangle$ as a function of time t in two dimension. $D_r = 1.0\,\tau_u^{-1}$, $D = 1.0\,\sigma^2/\tau_u$ are held constant. The data for $v_0\tau_u/\sigma = 1\,(\square)$, $130\,(\circ)$ are shown in the two figures. The dashed lines show plots of $\langle\delta r_\parallel^2\rangle$ and $\langle\delta \mathbf{r}_\perp^2\rangle$ obtained from Eq. (2.36) and (2.37). For the expressions of $t_{I,II}^\parallel$ and $t_{I,II}^\perp$, see the discussion after Eq. (2.38). The solid lines in the figures denote the intermediate scaling.

perpendicular components simplify to

$$\langle\delta r_\parallel^2\rangle = 2\left(D + \frac{v_0^2}{2D_r}\right)t + \frac{v_0^2}{D_r^2}\left(\frac{1}{12}e^{-4D_r t} - e^{-2D_r t} + \frac{8}{3}e^{-D_r t} - \frac{7}{4}\right), \tag{2.36}$$

$$\langle\delta \mathbf{r}_\perp^2\rangle = 2\left(D + \frac{v_0^2}{2D_r}\right)t + \frac{v_0^2}{D_r^2}\left(-\frac{1}{12}e^{-4D_r t} + \frac{4}{3}e^{-D_r t} - \frac{5}{4}\right). \tag{2.37}$$

For $D = 0$, these agree with the results obtained in [87]. In Fig. (2.10) we show a comparison of these analytic estimates with numerical simulations of ABP model at two different propulsion velocities v_0, in 2d. The analytic expressions of Eq. (2.36) and (2.37) are plotted by lines, and the simulation results by points. The results agree with each other. In the long time limit, both the components, $\langle\delta r_\parallel^2\rangle$ and $\langle\delta \mathbf{r}_\perp^2\rangle$, show the same diffusive scaling $\sim t$. However, at shorter time their respective behaviors differ. We can further use the analytic expressions to extract the observed crossovers in the dynamics of figure2.10. Performing an expansion around $t = 0$ in $2d$ we find,

$$\begin{aligned}\langle\delta r_\parallel^2\rangle &= 2Dt + \frac{1}{3}v_0^2 D_r^2 t^4 - \frac{7}{15}v_0^2 D_r^3 t^5 + \mathcal{O}(t^6),\\ \langle\delta \mathbf{r}_\perp^2\rangle &= 2Dt + \frac{2}{3}v_0^2 D_r t^3 - \frac{5}{6}v_0^2 D_r^2 t^4 + \mathcal{O}(t^5).\end{aligned} \tag{2.38}$$

The parallel component $\langle \delta r_{\parallel}^2 \rangle$ first crosses over from $\sim t$ to $\sim t^4$ at $t_I^{\parallel} = (6/\lambda^2)^{1/3}\tau_r$ followed by another crossover to $\sim t$ at $t_{II}^{\parallel} \approx (5/7)\tau_r$ independent of the amount of active drive $\lambda = v_0/\sqrt{DD_r}$. Note that both the crossovers will be observable only if $t_{II}^{\parallel} > t_I^{\parallel}$, requiring $\lambda > 4.1$.

The transverse fluctuations $\langle \delta \mathbf{r}_{\perp}^2 \rangle$ first crosses over from $\sim t$ to $\sim t^3$ scaling at $t_I^{\perp} = [3/\lambda^2]^{1/2}\tau_r$ followed by another crossover to $\sim t$ at $t_{II}^{\perp} \approx (4/5)\tau_r$ independent of λ. These two crossovers will be observable if $t_{II}^{\perp} > t_I^{\perp}$, requiring $\lambda > 2.2$. We present simulation results in 2d, and their comparison with analytic expressions in Fig. (2.10). In this figure, both the above mentioned conditions are satisfied for $\lambda = 130$, and broken for $\lambda = 1$. As a result, we observe the two crossovers only at $\lambda = 130$ in Fig. (2.10)(a) and (b). Whereas, the same figures for $\lambda = 1$ shows approximate diffusive scalings all through. The lines through the simulation results are plots of Eqs. (2.36) and (2.37). As is evident from Eq. (2.38), in the absence of translational diffusion, the short time scaling behaviors are dominated by $\langle \delta r_{\parallel}^2 \rangle \sim t^4$ and $\langle \delta \mathbf{r}_{\perp}^2 \rangle \sim t^3$, as was already been pointed out in [87].

2.8 Quartic order moment

The calculation of $\langle \mathbf{r}^4 \rangle$ involves the following steps: (i) $s\langle \mathbf{r}^4 \rangle_s = 4(d+2)D\langle \mathbf{r}^2 \rangle_s + 4v_0\langle (\hat{\boldsymbol{u}} \cdot \mathbf{r})\mathbf{r}^2 \rangle_s$, evaluating which requires us to consider the equation (ii) $[s + (d-1)D_r]\langle (\hat{\boldsymbol{u}} \cdot \mathbf{r})\mathbf{r}^2 \rangle_s = (4+2d)D\langle \hat{\boldsymbol{u}} \cdot \mathbf{r} \rangle_s + v_0\langle \mathbf{r}^2 \rangle_s + 2v_0\langle (\hat{\boldsymbol{u}} \cdot \mathbf{r})^2 \rangle_s$. This in turn requires us to consider the equation (iii) $(s + 2dD_r)\langle (\hat{\boldsymbol{u}} \cdot \mathbf{r})^2 \rangle_s = \frac{2D}{s} + 2D_r\langle r^2 \rangle_s + 2v_0\langle \hat{\boldsymbol{u}} \cdot \mathbf{r} \rangle_s$. Using Eq. (2.31) one can show that $\nabla_u^2[(\hat{\boldsymbol{u}} \cdot \mathbf{r})^2] = 2r^2 - 2d(\hat{\boldsymbol{u}} \cdot \mathbf{r})^2$. The expressions for $\langle \hat{\boldsymbol{u}} \cdot \mathbf{r} \rangle_s$ and $\langle \mathbf{r}^2 \rangle_s$ were already evaluated in Eqs. (2.21) and (2.22). Thus one can use all these steps to complete the calculation leading to

$$
\begin{aligned}
\langle \mathbf{r}^4 \rangle_s = \frac{8}{s^3} \bigg[& d(d+2)D^2 + Dv_0^2 \frac{(d+2)(3s + 2(d-1)D_r)}{(s + (d-1)D_r)^2} \\
& + v_0^4 \frac{3s + 2(d+2)D_r}{(s + (d-1)D_r)^2 (s + 2dD_r)} \bigg] .
\end{aligned}
\tag{2.39}
$$

Apart from the factor $d(d+2)$ in the first term, this agrees with Eq. (34) of Ref. [10]. Note that this result is independent of the initial orientation $\hat{\boldsymbol{u}}_0$ and so the difference persists even after averaging over initial conditions. Performing the inverse Laplace transform, we obtain the time evolution of the fourth moment in d-dimensions,

$$\begin{aligned}\langle \mathbf{r}^4(t)\rangle &= \frac{4(d-1)v_0^4 e^{-2dD_rt}}{d^3(d+1)^2D_r^4} - \frac{8\left(d^2v_0^4+10dv_0^4+25v_0^4\right)e^{-(d-1)D_rt}}{(d-1)^4(d+1)^2D_r^4} \\ &+ \frac{4\left(d^3v_0^4+23d^2v_0^4-7dv_0^4+v_0^4\right)}{(d-1)^4d^3D_r^4} \\ &+ \frac{8te^{-(d-1)D_rt}\left(d^3DD_rv_0^2+2d^2DD_rv_0^2-dDD_rv_0^2+dv_0^4-2DD_rv_0^2-7v_0^4\right)}{(d-1)^3(d+1)D_r^3} \\ &+ \frac{4t^2\left(d^5D^2D_r^2-3d^3D^2D_r^2+2d^3DD_rv_0^2+2d^2D^2D_r^2+2d^2DD_rv_0^2-4dDD_rv_0^2+dv_0^4+2v_0^4\right)}{(d-1)^2dD_r^2} \\ &- \frac{8t\left(d^4DD_rv_0^2+d^3DD_rv_0^2-2d^2DD_rv_0^2+d^2v_0^4+6dv_0^4-v_0^4\right)}{(d-1)^3d^2D_r^3}. \end{aligned} \tag{2.40}$$

Again in $d=2$ the relation simplifies to

$$\begin{aligned}\langle \mathbf{r}^4(t)\rangle &= \frac{8t^2\left(4D^2D_r^2+4DD_rv_0^2+v_0^4\right)}{D_r^2} + \frac{8te^{-D_rt}\left(12DD_rv_0^2-5v_0^4\right)}{3D_r^3} \\ &- \frac{2t\left(16DD_rv_0^2+15v_0^4\right)}{D_r^3} + \frac{v_0^4e^{-4D_rt}}{18D_r^4} - \frac{392v_0^4e^{-D_rt}}{9D_r^4} + \frac{87v_0^4}{2D_r^4}. \end{aligned} \tag{2.41}$$

For $D=0$ this agrees with the expression in [93] and we have also verified that our result for $d=3$ agrees with [91]. Eq. (2.41) is plotted by dashed lines in Fig. (2.11). As is clearly seen from the figure, the two dimension simulation data (points) agree well with this analytic expression. In the limit of $t \gg 1/D_r$, the first term in the above expression dominates to give $\langle \mathbf{r}^4(t)\rangle \sim t^2$. The change in scaling with t as observed from the figure can be better understood by considering the expansion of the expression in Eq. (2.41) around $t=0$,

$$\langle \mathbf{r}^4(t)\rangle = 32D^2t^2 + 16Dv_0^2t^3 + \left(v_0^2 - \frac{16}{3}DD_r\right)v_0^2t^4 - \frac{2}{3}v_0^2D_r\left(v_0^2-2DD_r\right)t^5 + \mathcal{O}(t^6).$$

This relation shows that at smallest time $\langle \mathbf{r}^4(t)\rangle \sim t^2$, which crosses over to $\langle \mathbf{r}^4(t)\rangle \sim t^3$ at $t_I = (2/\lambda^2)\tau_r$. A second crossover from $\sim t^3$ to $\sim t^4$ may appear at $t_{II} = [48/(3\lambda^2-16)]\tau_r$ provided $\lambda^2 > 16/3$. At a longer time, $t_{III} \approx \frac{1}{2}\frac{3\lambda^2-16}{\lambda^2-2}\tau_r$ the

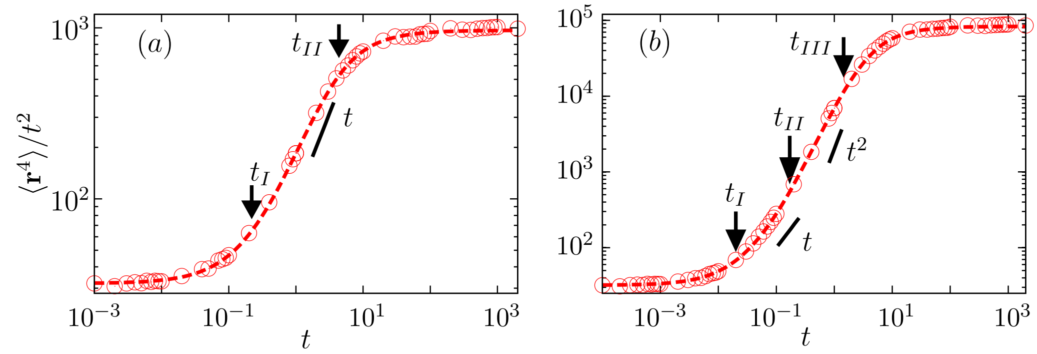

Figure 2.11: (color online) Evolution of the ratio $\langle r^4 \rangle / t^2$ with time in 2d. $D_r = 1.0\,\tau_u^{-1}$ and $D = 1.0\,\sigma^2/\tau_u$ are held constant. The points denote simulation results, and the dashed lines denote analytic prediction in Eq. (2.41). (a) $v_0 = 3\,\sigma/\tau_u$ shows two crossovers at $t_I = 0.22\,\tau_r$, $t_{II} = 4.36\,\tau_r$, (b) $v_0 = 10\,\sigma/\tau_u$ shows three crossovers at crossover times $t_I \approx 0.02\,\tau_r$, $t_{II} = 0.17\,\tau_r$ and $t_{III} = 1.45\,\tau_r$. The black solid lines in the two curves indicate the intermediate scaling behaviors.

time-dependence is expected to show a third cross- over back to $\langle \mathbf{r}^4(t) \rangle \sim t^2$. It is clear that whether all these crossovers will be observable depends on the activity parameter λ. For example, the requirement to observe the third crossover $t_{III} > t_{II}$ is satisfied only when $\lambda^2 > 56/3$. As can be seen from Fig. (2.11)(a), $\langle \mathbf{r}^4 \rangle$ shows $\sim t^2$ to $\sim t^3$ crossover at t_I, and a direct crossover back to $\sim t^2$ beyond t_{II} at $v_0 = 3\,\sigma/\tau_u$ that obeys the condition $\lambda^2 < 56/3$. On the other hand Fig. (2.11)(b) at $v_0 = 10\,\sigma/\tau_u$, satisfying the condition $\lambda^2 > 56/3$, clearly shows all the three crossovers discussed above. The crossover points indicated in the figures correspond to the expressions derived above.

Moreover, the expression for the fourth moment of the persistent walk corresponding to the WLC polymer in d-dimensions is easily obtainable by setting $D = 0$ in Eq. (2.39),

$$\langle \mathbf{r}^4 \rangle_s = 8 v_0^4 \frac{3s + 2(d+2)D_r}{s^3 (s + (d-1)D_r\,)^2\,(s + 2d\,D_r\,)}. \tag{2.42}$$

The inverse Laplace transform of this relation gives the evolution,

$$\begin{aligned}\langle \mathbf{r}^4(t)\rangle = 4v_0^4 \Bigg(&\frac{(d-1)e^{-2dD_r t}}{d^3(d+1)^2 D_r^4} - \frac{2\,(d+5)^2\, e^{-(d-1)D_r t}}{(d-1)^4(d+1)^2 D_r^4} - \frac{2\,(d^2+6d-1)\,t}{(d-1)^3 d^2 D_r^3} \\ &+ \frac{(d^3+23d^2-7d+1)}{(d-1)^4 d^3 D_r^4} - \frac{2(7-d)\,te^{-(d-1)D_r t}}{(d-1)^3(d+1)D_r^3} + \frac{(d+2)\,t^2}{(d-1)^2 d D_r^2}\Bigg). \end{aligned} \tag{2.43}$$

Replacing $\kappa = v_0/2D_r$, $l = v_0 t$ provides the well known result for $\langle \mathbf{r}^4(l)\rangle$ of WLC model [93].

2.9 End- to- end distribution with chain length

In the equivalent polymer model, the dynamical crossovers with observation time τ translate into similar behavior of the end-to-end separation $\langle \mathbf{r}^2\rangle$ with increasing contour length $L = v_0\tau$ for a polymer with a given $A = v_0/2D$ and $\kappa = v_0/2D_r$. In Fig. (2.12) we plot the distribution functions $p(\tilde{r})$ of the scaled separation $\tilde{r} = r/L$. For the given choice of parameters, $D_r = 1.0\tau_u^{-1}$, $v_0 = 10\,\sigma/\tau_u$ and $D = 0.1\,\sigma^2/\tau_u$, the persistence length of such a chain in 2d is $\ell_p = v_0/D_r = 10^3\,\bar{\ell}$, where $\bar{\ell} = \sqrt{D/D_r} = 10^{-2}\sigma$. As is clear from Fig. (2.12)(a), for the smallest chain lengths, $L < \bar{\ell}$, the distribution shows a Gaussian profile. In this regime, the dynamics of the corresponding ABP model remains dominated by the translational diffusion, and $\langle \mathbf{r}^2\rangle \approx 2dDt$. Equivalently, the polymer conformations remain dominated by the bond length fluctuations. With increasing contour length (time for ABP model), first the maximum at $\tilde{r} \approx 0$ starts to flatten as L approaches $\bar{\ell}$ (Fig. (2.12)(b)). For longer contours, $L = 10\,\bar{\ell}$, $100\,\bar{\ell}$, the peak shifts towards $\tilde{r} \approx 1$ (Fig. (2.12)(c), (d)). The bending rigidity starts to dominate the polymer conformations in this regime. In this model, for the persistence to start to dominate the polymer morphology, a relatively long chain is required. This behavior contrasts the current model from the WLC polymer, where the chain transforms from a rigid rod to flexible chain behavior monotonically, with increasing chain length. For longer chains, the position of the peak in $p(\tilde{r})$ fails to catch up to L as a result of effective polymer softening. This

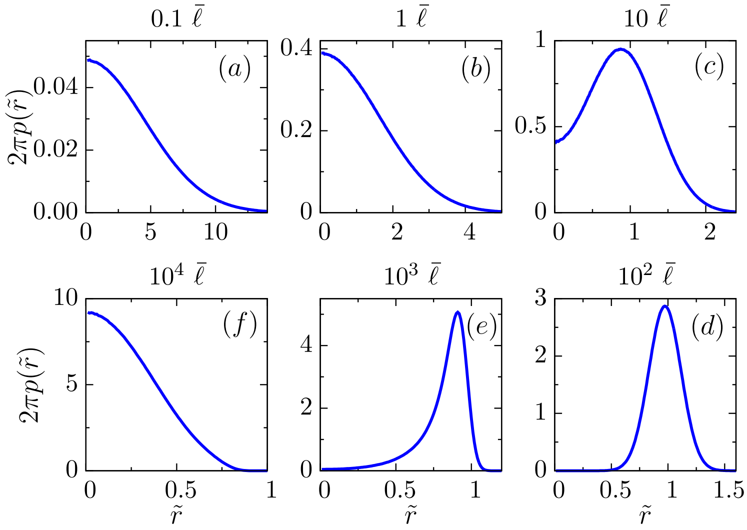

Figure 2.12: (color online) The displacement distributions at $D_r = 1.0\,\tau_u^{-1}$, $v_0 = 10\,\sigma/\tau_u$ and $D = 0.1\,\sigma^2/\tau_u$ over different time-segments indicated by the $v_0 t$ values shown in the figures. The persistence length of the mapped polymer $\ell_p = 10^3\bar{\ell}$. The length of trajectories considered are $L = 0.1\,\bar{\ell}\,(a), 1.0\,\bar{\ell}\,(b), 10\,\bar{\ell}\,(c), \ldots, 10^4\bar{\ell}\,(f)$.

behavior is reminiscent of the WLC polymer. At $L = 10^3\bar{\ell} \equiv \ell_p$, the peak shifts to a shorter relative separation $\tilde{r} \approx 900\bar{\ell}/L \lesssim 1$ (Fig. (2.12)(e)). For longest chains, $L \gg \ell_p$, the distribution gets back to an approximate Gaussian shape with the maximum shifting back to $\tilde{r} = \ell_p/L \approx 0$ (Fig. (2.12)(f)). This regime corresponds to $\langle \mathbf{r}^2 \rangle = 2d\,D_{\text{eff}}t$ of the ABP model.

Fig. (2.13) shows the full two-dimensional end-to-end distribution function $p(\tilde{x}, \tilde{y})$ as a contour plot. Here $\tilde{x} = x/L$ and $\tilde{y} = y/L$. It is evident how the symmetry of the distribution changes with increasing contour-length of the polymer. With L, the peak shifts towards positive x-axis, the orientation of the first end of the polymer, but the distribution around the peak remains circularly symmetric up to $L = 10\,\bar{\ell}$ (Fig. (2.13)(a), (b), and (c)). Beyond this point, even around the peak, the distribution gets rotationally asymmetric, opening up as a partial ring-like structure at $L = \ell_p = 10^3\bar{\ell}$ (Fig. (2.13)(d), (e)). For the longest chain of $L = 10^4\bar{\ell}$, the distribution recovers its spherical symmetry and gets back to the Gaussian profile (Fig. (2.13)(f)). It is interesting to note that in terms of the rigidity parameter L/ℓ_p the last two values of L falls at ℓ_p and $10\,\ell_p$. For the chain

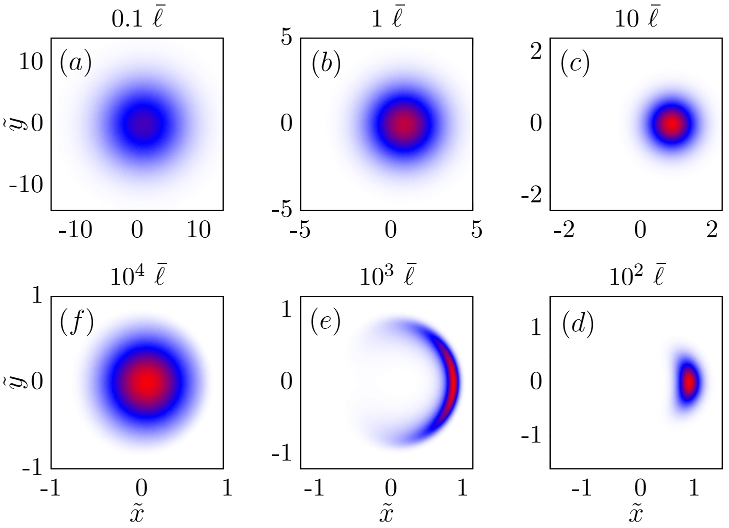

Figure 2.13: (color online) The 2d displacement distributions $p(\tilde{x}, \tilde{y})$ at $D_r = 1.0\,\tau_u^{-1}$, $v_0 = 10.0\,\sigma/\tau_u$ and $D = 0.1\,\sigma^2/\tau_u$ over different time segments τ, presented as heat maps. The length of trajectories considered are $L = v_0\tau = 0.1\,\bar{\ell}\,(a), 1.0\,\bar{\ell}\,(b), 10\,\bar{\ell}\,(c), \ldots, 10^4\bar{\ell}\,(f)$.

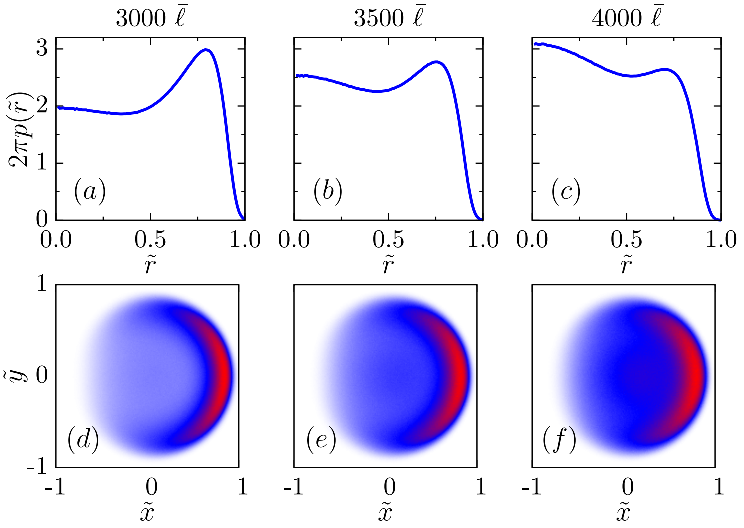

Figure 2.14: (color online) The change in distributions $p(\tilde{r})$ $[(a) - (c)]$ and $p(\tilde{x}, \tilde{y})$ $[(d) - (f)]$ at $D_r = 1.0\,\tau_u^{-1}$, $v_0 = 10.0\,\sigma/\tau_u$ and $D = 0.1\,\sigma^2/\tau_u$ for different contour lengths $L = v_0\tau$ in the regime of bimodality. The persistence length $\ell_p = 10^3\bar{\ell}$. The length of trajectories considered are $L = 3\ell_p\,[(a), (d)]\,3.5\ell_p\,[(b), (e)]$, $4\ell_p\,[(c), (f)]$.

in consideration, the effective spring-stiffness of the bonds $A = v_0/2D = 50\sigma^{-1}$ is large enough to suppress bond-length fluctuations to within 7%, allowing an approximate WLC description of the effective chain. The WLC polymer is known to show a rigid rod to Gaussian transition mediated by a bistable region between

$1 < L/\ell_p < 10$ (near $L/\ell_p \approx 3 - 4$) [93, 94]. We find a similar transition through bistability at $L/\ell_p = 3.5$ (Fig. (2.14)). The distributions obtained in Fig. (2.14) are reminiscent of the property of WLC polymer with one end tethered towards a fixed orientation [94].

2.10 Differentiation of ABP with active Ornstein-Uhlenbeck process(AOUP)

In experiments often one encounters a question as to which model is better suited to describe the observed spatiotemporal behavior of self propelled colloids [12]. Active Brownian particles (ABP), or a related model of active Ornstein-Uhlenbeck process (AOUP) are used sometimes for such descriptions.

2.10.1 AOUP model and calculation of moments

The over-damped motion in AOUP model is given by [8]

$$\begin{aligned} \dot{\mathbf{r}} &= \mathbf{v} + \sqrt{2D}\,\boldsymbol{\eta}(t) \\ \dot{\mathbf{v}} &= -\gamma\mathbf{v} + \sqrt{2D_v}\,\boldsymbol{\eta}^v(t). \end{aligned} \tag{2.44}$$

The Gaussian random processes are defined by $\langle \eta_i \rangle = 0$, $\langle \eta_i(t)\eta_j(t') \rangle = \delta_{ij}\delta(t-t')$, $\langle \eta_i^v \rangle = 0$, $\langle \eta_i^v(t)\eta_j^v(t') \rangle = \delta_{ij}\delta(t-t')$, where i, j denote components of the vectors. We assume $\boldsymbol{\eta}$ and $\boldsymbol{\eta}^v$ to be independent random processes. Given the Gaussian nature of the AOUP, it is straightforward to derive analytic expressions, including the probability distributions describing its dynamics [8]. The distribution function $p(\mathbf{r}(t), \mathbf{v}(t), t \,|\, \mathbf{r}(0), \mathbf{v}(0)\,)$ for a given initial condition denoted by $\mathbf{r}(0), \mathbf{v}(0)$ can be obtained from the knowledge of the first two cumulants. Directly solving Eq. (2.44) one can obtain the moments

$$\langle \mathbf{r} \rangle = \frac{\mathbf{v}(0)}{\gamma}\left(1 - e^{-\gamma t}\right), \tag{2.45}$$

$$\langle \mathbf{v} \rangle = \mathbf{v}(0)\, e^{-\gamma t}, \tag{2.46}$$

$$\langle \mathbf{r}^2 \rangle = 2dDt + \frac{2dD_v}{\gamma^3}\left[\gamma t - (1 - e^{-\gamma t})\right] + \langle \mathbf{r} \rangle^2 - \frac{dD_v}{\gamma^3}\left(1 - e^{-\gamma t}\right)^2, \tag{2.47}$$

$$\langle \mathbf{v}^2 \rangle = \mathbf{v}^2(0)\, e^{-2\gamma t} + \frac{dD_v}{\gamma}\left(1 - e^{-2\gamma t}\right), \tag{2.48}$$

$$\langle \mathbf{v} \cdot \mathbf{r} \rangle = \frac{\mathbf{v}^2(0)}{\gamma}\left(1 - e^{-\gamma t}\right) e^{-\gamma t} + \frac{dD_v}{\gamma^2}(1 - e^{-\gamma t})^2 . \tag{2.49}$$

2.10.2 Comparision with ABP

We make the following identifications between AOUP and ABP parameters:

$$\mathbf{v}^2(0) = \mathbf{v}_0^2, \quad \gamma = (d-1)D_r, \quad \frac{dD_v}{\gamma} = \mathbf{v}_0^2. \tag{2.50}$$

Then we see that the evolution of all the moments computed in Eqs. (2.45), (2.46), (2.47), (2.48), and (2.49) have exactly the same form as those obtained for the ABP. In particular we see that Eq. (2.47) simplifies to the form

$$\langle \mathbf{r}^2 \rangle = 2dDt + \frac{2dD_v}{\gamma^3}\left[\gamma t - (1 - e^{-\gamma t})\right]. \tag{2.51}$$

which can be compared with that for ABP obtained in Eq. (2.23), when γ and D_v are interpreted using Eq. (2.50). Similarly, after simplification $\langle \mathbf{v}^2 \rangle = \mathbf{v}^2(0)$, and $\langle \mathbf{v} \cdot \mathbf{r} \rangle = [\mathbf{v}^2(0)/\gamma]\,(1 - e^{-\gamma t})$.

2.10.3 Kurtosis : deviation from Gaussian process

The ABP and AOUP models can thus be clearly distinguished only in terms of higher moments. Let us first evaluate the fourth moment $\langle \mathbf{r}^4 \rangle$ for a general Gaussian process (such as the AOUP) in terms of the lower order moments. For this, we write

$\mathbf{r} = \delta\mathbf{r} + \langle\mathbf{r}\rangle$ so that

$$\begin{aligned}\langle\mathbf{r}^4\rangle &= \langle(\delta r_i + \langle r_i\rangle)^2\,(\delta r_j + \langle r_j\rangle)^2\rangle\\ &= \langle\delta r_i^2\delta r_j^2\rangle + 2\langle\delta r_i^2\rangle\langle r_j\rangle^2 + 4\langle r_i\rangle\langle r_j\rangle\langle\delta r_i\delta r_j\rangle + \langle r_i\rangle^2\langle r_j\rangle^2.\end{aligned}$$

Using Wick's theorem for Gaussian variables,

$$\langle\delta r_i^2\delta r_j^2\rangle = \langle\delta r_i^2\rangle\langle\delta r_j^2\rangle + 2\langle\delta r_i\delta r_j\rangle^2,$$

we then get

$$\langle\mathbf{r}^4\rangle = \langle\delta\mathbf{r}^2\rangle^2 + 2\langle\delta r_i\delta r_j\rangle^2 + 2\langle\delta\mathbf{r}^2\rangle\langle\mathbf{r}\rangle^2 + 4\langle r_i\rangle\langle r_j\rangle\langle\delta r_i\delta r_j\rangle + \langle\mathbf{r}\rangle^4. \tag{2.52}$$

This relation is true for any Gaussian process. Let us define the functional on the right hand side of the above equation as a generalized moment for an arbitrary process, not necessary Gaussian, and denote it by

$$\mu_4 := \langle\delta\mathbf{r}^2\rangle^2 + 2\langle\delta r_i\delta r_j\rangle^2 + 2\langle\delta\mathbf{r}^2\rangle\langle\mathbf{r}\rangle^2 + 4\langle r_i\rangle\langle r_j\rangle\langle\delta r_i\delta r_j\rangle + \langle\mathbf{r}\rangle^4. \tag{2.53}$$

From our explicit solution for the ABP and AOUP we find that

$$\langle\delta r_i(t)\delta r_j(t)\rangle = \frac{\delta_{ij}}{d}\langle\delta\mathbf{r}^2\rangle. \tag{2.54}$$

Replacing this relation in Eq. (2.52) we obtain

$$\mu_4 = \langle\mathbf{r}^2\rangle^2 + \frac{2}{d}\left(\langle\mathbf{r}^2\rangle^2 - \langle\mathbf{r}\rangle^4\right). \tag{2.55}$$

Note that for AOUP we would have $\langle\mathbf{r}^4\rangle = \mu_4$ but this would not be the case for ABP.

In Eq. (2.40) we have already computed the explicit form of $\langle\mathbf{r}^4\rangle$ for ABP. It is

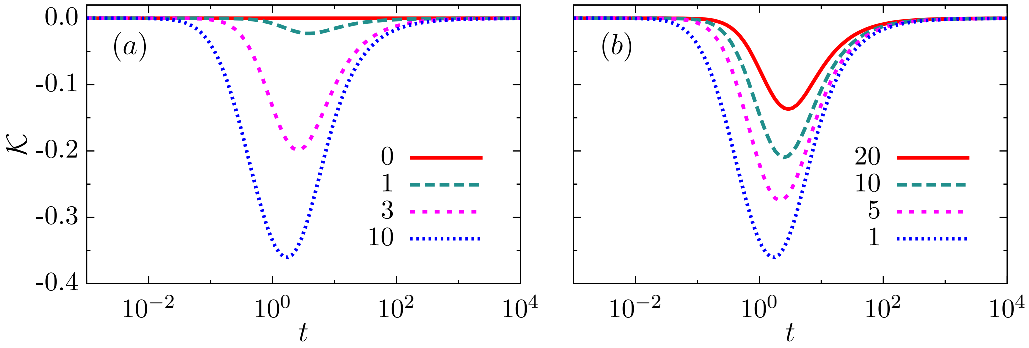

Figure 2.15: (color online) Deviation from Gaussian nature in terms of $\mathcal{K}$ is shown as a function of time t expressed in units of $\tau_r = 1/D_r$. The translational diffusion $D = 1.0\,\sigma^2/\tau_u$ is held constant. (a) Plot with $D_r = 1.0\,\tau_u^{-1}$ for $v_0\,\tau_u/\sigma = 0,\ 1,\ 3,\ 10$. (b) Plot at $v_0 = 10\,\sigma/\tau_u$ for $D_r\tau_u = 1,\ 5,\ 10,\ 20$.

then straightforward to evaluate the kurtosis in d-dimensions defined as

$$\mathcal{K} = \frac{\langle \mathbf{r}^4 \rangle}{\mu_4} - 1. \tag{2.56}$$

By definition, this quantity is identically zero for the AOUP. In Fig. (2.15) we show plots of $\mathcal{K}$ obtained for the ABP model, using our analytical expressions for $\langle \mathbf{r}^4 \rangle$, and that of $\langle \delta\mathbf{r}^2 \rangle$, and $\langle \mathbf{r} \rangle$. The kurtosis was calculated numerically in earlier studies of ABP [8, 9]. The two plots in Fig. (2.15) show variation of $\mathcal{K}$ with time for different amount of activity, measured in terms of active speed v_0 (a) and rotational diffusion of active orientation D_r (b). The plots in Fig. (2.15) show the time dependence of $\mathcal{K}$ at fixed translational diffusion $D = 1.0\,\sigma^2/\tau_u$. At $v_0\tau_u/\sigma = 0$, the ABP motion is the same as equilibrium diffusion showing $\mathcal{K} = 0$ in Fig. (2.15)(a). With increasing v_0 the deviation from Gaussian nature characterized by the amplitude of $\mathcal{K}$ becomes more pronounced and prevails for longer duration in time. Beyond $v_0 = 100\,\sigma/\tau_u$ the Kurtosis touches a maximum amplitude of $\mathcal{K} \approx -0.4$, and the curve does not change appreciably with further increases in v_0. On the other hand, as is shown in Fig. (2.15)(b), the deviation from zero of $\mathcal{K}$ reduces with increasing orientational diffusion D_r, better randomizing the orientation of activity bringing the evolution back towards equilibrium behavior. Over long enough time the trajectories behave as that of diffusion, leading to $\mathcal{K} = 0$ for all v_0.

The measure $\mathcal{K}$, in terms of $\langle \mathbf{r}^4 \rangle$, $\langle \delta \mathbf{r}^2 \rangle$ and $\langle \mathbf{r} \rangle$, is easily obtainable from observed trajectories of self propelled colloids. This would suffice to deduce if the properties shown by a self propelled particle is better described by the AOUP or the ABP model, depending on whether $\mathcal{K}$ remains vanishingly small all through the evolution, or deviates from zero significantly in the intermediate time window as in ABP. Clearly, this measure requires much less information with respect to the measurement of the complete distribution functions proposed in [12].

2.11 Conclusions

In this chapter, we studied free ABPs in the presence of translational thermal noise. We have established a mapping of the ABP trajectories to an equivalent polymer model. The bond stiffness and bending rigidity of the mapped polymer are determined by the active speed, orientational diffusion, and thermal noise in the ABP model. In the limit of vanishing orientational diffusivity, the ABP trajectories map to a Gaussian polymer under directed external force. The other limit of vanishing translational diffusion in the ABP, reduces the mapped polymer to the well known WLC model of the semiflexible chain. Comparisons of the distribution functions for non-equilibrium displacements in ABP, and the end-to-end separations in the equilibrium polymer model showed good agreement. Remarkably, with increasing trajectory length the mapped polymer undergoes *re-entrant* transitions from a Gaussian chain, to rigid filament, back to a Gaussian chain via a pronounced bimodality which is a characteristic of the semiflexible polymer.

Secondly, we have shown how arbitrary moments of the position and active orientation vectors of ABPs in arbitrary dimensions can be calculated using the governing Fokker-Planck equation. For this we utilized a Laplace transform approach used earlier for the WLC model [91]. Our calculation differs significantly from other recent analytic approaches employed for ABPs [10, 87, 88]. The expressions for moments that we obtained were compared against numerical simulations, and have been utilized to analyze all the observed dynamical crossovers. Finally, we derived an analytical expression for the kurtosis of position vector for ABPs, and have shown how it differs from a related AOUP model. This can be utilized to analyze observed trajectories of self propelled colloids, to identify if they can be described by the AOUP, or are better described by the ABP model.

3

Active Brownian particle: fluctuation in the speed

3.1 Introduction

Examples of self propelled entities are abound in nature [2, 3]. They range from sub-micron scale elements like motor proteins [33, 34], bacteria [99, 100] and other motile cells [42–44] to macro-scale entities like birds and animals [46]. The examples of artificial active elements, while restricted, are increasing with time – they include colloidal microswimmers, active rollers, vibrated rods and asymmetric disks [2, 3]. Motile cells often perform persistent motion and can sense and respond to extra-cellular chemical signals [101]. The directed motion under such guidance cues has been analyzed in experiments [102, 103]. The energy pump generating self propulsion, be it in motile cells or in active colloids, involves stochastic processes and thus the active speed appears with inherent fluctuations [30, 79, 101]. Moreover, analysis of the dynamics of a tracer particle in an interacting system of active Brownian particles (ABP) with individual particles self propelling with a constant active speed requires consideration of speed fluctuations, as (i) in an assembly of ABPs inter-particle collision changes the speed of an individual particle in the heading direction [104, 105], (ii) in an active polymer, the active speed of individual bonds and as a result that of its center of mass undergoes fluctuations due to bonding, bending and self-avoidance [106, 107]. In the previous chapter, when we considered the dynamics of ABPs, we ignored this speed fluctuation and focussed primarily on the directional fluctuations in active orientation.

In this chapter, we consider the Schienbein-Gruler type active speed generation [15, 101] for ABPs. This involves an Ornstein-Uhlenbeck process leading to speed fluctuations around a well-defined mean, unlike the constant active speed assumed in the previous chapter. The heading direction of self-propulsion undergoes orientational diffusion, as before. In addition, the motion of ABPs are influenced by translational thermal noise. We extend the Fokker-Planck equation based method presented in the previous chapter to obtain arbitrary moments of the dynamics of speed-fluctuating ABPs in general d-dimensions, both in the presence and absence of external directed force that can generate a directed motion in the long time limit. The competition between the speed relaxation time with other time-scales, e.g., the persistence time leads to new crossovers. The direct calculation presented here allows for coevolution of different dynamical variables and does not require any time-scale separation. Our general results for mean squared displacements when interpreted for two-dimensions agree with Ref. [15, 108] when a clear time-scale separation for speed fluctuations is applicable, such that one can use the steady state speed correlation. We, in particular, analyze the changes due to the speed fluctuations, e.g., the short time asymmetric fluctuations in the ABP displacements. The analysis shows an intermediate time regime of clear sub-diffusive scaling in the positional fluctuations parallel to the starting orientation, a behavior that disappears in the limit of constant active speed. The main achievements of this chapter are the following: (i) We derive the second and fourth moment of displacement vector, its fluctuations, and fluctuations in its projection along the initial heading direction and in directions perpendicular to it. (ii) We show and analyze the presence of multiple crossovers in the mean-squared displacement and fluctuations of displacement vectors. (iii) We show that in the intermediate time-scales, the kurtosis of displacement vector measuring the deviations from possible normal distributions changes between positive and negative values before returning to Gaussian behavior at long times, controlled by the competition between speed and orientational fluctuations.

The chapter is organized as follows. In Section-3.2, we describe the model. In Section-3.3, we present the Laplace transform method starting from the Fokker-Planck equation to derive the general equation to calculate arbitrary moments of dynamical variables in d-dimensions. In the following sections we present calculations of particular quantities of interest: (a) the mean speed and speed fluctuations (Section-3.4), (b) the speed, orientation and velocity auto-correlation functions (Section-3.5), (d) the mean-squared displacement and displacement fluctuations (Section-3.6). In each case, we discuss separately the dynamical properties in the absence and presence of external directed drive. In Section-3.7, we calculate the fourth order moments of displacement and the kurtosis to characterize the non-Gaussian nature of displacement fluctuations. The kurtosis shows positive and negative maxima in time corresponding to relaxations of speed and orientational fluctuations. While the speed fluctuations enter as a bond-length fluctuations, the external directed force on ABPs enters the polymer model to stretch each bond along the force direction locally. Finally, in Section-3.8 we summarize our results and conclude.

3.2 Model

The active Brownian particle (ABP) with fluctuating speed in d-dimension is described by its position $\mathbf{r} = (r_1, r_2, \ldots, r_d)$ and its velocity $\boldsymbol{v}$ represented by the speed v and orientation $\hat{\boldsymbol{u}} = (u_1, u_2, \ldots, u_d)$, which is a unit vector in d-dimensions. Let the infinitesimal increments at time t are denoted by $dr_i = r_i(t + dt) - r_i(t)$, $dv = v(t + dt) - v(t)$, and $du_i = u_i(t + dt) - u_i(t)$. In Ito convention [97, 98, 109], the equation of motion of the ABP with stochastic change of speed is given by

$$dr_i = v(t)u_i\,dt + \mu F_i\,dt + dB_i^t(t), \tag{3.1}$$

$$dv = -\gamma_v(v - v_0)\,dt + dB^s(t), \tag{3.2}$$

$$du_i = (\delta_{ij} - u_i u_j)\,dB_j^r(t) - (d-1)D_r u_i\,dt. \tag{3.3}$$

Eq. (3.1) represents time evolution of position of the particle. The first term on the right-hand side contains the active time dependent speed $v(t)$ and orientation $\hat{\boldsymbol{u}}(t)$. These two variables evolve independently. The second term on the right-hand side is due to an external force providing a long-time directed motion. The third term denotes a translational diffusion due to thermal fluctuations modeled by a Gaussian white noise $\boldsymbol{dB}^t$ with mean zero and variance $\langle dB_i^t dB_j^t\rangle = 2D\delta_{ij}\,dt$.

Eq. (3.2) represents generation of the active speed via an Ornstein-Uhlenbeck process. The relaxation time for speed fluctuations around the mean value v_0 is given by γ_v^{-1}. The Gaussian stochastic process $dB^s(t)$ obeys $\langle dB^s(t)\rangle = 0$, $\langle dB^s dB^s\rangle = 2D_v dt$, with D_v governing the amount of fluctuations. This process does not ascertain a positive speed always, with larger D_v allowing for larger fluctuations and as a result larger excursions towards negative speed with respect to the heading direction. Here, it is instructive to note that such fluctuations with an effective negative speed can arise, e.g., in an assembly of repulsively interacting ABPs [104, 105] due to increased frontal collisions with increasing particle density. The probability of negative speed increases with increase of the ratio D_v/γ_v and decreases with increasing v_0 (see Fig. 3.13 in Appendix-3.9.2).

Eq. (3.3) represents the orientational diffusion of the heading direction. The Gaussian white noise $\boldsymbol{dB}^r$ have mean zero and variance $\langle dB_i^r dB_j^r\rangle = 2D_r\delta_{ij}\,dt$. Alternatively, we can write this equation in the Stratonovich form $du_i = (\delta_{ij} -$

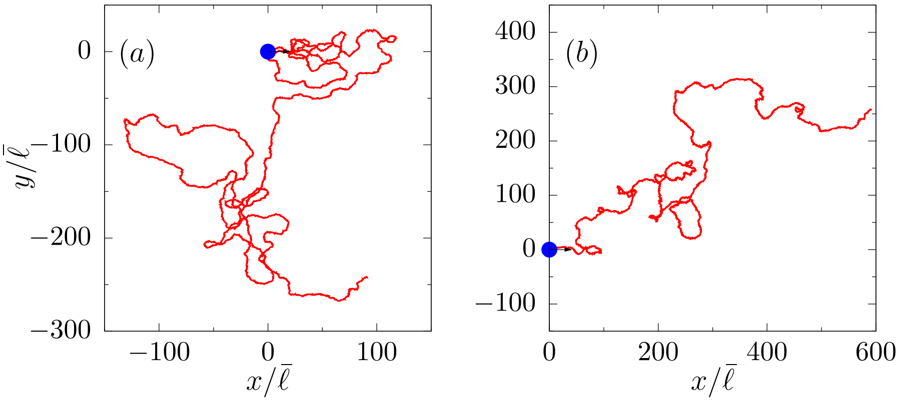

Figure 3.1: (color online) Typical ABP trajectories in two-dimensions (2d) over a duration $t = 100\,\tau_r$ are shown in the absence (a) and (b) presence of external drive: (a) Persistent motion at $\tilde{\boldsymbol{F}}_0 = 0$, (b) Directed persistent motion at $\tilde{\boldsymbol{F}}_0 = 5\,\hat{r}$ with $\hat{r} = \hat{x} + \hat{y}$ in cartesian coordinates. The plots use $Pe = 20$, $\tilde{D}_v = 1$, and $\tilde{\gamma_v} = 1$. The blue point with arrow in each plot shows starting position and orientation of the ABP. In these plots we used the initial active speed $v_1 = \bar{v}Pe$ and heading direction $\hat{\boldsymbol{u}}_0 = \hat{x}$ along the x-axis.

$u_i u_j) \circ dB^r_j(t)$. The form of Eq. (3.3) ensures the normalization $\mathbf{u}^2 = 1$ at all times.

It is straightforward to perform a direct numerical simulation of Eqs. (3.1), (3.2), and (3.3) using the Euler-Maruyama integration to generate trajectories as illustrated in Fig. (3.1). A typical trajectory in the absence of external force is shown in Fig. (3.1)(a) and in the presence of constant external force is shown in Fig. (3.1)(b).

We set $\tau_r = 1/D_r$ as the unit of time, and $\bar{\ell} = \sqrt{D/D_r}$ as the unit of length. All the speeds and velocities are expressed in units of $\bar{v} = \bar{\ell}/\tau_r = \sqrt{DD_r}$. The dimensionless quantities controlling speed-fluctuation and speed-relaxation are $\tilde{D}_v = D_v\tau_r/\bar{v}^2 = D_v/DD_r^2$ and $\tilde{\gamma_v} = \gamma_v/D_r$. The mean active speed is expressed as a dimensionless Péclet number Pe$= v_0/\bar{v} = v_0/\sqrt{DD_r}$. The dimensionless external drive is $\tilde{\boldsymbol{F}} = \mu\mathbf{F}/\bar{v}$.

3.3 Calculation of moments from Fokker-Planck equation

In this section, we present a general framework for the calculation of arbitrary moments [107, 109]. The probability distribution $P(\mathbf{r}, v, \hat{\boldsymbol{u}}, t)$ of the position $\mathbf{r}$, the speed $v(t)$ and the active orientation $\hat{\boldsymbol{u}}$ of the particle follows the Fokker-Planck equation

$$\begin{aligned}\partial_t P(\mathbf{r}, v, \hat{\boldsymbol{u}}, t) &= D\nabla^2 P + D_r \nabla_u^2 P + D_v \partial_v^2 P - v\, \hat{\boldsymbol{u}} \cdot \nabla P + \gamma_v P \\ &+ \gamma_v (v - v_0)\partial_v P - \mu \boldsymbol{F} \cdot \nabla P \end{aligned} \tag{3.4}$$

where ∇ is the d-dimensional Laplacian operator, and ∇_u is the Laplacian in the $(d-1)$ dimensional orientation space, $\boldsymbol{F}$ is the directed constant force.

In terms of the Laplace transform $\tilde{P}(\mathbf{r}, v, \hat{\boldsymbol{u}}, s) = \int_0^\infty dt\, e^{-st}\, P(\mathbf{r}, v, \hat{\boldsymbol{u}}, t)$, the Fokker-Planck equation takes the form,

$$\begin{aligned}&- P(\mathbf{r}, v, \hat{\boldsymbol{u}}, 0) + (s - \gamma_v)\tilde{P}(\mathbf{r}, v, \hat{\boldsymbol{u}}, s) = D\nabla^2 \tilde{P} + D_r \nabla_u^2 \tilde{P} + D_v \partial_v^2 \tilde{P} \\ &- v\, \hat{\boldsymbol{u}} \cdot \nabla \tilde{P} + \gamma_v (v - v_0)\partial_v \tilde{P} - \mu \boldsymbol{F} \cdot \nabla \tilde{P}.\end{aligned}$$

Defining the mean of an observable $\langle \psi \rangle_s = \int d\mathbf{r}\, dv\, d\hat{\boldsymbol{u}}\, \psi(\mathbf{r}, v, \hat{\boldsymbol{u}}) \tilde{P}(\mathbf{r}, v, \hat{\boldsymbol{u}}, s)$, multiplying the above equation by $\psi(\mathbf{r}, v, \hat{\boldsymbol{u}})$ and integrating over all possible $(\mathbf{r}, v, \hat{\boldsymbol{u}})$ we obtain,

$$\begin{aligned}&- \langle \psi \rangle_0 + (s - \gamma_v)\langle \psi \rangle_s = D\langle \nabla^2 \psi \rangle_s + D_r \langle \nabla_u^2 \psi \rangle_s + D_v \langle \partial_v^2 \psi \rangle_s + \langle v\, \hat{\boldsymbol{u}} \cdot \nabla \psi \rangle_s \\ &- \gamma_v \langle \partial_v [(v - v_0)\psi] \rangle_s + \mu \langle \boldsymbol{F} \cdot \nabla \psi \rangle_s,\end{aligned}$$

where the initial condition sets $\langle \psi \rangle_0 = \int d\mathbf{r}\, dv\, d\hat{\boldsymbol{u}}\, \psi(\mathbf{r}, v, \hat{\boldsymbol{u}}) P(\mathbf{r}, v, \hat{\boldsymbol{u}}, 0)$. This equation simplifies to

$$\begin{aligned}&-\langle\psi\rangle_0+s\langle\psi\rangle_s=D\langle\nabla^2\psi\rangle_s+D_r\langle\nabla_u^2\psi\rangle_s+D_v\langle\partial_v^2\psi\rangle_s+\langle v\,\hat{\boldsymbol{u}}\cdot\nabla\psi\rangle_s\\&-\gamma_v\langle(v-v_0)\partial_v\psi\rangle_s+\mu\langle\boldsymbol{F}\cdot\nabla\psi\rangle_s.\end{aligned}\tag{3.5}$$

Without any loss of generality, we consider the initial condition $P(\mathbf{r},v,\hat{\boldsymbol{u}},0)=\delta(\mathbf{r})\delta(v-v_1)\delta(\hat{\boldsymbol{u}}-\hat{\boldsymbol{u}}_0)$, where v_1 is a speed that in general is different from v_0. Eq. (3.5) can be utilized to compute exact moments of any dynamical variable in d-dimensions as a function of time.

3.4 Active speed

In this section, we first calculate the average active speed and speed fluctuations. We show how the speed fluctuations saturate over a long time. Next we calculate two-time auto-correlation functions for the heading direction, active speed, and finally for ABP velocity.

3.4.1 Mean speed

To calculate the evolution of active speed, we use $\psi=v$ and the initial condition $\langle\psi\rangle_0=v_1$ in Eq. (3.5). Other terms required for the calculation are: $\langle\nabla^2\psi\rangle_s=0$, $\langle\nabla_u^2\psi\rangle_s=0$, $\langle\partial_v^2\psi\rangle_s=0$, $\langle v\hat{\boldsymbol{u}}\cdot\nabla\psi\rangle_s=0$, $\langle\boldsymbol{F}\cdot\nabla\psi\rangle_s=0$, $\langle(v-v_0)\partial_v\psi\rangle_s=\langle v\rangle_s-v_0\langle 1\rangle_s=\langle v\rangle_s-v_0/s$. In the last relation we used $\langle 1\rangle_s=\int d\mathbf{r}\;d\hat{\boldsymbol{u}}\;dv\tilde{P}=\int d\mathbf{r}\;d\hat{\boldsymbol{u}}\;dv\int_0^\infty dt\;e^{-st}P=\int_0^\infty dt\;e^{-st}\{d\mathbf{r}\;d\hat{\boldsymbol{u}}\;dvP\}=\int_0^\infty dt\;e^{-st}=1/s$. Thus from Eq. (3.5), we get $\langle v\rangle_s=v_1/(s+\gamma_v)+v_0\gamma_v/s(s+\gamma_v)$. The inverse Laplace transform of this relation gives

$$\langle v\rangle(t)=v_1e^{-\gamma_v t}+v_0(1-e^{-\gamma_v t}).\tag{3.6}$$

At the long time limit of $t\gg\gamma_v^{-1}$ this gives the steady state value $\langle v\rangle=v_0$.

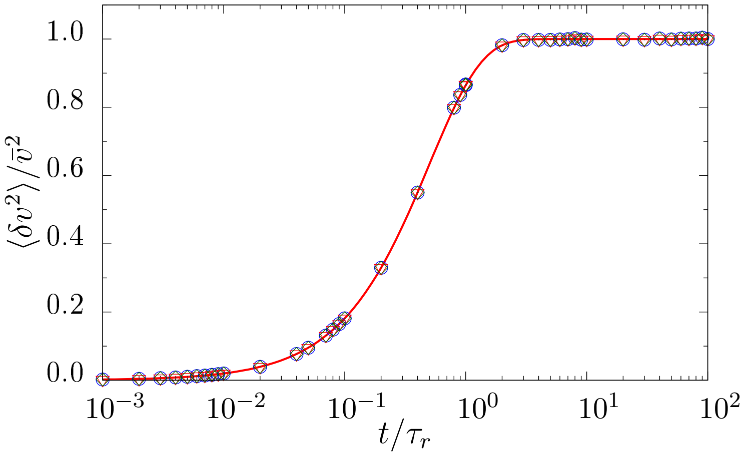

Figure 3.2: (color online) Speed fluctuation $\langle \delta v^2 \rangle$ as a function of time t/τ_r at $\tilde{D_v} = 1$ and $\tilde{\gamma_v} = 1$ in 2d for $Pe = 0.1(\circ)$, $1(\triangledown)$, $10(\diamond)$. The points are simulation results and the solid line is a plot of Eq. (3.8).

3.4.2 Speed fluctuation

The speed fluctuations can be calculated using $\psi = v^2$ and the initial condition $\langle \psi \rangle_0 = v_1^2$ in Eq. (3.5). The other terms involved in the calculation are: $\langle \nabla^2 \psi \rangle_s = 0$, $\langle \nabla_u^2 \psi \rangle_s = 0$, $\langle \partial_v^2 \psi \rangle_s = \langle 2 \rangle_s = 2/s$, $\langle v \hat{\boldsymbol{u}} \cdot \nabla \psi \rangle_s = 0$, $\langle \boldsymbol{F} \cdot \nabla \psi \rangle_s = 0$, $\langle (v - v_0) \partial_v \psi \rangle_s = 2\langle v^2 \rangle_s - 2v_0 \langle v \rangle_s$. Thus, we get from Eq. (3.5), $\langle v^2 \rangle_s = (s + 2\gamma_v)^{-1}[v_1^2 + 2\gamma_v v_0 \langle v \rangle_s + 2D_v/s]$. The inverse Laplace transform gives

$$\langle v^2 \rangle(t) = \left[v_1 e^{-\gamma_v t} + v_0 \left(1 - e^{-\gamma_v t} \right) \right]^2 + \frac{D_v}{\gamma_v} \left(1 - e^{-2\gamma_v t} \right). \tag{3.7}$$

As a result, using Eq. (3.6), the speed fluctuation reads,

$$\langle \delta v^2 \rangle = \langle v^2 \rangle - \langle v \rangle^2 = \frac{D_v}{\gamma_v} \left(1 - e^{-2\gamma_v t} \right) \tag{3.8}$$

The direct calculation (see Eq. (3.61) in Appendix-(3.9.1)) utilizing governing Eq. (3.2) for speed leads to the speed fluctuation same as Eq. (3.8). In the long time limit($t > 1/2\gamma_v$), the equation gives the constant fluctuation $\langle \delta v^2 \rangle = D_v/\gamma_v$. Eq. (3.8) compared with simulation results shown in Fig. (3.2). With the small relaxation time scale (large γ_v) of speed, one can ensure rapid saturation of speed fluctuation ensure speed in a small-time($t > 1/2\gamma_v$) from a Gaussian speed distribution.

3.5 Correlation functions

The evolution of heading direction $\hat{\boldsymbol{u}}$ is and independent stochastic process, and thus does not get influenced by the speed fluctuations. The persistence of heading direction decays as $\langle \hat{\boldsymbol{u}}(t) \rangle = \hat{\boldsymbol{u}}_0 e^{-(d-1)D_r t}$ and as a result the correlation

$$\langle \hat{\boldsymbol{u}}(t) \cdot \hat{\boldsymbol{u}}(0) \rangle = e^{-(d-1)D_r t}, \tag{3.9}$$

as was shown in the previous chapter. The auto-correlation function of active speed can be directly calculated from Eq. (3.2) as is shown in Appendix-3.9.1,

$$\langle \delta v(t_1) \delta v(t_2) \rangle = \frac{D_v}{\gamma_v} \left[e^{-\gamma_v |t_1 - t_2|} - e^{-\gamma_v (t_1 + t_2)} \right], \tag{3.10}$$

where $\delta v(t) = v(t) - \langle v(t) \rangle$. In the steady state limit of t_1, $t_2 \to \infty$, writing the time gap $\tau = |t_1 - t_2|$ one gets the simplified expression

$$\langle \delta v(\tau) \delta v(0) \rangle = (D_v/\gamma_v) e^{-\gamma_v \tau}. \tag{3.11}$$

Moreover, the velocity correlation can be calculated directly from the Langevin equations, giving $\langle \mathbf{v}(t) \rangle = \langle v(t) \rangle \langle \hat{\boldsymbol{u}}(t) \rangle + \mu \mathbf{F}(t)$ and $\langle \mathbf{v}(t_1) \cdot \mathbf{v}(t_2) \rangle = \langle v(t_1) v(t_2) \rangle \langle \hat{\boldsymbol{u}}(t_1) \cdot \hat{\boldsymbol{u}}(t_2) \rangle + 2D\delta(t_1 - t_2) + \mu^2 \mathbf{F}(t_1) \cdot \mathbf{F}(t_2)$. Thus, direct calculation leads to

$$\begin{aligned} \langle \mathbf{v}(t_1) \cdot \mathbf{v}(t_2) \rangle = & \left[\frac{D_v}{\gamma_v} \left(e^{-\gamma_v (t_1 - t_2)} - e^{-\gamma_v (t_1 + t_2)} \right) + \langle v(t_1) \rangle \langle v(t_2) \rangle \right] e^{-(d-1)D_r (t_1 - t_2)} \\ & + 2D\delta(t_1 - t_2) + \mu^2 \boldsymbol{F}(t_1) \cdot \boldsymbol{F}(t_2) \end{aligned}$$

The decay of velocity correlation is dictated by two time constants, the speed correlation time γ_v^{-1} and the persistence time of the heading direction D_r^{-1}. The autocorrelation between fluctuations of velocity $\delta \mathbf{v}(t) = \mathbf{v}(t) - \langle \mathbf{v}(t) \rangle$ is given by

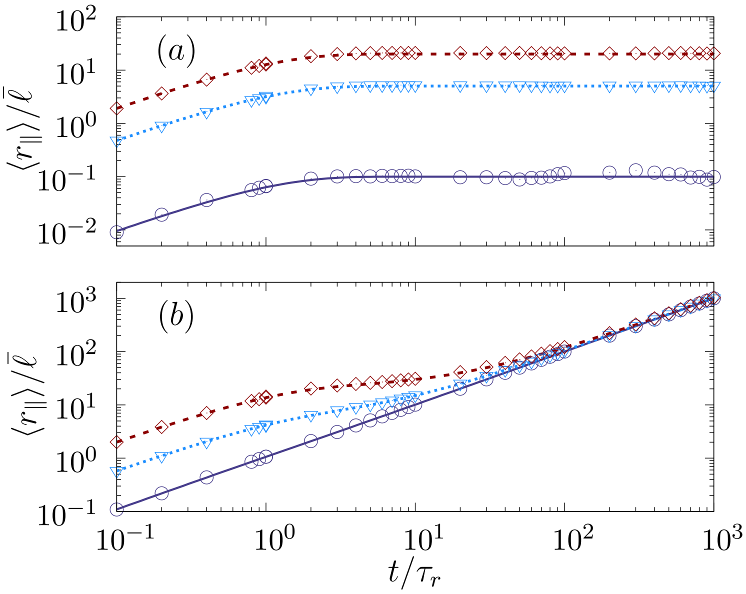

Figure 3.3: (color online) Displacement in the initial orientation $\langle r_{\parallel}\rangle$ as a function of time t at $D_v\tau_r/\bar{v}^2 = 1$ and $\gamma_v\tau_r = 1$ in 2d for $Pe \equiv v_0/\bar{v} = 0.1(\circ)$, $5(\triangledown)$, $20(\Diamond)$. The points denote simulation results, and lines depict $\langle r_{\parallel}\rangle = \langle \mathbf{r}\rangle \cdot \hat{\boldsymbol{u}}_0$ using Eq. (3.14). (a) Displacements for the persistent ABP in the absence of external force, $\mu\boldsymbol{F}_0/\bar{v} = 0$. (b) Displacements in the presence of external force, $\mu\boldsymbol{F}_0/\bar{v} = \hat{r}$. The initial speed and heading directions are chosen to be $v_1 = v_0$ and $\hat{\boldsymbol{u}}_0 = \hat{x}$, respectively.

$\langle\delta\mathbf{v}(t_1)\delta\mathbf{v}(t_2)\rangle$. Note that the mean velocity at time t is given by $\langle\mathbf{v}(t)\rangle = \langle v(t)\rangle\langle\hat{\boldsymbol{u}}(t)\rangle + \mu\boldsymbol{F}(t)$, where $\langle v(t)\rangle$ is given by Eq. (3.6) and $\langle\hat{\boldsymbol{u}}(t)\rangle = \hat{\boldsymbol{u}}_0 e^{-(d-1)D_r t}$. Therefore, $\langle\mathbf{v}(t)\rangle = [v_1 e^{-\gamma_v t} + v_0(1-e^{-\gamma_v t})]\,\hat{\boldsymbol{u}}_0 e^{-(d-1)D_r t} + \mu\boldsymbol{F}(t)$. The expression simplifies in the steady state limit in which $\langle v(t)\rangle = v_0$, $\langle\mathbf{v}(t)\rangle = \mu\mathbf{F}(t)$, using t_1, $t_2 \to \infty$ and writing $t_1 - t_2 = \tau$ we get

$$\langle\delta\mathbf{v}(\tau)\delta\mathbf{v}(0)\rangle = \left[v_0^2 + \frac{D_v}{\gamma_v}e^{-\gamma_v\tau}\right] e^{-(d-1)D_r\tau} + 2D\delta(\tau). \tag{3.12}$$

3.6 Displacement

In this section, we compute various moments of the displacement vector. We begin by using $\psi = \mathbf{r}$, and initial location $\langle\psi\rangle_0 = \mathbf{0}$ to be the origin. The calculation requires using $\langle\nabla^2\psi\rangle_s = 0$, $\langle\nabla_u^2\psi\rangle_s = 0$, $\langle\partial_v^2\psi\rangle_s = 0$, $\langle v\,\hat{\boldsymbol{u}}\cdot\nabla\psi\rangle_s = \langle v\hat{\boldsymbol{u}}\rangle_s$, $\langle(v-v_0)\partial_v\psi\rangle_s = 0$, and $\langle\boldsymbol{F}\cdot\nabla\psi\rangle_s = \langle\boldsymbol{F}\rangle_s$ in Eq. (3.5). This gives $\langle\mathbf{r}\rangle_s =$

$\left(\langle v\hat{u}\rangle_s + \mu\langle \boldsymbol{F}\rangle_s + \mathbf{r}_0\right)/s$. Using Eq. (3.5) we find $\langle v\hat{\boldsymbol{u}}\rangle_s = \frac{1}{s+\gamma_v+(d-1)D_r}\left[v_1\hat{u}_0 + \gamma_v v_0\langle\hat{u}\rangle_s\right]$, $\langle\hat{\boldsymbol{u}}\rangle_s = \hat{\boldsymbol{u}}_0/(s+(d-1)D_r)$, and use $\langle\boldsymbol{F}\rangle_s = \boldsymbol{F}_0/s$ where $\boldsymbol{F}_0$ is the constant external force vector. This allows us to obtain

$$\langle\mathbf{r}\rangle_s = \frac{(v_1-v_0)\hat{\boldsymbol{u}}_0}{s(s+(d-1)D_r+\gamma_v)} + \frac{v_0\,\hat{\boldsymbol{u}}_0}{s(s+(d-1)D_r)} + \frac{\mu\boldsymbol{F}_0}{s^2}, \tag{3.13}$$

that leads to

$$\langle\mathbf{r}\rangle(t) = \frac{(v_1-v_0)\hat{\boldsymbol{u}}_0}{(d-1)D_r+\gamma_v}\left(1-e^{-((d-1)D_r+\gamma_v)t}\right) + \frac{v_0\,\hat{\boldsymbol{u}}_0}{(d-1)D_r}\left(1-e^{-(d-1)D_r t}\right) + \mu\boldsymbol{F}_0 t. \tag{3.14}$$

after performing the inverse Laplace transform. In Fig. 3.3 we show a comparison of this estimate of displacement in the direction of original heading orientation $\langle r_\parallel\rangle = \langle\mathbf{r}\rangle\cdot\hat{\boldsymbol{u}}_0$ as obtained from Eq. (3.14) with numerical simulations.

3.6.1 Position-orientation cross-correlation: $\langle\hat{\boldsymbol{u}}\cdot\mathbf{r}\rangle$

In this section, we calculate the equal-time cross-correlation $\langle\hat{\boldsymbol{u}}\cdot\mathbf{r}\rangle$ between the displacement and heading direction of ABPs, using $\psi = \hat{\boldsymbol{u}}\cdot\mathbf{r}$ and the initial condition $\langle\psi\rangle_0 = 0$ in Eq. (3.5). The calculation uses the relations: $\langle\nabla^2\psi\rangle_s = 0$, $\langle\nabla_u^2\psi\rangle_s = -(d-1)D_r\langle\hat{\boldsymbol{u}}\cdot\mathbf{r}\rangle_s$, $\langle\partial_v^2\psi\rangle_s = 0$, $\langle v\,\hat{\boldsymbol{u}}\cdot\nabla\psi\rangle_s = \langle v\rangle_s$, $\langle(v-v_0)\partial_v\psi\rangle_s = 0$, and $\langle\boldsymbol{F}\cdot\nabla\psi\rangle_s = \langle\boldsymbol{F}\cdot\hat{\boldsymbol{u}}\rangle_s$. As a result, one gets $\langle\hat{\boldsymbol{u}}\cdot\mathbf{r}\rangle_s = \left(\langle v\rangle_s + \mu\langle\boldsymbol{F}\cdot\hat{\boldsymbol{u}}\rangle_s\right)/(s+(d-1)D_r)$. To completely determine the cross-correlation in the Laplace space, we utilize Eq. (3.5) further to obtain $\langle v\rangle_s = v_1/(s+\gamma_v)+\gamma_v v_0/s(s+\gamma_v)$, $\langle\boldsymbol{F}\cdot\hat{\boldsymbol{u}}\rangle_s = \boldsymbol{F}_0\cdot\hat{\boldsymbol{u}}_0/(s+(d-1)D_r)$ where $\boldsymbol{F}_0$ is assumed to be a constant external force. These results lead to

$$\langle\hat{\boldsymbol{u}}\cdot\mathbf{r}\rangle_s = \frac{v_1-v_0}{(s+\gamma_v)(s+(d-1)D_r)} + \frac{v_0}{s(s+(d-1)D_r)} + \frac{\mu\boldsymbol{F}_0\cdot\hat{\boldsymbol{u}}_0}{(s+(d-1)D_r)^2}. \tag{3.15}$$

The inverse Laplace transform of Eq. (3.15) gives

$$\langle \hat{\boldsymbol{u}} \cdot \mathbf{r} \rangle(t) = \frac{v_1 - v_0}{(d-1)D_r - \gamma_v} \left(e^{-\gamma_v t} - e^{-(d-1)D_r t} \right) + \frac{v_0}{(d-1)D_r} \left(1 - e^{-(d-1)D_r t} \right)$$
$$+ \mu \boldsymbol{F}_0 \cdot \hat{\boldsymbol{u}}_0 \, t \, e^{-(d-1)D_r t}. \tag{3.16}$$

In the absence of external force $\boldsymbol{F} = 0$, this relation describes the cross-correlation for ABPs with speed fluctuations. It is interesting to note that for initial active speed $v_1 = v_0$, the cross-correlation reduces to $\langle \hat{\boldsymbol{u}} \cdot \mathbf{r} \rangle(t) = v_0 \left(1 - e^{-(d-1)D_r t} \right) / (d-1)D_r$, an expression that is the same as ABPs in the absence of active speed fluctuations as described in the previous chapter.

In the presence of constant external force, we plot the cross-correlation as a function of time in Fig. 3.4, using $v_1 = v_0$ that simplifies the relation in Eq. (3.16) to

$$\langle \hat{\boldsymbol{u}} \cdot \mathbf{r} \rangle(t) = \frac{v_0}{(d-1)D_r} \left(1 - e^{-(d-1)D_r t} \right) + \mu \boldsymbol{F}_0 \cdot \hat{\boldsymbol{u}}_0 \, t \, e^{-(d-1)D_r t}. \tag{3.17}$$

The plot clearly shows non-monotonic variation with the maximum appearing at time

$$t_m D_r = \frac{1}{(d-1)} \left(1 + \frac{v_0}{\mu \mathbf{F}_0 \cdot \hat{\boldsymbol{u}}_0} \right). \tag{3.18}$$

Clearly, in the absence of external force such maxima and non-monotonic features disappear. For $d = 2$, and with the choice $\mu \mathbf{F}_0 \cdot \hat{\boldsymbol{u}}_0 / \bar{v} = \hat{r}$, $\hat{\boldsymbol{u}}_0 = \hat{x}$, the location of maxima in Fig. 3.4 are given by $t_m/\tau_r = 1 + Pe$.

3.6.2 Mean squared displacement

Here we present an exact computation of the mean squared displacement $\langle \mathbf{r}^2 \rangle$ in the presence of a directed force $\boldsymbol{F}_0$. We use $\psi = \mathbf{r}^2$ and the initial condition $\langle \mathbf{r}^2 \rangle_0 = 0$ in Eq. (3.5). The calculation of the moment uses the relations $\langle \nabla_u^2 \mathbf{r}^2 \rangle_s = 0$, $\langle \nabla^2 \mathbf{r}^2 \rangle_s = 2d \langle 1 \rangle_s = 2d/s$ using $\langle 1 \rangle_s = 1/s$, $\langle v \, \hat{\boldsymbol{u}} \cdot \nabla \mathbf{r}^2 \rangle_s = 2 \langle v \, \hat{\boldsymbol{u}} \cdot \mathbf{r} \rangle_s$ and $\langle \boldsymbol{F} \cdot \nabla \mathbf{r}^2 \rangle_s = 2 \langle \boldsymbol{F} \cdot \mathbf{r} \rangle_s$.

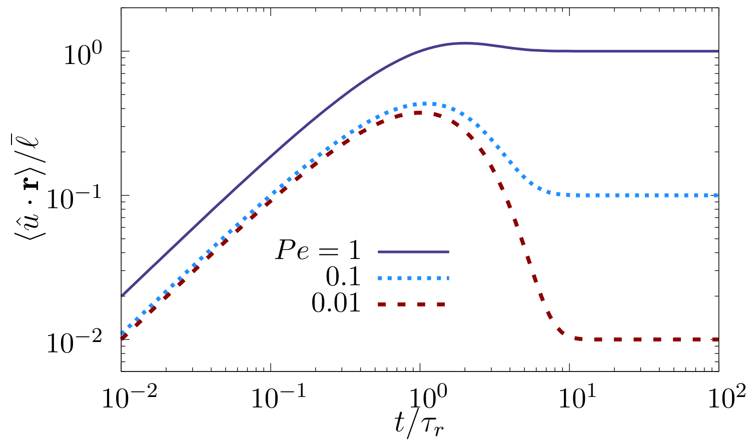

Figure 3.4: (color online) The position-orientation cross-correlation $\langle \hat{\boldsymbol{u}} \cdot \mathbf{r}\rangle$ as a function of time t at $D_v\tau_r/\bar{v}^2 = 1$ and $\gamma_v\tau_r = 1$ in 2d for $Pe = 1,\ 0.1,\ 0.01$. The lines depict Eq. (3.16) with the initial speed $v_1 = v_0$ and heading direction $\hat{\boldsymbol{u}}_0 = \hat{x}$. In the presence of external drive $\mu\boldsymbol{F}_0/\bar{v} = \hat{r}$, the cross correlation varies non-monotonically to finally saturate to $\langle \hat{\boldsymbol{u}} \cdot \mathbf{r}\rangle/\bar{\ell} = Pe$ in $d = 2$. The maxima for each Pe value appear at time points $t_m/\tau_r = 1 + Pe$.

Moreover, $\langle v\,\hat{\boldsymbol{u}}\cdot\nabla\mathbf{r}^2\rangle_s = 2\langle v\,\hat{\boldsymbol{u}}\cdot\mathbf{r}\rangle_s$ and $\langle \boldsymbol{F}\cdot\nabla\mathbf{r}^2\rangle_s = 2\langle \boldsymbol{F}\cdot\mathbf{r}\rangle_s$. Thus Eq. (3.5) leads to

$$\langle \mathbf{r}^2\rangle_s = \frac{1}{s}\left[\frac{2dD}{s} + 2\langle v\,\hat{\boldsymbol{u}}\cdot\mathbf{r}\rangle_s + 2\mu\langle \boldsymbol{F}\cdot\mathbf{r}\rangle_s\right] \tag{3.19}$$

To complete the calculation, one needs to evaluate $\langle v\,\hat{\boldsymbol{u}}\cdot\mathbf{r}\rangle_s$ and $\langle \boldsymbol{F}\cdot\mathbf{r}\rangle_s$, again, using the same Eq. (3.5). One may proceed like before, using $\psi = v\,\hat{\boldsymbol{u}}\cdot\mathbf{r}$ and $\langle\psi\rangle_0 = 0$, $\langle\nabla^2\psi\rangle_s = 0$, $\langle\nabla_u^2(v\,\hat{\boldsymbol{u}}\cdot\mathbf{r})\rangle_s = -(d-1)\langle v\hat{\boldsymbol{u}}\cdot\mathbf{r}\rangle_s$, $\langle v\hat{\boldsymbol{u}}\cdot\nabla(v\,\hat{\boldsymbol{u}}\cdot\mathbf{r})\rangle_s = \langle v^2\hat{\boldsymbol{u}}^2\rangle_s = \langle v^2\rangle_s$, $\langle \boldsymbol{F}\cdot\nabla(v\,\hat{\boldsymbol{u}}\cdot\mathbf{r})\rangle_s = \langle v\boldsymbol{F}\cdot\hat{\boldsymbol{u}}\rangle_s$ to obtain

$$\langle v\,\hat{\boldsymbol{u}}\cdot\mathbf{r}\rangle_s = \frac{1}{(s+(d-1)D_r+\gamma_v)}\left[\langle v^2\rangle_s + \gamma_v v_0\langle\hat{\boldsymbol{u}}\cdot\mathbf{r}\rangle_s + \mu\langle v\boldsymbol{F}\cdot\hat{\boldsymbol{u}}\rangle_s\right].$$

Further,

$$\begin{aligned}
\langle v^2\rangle_s &= \frac{1}{s+2\gamma_v}\left[v_1^2 + 2D_v\langle 1\rangle_s + \frac{2\gamma_v v_0}{s+\gamma_v}\left[v_1 + \gamma_v v_0\langle 1\rangle_s\right]\right],\\
\langle \hat{\boldsymbol{u}}\cdot\mathbf{r}\rangle_s &= \frac{v_1 - v_0}{(s+\gamma_v)(s+(d-1)D_r)} + \frac{v_0}{s(s+(d-1)D_r)} + \frac{\mu\boldsymbol{F}_0\cdot\hat{\boldsymbol{u}}_0}{(s+(d-1)D_r)^2},\\
\langle v\boldsymbol{F}\cdot\hat{\boldsymbol{u}}\rangle_s &= \frac{v_1(\boldsymbol{F}_0\cdot\hat{\boldsymbol{u}}_0)}{(s+(d-1)D_r)}.
\end{aligned}$$

Similarly, we calculate

$$\langle \boldsymbol{F}\cdot\mathbf{r}\rangle_s = \frac{1}{s}\left[\langle v\boldsymbol{F}\cdot\hat{\boldsymbol{u}}\rangle_s + \mu\langle \boldsymbol{F}^2\rangle_s\right],$$

with $\langle \boldsymbol{F}^2\rangle_s = \boldsymbol{F}_0^2/s$ where $\boldsymbol{F}_0$ is a time-independent external force.

Thus, plugging these relations back in the expression of $\langle \mathbf{r}^2\rangle_s$ in Eq. (3.19), we obtain

$$\begin{aligned}
\langle \mathbf{r}^2\rangle_s = \frac{2dD}{s^2} &+ \frac{2v_1\mu\boldsymbol{F}_0\cdot\hat{\boldsymbol{u}}_0}{s^2(s+(d-1)D_r)} + \frac{4D_v}{s^2(s+2\gamma_v)(s+(d-1)D_r+\gamma_v)}\\
&+ \frac{2\gamma_v v_0}{s(s+(d-1)D_r)(s+\gamma_v)(s+(d-1)D_r+\gamma_v)}\left(v_1 + \frac{\gamma_v v_0}{s}\right)\\
&+ \frac{2}{s(s+(d-1)D_r+\gamma_v)(s+2\gamma_v)}\left[v_1^2 + \frac{2\gamma_v v_0}{(s+\gamma_v)}\left(v_1 + \frac{\gamma_v v_0}{s}\right)\right]\\
&+ \frac{2\mu\boldsymbol{F}_0\cdot\hat{\boldsymbol{u}}_0}{s(s+(d-1)D_r)(s+(d-1)D_r+\gamma_v)}\left(v_1 + \frac{\gamma_v v_0}{s+(d-1)D_r}\right) + \frac{2\mu^2\boldsymbol{F}_0^2}{s^3} \qquad (3.20)
\end{aligned}$$

Performing the inverse Laplace transform, this leads to

$$
\begin{aligned}
\langle \mathbf{r}^2 \rangle = {} & \mu^2 \boldsymbol{F}_0^2 t^2 - \frac{2v_0 \mu \boldsymbol{F}_0 \cdot \hat{\boldsymbol{u}}_0 t e^{-(d-1)D_r t}}{(d-1)D_r} + \frac{\left(D_v - \gamma_v (v_0 - v_1)^2\right) e^{-2\gamma_v t}}{\gamma_v^2((d-1)D_r - \gamma_v)} \\
& + \frac{2(2(d-1)D_r - \gamma_v) v_0 (v_0 - v_1) e^{-\gamma_v t}}{(d-1)D_r \gamma_v ((d-1)D_r - \gamma_v)} \\
& + \frac{2v_0 \left[\mu \boldsymbol{F}_0 \cdot \hat{\boldsymbol{u}}_0 (D_r - dD_r + \gamma_v)^2 - \gamma_v^2 v_0\right] e^{-(d-1)D_r t}}{(d-1)^2 D_r^2 ((d-1)D_r - \gamma_v)\gamma_v} \\
& + \frac{2v_1 \left[-\mu \boldsymbol{F}_0 \cdot \hat{\boldsymbol{u}}_0 (D_r - dD_r + \gamma_v)^2 + (d-1)D_r \gamma_v v_0\right] e^{-(d-1)D_r t}}{(d-1)^2 D_r^2 ((d-1)D_r - \gamma_v)\gamma_v} \\
& - \frac{2(d-1)D_r \gamma_v \left[2D_v - \gamma_v (v_0 - v_1)(\mu \boldsymbol{F}_0 \cdot \hat{\boldsymbol{u}}_0 + v_0 - v_1)\right] e^{-((d-1)D_r + \gamma_v)t}}{(d-1)D_r((d-1)D_r - \gamma_v)\gamma_v((d-1)D_r + \gamma_v)^2} \\
& - \frac{2(d-1)^3 D_r^3 \mu \boldsymbol{F}_0 \cdot \hat{\boldsymbol{u}}_0 (v_0 - v_1) e^{-((d-1)D_r + \gamma_v)t}}{(d-1)D_r((d-1)D_r - \gamma_v)\gamma_v((d-1)D_r + \gamma_v)^2} \\
& - \frac{2\left[(d-1)^2 D_r^2 \gamma_v (v_0 - v_1) v_1 + \gamma_v^3 v_0 (-v_0 + v_1)\right] e^{-((d-1)D_r + \gamma_v)t}}{(d-1)D_r((d-1)D_r - \gamma_v)\gamma_v((d-1)D_r + \gamma_v)^2} \\
& + \frac{2\left[(d-1)^2 dD D_r^2 \gamma_v + \gamma_v^2 \left(v_0^2 + \mu \boldsymbol{F}_0 \cdot \hat{\boldsymbol{u}}_0 v_1\right)\right] t}{(d-1)D_r \gamma_v ((d-1)D_r + \gamma_v)} \\
& + \frac{2(d-1)D_r \left[D_v + \gamma_v \left(dD\gamma_v + v_0^2 + \mu \boldsymbol{F}_0 \cdot \hat{\boldsymbol{u}}_0 v_1\right)\right] t}{(d-1)D_r \gamma_v ((d-1)D_r + \gamma_v)} \\
& + \frac{2(d-1)D_r \gamma_v^3 (\mu \boldsymbol{F}_0 \cdot \hat{\boldsymbol{u}}_0 (v_0 - v_1) + v_0(-3v_0 + v_1))}{(d-1)^2 D_r^2 \gamma_v^2 ((d-1)D_r + \gamma_v)^2} \\
& - \frac{2\gamma_v^4 \left(v_0^2 - \mu \boldsymbol{F}_0 \cdot \hat{\boldsymbol{u}}_0 (v_0 - v_1)\right)}{(d-1)^2 D_r^2 \gamma_v^2 ((d-1)D_r + \gamma_v)^2} \\
& - \frac{(d-1)^3 D_r^3 (D_v + \gamma_v (v_0 - v_1)(3v_0 + v_1))}{(d-1)^2 D_r^2 \gamma_v^2 ((d-1)D_r + \gamma_v)^2} \\
& - \frac{(d-1)^2 D_r^2 \gamma_v \left(3D_v + \gamma_v \left(7v_0^2 - 4v_0 v_1 - v_1^2\right)\right)}{(d-1)^2 D_r^2 \gamma_v^2 ((d-1)D_r + \gamma_v)^2} \qquad (3.21)
\end{aligned}
$$

Considering the initial active speed $v_1 = v_0$, Eq. (3.21) simplifies to

$$
\begin{aligned}
\langle \mathbf{r}^2 \rangle = {} & 2d \left(D + \frac{(v_0^2 + v_0 \mu \boldsymbol{F}_0 \cdot \hat{\boldsymbol{u}}_0)}{(d-1)dD_r} \right) t - \frac{2(v_0^2 + v_0 \mu \boldsymbol{F}_0 \cdot \hat{\boldsymbol{u}}_0)}{(d-1)^2 D_r^2} \left(1 - e^{-(d-1)D_r t}\right) \\
& + \frac{2D_v}{\gamma_v(\gamma_v + (d-1)D_r)} \left[t - \frac{1 - e^{-(\gamma_v + (d-1)D_r)t}}{(\gamma_v + (d-1)D_r)} - \frac{1 - e^{-2\gamma_v t}}{2\gamma_v} + \frac{e^{-2\gamma_v t} - e^{-(\gamma_v + (d-1)D_r)t}}{((d-1)D_r - \gamma_v)} \right] \\
& + \frac{2v_0 \mu \boldsymbol{F}_0 \cdot \hat{\boldsymbol{u}}_0}{(d-1)^2 D_r^2} \left[\left(1 - e^{-(d-1)D_r t}\right) - (d-1)D_r t e^{-(d-1)D_r t} \right] + \mu^2 \boldsymbol{F}_0^2 t^2 \qquad (3.22)
\end{aligned}
$$

Note that for the special case of $(d-1)D_r = \gamma_v$, Eq. (3.22) can be further simplified by using the L'Hôpital's rule, or, directly substituting $(d-1)D_r = \gamma_v$ in Eq. (3.20) to calculate $\langle \mathbf{r}^2 \rangle$.

Persistent motion

In the absence of external force $\boldsymbol{F}_0 = 0$ the second moment of displacement simplifies to

$$\begin{aligned}\langle \mathbf{r}^2 \rangle &= 2dDt + \frac{2v_0^2}{(d-1)D_r}\left(t - \frac{1-e^{-(d-1)D_r t}}{(d-1)D_r}\right) \\ &+ \frac{2D_v}{\gamma_v(\gamma_v + (d-1)D_r)}\left(t - \frac{1-e^{-(\gamma_v+(d-1)D_r)t}}{\gamma_v + (d-1)D_r}\right) \\ &- \frac{2D_v}{\gamma_v(\gamma_v + (d-1)D_r)}\left[\frac{1-e^{-2\gamma_v t}}{2\gamma_v} - \frac{e^{-2\gamma_v t} - e^{-(\gamma_v+(d-1)D_r)t}}{\gamma_v - (d-1)D_r}\right].\end{aligned} \tag{3.23}$$

In the limits of $D_v \to 0$ and $\gamma_v \to \infty$, Eq. (3.23) reduces to that of free ABPs in the absence of speed fluctuations, as shown in the previous chapter [107]. The structure of the second and third terms in Eq. (3.23) can describe two ballistic diffusive crossovers [108]. As we show in the following, the presence of the fourth term allows for further crossovers. Moreover, the presence of translational diffusion makes the short time dynamics diffusive. Here, it is instructive to note that the calculations of lower moments can be performed directly using the Langevin equations. For example, the formal solution for the position vector, $\mathbf{r}(t) = \int_0^t dt' v(t')\hat{\boldsymbol{u}}(t') + \int_0^t \boldsymbol{dB}^t(t')$ in the absence of external force leads to the second moment

$$\langle \mathbf{r}^2 \rangle = \int_0^t dt_1 \int_0^t dt_2 \, \langle v(t_1)v(t_2)\rangle \, \langle \hat{\boldsymbol{u}}(t_1) \cdot \hat{\boldsymbol{u}}(t_2)\rangle + \int_0^t \int_0^t \langle \boldsymbol{dB}^t(t_1) \cdot \boldsymbol{dB}^t(t_2)\rangle, \tag{3.24}$$

where the cross terms are zero as they describe independent stochastic processes with $\langle \boldsymbol{dB}^t \rangle = 0$. By substituting the speed correlation function from Eq. (3.10) and the orientational correlation function from Eq. (3.9) in Eq. (3.24), and performing the integrations, one gets the same mean squared displacement relation as in Eq. (3.23).

In Fig.3.5 we compare our analytic prediction for the second moment of displacement in Eq. (3.23) with direct numerical simulation results in 2d ($d = 2$) to show excellent agreement between them. Here, it is instructive to note the difference of our d-dimensional expression for $\langle \mathbf{r}^2 \rangle$ shown in Eq. (3.23) from earlier results for 2d obtained in Ref. [15, 108]. The difference stems from an assumption of time-scale separation used in these earlier publications, where the speed fluctuations were assumed to be in steady state. This can be easily seen by noting that instead of using the general result for $\langle v(t_1)v(t_2) \rangle$ of Eq. (3.10), if one uses the steady state limit of the correlation for active speed as in Eq. (3.11), the expression in Eq. (3.24) lead to the previously obtained relation for the second moment of displacement [15, 108]

$$\langle \mathbf{r}^2 \rangle = 4D\,t + 2v_0^2 \left(\frac{t}{D_r} - \frac{1 - e^{-D_r t}}{D_r^2} \right) + \frac{2D_v}{\gamma_v} \left(\frac{t}{(\gamma_v + D_r)} - \frac{1 - e^{-(\gamma_v + D_r)t}}{(\gamma_v + D_r)^2} \right). \tag{3.25}$$

As is clearly shown in Fig.3.5, while our calculation in Eq. (3.23) exactly captures the behavior observed in numerical simulations, the earlier result shown in Eq. (3.25) cannot capture the qualitative behavior of $\langle \mathbf{r}^2 \rangle(t)$, e.g., at small γ_v/D_r and large Pe. Fig.3.5 shows multiple ballistic diffusive crossovers, which we consider in detail in the following.

Multiple crossovers and crossover timescales: To elucidate the crossovers permitted by Eq. (3.23), we focus on its behavior in different time regimes. First we note that in the two limits of the shortest and longest times $\langle \mathbf{r}^2 \rangle$ shows diffusive behavior, albeit with two significantly different diffusion constants. In the short time limit

$$\langle \mathbf{r}^2 \rangle \approx 2d\,D\,t \tag{3.26}$$

and in the long time limit

$$\langle \mathbf{r}^2 \rangle \approx 2d \left[D + \frac{v_0^2}{d(d-1)D_r} + \frac{D_v}{d\gamma_v[\gamma_v + (d-1)D_r]} \right] t. \tag{3.27}$$

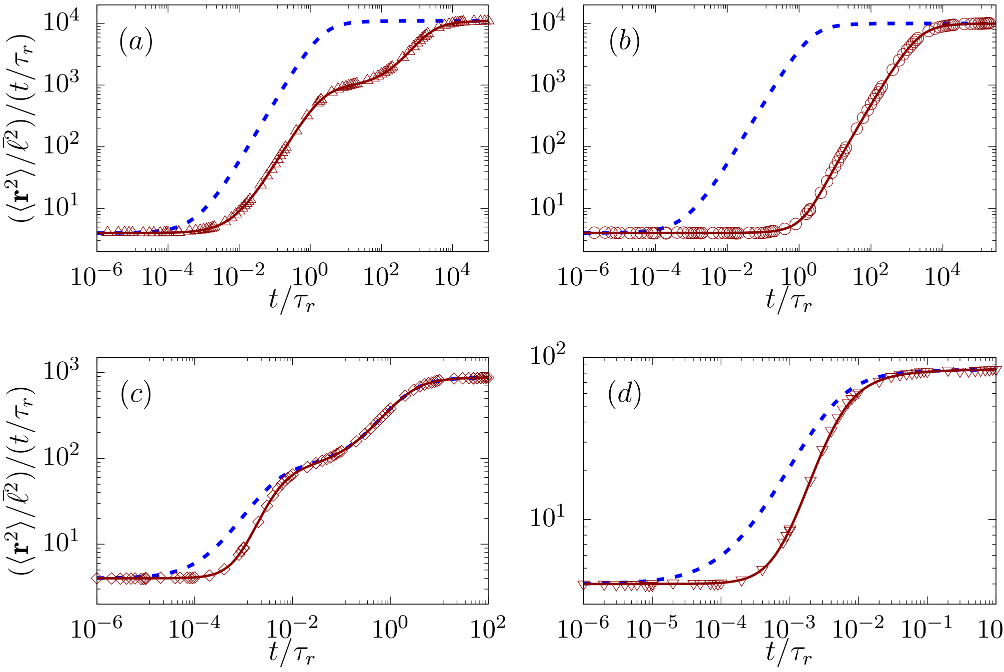

Figure 3.5: (color online) Time dependence of $\langle \mathbf{r}^2\rangle/t$ in 2d, in the absence of external force. The slow and fast relaxations of active speed are considered in (a,b) $\gamma_v\tau_r \ll 1$, and (c,d) $\gamma_v\tau_r \gg 1$, respectively. The points denote simulation results, the solid lines depict Eq. (3.23) with $d=2$, and the dashed lines depict Eq. (3.25). Parameter values used in (a,b): $\gamma_v\tau_r = 5\times 10^{-4}$, $D_v\tau_r/\bar{v}^2 = 2.5$ with $Pe \equiv v_0/\bar{v} = 22.36$ (a) and 1.12 (b). Parameter values used in (c,d): $\gamma_v\tau_r = 5\times 10^{2}$, $D_v\tau_r/\bar{v}^2 = 10^7$ with $Pe \equiv v_0/\bar{v} = 20$ (c) and 1 (d). Initial conditions are chosen such as the active speed speed $v_1/\bar{v} = Pe$ and the heading direction $\hat{\boldsymbol{u}}_0 = \hat{x}$ is along the x-axis.

For the smallest time scales, we expand $\langle \mathbf{r}^2\rangle$ in Eq. (3.23) around $t=0$ to obtain

$$\langle \mathbf{r}^2\rangle \;=\; 2dDt + v_0^2t^2 - \frac{1}{3}\left((d-1)D_rv_0^2 - 2D_v\right)t^3 + \mathcal{O}(t^4). \tag{3.28}$$

This shows a crossover from diffusive $\langle \mathbf{r}^2\rangle \sim t$ to ballistic behavior $\langle \mathbf{r}^2\rangle \sim t^2$ at $t_I = 2dD/v_0^2$, with the crossover point obtained by comparing the first and second terms of the above expansion. Such crossovers have been observed in Fig. 3.5. Comparing the second and third terms in the above expansion, one can identify a possible second crossover from ballistic to diffusive behavior at $t_{II} = 3v_0^2/[(d-1)D_rv_0^2 - 2D_v]$, provided $(d-1)D_rv_0^2 > 2D_v$. Further insights can be drawn by separately considering the limits of (i) slow speed relaxation and (ii) slow orientational relaxation separately.

(i) **Slow relaxation of active speed;** $\gamma_v \ll (d-1)D_r$: Using $(d-1)D_r t \gg 1$ and $2\gamma_v t \ll 1$, we can write $\exp[-(d-1)D_r t] \approx 0$, $\exp[-((d-1)D_r + \gamma_v)t] \approx 0$ and expand $\exp(-2\gamma_v t)$ around $2\gamma_v t = 0$ in Eq. (3.23) to get

$$\langle \mathbf{r}^2 \rangle = \left(2dD + \frac{2v_0^2}{(d-1)D_r} + \frac{4D_v}{(d-1)^2 D_r^2 - \gamma_v^2} \right) t + \frac{2D_v}{(d-1)D_r - \gamma_v} t^2 + \mathcal{O}(t^3). \tag{3.29}$$

a third crossover $\langle \mathbf{r}^2 \rangle \sim t$ to $\sim t^2$ expect at $t_{III} \sim [2dD + 2v_0^2/(d-1)D_r + 4D_v/((d-1)^2 D_r^2 - \gamma_v^2)]\,[(d-1)D_r - \gamma_v]/2D_v$ with condition $(d-1)D_r \gg 2\gamma_v$. The final crossover point to the long-time diffusive limit denoted by Eq. (3.27) can be calculated by comparing the last term in Eq. (3.29) with Eq. (3.27). This crossover time turns out to be $t_{IV} \sim [2dD + 2v_0^2/(d-1)D_r + 2D_v/\gamma_v((d-1)D_r + \gamma_v)]\,[(d-1)D_r - \gamma_v)]/2D_v$.

Moreover, at small Pe, the diffusive-ballistic crossover at t_I can be preempted by a different ballistic-diffusive crossover at t_I^* that can be determined by comparing the first term in Eq. (3.28) with the second term in Eq. (3.29). This gives $t_I^* = dD[(d-1)D_r - \gamma_v]/D_v$, a crossover point independent of active speed v_0.

Such crossovers for $\langle \mathbf{r}^2 \rangle$ in 2d in the limit of $\gamma_v \tau_r \ll 1$ are illustrated in Fig. 3.6.(a). The graphs depict the expression in Eq. (3.23) using parameter values $\tilde{\gamma_v} = \gamma_v \tau_r = 5 \times 10^{-4}$, $\tilde{D_v} = D_v \tau_r / \bar{v}^2 = 2.5$. The solid line at larger $Pe\,(= 22.36)$ shows all four diffusive- ballistic- diffusive crossovers discussed above, as the requirement $t_I < t_{II} < t_{III} < t_{IV}$ is satisfied. In this case, the crossover times are $t_I \equiv t_I/\tau_r \sim 4/Pe^2 \approx 0.008$, $t_{II} \equiv t_{II}/\tau_r = 3Pe^2/(Pe^2 - 2\tilde{D_v}) \approx 3.03$, $t_{III} \equiv t_{III}/\tau_r = [4 + 2Pe^2 + 4\tilde{D_v}/(1 - \tilde{\gamma_v}^2)](1 - \tilde{\gamma_v})/2\tilde{D_v} \approx 202.8$, and $t_{IV} \equiv t_{IV}/\tau_r = [4 + 2Pe^2 + 2\tilde{D_v}/\{\tilde{\gamma_v}(1 + \tilde{\gamma_v})\}]\,(1 - \tilde{\gamma_v})/2\tilde{D_v} \approx 2200$, as pointed out in Fig. (3.6)(a).

For $Pe = v_0/\bar{v} = 1.12$, $\langle \mathbf{r}^2 \rangle$ denoted by the dashed line in Fig. 3.6.(a) shows only two crossovers: (a) a diffusive-ballistic crossover at $t_I^* \equiv t_I^*/\tau_r = 2(1 - \tilde{\gamma_v})/\tilde{D_v} = 0.8$ and (b) a ballistic-diffusive crossover at $t_{IV} \equiv t_{IV}/\tau_r \approx 2000$. In this case $t_I^* < t_I = 3.2$, thus the first diffusive-ballistic crossover is preempted by t_I^*. Other possible intermediate crossovers disappear due to the following reasons. The possible ballistic-diffusive crossover point $t_{II} < 0$ for these parameters. In its absence,

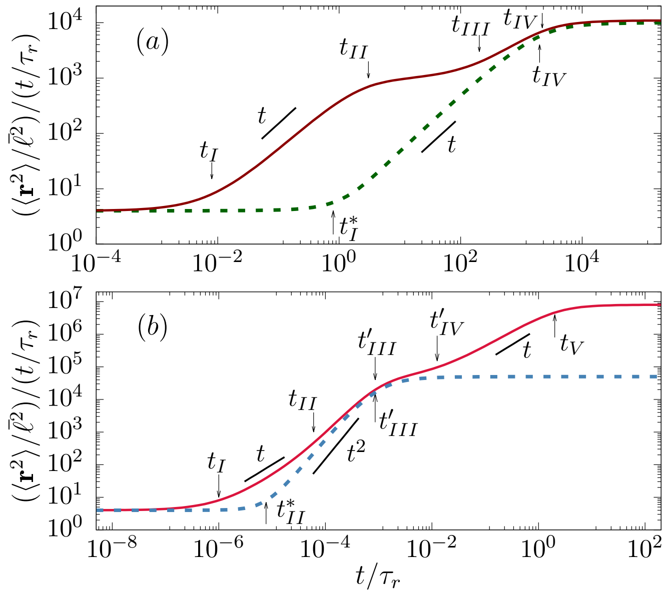

Figure 3.6: (color online) Persistent motion. Mean squared displacement $\langle \mathbf{r}^2\rangle$ as in Eq. (3.23) as a function of time t in two dimension, $d = 2$. (a) Parameters used are $\tilde{\gamma_v} = \gamma_v\tau_r = 5\times10^{-4}$, $\tilde{D_v} = D_v\tau_r/\bar{v}^2 = 2.5$ with $Pe = v_0/\bar{v} = 22.36$ (solid line), 1.12 (dashed line). The solid line shows four crossover with crossover times $t_I/\tau_r = 0.008$, $t_{II}/\tau_r = 3.03$, $t_{III}/\tau_r = 202.8$ and $t_{IV}/\tau_r = 2200$. The dashed line shows two crossovers: : a diffusive-ballistic crossover at $t_I^*/\tau_r = 0.8$ and a ballistic-diffusive crossover at $t_{IV}/\tau_r = 2000$. (b) Parameters used are $\tilde{\gamma_v} = \gamma_v\tau_r = 2\times10^3$, $\tilde{D_v} = D_v\tau_r/\bar{v}^2 = 10^{11}$, with $Pe = v_0/\bar{v} = 2\times10^3$ (solid line), 10 (dashed line). The solid line shows five crossover with crossover times $t_I/\tau_r = 10^{-6}$, $t_{II}/\tau_r = 6\times10^{-5}$, $t'_{III}/\tau_r = 8.6\times10^{-4}$ and $t'_{IV}/\tau_r = 1.25\times10^{-2}$, and $t_V = 2.02$. The dashed line shows two crossovers with crossover times $t^*_{II}/\tau_r = 7.75\times10^{-6}$ and $t'_{III}/\tau_r = 8.6\times10^{-4}$. Initial activity: speed $v_1/\bar{v} = Pe$ and orientation along x-axis, $\hat{\boldsymbol{u}}_0 = \hat{x}$.

$t_{III} \approx 3.3$ signifying a possible diffusive-ballistic crossover cannot show any change in the already ballistic property of the ABP in that time regime.

(ii) **Fast relaxation of active speed;** $\gamma_v \gg (d-1)D_r$: The scenario of short-time diffusive-ballistic crossover at $t_I = 2dD/v_0^2$ remains unchanged. As indicated before, at $t_{II} = 3v_0^2/((d-1)D_r v_0^2 - 2D_v)$ with $2D_v > (d-1)D_r v_0^2$, a possible second crossover from $\langle \mathbf{r}^2\rangle \sim t^2$ to $\langle \mathbf{r}^2\rangle \sim t^3$ can appear. In the limit of $(d-1)D_r t \ll 1$ and $2\gamma_v t \gg 1$, we can use $\exp(-2\gamma_v t) \approx 0$, $\exp[-((d-1)D_r + \gamma_v)t] \approx 0$ and expand $\exp[-(d-1)D_r t]$ around $D_r t = 0$ in Eq. (3.23) to get

$$\langle \mathbf{r}^2\rangle = \left(2dD + \frac{2D_v}{\gamma_v((d-1)D_r + \gamma_v)}\right)t + v_0^2 t^2 + \mathcal{O}(t^3). \tag{3.30}$$

Comparing the third term in Eq. (3.28) and the first term in Eq. (3.30), we estimate the crossover time from $\langle \mathbf{r}^2 \rangle \sim t^3$ to $\langle \mathbf{r}^2 \rangle \sim t$ to be at $t'_{III} = \left[3 \frac{2dD + 2D_v / \{\gamma_v((d-1)D_r + \gamma_v)\}}{2D_v - (d-1)D_r v_0^2} \right]^{1/2}$. A fourth crossover $\langle \mathbf{r}^2 \rangle \sim t$ to $\langle \mathbf{r}^2 \rangle \sim t^2$ is expected at $t'_{IV} = (2dD + 2D_v/(\gamma_v((d-1)D_r + \gamma_v))/v_0^2$. The final ballistic-diffusive crossover in this limit of $(d-1)D_r \ll 2\gamma_v$ can be obtained by comparing the second term in Eq. (3.30) with Eq. (3.27). This gives the final crossover time $t_V = (2dD + 2v_0^2/(d-1)D_r + 2D_v/\gamma_v((d-1)D_r + \gamma_v))/v_0^2$.

There is also a possibility of getting a direct crossover from $\langle \mathbf{r}^2 \rangle \sim t$ to $\langle \mathbf{r}^2 \rangle \sim t^3$ at $t^*_{II} = [6dD/(2D_v - (d-1)D_r v_0^2)]^{1/2}$ if $t^*_{II} < t_I$. The crossover point t^*_{II} is obtained by comparing the first and the third term of Eq. (3.28). A direct final crossover from $\langle \mathbf{r}^2 \rangle \sim t^3$ to $\langle \mathbf{r}^2 \rangle \sim t$ can appear at $t_{VI} = \{6d[D + \frac{v_0^2}{d(d-1)D_r} + \frac{D_v}{d\gamma_v[\gamma_v + (d-1)D_r]}]/[2D_v - (d-1)D_r v_0^2]\}^{1/2}$ if $t_{VI} < t'_{III}$, otherwise the final crossover will be at t'_{III}. The estimate of t_{VI} is obtained by comparing the third term in Eq. (3.28) with Eq. (3.27).

Such crossovers for $\langle \mathbf{r}^2 \rangle$ in 2d in the limit of $\gamma_v \tau_r \gg 1$ are illustrated in Fig. 3.6.(b). The graphs depict the expression in Eq. (3.23) using parameter values $\tilde{\gamma_v} = \gamma_v \tau_r = 2 \times 10^3$, $\tilde{D_v} = D_v \tau_r / \bar{v}^2 = 10^{11}$. The solid line at $Pe = v_0/\bar{v} = 2 \times 10^3$ exhibit all possible five crossovers $\langle \mathbf{r}^2 \rangle \sim t$ to $\sim t^2$, to $\sim t^3$, to $\sim t$, to $\sim t^2$ to finally $\sim t$ as the requirement $t_I < t_{II} < t'_{III} < t'_{IV} < t_V$ is satisfied. The crossover times are $t_I \equiv t_I/\tau_r \sim 4/Pe^2 = 1 \times 10^{-6}$, $t_{II} \equiv t_{II}/\tau_r \sim 3Pe^2/(Pe^2 - 2\tilde{D_v}^2) \approx 6 \times 10^{-5}$, $t'_{III} \equiv t'_{III}/\tau_r = \left[3 \left(4 + 2\tilde{D_v}/\{\tilde{\gamma_v}(1+\tilde{\gamma_v})\} \right) / (2\tilde{D_v} - Pe^2) \right]^{1/2} \approx 8.6 \times 10^{-4}$, $t'_{IV} \equiv t'_{IV}/\tau_r = [4 + 2\tilde{D_v}/\{\tilde{\gamma_v}(1+\tilde{\gamma_v})\}]/Pe^2 \approx 1 \times 10^{-2}$, $t_V \equiv t_V/\tau_r = [4 + 2Pe^2 + 2\tilde{D_v}/\{\tilde{\gamma_v}(1+\tilde{\gamma_v})\}]/Pe^2 \approx 2$. They are identified by arrows on the solid line in Fig. (3.6)(b).

For $Pe = v_0/\bar{v} = 10$, $\langle \mathbf{r}^2 \rangle$ denoted by the dashed line in Fig. (3.6)(b)) shows only two crossovers: the first from $\langle \mathbf{r}^2 \rangle \sim t$ to $\langle \mathbf{r}^2 \rangle \sim t^3$ at t^*_{II}, and the second going back to $\langle \mathbf{r}^2 \rangle \sim t$ at t_{VI}. Here, $t^*_{II} \equiv t^*_{II}/\tau_r = [12/(2\tilde{D_v} - Pe^2)]^{1/2} \approx 7.75 \times 10^{-6}$ as $t^*_{II} < t_I \approx 0.04$. Because of the large value of $\tilde{D_v}$ chosen, the $\langle \mathbf{r}^2 \rangle \sim t^3$ to $\langle \mathbf{r}^2 \rangle \sim t$ crossover appears at $t'_{III} \equiv t'_{III}/\tau_r \approx 8.6 \times 10^{-4}$, as $t_{VI}/\tau_r = \left[12 \times \frac{1 + \frac{Pe^2}{2} + \frac{\tilde{D_v}}{\tilde{\gamma_v}(1+\tilde{\gamma_v})}}{2\tilde{D_v} - Pe^2} \right]^{1/2} = 10^{-3} > t'_{III}$.

We present a brief summary of the dominance of different kinds of fluctuations in different time regimes in Table-3.1.

Table 3.1: $\langle \mathbf{r}^2 \rangle$ scaling: characterizing dominance of fluctuation in diffrent regime

$t \longrightarrow$

$\langle \mathbf{r}^2 \rangle$	$\sim t$	$\sim t^2$	$\sim t$	$\sim t^2$	$\sim t$
$(d-1)D_r \gg \gamma_v$	thermal	orientation	thermal + orientation	speed	thermal + orientation + speed
$(d-1)D_r \ll \gamma_v$	thermal	speed	thermal + speed	orientation	thermal + speed + orientation

Directed persistent motion

The mean squared displacements in the presence of constant external force force, can be directly analyzed using the Eq. (3.22). For two dimensions, setting $d = 2$ in Eq. (3.22) with initial condition $v_1 = v_0$ and rearranging terms, we get

$$\begin{aligned}\langle \mathbf{r}^2 \rangle &= 4D\,t + 2v_0^2\left(\frac{t}{D_r} - \frac{1-e^{-D_r t}}{D_r^2}\right) + \frac{2D_v}{\gamma_v}\left(\frac{t}{(\gamma_v + D_r)} - \frac{1-e^{-(\gamma_v+D_r)t}}{(\gamma_v+D_r)^2}\right)\\ &- \frac{2D_v}{\gamma_v(\gamma_v+D_r)}\left[\frac{1-e^{-2\gamma_v t}}{2\gamma_v} + \frac{e^{-2\gamma_v t} - e^{-(\gamma_v+D_r)t}}{(\gamma_v - D_r)}\right] + \frac{2v_0\mu \boldsymbol{F}_0\cdot\hat{\boldsymbol{u}}_0}{D_r}\left(1-e^{-D_r t}\right)t\\ &+ \mu^2 \boldsymbol{F}_0^2 t^2 \end{aligned} \tag{3.31}$$

with the components of external force denoted by $\boldsymbol{F}_0 = (F_0^x, F_0^y)$. As has been indicated before, the second moment $\langle \mathbf{r}^2 \rangle$ can also be calculated directly from the solution of Langevin equations,

$$\mathbf{r}(t) = \int_0^t dt' v(t')\hat{\boldsymbol{u}}(t') + \int_0^t \boldsymbol{dB}^t(t') + \mu \int_0^t dt' \boldsymbol{F}(t').$$

Thus the mean squared displacement is given by

$$\begin{aligned}\langle \mathbf{r}^2 \rangle &= 2\int_0^t dt_1 \int_0^{t_1} dt_2 \left[\langle v(t_1)v(t_2)\rangle \langle \hat{\boldsymbol{u}}(t_1)\cdot \hat{\boldsymbol{u}}(t_2)\rangle\right] + 2\int_0^t \int_0^{t_1} \langle \boldsymbol{dB}^t(t_1)\boldsymbol{dB}^t(t_2)\rangle \\ &+ 2\mu \int_0^t dt_1 \int_0^{t_1} dt_2 \left[\langle v(t_2)\rangle \langle \boldsymbol{F}(t_1)\cdot \hat{\boldsymbol{u}}(t_2)\rangle + \langle v(t_1)\rangle \langle \boldsymbol{F}(t_2)\cdot \hat{\boldsymbol{u}}(t_1)\rangle\right] \\ &+ 2\mu^2 \int_0^t dt_1 \int_0^{t_1} dt_2 \langle \boldsymbol{F}(t_1)\cdot \boldsymbol{F}(t_2)\rangle, \end{aligned} \tag{3.32}$$

where cross terms are zero as $\langle \boldsymbol{dB}^t\rangle = 0$ and speed $v(t)$, orientation $\hat{\boldsymbol{u}}(t)$ evolve independently. By substituting the speed correlation function from Eq. (3.10) and orientational correlation from Eq. (3.9) in Eq. (3.32), and after performing the integrations, one gets the same mean squared displacement as in Eq. (3.31).

Multiple crossovers and crossover time scales: In order to show the different regimes that Eq. (3.22) permits, we analyze the expression for $\langle \mathbf{r}^2\rangle$ in different time regimes. In the limit of smallest time $t \to 0$, expanding all the exponential functions around $t = 0$ in Eq. (3.22), we get

$$\begin{aligned}\langle \mathbf{r}^2 \rangle &= 2dDt + \left(v_0^2 + 2v_0\mu \boldsymbol{F}_0\cdot \hat{\boldsymbol{u}}_0 + \mu^2 \boldsymbol{F}_0^2\right) t^2 \\ &- \frac{1}{3}\left((d-1)D_r v_0^2 - 2D_v + 3(d-1)D_r v_0 \mu \boldsymbol{F}_0 \cdot \hat{\boldsymbol{u}}_0\right) t^3 + \mathcal{O}(t^4). \end{aligned} \tag{3.33}$$

This shows that the initial $\langle \mathbf{r}^2\rangle \sim t$ behavior crosses over to the ballistic $\langle \mathbf{r}^2\rangle \sim t^2$ regime at $t_I = 2dD/(v_0^2 + 2v_0\mu \boldsymbol{F}_0\cdot \hat{\boldsymbol{u}}_0 + \mu^2 \boldsymbol{F}_0\cdot \boldsymbol{F}_0)$. A second possible crossover from $\langle \mathbf{r}^2\rangle \sim t^2$ to $\langle \mathbf{r}^2\rangle \sim t$ may appear at $t_{II} = 3(v_0^2 + 2v_0\mu \boldsymbol{F}_0\cdot \hat{\boldsymbol{u}}_0 + \mu^2 \boldsymbol{F}_0\cdot \boldsymbol{F}_0)/((d-1)D_r v_0^2 - 2D_v + 3(d-1)D_r v_0\mu \boldsymbol{F}_0\cdot \hat{\boldsymbol{u}}_0)$. At large D_v the sign of the denominator can change, where $|t_{II}|$ will denote a crossover from $\langle \mathbf{r}^2\rangle \sim t^2$ to $\langle \mathbf{r}^2\rangle \sim t^3$.

In the other limit of longest times ($t \to \infty$), all the exponentials drop out of the Eq. (3.22) to give

$$\langle \mathbf{r}^2 \rangle = \left[2dD + \frac{2(v_0^2 + v_0\mu \boldsymbol{F}_0\cdot \hat{\boldsymbol{u}}_0)}{(d-1)D_r} + \frac{2D_v}{\gamma_v((d-1)D_r + \gamma_v)}\right] t + \mu^2 \boldsymbol{F}_0^2 t^2. \tag{3.34}$$

(i) **Slow relaxation of active speed;** $\gamma_v \ll (d-1)D_r$: In the limit of $(d-1)D_r t \gg 1$ and $2\gamma_v t \ll 1$, we use $\exp[-(d-1)D_r t] = 0$, $\exp[-((d-1)D_r + \gamma_v)t] = 0$ and expand $\exp(-2\gamma_v t)$ around $2\gamma_v t = 0$ in Eq. (3.23), to get

$$\langle \mathbf{r}^2 \rangle = \left(2dD + \frac{2(v_0^2 + v_0 \mu \boldsymbol{F}_0 \cdot \hat{\boldsymbol{u}}_0)}{(d-1)D_r} + \frac{4D_v}{((d-1)^2 D_r^2 - \gamma_v^2)} \right) t + \frac{2D_v}{((d-1)D_r - \gamma_v)} t^2 + \mathcal{O}(t^3). \tag{3.35}$$

This shows the possibility of a third crossover $\langle \mathbf{r}^2 \rangle \sim t$ to $\langle \mathbf{r}^2 \rangle \sim t^2$ at $t_{III} \sim (2dD + 2(v_0^2 + v_0\mu\boldsymbol{F}_0 \cdot \hat{\boldsymbol{u}}_0)/(d-1)D_r + 4D_v/((d-1)^2 D_r^2 - \gamma_v^2))((d-1)D_r - \gamma_v)/2D_v$. In the longest times, we compare the quadratic in t term in Eq. (3.35) with the linear t term in Eq. (3.34) to get a fourth ballistic-diffusive crossover at $t_{IV} \sim [2dD + 2(v_0^2 + v_0\mu\boldsymbol{F}_0 \cdot \hat{\boldsymbol{u}}_0)/(d-1)D_r + 2D_v/(\gamma_v((d-1)D_r + \gamma_v))]((d-1)D_r - \gamma_v)/2D_v$ with the condition $(d-1)D_r \gg 2\gamma_v$. The final diffusive-ballistic crossover can appear at $t_V \sim [2dD + 2v_0^2/(d-1)D_r + 2D_v/\gamma_v((d-1)D_r + \gamma_v)]/\mu^2\boldsymbol{F}_0^2$, with the crossover point obtained by comparing the linear and quadratic in t terms in Eq. (3.34).

In the case of $t_{II} < t_I$, the first diffusive-ballistic crossover disappears, as a result removing the following ballistic-diffusive crossover. Thus it reduces the number of possible crossovers to three: $\langle \mathbf{r}^2 \rangle \sim t$ to $\sim t^2$ to $\sim t$ and then back to t^2 for longest times. The new first crossover then can appear at $t_I^* = 2dD((d-1)D_r - \gamma_v)/2D_v$, calculated from comparing the linear in t term in Eq. (3.33) with the quadratic in t term in Eq. (3.35). The crossovers at t_I, t_{II}, t_{III} disappear. The rest of the crossovers at t_{IV} and t_V remain unaltered. Thus in this case, the second possible crossover from $\langle \mathbf{r}^2 \rangle \sim t^2$ to $\sim t$ can appear at t_{IV} and the final diffusive-ballistic crossover appears at t_V.

The different crossovers for $\langle \mathbf{r}^2 \rangle$ in 2d with crossover times identified is shown in Fig. (3.7)(a). The initial conditions are $v_1 = v_0$ and initial heading direction $\hat{\boldsymbol{u}}_0$ along the x-axis. The parameter values used are $\tilde{\gamma_v} = \gamma_v \tau_r = 5 \times 10^{-4}$, $\tilde{D_v} = D_v \tau_r / \bar{v}^2 = 2.5$, and $\tilde{\boldsymbol{F}_0} = \mu \boldsymbol{F}_0 / \bar{v} = 2.2 \times 10^{-2}\ \hat{r}$.

The solid line corresponding to $Pe = v_0/\bar{v} = 22.36$ in Fig. (3.7)(a) exhibits

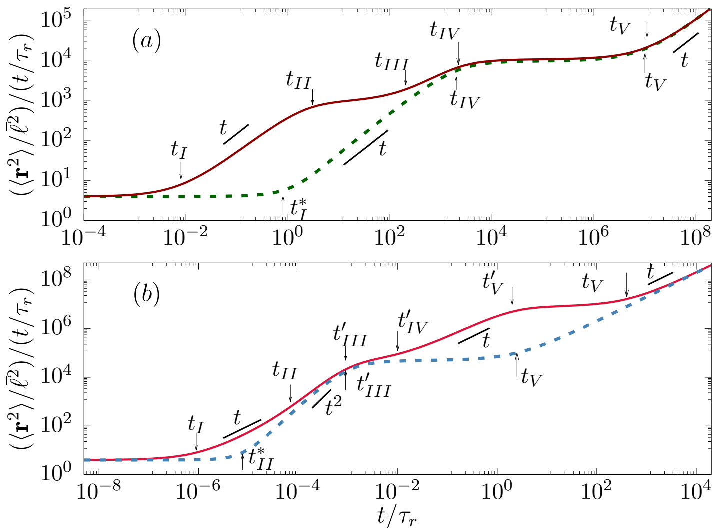

Figure 3.7: (color online) Directed persistent motion. Mean squared displacements $\langle \mathbf{r}^2 \rangle$ as in Eq. (3.31) are depicted as a function of time t for directed persistent motion with speed fluctuation in 2d. The initial condition is set by speed $v_1/\bar{v} = Pe$ and heading direction $\hat{\boldsymbol{u}}_0 = \hat{x}$. (a) Parameters used are $\tilde{\gamma_v} = \gamma_v \tau_r = 5 \times 10^{-4}$, $\tilde{D_v} = D_v \tau_r / \bar{v}^2 = 2.5$, and $\tilde{\boldsymbol{F}}_0 = \mu \boldsymbol{F}_0 / \bar{v} = 2.2 \times 10^{-2}\ \hat{r}$ with $\hat{r} = \hat{x} + \hat{y}$, active speed $Pe = v_0/\bar{v} = 22.36$ (solid line) and 1.12 (dashed line). The solid line exhibits five crossovers with crossover times $t_I/\tau_r = 8 \times 10^{-3}$, $t_{II}/\tau_r = 3.03$, $t_{III}/\tau_r = 202.9$ and $t_{IV}/\tau_r = 2199$, and $t_V/\tau_r = 1.1 \times 10^7$. The dashed line shows three crossovers with crossover times $t_I^*/\tau_r = 0.8$, $t_{IV}/\tau_r = 2 \times 10^3$, $t_V/\tau_r = 10^7$. (b) Parameters used are $\tilde{\gamma_v} = \gamma_v \tau_r = 2 \times 10^3$, $\tilde{D_v} = D_v \tau_r / \bar{v}^2 = 10^{11}$, and $\tilde{\boldsymbol{F}}_0 = \mu \boldsymbol{F}_0 / \bar{v} = 10^2\ \hat{r}$, active speed $Pe = v_0/\bar{v} = 2 \times 10^3$ (solid line) and 10 (dashed line). The solid line exhibits six crossover with crossover times $t_I/\tau_r = 10^{-6}$, $t_{II}/\tau_r = 6 \times 10^{-5}$, $t_{III}/\tau_r = 0.0016$ and $t_{IV}/\tau_r = 0.0225$, $t_V/\tau_r = 2.02$, and $t_{VI}/\tau_r = 4 \times 10^2$. The dashed line shows three crossovers with crossover times $t_{II}^*/\tau_r = 7.7 \times 10^{-6}$, $t'_{III}/\tau_r = 9 \times 10^{-4}$, $t_V/\tau_r = 2.5$.

all the possible crossovers discussed above, from $\langle \mathbf{r}^2 \rangle \sim t$ to $\sim t^2$ to $\sim t$ to $\sim t^2$ to $\sim t$ to finally $\sim t^2$ as the requirement $t_I < t_{II} < t_{III} < t_{IV} < t_V$ is satisfied. In this case, $t_I \equiv t_I/\tau_r = 4/(Pe^2 + 2Pe\tilde{\boldsymbol{F}}_0 \cdot \hat{\boldsymbol{u}}_0 + \tilde{\boldsymbol{F}}_0^2) \approx 0.008$, $t_{II} \equiv t_{II}/\tau_r = 3(Pe^2 + 2Pe\tilde{\boldsymbol{F}}_0 \cdot \hat{\boldsymbol{u}}_0 + \tilde{\boldsymbol{F}}_0^2)/(Pe^2 - 2\tilde{D}_v + 3Pe\tilde{\boldsymbol{F}}_0 \cdot \hat{\boldsymbol{u}}_0) \approx 3.03$, $t_{III} \equiv t_{III}/\tau_r \sim [4 + 2(Pe^2 + Pe\tilde{\boldsymbol{F}}_0 \cdot \hat{\boldsymbol{u}}_0) + 4\tilde{D}_v/(1 - \tilde{\gamma_v}^2)](1 - \tilde{\gamma_v})/2\tilde{D}_v \approx 202.9$, $t_{IV} \equiv t_{IV}/\tau_r \sim [4 + 2(Pe^2 + Pe\tilde{\boldsymbol{F}}_0 \cdot \hat{\boldsymbol{u}}_0) + 2\tilde{D}_v/\{\tilde{\gamma_v}(1 + \tilde{\gamma_v})\}](1 - \tilde{\gamma_v})/2\tilde{D}_v \approx 2199$, and $t_V \equiv t_V/\tau_r \sim [4 + 2Pe^2 + 2\tilde{D}_v/\{\tilde{\gamma_v}(1 + \tilde{\gamma_v})\}]/\tilde{\boldsymbol{F}}_0^2 \approx 1.1 \times 10^7$ pointed out in Fig. (3.7)(a).

The dashed line in Fig. (3.7)(a) corresponds to $Pe = v_0/\bar{v} = 1.12$ and shows two diffusive-ballistic crossovers with one intermediate ballistic-diffusive crossover. The crossover times are $t_I^* \equiv t_I^*/\tau_r \sim 4(1 - \tilde{\gamma_v})/2\tilde{D}_v \approx 0.8$, $t_{IV} \equiv t_{IV}/\tau_r \sim [4 +$

$2(Pe^2 + Pe\tilde{\boldsymbol{F}}_0 \cdot \hat{\boldsymbol{u}}_0) + 2\tilde{D}_v/\{\tilde{\gamma}_v(1+\tilde{\gamma}_v)\}](1-\tilde{\gamma}_v)/2\tilde{D}_v \approx 2 \times 10^3$, and $t_V \equiv t_V/\tau_r \sim [4 + 2Pe^2 + 2\tilde{D}_v/\{\tilde{\gamma}_v(1+\tilde{\gamma}_v)\}]/\tilde{\boldsymbol{F}}_0^2 \approx 1 \times 10^7$. In this case $t_I^* < t_I \approx 3.2$, thus the first diffusive-ballistic crossover is preempted by t_I^*. Other possible intermediate crossovers disappear due to the following reasons. The possible ballistic-diffusive crossover point $t_{II} < 0$ for these parameters. In its absence, $t_{III} \approx 3.3$ signifying a possible diffusive-ballistic crossover cannot show any change in the already ballistic property of the ABP in that time regime.

(ii) **Fast relaxation of active speed;** $\gamma_v \gg (d-1)D_r$: In this case, again, the first two crossovers from diffusive to ballistic to diffusive regime appears at t_I and t_{II}, respectively. The following crossovers change due to the consideration of the fast relaxation of active speed. As $(d-1)D_r t \ll 1$ and $2\gamma_v t \gg 1$, we use $\exp(-2\gamma_v t) = 0$, $\exp[-((d-1)D_r + \gamma_v)t] = 0$ and expand $\exp[-(d-1)D_r t]$ around $D_r t = 0$ in Eq. (3.22) to get

$$\begin{aligned}\langle \mathbf{r}^2 \rangle = &\left(2dD + \frac{2D_v}{\gamma_v((d-1)D_r + \gamma_v)}\right) t + (v_0^2 + 2v_0\mu\boldsymbol{F}_0 \cdot \hat{\boldsymbol{u}}_0 + \mu^2\boldsymbol{F}_0^2)t^2 \\ &+ \mathcal{O}(t^3). \end{aligned} \tag{3.36}$$

Moreover, at large D_v the sign of the denominator in the expression of t_{II} can change. In that case, $|t_{II}|$ denotes a crossover from $\langle \mathbf{r}^2 \rangle \sim t^2$ to $\langle \mathbf{r}^2 \rangle \sim t^3$.

Comparing the cubic term in t in Eq (3.33) with the linear in t term in Eq. (3.36), we get the crossover from $\langle \mathbf{r}^2 \rangle \sim t^3$ to $\sim t$ at

$$t'_{III} = \left[3\left(2dD + 2D_v/\gamma_v((d-1)D_r + \gamma_v)\right)/(2D_v - (d-1)D_r v_0^2 - 3(d-1)D_r v_0 \mu \boldsymbol{F}_0 \cdot \hat{\boldsymbol{u}}_0)\right]^{1/2}.$$

A fourth crossover $\langle \mathbf{r}^2 \rangle \sim t$ to $\sim t^2$ is expected at $t'_{IV} \sim (2dD + 2D_v/(\gamma_v((d-1)D_r + \gamma_v))/(v_0^2 + 2v_0\mu\boldsymbol{F}_0 \cdot \hat{\boldsymbol{u}}_0 + \mu^2\boldsymbol{F}_0^2)$. This is obtained by comparing the first two terms in Eq. (3.36). The fifth crossover point $t'_V = (2dD + 2v_0^2/(d-1)D_r + 2D_v/\gamma_v((d-1)D_r + \gamma_v))/(v_0^2 + 2v_0\mu\boldsymbol{F}_0 \cdot \hat{\boldsymbol{u}}_0 + \mu^2\boldsymbol{F}_0^2)$ from ballistic to diffusive behavior is obtained by comparing the ballistic term in Eq. (3.36) with the diffusive term in Eq. (3.34). The final diffusive-ballistic crossover point $t_V = [2dD + 2v_0^2/(d-1)D_r + 2D_v/\gamma_v((d-$

$1)D_r + \gamma_v)]/\mu^2 \boldsymbol{F}_0^2$ remains unchanged, as it is obtained by comparing the linear and quadratic in t terms in Eq. (3.34), as before.

With changing parameter values, if the sequence of time scales from small to large changes, the number of crossovers get altered. For example, if $t_{II} < t_I$ the first ballistic-diffusive crossover disappears and, as a result, so does the following ballistic-diffusive crossover. The first crossover under such a condition is from $\langle \mathbf{r}^2 \rangle \sim t$ to $\langle \mathbf{r}^2 \rangle \sim t^3$ and can appear at $t^*_{II} \sim [6dD/(2D_v - (d-1)D_r v_0^2 - 3(d-1)D_r v_0 \mu \boldsymbol{F}_0 \cdot \hat{\boldsymbol{u}}_0)]^{1/2}$. This point is calculated by comparing the linear and the cubic order terms in t in Eq. (3.33). The following crossovers may appear at t'_{III}, t'_{IV}, t'_V, and t_V. However, if $t'_{IV} < t'_{III}$, this sequence of crossovers also get modified, losing two more crossovers. In that case, the next crossover can appear at

$$t^*_V = \left(\frac{3\left[2dD + \frac{2(v_0^2 + v_0 \mu \boldsymbol{F}_0 \cdot \hat{\boldsymbol{u}}_0)}{(d-1)D_r} + \frac{2D_v}{\gamma_v((d-1)D_r + \gamma_v)}\right]}{[(d-1)D_r v_0^2 - 2D_v + 3(d-1)D_r v_0 \mu \boldsymbol{F}_0 \cdot \hat{\boldsymbol{u}}_0]} \right)^{1/2}$$

obtained by comparing the t^3-order term in Eq. (3.33) with the linear order term in t in Eq. (3.34). The final diffusive-ballistic crossover will remain at t_V, as before.

The different crossovers for $\langle \mathbf{r}^2 \rangle$ in 2d with crossover times identified is shown in Fig. (3.7)(b). The initial conditions are $v_1 = v_0$ and initial heading direction $\hat{\boldsymbol{u}}_0$ along the x-axis. The parameter values used are $\tilde{\gamma}_v = \gamma_v \tau_r = 2 \times 10^3$, $\tilde{D}_v = D_v \tau_r / \bar{v}^2 = 10^{11}$, and $\tilde{\boldsymbol{F}}_0 = \mu \boldsymbol{F}_0 / \bar{v} = 10^2\ \hat{r}$.

The solid line, $Pe = v_0/\bar{v} = 2 \times 10^3$ in Fig. (3.7)(b) exhibit all possible six crossovers $\langle \mathbf{r}^2 \rangle \sim t$ to $\sim t^2$, to $\sim t^3$, to $\sim t$, to $\sim t^2$, to $\sim t$ to finally $\sim t^2$ as the requirement $t_I < t_{II} < t_{III} < t_{IV} < t_V < t_{VI}$ satisfied. In this case, the crossover times are $t_I \equiv t_I/\tau_r \sim 4/(Pe^2 + 2Pe\tilde{\boldsymbol{F}}_0 \cdot \hat{\boldsymbol{u}}_0 + \tilde{\boldsymbol{F}}_0^2) \approx 9 \times 10^{-7}$, $t_{II} \equiv t_{II}/\tau_r \sim 3(Pe^2 + 2Pe\tilde{\boldsymbol{F}}_0 \cdot \hat{\boldsymbol{u}}_0 + \tilde{\boldsymbol{F}}_0^2)/(Pe^2 - 2\tilde{D}_v) \approx 7 \times 10^{-5}$, $t'_{III} \equiv t'_{III}/\tau_r \sim \left[3\left(4 + 2\tilde{D}_v/\tilde{\gamma}_v(1+\tilde{\gamma}_v)\right)/(2\tilde{D}_v - Pe^2 - 3Pe\tilde{\boldsymbol{F}}_0 \cdot \hat{\boldsymbol{u}}_0)\right]^{1/2} \approx 9 \times 10^{-4}$, $t'_{IV} \equiv t'_{IV}/\tau_r \sim (4 + 2\tilde{D}_v/\tilde{\gamma}_v(1+\tilde{\gamma}_v))/(Pe^2 + 2Pe\tilde{\boldsymbol{F}}_0 \cdot \hat{\boldsymbol{u}}_0 + \tilde{\boldsymbol{F}}_0^2) \approx 1 \times 10^{-2}$, $t'_V \equiv t'_V/\tau_r \sim [4 + 2Pe^2 + 2\tilde{D}_v/\{\tilde{\gamma}_v(1+\tilde{\gamma}_v)\}]/(Pe^2 + 2Pe\tilde{\boldsymbol{F}}_0 \cdot \hat{\boldsymbol{u}}_0 + \tilde{\boldsymbol{F}}_0^2) \approx 2$, and $t_V \equiv t_V/\tau_r \sim [4 + 2Pe^2 +$

$2\tilde{D}_v/\{\tilde{\gamma}_v(1+\tilde{\gamma}_v)\}]/\tilde{\boldsymbol{F}}_0^2 \approx 4 \times 10^2$ pointed out in Fig. (3.7)(b).

The dashed line, $Pe = v_0/\bar{v} = 10$ in Fig. (3.7)(b) shows three crossovers from $\langle \mathbf{r}^2 \rangle \sim t$ to $\langle \mathbf{r}^2 \rangle \sim t^3$ to $\langle \mathbf{r}^2 \rangle \sim t$ to finally $\langle \mathbf{r}^2 \rangle \sim t^2$. The crossover times are $t^*_{II}/\tau_r \sim (12/(2\tilde{D}_v - Pe^2 - 3Pe\tilde{\boldsymbol{F}}_0 \cdot \hat{\boldsymbol{u}}_0))^{1/2} \approx 7.7 \times 10^{-6}$,

$t'_{III}/\tau_r \sim \left[3\left(4 + 2\tilde{D}_v/\{\tilde{\gamma}_v(1+\tilde{\gamma}_v)\}\right)/(2\tilde{D}_v - Pe^2 - 3Pe\tilde{\boldsymbol{F}}_0 \cdot \hat{\boldsymbol{u}}_0)\right]^{1/2} \approx 9\times 10^{-4}$, and $t_V \equiv t_V/\tau_r \sim (4 + 2\tilde{D}_v/\{\tilde{\gamma}_v(1+\tilde{\gamma}_v)\})/\tilde{\boldsymbol{F}}_0^2 \approx 2.5$. The first crossover between $\langle \mathbf{r}^2 \rangle \sim t$ and $\sim t^3$ appears at t^*_{II}, as $t^*_{II} < t_I \approx 3.3 \times 10^{-4}$ preempting the possible crossover at t_I. The second crossover $\langle \mathbf{r}^2 \rangle \sim t^3$ to $\sim t$ appears at t'_{III} with $t'_{III} < t'_{IV} \approx 4.1$. The other possible crossovers $\langle \mathbf{r}^2 \rangle \sim t$ to $\sim t^2$ to $\sim t$ are absent as $t'_V \approx t'_{IV}$. The final crossover $\langle \mathbf{r}^2 \rangle \sim t$ to $\sim t^2$ appears at t_V as before.

3.6.3 Displacement fluctuation

In this section, we compute displacement fluctuation $\langle \delta\mathbf{r}^2 \rangle$ and analyze the multiple crossovers with crossover timescales.

Persistent motion

Displacement fluctuation defined as $\langle \delta\mathbf{r}^2 \rangle = \langle \mathbf{r}^2 \rangle - \langle \mathbf{r} \rangle^2$ where $\langle \mathbf{r}^2 \rangle$, Eq. (3.23) and $\langle \mathbf{r} \rangle$, Eq. (3.14) already calculated. Thus, $\langle \delta\mathbf{r}^2 \rangle$

$$\begin{aligned}\langle \delta\mathbf{r}^2 \rangle &= 2d\left(D + \frac{v_0^2}{(d-1)dD_r}\right)t - \frac{v_0^2}{(d-1)^2D_r^2}\left(3 - 4\,e^{-(d-1)D_rt} + e^{-2(d-1)D_rt}\right)\\ &+ \frac{2D_v}{\gamma_v(\gamma_v+(d-1)D_r)}\left[t - \frac{1-e^{-(\gamma_v+(d-1)D_r)t}}{(\gamma_v+(d-1)D_r)} - \frac{1-e^{-2\gamma_vt}}{2\gamma_v} + \frac{e^{-2\gamma_vt} - e^{-(\gamma_v+(d-1)D_r)t}}{((d-1)D_r-\gamma_v)}\right]\end{aligned} \tag{3.37}$$

Setting $d = 2$, we get

$$\begin{aligned}\langle \delta\mathbf{r}^2 \rangle &= 4\left(D + \frac{v_0^2}{2D_r}\right)t - \frac{v_0^2}{D_r^2}\left(3 - 4\,e^{-D_rt} + e^{-2D_rt}\right)\\ &+ \frac{2D_v}{\gamma_v(\gamma_v+D_r)}\left[t - \frac{1-e^{-(\gamma_v+D_r)t}}{(\gamma_v+D_r)} - \frac{1-e^{-2\gamma_vt}}{2\gamma_v} + \frac{e^{-2\gamma_vt} - e^{-(\gamma_v+D_r)t}}{(D_r-\gamma_v)}\right]\end{aligned} \tag{3.38}$$

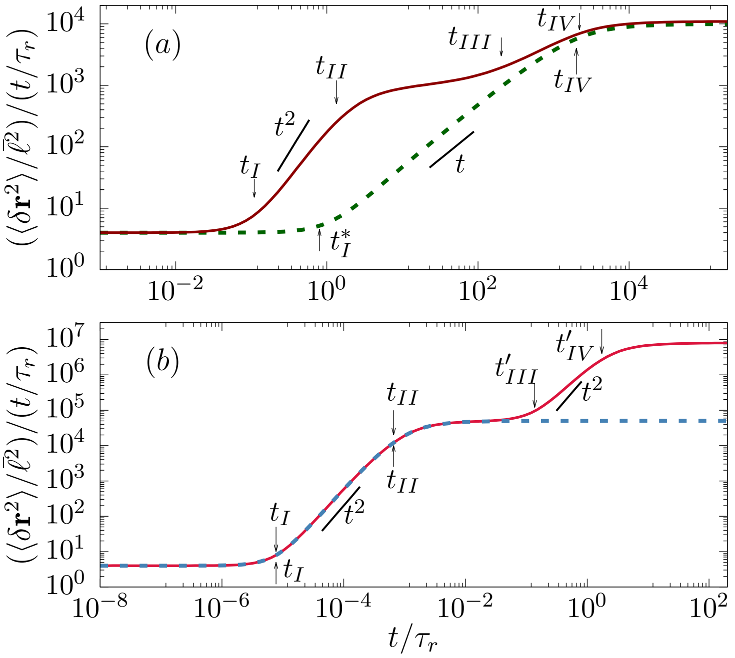

Figure 3.8: (color online) Displacement fluctuations $\langle\delta\mathbf{r}^2\rangle$ in Eq. (3.38) as a function of time t in $d=2$. (a) Parameters used are $\tilde{\gamma_v}=\gamma_v\tau_r=5\times10^{-4}$, $\tilde{\gamma_v}=D_v\tau_r/\bar{v}^2=2.5$ with active speed $Pe=v_0/\bar{v}=22.36$ (solid line), 1.12 (dashed line). The solid line shows four crossovers with crossover times $t_I/\tau_r=0.008$, $t_{II}/\tau_r=3.03$, $t_{III}/\tau_r=202.8$ and $t_{IV}/\tau_r=2.2\times10^3$. The dashed line shows two crossovers with crossover times $t_I^*/\tau_r=0.8$ and $t_{IV}/\tau_r=2\times10^3$. (b) Parameters used are $\tilde{\gamma_v}=\gamma_v\tau_r=2\times10^3$, $\tilde{D_v}=D_v\tau_r/\bar{v}^2=10^{11}$ with $Pe=v_0/\bar{v}=2\times10^3$ (solid line), 10 (dashed line). The solid line exhibits four crossovers with crossover times $t_I/\tau_r=8\times10^{-6}$, $t_{II}/\tau_r=7\times10^{-4}$, $t'_{III}/\tau_r=1.4\times10^{-1}$ and $t'_{IV}/\tau_r=1.7$. The dashed line shows two crossovers with crossover times $t_I/\tau_r=8\times10^{-6}$, $t_{II}/\tau_r=7\times10^{-4}$.

From which we can redefine $\sqrt{\langle\delta\mathbf{r}^2\rangle}$ spread of displacement of different independent configurations starting from same initial condition($\mathbf{r}$, v, $\hat{\boldsymbol{u}}$) at time t. In the small time limit of $t\to0$ (i.e., $D_rt\ll1$, $\gamma_vt\ll1$), expanding $\langle\delta\mathbf{r}^2\rangle$ in Eq. (3.37) around $t=0$ leads to,

$$\begin{aligned}\langle\delta\mathbf{r}^2\rangle &= 2dDt+\frac{2}{3}(D_v+(d-1)D_rv_0^2)t^3-\frac{1}{6}((d-1)D_rD_v+3D_v\gamma_v\\&\quad+3(d-1)^2D_r^2v_0^2)t^4+\mathcal{O}(t^5).\end{aligned}\tag{3.39}$$

This allows a crossover from $\langle\delta\mathbf{r}^2\rangle\sim t$ to $\sim t^3$ at $t_I=\sqrt{3dD/(D_v+(d-1)D_rv_0^2)}$. Moreover, a second possible crossover $\langle\delta\mathbf{r}^2\rangle\sim t^3$ to $\sim t$ may appear at $t_{II}=4(D_v+(d-1)D_rv_0^2)/((d-1)D_rD_v+3D_v\gamma_v+3v_0^2(d-1)^2D_r^2)$. In the long time limit of $t \to \infty$ (i.e., $D_r t \gg 1$, $\gamma_v t \gg 1$), $\langle \delta\mathbf{r}^2 \rangle$ in Eq. (3.37) leads to

$$\langle \delta\mathbf{r}^2 \rangle = \left(2dD + \frac{2v_0^2}{(d-1)D_r} + \frac{2D_v}{\gamma_v(\gamma_v + (d-1)D_r)} \right) t, \tag{3.40}$$

which gives a diffusive scaling $\langle \delta\mathbf{r}^2 \rangle = 2dD_{\text{eff}}t$ with the effective diffusion constant in d-dimensions,

$$D_{\text{eff}} = \left(D + \frac{v_0^2}{(d-1)dD_r} \right) + \frac{D_v}{d\gamma_v((d-1)D_r + \gamma_v)}.$$

(i) **Slow relaxation of active speed;** $\gamma_v \ll (d-1)D_r$: In the limit of $(d-1)D_r t \gg 1$ and $2\gamma_v t \ll 1$, $\langle \delta\mathbf{r}^2 \rangle$ in Eq. (3.37) leads to

$$\langle \delta\mathbf{r}^2 \rangle = \left(2dD + \frac{2v_0^2}{(d-1)D_r} + \frac{4D_v}{((d-1)^2 D_r^2 - \gamma_v^2)} \right) t + \frac{2D_v}{((d-1)D_r - \gamma_v)} t^2 + \mathcal{O}(t^3). \tag{3.41}$$

This allows a third crossover from $\langle \delta\mathbf{r}^2 \rangle \sim t$ to $\langle \delta\mathbf{r}^2 \rangle \sim t^2$ at $t_{III} \sim (2dD + 2v_0^2/(d-1)D_r + 4D_v/((d-1)^2 D_r^2 - \gamma_v^2))((d-1)D_r - \gamma_v)/2D_v$. Finally, a crossover from $\langle \delta\mathbf{r}^2 \rangle \sim t^2$ to $\sim t$ may appear at $t_{IV} \sim [2dD + 2v_0^2/(d-1)D_r + 2D_v/\{\gamma_v(\gamma_v + (d-1)D_r)\}]((d-1)D_r - \gamma_v)/2D_v$.

In the case of $t_{II} < t_I$, the number of possible crossovers reduces to two: from $\langle \delta\mathbf{r}^2 \rangle \sim t$ to $\sim t^2$ to $\sim t$. Following a procedure similar to the analysis of crossovers in $\langle \mathbf{r}^2 \rangle$, we find that the first crossover from $\langle \delta\mathbf{r}^2 \rangle \sim t$ to $\sim t^2$ appears at $t_I^* \sim 2dD((d-1)D_r - \gamma_v)/2D_v$, obtained by comparing Eq. (3.39) and Eq. (3.41). The second crossover $\langle \delta\mathbf{r}^2 \rangle \sim t^2$ to $\sim t$ appears at $t_{IV} \sim [2dD + 2v_0^2/(d-1)D_r + 2D_v/\{\gamma_v(\gamma_v + (d-1)D_r)\}]((d-1)D_r - \gamma_v)/2D_v$, obtained by comparing Eq. (3.41) and Eq. (3.40).

The possible crossovers of $\langle \delta\mathbf{r}^2 \rangle$ in 2d in the limit of $\gamma_v \tau_r \ll 1$ identifying the crossover times are shown in Fig. (3.8)(a). Parameter values are $\tilde{\gamma_v} = \gamma_v \tau_r = 5 \times 10^{-4}$, $\tilde{D_v} = D_v \tau_r / \bar{v}^2 = 2.5$. The solid line, $Pe = v_0/\bar{v} = 22.36$ in Fig. (3.8)(a) exhibits all the four crossovers $\langle \delta\mathbf{r}^2 \rangle \sim t$ to $\sim t^3$, to $\sim t$, to $\sim t^2$, to finally $\sim t$ as the requirement $t_I < t_{II} < t_{III} < t_{IV}$ is satisfied. The crossover times are

$t_I \equiv t_I/\tau_r \sim \sqrt{6/(Pe^2+\tilde{D}_v)} \approx 0.11$, $t_{II} \equiv t_{II}/\tau_r \sim 4(Pe^2+\tilde{D}_v)/(3Pe^2+3\tilde{D}_v\tilde{\gamma_v}+\tilde{D}_v) \approx 1.34$, $t_{III} \equiv t_{III}/\tau_r \sim [4+2Pe^2+4\tilde{D}_v/(1-\tilde{\gamma_v}^2)](1-\tilde{\gamma_v})/2\tilde{D}_v \approx 202.8$ and $t_{IV} \equiv t_{IV}/\tau_r \sim [4+2Pe^2+2\tilde{D}_v/\{\tilde{\gamma_v}(1+\tilde{\gamma_v})\}](1-\tilde{\gamma_v})/2\tilde{D}_v \approx 2200$. The dashed line at $Pe = v_0/\bar{v} = 1.12$ in Fig. (3.8)(a) shows two crossovers $\langle \delta \mathbf{r}^2 \rangle \sim t$ to $\sim t^2$ to $\sim t$ as $t_{II} < t_I$. The crossover times are $t_I^* \equiv t_I^*/\tau_r \sim 2(1-\tilde{\gamma_v})/\tilde{D}_v \approx 0.8$ and $t_{IV} \equiv t_{IV}/\tau_r \approx 2 \times 10^3$. Here, the first diffusive- ballistic crossover appears at t_I^* as $t_I^* < t_I \approx 1.3$.

(ii) **Fast relaxation of active speed;** $\gamma_v \gg (d-1)D_r$: In the other limit of $(d-1)D_r t \ll 1$ and $2\gamma_v t \gg 1$, using $e^{-2\gamma_v t} = 0$, $e^{-((d-1)D_r+\gamma_v)t} = 0$ and expanding of $e^{-D_r t}$ around $D_r t = 0$, Eq. (3.37) leads to

$$\langle \delta \mathbf{r}^2 \rangle \simeq \left(2dD + \frac{2D_v}{\gamma_v((d-1)D_r+\gamma_v)} \right) t + \frac{2}{3}(d-1)D_r v_0^2 t^3. \tag{3.42}$$

This predicts a third possible crossover from $\langle \delta \mathbf{r}^2 \rangle \sim t$ to $\sim t^3$ at

$t'_{III} \sim [3(dD + D_v/\{\gamma_v((d-1)D_r+\gamma_v)\})/(d-1)D_r v_0^2]^{1/2}$. The final crossover $\langle \delta \mathbf{r}^2 \rangle \sim t^3$ to $\sim t$ can appear at

$t'_{IV} \sim [3(dD + v_0^2/(d-1)D_r + D_v/\{\gamma_v((d-1)D_r+\gamma_v)\})/(d-1)D_r v_0^2]^{1/2}$, with the crossover point obtained by comparing the t^3 order term in Eq. (3.42) with t order term in Eq. (3.40). If $t'_{IV} \le t'_{III}$ these last two crossovers will not be possible.

We demonstrate such crossovers in 2d, in the limit of $\gamma_v \tau_r \gg 1$, in Fig. (3.8)(b). The parameter values used are $\tilde{\gamma_v} = \gamma_v \tau_r = 2 \times 10^3$, $\tilde{D}_v = D_v \tau_r/\bar{v}^2 = 10^{11}$. The solid line in Fig. (3.8)(b) depicts the behavior at $Pe = v_0/\bar{v} = 2 \times 10^3$. This exhibits all four crossovers from $\langle \mathbf{r}^2 \rangle \sim t$ to $\langle \mathbf{r}^2 \rangle \sim t^2$ to $\langle \mathbf{r}^2 \rangle \sim t$ to $\langle \mathbf{r}^2 \rangle \sim t^2$ to finally $\langle \mathbf{r}^2 \rangle \sim t$ as the requirement $t_I < t_{II} < t_{III} < t_{IV}$ is satisfied. In this case, $t_I \equiv t_I/\tau_r \sim \left[6/(\tilde{D}_v + Pe^2)\right]^{1/2} \approx 8 \times 10^{-6}$, $t_{II} \equiv t_{II}/\tau_r \sim 4(\tilde{D}_v + Pe^2)/\left[\tilde{D}_v + 3\tilde{D}_v\tilde{\gamma_v} + 3Pe^2\right] \approx 7 \times 10^{-4}$,

$t'_{III} \equiv t'_{III}/\tau_r \sim \left[3[2+\tilde{D}_v/\{\tilde{\gamma_v}(1+\tilde{\gamma_v})\}]/Pe^2\right]^{1/2} \approx 1.4 \times 10^{-1}$, and $t'_{IV} \equiv t'_{IV}/\tau_r \sim \left[3(2+Pe^2+\tilde{D}_v/\{\tilde{\gamma_v}(1+\tilde{\gamma_v})\})/Pe^2\right]^{1/2} \approx 1.7$ and are identified in Fig. (3.8)(b). The dashed line corresponding to $Pe = v_0/\bar{v} = 10$ in Fig. (3.8)(b) shows two crossovers from $\langle \delta \mathbf{r}^2 \rangle \sim t$, to $\langle \delta \mathbf{r}^2 \rangle \sim t^3$ to finally $\langle \delta \mathbf{r}^2 \rangle \sim t$. As $t'_{III} \approx t'_{IV} \approx 27.4$, the crossover from $\langle \delta \mathbf{r}^2 \rangle \sim t$ to $\sim t^3$ is absent. The crossover times are $t_I \equiv t_I/\tau_r \sim \left[6/(\tilde{D}_v + Pe^2)\right]^{1/2} \approx 8\times 10^{-6}$ and $t_{II} \equiv t_{II}/\tau_r \sim 4(\tilde{D}_v + Pe^2)/\left(\tilde{D}_v + 3\tilde{D}_v\tilde{\gamma}_v + 3Pe^2\right) \approx 7 \times 10^{-4}$.

Directed persistent motion: Displacement fluctuations $\langle \delta \mathbf{r}^2 \rangle = \langle \mathbf{r}^2 \rangle - \langle \mathbf{r} \rangle^2$ in the presence of external force can be directly calculated using the expressions of $\langle \mathbf{r}^2 \rangle$ from Eq. (3.22) and $\langle \mathbf{r} \rangle$ from Eq. (3.14). The initial position is assumed to be $\mathbf{r}_0 = \mathbf{0}$, without any loss of generality. It is straightforward to check that $\langle \delta \mathbf{r}^2 \rangle$ shows the same displacement fluctuations as in Eq. (3.37) obtained for persistent motion. As a result, at long times, while the mean squared displacement in the presence of external force shows a ballistic behavior $\langle \mathbf{r}^2 \rangle \sim t^2$, in contrast, the displacement fluctuation shows a diffusive behavior $\langle \delta \mathbf{r}^2 \rangle \sim t$.

3.6.4 Components of displacement fluctuation

The positional spread of the ABP in parallel and perpendicular perpendicular direction with respect to the initial heading direction $\hat{\boldsymbol{u}}_0$ is studied here to identify any possible anisotropy in the dynamics. The mean displacements $\langle r_\parallel \rangle = \langle \mathbf{r} \rangle \cdot \hat{\boldsymbol{u}}_0 \neq 0$ and $\langle \mathbf{r}_\perp \rangle = \langle \mathbf{r} \rangle - \langle r_\parallel \rangle \hat{\boldsymbol{u}}_0$. Here $\langle \mathbf{r}_\perp \rangle = 0$ in the absence of external drive. In this section, we compute the parallel and normal components of displacement fluctuation.

Parallel component

We consider the initial active speed $v_1 = v_0$. Let us assume the initial orientation of activity is towards the x-axis, $\hat{\boldsymbol{u}}_0 = \hat{x}$. The constant external force is $\boldsymbol{F} = F_0\, \hat{r}$ where $\hat{r}$ is the d-dimensional unit vector in the cartesian coordinate. We use Eq. (3.5). Here $r_\parallel^2 = x^2$, giving $\langle \psi \rangle_0 = 0$, $\langle \nabla_r^2 \psi \rangle_s = 2\langle 1 \rangle_s$, $\langle \nabla_u^2 \psi \rangle_s = 0$, $\langle \partial_v^2 \psi \rangle_s = 0$,

$\langle (v-v_0)\partial_v \psi\rangle_s = 0$, $\langle v\hat{\boldsymbol{u}}\cdot\nabla\psi\rangle_s = 2\langle vxu_x\rangle_s$, and $\langle \boldsymbol{F}\cdot\nabla\psi\rangle_s = 2F_0\langle r_\parallel\rangle_s$. Thus we find

$$\langle r_\parallel^2\rangle_s = \frac{1}{s}\left[2D\langle 1\rangle_s + 2\langle vxu_x\rangle_s + 2\mu F_0\langle r_\parallel\rangle_s\right],$$

where $\langle r_\parallel\rangle_s = v_0/s(s+(d-1)D_r) + \mu F_0/s^2$, already calculated in Section-(3.6). To proceed we consider $\psi = vxu_x$, giving $\langle\psi\rangle_0 = 0$, $\langle\nabla_r^2\psi\rangle_s = 0$, $\langle\nabla_u^2\psi\rangle_s = -(d-1)\langle vxu_x\rangle_s$, $\langle\hat{\boldsymbol{u}}\cdot\nabla\psi\rangle_s = \langle vu_x^2\rangle_s$, and $\langle\boldsymbol{F}\cdot\nabla\psi\rangle_s = F_0\langle vu_x\rangle_s$, leading to $\langle vxu_x\rangle_s = [\langle v^2u_xu_x\rangle_s + \gamma_v v_0\langle xu_x\rangle_s + \mu F_0\langle vu_x\rangle_s]/(s+(d-1)D_r+\gamma_v)$. Further, $\langle vu_x\rangle_s = v_0/(s+(d-1)D_r)$, $\langle xu_x\rangle_s = (\langle vu_xu_x\rangle_s + \mu F_0\langle u_x\rangle_s)/(s+(d-1)D_r)$. Substituting these we get,

$$\langle vxu_x\rangle_s = \frac{1}{s+(d-1)D_r+\gamma_v}\left[\langle v^2u_xu_x\rangle_s + \frac{\gamma_v v_0\langle vu_xu_x\rangle_s}{(s+(d-1)D_r)}\right] + \frac{v_0\mu F_0}{(s+(d-1)D_r)^2},$$

Further, we calculate, $\langle vu_xu_x\rangle_s = \frac{v_0(s+2D_r)}{s(s+2dD_r)}$ and

$$\langle vvu_xu_x\rangle_s = \frac{v_0^2(s+2D_r)}{s(s+2dD_r)} + \frac{4D_rD_v}{s(s+2\gamma_v)(s+2dD_r)} + \frac{2D_v(s+2\gamma_v+2D_r)}{(s+2\gamma_v)(s+2dD_r)(s+2\gamma_v+2dD_r)}.$$

We use $\psi = u_x^2$ to find $\langle\psi\rangle_0 = 1$, $\langle\nabla_r^2\psi\rangle_s = 0$, $\langle\nabla_u^2\psi\rangle_s = -2d\langle u_x^2\rangle_s + 2/s$, $\langle\hat{\boldsymbol{u}}\cdot\nabla\psi\rangle_s = 0$ to get $-1 + s\langle u_xu_x\rangle_s = -2dD_r\langle u_xu_x\rangle_s + 2D_r/s$ giving $\langle u_xu_x\rangle_s = (s+2D_r)/s(s+2dD_r)$. Thus putting together these relations, we obtain $\langle r_\parallel^2\rangle$ in the Laplace space

$$\begin{aligned}\langle r_\parallel^2\rangle_s &= \frac{2D}{s^2} + \frac{2v_0^2(s+2D_r)}{s^2(s+(d-1)D_r)(s+2dD_r)}\\ &+ \frac{8D_rD_v}{s^2(s+2\gamma_v)(s+2dD_r)(s+\gamma_v+(d-1)D_r)}\\ &+ \frac{4D_v(s+2\gamma_v+2D_r)}{s(s+2\gamma_v)(s+2dD_r)(s+2\gamma_v+2dD_r)(s+\gamma_v+(d-1)D_r)}\\ &+ \frac{2v_0\mu F_0(2s+(d-1)D_r)}{s^2(s+(d-1)D_r)^2} + \frac{2\mu^2F_0^2}{s^3}.\end{aligned} \tag{3.43}$$

Performing the inverse Laplace transform we find,

$$
\begin{aligned}
&\langle r_{\parallel}^2\rangle = 2\left(D + \frac{v_0^2}{(d-1)dD_r}\right)t \\
&+ \frac{v_0^2}{D_r^2}\left(\frac{(d-1)e^{-2dD_rt}}{d^2(d+1)} + \frac{2(3-d)e^{-(d-1)D_rt}}{(d-1)^2(d+1)} + \frac{d^2-4d+1}{(d-1)^2d^2}\right) \\
&+ 8D_rD_v\left[\frac{-d^2D_r^2 - 4d\gamma_vD_r + dD_r^2 - \gamma_v^2 + \gamma_vD_r}{8d^2\gamma_v^2D_r^2((d-1)D_r+\gamma_v)^2} + \frac{t}{4d\gamma_vD_r((d-1)D_r+\gamma_v)}\right] \\
&+ \frac{8D_rD_ve^{-2dD_rt}}{8d^2D_r^2(dD_r-\gamma_v)((d+1)D_r-\gamma_v)} \\
&- 8D_rD_v\frac{e^{-((d-1)D_r+\gamma_v)t}}{((d+1)D_r-\gamma_v)((d-1)D_r-\gamma_v)((d-1)D_r+\gamma_v)^2} \\
&+ 8D_rD_v\frac{e^{-2\gamma_vt}}{8\gamma_v^2(dD_r-\gamma_v)((d-1)D_r-\gamma_v)}
\end{aligned}
$$

$$\begin{aligned}
&+ 4D_v\left[\frac{D_r+\gamma_v}{4d\gamma_v D_r(dD_r+\gamma_v)((d-1)D_r+\gamma_v)} - \frac{(d-1)e^{-(2dD_r+2\gamma_v)t}}{4d\gamma_v(dD_r+\gamma_v)((d+1)D_r+\gamma_v)}\right]\\
&+ 4D_v\frac{((d-1)D_r-\gamma_v)e^{-2dD_rt}}{4d\gamma_v D_r(dD_r-\gamma_v)((d+1)D_r-\gamma_v)}\\
&+ 4D_v\left[\frac{((3-d)D_r+\gamma_v)e^{-((d-1)D_r+\gamma_v)t}}{((d+1)^2D_r^2-\gamma_v^2)((d-1)^2D_r^2-\gamma_v^2)} - \frac{e^{-2\gamma_v t}}{4d\gamma_v(dD_r-\gamma_v)((d-1)D_r-\gamma_v)}\right]\\
&+ \frac{2v_0\mu F_0}{(d-1)D_r}(1-e^{-(d-1)D_rt})t + \mu^2F_0^2t^2.
\end{aligned} \tag{3.44}$$

The parallel component of the displacement fluctuation $\langle \delta r_\parallel^2\rangle = \langle r_\parallel^2\rangle - \langle r_\parallel\rangle^2$ is,

$$\begin{aligned}
&\langle \delta r_\parallel^2\rangle = 2\left(D + \frac{v_0^2}{(d-1)dD_r}\right)t\\
&+ \frac{v_0^2}{D_r^2}\left(\frac{(d-1)e^{-2dD_rt}}{d^2(d+1)} + \frac{8e^{-(d-1)D_rt}}{(d-1)^2(d+1)} - \frac{e^{-2(d-1)D_rt}}{(d-1)^2} - \frac{4d-1}{(d-1)^2d^2}\right)\\
&+ 8D_rD_v\left[\frac{-d^2D_r^2-4d\gamma_vD_r+dD_r^2-\gamma_v^2+\gamma_vD_r}{8d^2\gamma_v^2D_r^2((d-1)D_r+\gamma_v)} + \frac{t}{4d\gamma_vD_r((d-1)D_r+\gamma_v)}\right]\\
&+ \frac{8D_rD_ve^{-2dD_rt}}{8d^2D_r^2(dD_r-\gamma_v)((d+1)D_r-\gamma_v)}\\
&- 8D_rD_v\frac{e^{-((d-1)D_r+\gamma_v)t}}{((d+1)D_r-\gamma_v)((d-1)D_r-\gamma_v)((d-1)D_r+\gamma_v)^2}\\
&+ 8D_rD_v\frac{e^{-2\gamma_vt}}{8\gamma_v^2(dD_r-\gamma_v)((d-1)D_r-\gamma_v)}\\
&+ 4D_v\left[\frac{D_r+\gamma_v}{4d\gamma_v D_r(dD_r+\gamma_v)((d-1)D_r+\gamma_v)} - \frac{(d-1)e^{-(2dD_r+2\gamma_v)t}}{4d\gamma_v(dD_r+\gamma_v)((d+1)D_r+\gamma_v)}\right]\\
&+ 4D_v\frac{((d-1)D_r-\gamma_v)e^{-2dD_rt}}{4d\gamma_v D_r(dD_r-\gamma_v)((d+1)D_r-\gamma_v)}\\
&+ 4D_v\left[\frac{((3-d)D_r+\gamma_v)e^{-((d-1)D_r+\gamma_v)t}}{((d+1)^2D_r^2-\gamma_v^2)((d-1)^2D_r^2-\gamma_v^2)} - \frac{e^{-2\gamma_v t}}{4d\gamma_v(dD_r-\gamma_v)((d-1)D_r-\gamma_v)}\right],
\end{aligned} \tag{3.45}$$

independent of the external force $\boldsymbol{F}_0$.

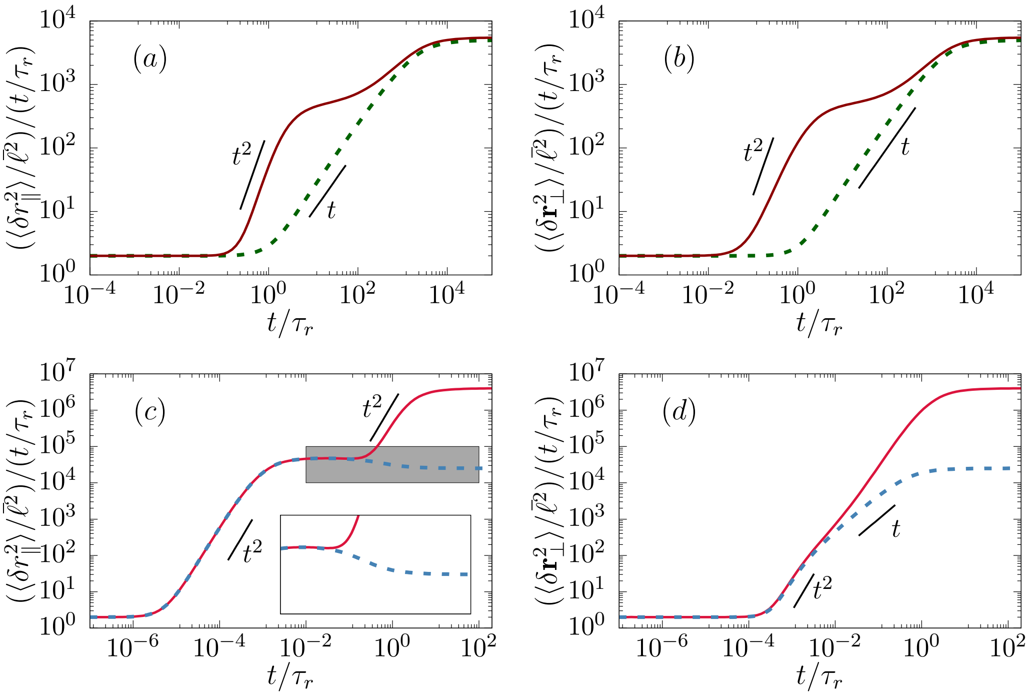

Figure 3.9: (color online) Components of displacement fluctuation, (a, c) $\langle \delta r_{\parallel}^2\rangle$ and (b, d) $\langle \delta \mathbf{r}_{\perp}^2\rangle$ as a function of time t in 2d. (a, b) $\tilde{\gamma_v} = \gamma_v \tau_r = 5 \times 10^{-4}$, $\tilde{D_v} = D_v \tau_r/\bar{v}^2 = 2.5$ with $Pe = v_0/\bar{v} = 22.36$ (solid line), 1.12 (dashed line). (c, d) $\tilde{\gamma_v} = \gamma_v \tau_r = 2 \times 10^3$, $\tilde{D_v} = D_v \tau_r/\bar{v}^2 = 10^{11}$ with $Pe = v_0/\bar{v} = 2 \times 10^3$ (solid line), 10 (dashed line). The inset in Figure (c) (zoomed in view of the shaded region in main figure) shows a sub-diffusive behavior in the parallel component of displacement fluctuation over an intermediate time regime.

Perpendicular component

The fluctuation in the perpendicular component $\langle \delta \mathbf{r}_{\perp}^2\rangle = \langle \delta \mathbf{r}^2\rangle - \langle \delta r_{\parallel}^2\rangle$. This implies,

$$\begin{aligned}
\langle \delta \mathbf{r}_{\perp}^2\rangle &= 2(d-1)\left(D + \frac{v_0^2}{(d-1)dD_r}\right)t \\
&+ \frac{v_0^2}{D_r^2}\left(\frac{4e^{-(d-1)D_r t}}{d^2-1} - \frac{(d-1)e^{-2dD_r t}}{d^2(d+1)} - \frac{3d-1}{d^2(d-1)}\right) \\
&+ \frac{2D_v}{\gamma_v(\gamma_v+(d-1)D_r)}\left[t - \frac{1-e^{-(\gamma_v+(d-1)D_r)t}}{(\gamma_v+(d-1)D_r)} - \frac{1-e^{-2\gamma_v t}}{2\gamma_v} + \frac{e^{-2\gamma_v t} - e^{-(d-1)D_r t}}{((d-1)D_r-\gamma_v)}\right] \\
&- 8D_r D_v\left[\frac{-d^2D_r^2 - 4d\gamma_v D_r + dD_r^2 - \gamma_v^2 + \gamma_v D_r}{8d^2\gamma_v^2 D_r^2((d-1)D_r+\gamma_v)} + \frac{t}{4d\gamma_v D_r((d-1)D_r+\gamma_v)}\right]
\end{aligned}$$

$$
\begin{aligned}
&- \frac{8D_rD_v e^{-2dD_rt}}{8d^2D_r^2(dD_r-\gamma_v)((d+1)D_r-\gamma_v)} \\
&+ 8D_rD_v \frac{e^{-((d-1)D_r+\gamma_v)t}}{((d+1)D_r-\gamma_v)((d-1)D_r-\gamma_v)((d-1)D_r+\gamma_v)^2} \\
&- 8D_rD_v \frac{e^{-2\gamma_v t}}{8\gamma_v^2(dD_r-\gamma_v)((d-1)D_r-\gamma_v)} \\
&- 4D_v \left[\frac{D_r+\gamma_v}{4d\gamma_vD_r(dD_r+\gamma_v)((d-1)D_r+\gamma_v)} - \frac{(d-1)e^{-(2dD_r+2\gamma_v)t}}{4d\gamma_v(dD_r+\gamma_v)((d+1)D_r+\gamma_v)} \right] \\
&- 4D_v \frac{((d-1)D_r-\gamma_v)e^{-2dD_rt}}{4d\gamma_vD_r(dD_r-\gamma_v)((d+1)D_r-\gamma_v)} \\
&- 4D_v \left[\frac{((3-d)D_r+\gamma_v)e^{-((d-1)D_r+\gamma_v)t}}{((d+1)^2D_r^2-\gamma_v^2)((d-1)^2D_r^2-\gamma_v^2)} - \frac{e^{-2\gamma_v t}}{4d\gamma_v(dD_r-\gamma_v)((d-1)D_r-\gamma_v)} \right]
\end{aligned}
\tag{3.46}
$$

In Fig. (3.9) we show various possible features of $\langle \delta r_{\parallel}^2 \rangle$ and $\langle \delta \mathbf{r}_{\perp}^2 \rangle$ at different parameter regimes.

3.7 Fourth order moments and kurtosis

In this section, we calculate the fourth-order moments of speed and displacement analytically. For speed, the fourth-order moment is consistent with its Gaussian process. We compare the analytic predictions of the fourth-order moment of displacement with simulation results. We further compute the kurtosis of displacement to capture the deviations of the ABP dynamics from Gaussian processes.

3.7.1 Fourth moment of speed

We consider the initial active speed of the particle to be $v_1 = Pe\bar{v}$ and the initial position at the origin. In the similar procedure of calculation of lower-order moments, using Eq. (3.5), we get,

$$
\langle v^4 \rangle_s = \frac{1}{s+4\gamma_v} \left[v_0^4 + 12D_v\langle v^2 \rangle_s + 4\gamma_v v_0 \langle v^3 \rangle_s \right],
$$

where, $\langle v^2\rangle_s = v_0^2/s + 2D_v/s(s+2\gamma_v)$, $\langle v^3\rangle_s = v_0^3/s + 6D_v v_0/s(s+2\gamma_v)$. Finally, fourth order moment of speed in Laplace space,

$$\langle v^4\rangle_s = \frac{v_0^4}{s} + \frac{12D_v v_0^2}{s(s+2\gamma_v)} + \frac{24D_v^2}{s(s+2\gamma_v)(s+4\gamma_v)}.$$

Inverese Laplace transform leads to

$$\langle v^4\rangle = v_0^4 + \frac{6D_v(\gamma_v v_0^2 + D_v)}{\gamma_v^2}\left(1-e^{-2\gamma_v t}\right) - \frac{3D_v^2}{\gamma_v^2}\left(1-e^{-4\gamma_v t}\right).$$

Writing $v = \delta v + \langle v\rangle$, Wick's theorem for a Gaussian process predicts $\langle v^4\rangle = \langle v\rangle^4 + 6\langle v\rangle^2\langle\delta v^2\rangle + 3\langle\delta v^2\rangle^2$. The above expression agrees with this behavior.

3.7.2 Fourth moment of displacement

As before, using Eq. (3.5), we get

$$\langle \mathbf{r}^4\rangle_s = \frac{1}{s}\left[4(d+2)D\langle\mathbf{r}^2\rangle_s + 4\langle v(\hat{\boldsymbol{u}}\cdot\mathbf{r})\mathbf{r}^2\rangle_s + 4\mu\langle(\boldsymbol{F}\cdot\mathbf{r})\mathbf{r}^2\rangle_s\right], \tag{3.47}$$

where $\langle\mathbf{r}^2\rangle_s$ was already calculated,

$$\langle v(\hat{\boldsymbol{u}}\cdot\mathbf{r})\mathbf{r}^2\rangle_s = \frac{1}{s+(d-1)D_r+\gamma_v}\left[2(2+d)D\langle v\hat{\boldsymbol{u}}\cdot\mathbf{r}\rangle_s + \langle v^2\mathbf{r}^2\rangle_s + 2\langle v^2(\hat{\boldsymbol{u}}\cdot\mathbf{r})^2\rangle_s\right.$$
$$\left.+\gamma_v v_0\langle(\hat{\boldsymbol{u}}\cdot\mathbf{r})\mathbf{r}^2\rangle_s + \mu\langle v(\boldsymbol{F}\cdot\hat{\boldsymbol{u}})\mathbf{r}^2\rangle_s + 2\mu\langle v(\boldsymbol{F}\cdot\mathbf{r})(\hat{\boldsymbol{u}}\cdot\mathbf{r})\rangle_s\right],$$

and,

$$\langle v\hat{\boldsymbol{u}}\cdot\mathbf{r}\rangle_s = \frac{1}{s+(d-1)D_r+\gamma_v}\left[\langle v^2\rangle_s + \gamma_v v_0\langle\hat{\boldsymbol{u}}\cdot\mathbf{r}\rangle_s + \mu\langle v\boldsymbol{F}\cdot\hat{\boldsymbol{u}}\rangle_s\right],$$
$$\langle v^2\mathbf{r}^2\rangle_s = \frac{1}{s+2\gamma_v}\left[2dD\langle v^2\rangle_s + 2\langle v^3\hat{\boldsymbol{u}}\cdot\mathbf{r}\rangle_s + 2D_v\langle\mathbf{r}^2\rangle_s + 2\gamma_v v_0\langle v\mathbf{r}^2\rangle_s + 2\mu\langle v^2\boldsymbol{F}\cdot\mathbf{r}\rangle_s\right],$$
$$\langle v^2(\hat{\boldsymbol{u}}\cdot\mathbf{r})^2\rangle_s = \frac{1}{s+2dD_r+2\gamma_v}\left[2D\langle v^2\rangle_s + 2D_r\langle v^2\mathbf{r}^2\rangle_s + 2D_v\langle(\hat{\boldsymbol{u}}\cdot\mathbf{r})^2\rangle_s + 2\langle v^3\hat{\boldsymbol{u}}\cdot\mathbf{r}\rangle_s\right.$$
$$\left.+2\gamma_v v_0\langle v(\hat{\boldsymbol{u}}\cdot\mathbf{r})^2\rangle_s + 2\mu\langle v^2(\boldsymbol{F}\cdot\hat{\boldsymbol{u}})(\hat{\boldsymbol{u}}\cdot\mathbf{r})\rangle_s\right],$$

$$\langle(\hat{\boldsymbol{u}}\cdot\mathbf{r})\mathbf{r}^2\rangle_s = \frac{1}{s+(d-1)D_r}\Big[2(2+d)D\langle\hat{\boldsymbol{u}}\cdot\mathbf{r}\rangle_s + \langle v\mathbf{r}^2\rangle_s + 2\langle v(\hat{\boldsymbol{u}}\cdot\mathbf{r})^2\rangle_s$$

$$+\mu\langle(\boldsymbol{F}\cdot\hat{\boldsymbol{u}})\mathbf{r}^2\rangle_s + 2\mu\langle(\boldsymbol{F}\cdot\mathbf{r})(\hat{\boldsymbol{u}}\cdot\mathbf{r})\rangle_s\Big],$$

We list all the required quantities in the following,

$$\langle v^2\rangle_s = \frac{v_0^2}{s} + \frac{2D_v}{s(s+2\gamma_v)},$$

$$\langle v^3\rangle_s = \frac{v_0^3}{s} + \frac{6D_v v_0}{s(s+2\gamma_v)},$$

$$\langle v^4\rangle_s = \frac{v_0^4}{s} + \frac{12D_v v_0^2}{s(s+2\gamma_v)} + \frac{24D_v^2}{s(s+2\gamma_v)(s+4\gamma_v)},$$

$$\langle\hat{\boldsymbol{u}}\cdot\mathbf{r}\rangle_s = \frac{1}{(s+(d-1)D_r)}\left[v_0\langle 1\rangle_s + \mu\langle\boldsymbol{F}\cdot\hat{\boldsymbol{u}}\rangle_s\right],$$

$$\langle(\hat{\boldsymbol{u}}\cdot\mathbf{r})^2\rangle_s = \frac{1}{s+2dD_r}\Big[2D\langle 1\rangle_s + 2D_r\langle\mathbf{r}^2\rangle_s + 2\langle v\hat{\boldsymbol{u}}\cdot\mathbf{r}\rangle_s + 2\mu\langle(\boldsymbol{F}\cdot\hat{\boldsymbol{u}})(\hat{\boldsymbol{u}}\cdot\mathbf{r})\rangle_s\Big],$$

$$\langle v^2\hat{\boldsymbol{u}}\cdot\mathbf{r}\rangle_s = \frac{1}{s+(d-1)D_r+2\gamma_v}\Big[2D_v\langle\hat{\boldsymbol{u}}\cdot\mathbf{r}\rangle_s + \langle v^3\rangle_s + 2\gamma_v v_0\langle v\hat{\boldsymbol{u}}\cdot\mathbf{r}\rangle_s$$

$$+2\mu\langle v^2\boldsymbol{F}\cdot\hat{\boldsymbol{u}}\rangle_s\Big],$$

$$\langle v^3\hat{\boldsymbol{u}}\cdot\mathbf{r}\rangle_s = \frac{1}{s+(d-1)D_r+3\gamma_v}\Big[6D_v\langle v(\hat{\boldsymbol{u}}\cdot\mathbf{r})\rangle_s + \langle v^4\rangle_s + 3\gamma_v v_0\langle v^2\hat{\boldsymbol{u}}\cdot\mathbf{r}\rangle_s$$

$$+2\mu\langle v^3\boldsymbol{F}\cdot\hat{\boldsymbol{u}}\rangle_s\Big],$$

$$\langle v\mathbf{r}^2\rangle_s = \frac{1}{s+\gamma_v}\Big[2dD\langle v\rangle_s + 2\langle v^2\hat{\boldsymbol{u}}\cdot\mathbf{r}\rangle_s + \gamma_v v_0\langle\mathbf{r}^2\rangle_s + 2\mu\langle v\boldsymbol{F}\cdot\mathbf{r}\rangle_s\Big],$$

$$\langle v(\hat{\boldsymbol{u}}\cdot\mathbf{r})^2\rangle_s = \frac{1}{s+2dD_r+\gamma_v}\Big[2D\langle v\rangle_s + 2D_r\langle v\mathbf{r}^2\rangle_s + 2\langle v^2\hat{\boldsymbol{u}}\cdot\mathbf{r}\rangle_s + \gamma_v v_0\langle(\hat{\boldsymbol{u}}\cdot\mathbf{r})^2\rangle_s$$

$$+2\mu\langle v(\boldsymbol{F}\cdot\hat{\boldsymbol{u}})(\hat{\boldsymbol{u}}\cdot\mathbf{r})\rangle_s\Big],$$

and,

$$\langle\boldsymbol{F}\cdot\hat{\boldsymbol{u}}\rangle_s = \frac{\boldsymbol{F}_0\cdot\hat{\boldsymbol{u}}_0}{s+(d-1)D_r} \quad , \quad \langle(\boldsymbol{F}\cdot\hat{\boldsymbol{u}})^2\rangle_s = \frac{(\boldsymbol{F}_0\cdot\hat{\boldsymbol{u}}_0)^2}{s+2dD_r}$$

$$\langle v\boldsymbol{F}\cdot\hat{\boldsymbol{u}}\rangle_s = \frac{v_0\boldsymbol{F}_0\cdot\hat{\boldsymbol{u}}_0}{s+(d-1)D_r},$$

$$\langle v^2\boldsymbol{F}\cdot\hat{\boldsymbol{u}}\rangle_s = \frac{v_0^2\boldsymbol{F}_0\cdot\hat{\boldsymbol{u}}_0}{s+(d-1)D_r} + \frac{2D_v\boldsymbol{F}_0\cdot\hat{\boldsymbol{u}}_0}{(s+(d-1)D_r)(s+(d-1)D_r+2\gamma_v)},$$

$$
\begin{aligned}
&\langle v^3 \boldsymbol{F}\cdot\hat{\boldsymbol{u}}\rangle_s = \frac{v_0^3 \boldsymbol{F}_0\cdot\hat{\boldsymbol{u}}_0}{s+(d-1)D_r} + \frac{6D_v v_0 \boldsymbol{F}_0\cdot\hat{\boldsymbol{u}}_0}{(s+(d-1)D_r)(s+(d-1)D_r+3\gamma_v)},\\
&\langle (\boldsymbol{F}\cdot\hat{\boldsymbol{u}})(\hat{\boldsymbol{u}}\cdot\mathbf{r})\rangle_s = \frac{1}{s+2dD_r}\left[2D_r\langle \boldsymbol{F}\cdot\mathbf{r}\rangle_s + \langle v(\boldsymbol{F}\cdot\hat{\boldsymbol{u}})\rangle_s + \mu\langle(\boldsymbol{F}\cdot\hat{\boldsymbol{u}})^2\rangle_s\right],\\
&\langle \boldsymbol{F}\cdot\mathbf{r}\rangle_s = \frac{1}{s}\left[\langle v\boldsymbol{F}\cdot\hat{\boldsymbol{u}}\rangle_s + \mu\boldsymbol{F}_0^2/s\right],\\
&\langle v\boldsymbol{F}\cdot\mathbf{r}\rangle_s = \frac{1}{s+\gamma_v}\left[\langle v^2\boldsymbol{F}\cdot\hat{\boldsymbol{u}}\rangle_s + \gamma_v v_0\langle \boldsymbol{F}\cdot\mathbf{r}\rangle_s + \mu\boldsymbol{F}_0^2\langle v\rangle_s\right],\\
&\langle v^2\boldsymbol{F}\cdot\mathbf{r}\rangle_s = \frac{1}{s+2\gamma_v}\left[\langle v^3\boldsymbol{F}\cdot\hat{\boldsymbol{u}}\rangle_s + 2\gamma_v v_0\langle v\boldsymbol{F}\cdot\mathbf{r}\rangle_s + \mu\boldsymbol{F}_0^2\langle v^2\rangle_s\right],\\
&\langle (\boldsymbol{F}\cdot\mathbf{r})(\hat{\boldsymbol{u}}\cdot\mathbf{r})\rangle_s = \frac{1}{s+(d-1)D_r}[2D\langle \boldsymbol{F}\cdot\hat{\boldsymbol{u}}\rangle_s + \langle v(\boldsymbol{F}\cdot\hat{\boldsymbol{u}})(\hat{\boldsymbol{u}}\cdot\mathbf{r})\rangle_s\\
&+\langle v\boldsymbol{F}\cdot\mathbf{r}\rangle_s + \mu\langle(\boldsymbol{F}\cdot\mathbf{r})(\boldsymbol{F}\cdot\hat{\boldsymbol{u}})\rangle_s + \mu\boldsymbol{F}_0^2\langle\hat{\boldsymbol{u}}\cdot\mathbf{r}\rangle_s],\\
&\langle v(\boldsymbol{F}\cdot\hat{\boldsymbol{u}})^2\rangle_s = \frac{1}{s+2dD_r+\gamma_v}\left[2D_r\boldsymbol{F}_0^2\langle v\rangle_s + v_0(\boldsymbol{F}_0\cdot\hat{\boldsymbol{u}}_0)^2 + \gamma_v v_0\langle(\boldsymbol{F}\cdot\hat{\boldsymbol{u}})^2\rangle_s\right],\\
&\langle v^2(\boldsymbol{F}\cdot\hat{\boldsymbol{u}})^2\rangle_s = \frac{1}{s+2dD_r+2\gamma_v}\left[2D_r\boldsymbol{F}_0^2\langle v^2\rangle_s + v_0^2(\boldsymbol{F}_0\cdot\hat{\boldsymbol{u}}_0)^2 + 2D_v\langle(\boldsymbol{F}\cdot\hat{\boldsymbol{u}})^2\rangle_s\right.\\
&\left.+2\gamma_v v_0\langle v(\boldsymbol{F}\cdot\hat{\boldsymbol{u}})^2\rangle_s\right],\\
&\langle v(\boldsymbol{F}\cdot\hat{\boldsymbol{u}})(\hat{\boldsymbol{u}}\cdot\mathbf{r})\rangle_s = \frac{1}{s+2dD_r+\gamma_v}\left[2D_r\langle v\boldsymbol{F}\cdot\mathbf{r}\rangle_s + \langle v^2\boldsymbol{F}\cdot\hat{\boldsymbol{u}}\rangle_s\right.\\
&\left.+\gamma_v v_0\langle(\boldsymbol{F}\cdot\hat{\boldsymbol{u}})(\hat{\boldsymbol{u}}\cdot\mathbf{r})\rangle_s + \mu\langle v(\boldsymbol{F}\cdot\hat{\boldsymbol{u}})^2\rangle_s\right],\\
&\langle v^2(\boldsymbol{F}\cdot\hat{\boldsymbol{u}})(\hat{\boldsymbol{u}}\cdot\mathbf{r})\rangle_s = \frac{1}{s+2dD_r+2\gamma_v}\left[2D_r\langle v^2\boldsymbol{F}\cdot\mathbf{r}\rangle_s + 2D_v\langle(\boldsymbol{F}\cdot\hat{\boldsymbol{u}})(\hat{\boldsymbol{u}}\cdot\mathbf{r})\rangle_s\right.\\
&\left.+\langle v^3\boldsymbol{F}\cdot\hat{\boldsymbol{u}}\rangle_s + 2\gamma_v v_0\langle v(\boldsymbol{F}\cdot\hat{\boldsymbol{u}})(\hat{\boldsymbol{u}}\cdot\mathbf{r})\rangle_s + \mu\langle v^2(\boldsymbol{F}\cdot\hat{\boldsymbol{u}})^2\rangle_s\right],\\
&\langle(\boldsymbol{F}\cdot\hat{\boldsymbol{u}})\mathbf{r}^2\rangle_s = \frac{1}{s+(d-1)D_r}[2dD\langle\boldsymbol{F}\cdot\hat{\boldsymbol{u}}\rangle_s + 2\langle v(\boldsymbol{F}\cdot\hat{\boldsymbol{u}})(\hat{\boldsymbol{u}}\cdot\mathbf{r})\rangle_s\\
&+2\mu\langle(\boldsymbol{F}\cdot\mathbf{r})(\boldsymbol{F}\cdot\hat{\boldsymbol{u}})\rangle_s],\\
&\langle v(\boldsymbol{F}\cdot\hat{\boldsymbol{u}})\mathbf{r}^2\rangle_s = \frac{1}{s+(d-1)D_r+\gamma_v}\left[2dD\langle v\boldsymbol{F}\cdot\hat{\boldsymbol{u}}\rangle_s + 2\langle v^2(\boldsymbol{F}\cdot\hat{\boldsymbol{u}})(\hat{\boldsymbol{u}}\cdot\mathbf{r})\rangle_s\right.\\
&\left.+\gamma_v v_0\langle(\boldsymbol{F}\cdot\hat{\boldsymbol{u}})\mathbf{r}^2\rangle_s + 2\mu\langle v(\boldsymbol{F}\cdot\mathbf{r})(\boldsymbol{F}\cdot\hat{\boldsymbol{u}})\rangle_s\right],\\
&\langle(\boldsymbol{F}\cdot\mathbf{r})(\boldsymbol{F}\cdot\hat{\boldsymbol{u}})\rangle_s = \frac{1}{s+(d-1)D_r}\left[\langle v(\boldsymbol{F}\cdot\hat{\boldsymbol{u}})^2\rangle_s + \mu\boldsymbol{F}_0^2\langle(\boldsymbol{F}\cdot\hat{\boldsymbol{u}})\rangle_s\right],\\
&\langle v(\boldsymbol{F}\cdot\mathbf{r})(\boldsymbol{F}\cdot\hat{\boldsymbol{u}})\rangle_s = \frac{1}{s+(d-1)D_r+\gamma_v}\left[\langle v^2(\boldsymbol{F}\cdot\hat{\boldsymbol{u}})^2\rangle_s + \gamma_v v_0\langle(\boldsymbol{F}\cdot\mathbf{r})(\boldsymbol{F}\cdot\hat{\boldsymbol{u}})\rangle_s\right.\\
&\left.+\mu\boldsymbol{F}_0^2\langle v\boldsymbol{F}\cdot\hat{\boldsymbol{u}}\rangle_s\right],
\end{aligned}
$$

$$\langle v(\boldsymbol{F}\cdot\mathbf{r})(\hat{\boldsymbol{u}}\cdot\mathbf{r})\rangle_s = \frac{1}{s+(d-1)D_r+\gamma_v}\left[2D\langle v\boldsymbol{F}\cdot\hat{\boldsymbol{u}}\rangle_s + \langle v^2(\boldsymbol{F}\cdot\hat{\boldsymbol{u}})(\hat{\boldsymbol{u}}\cdot\mathbf{r})\rangle_s\right.$$
$$\left. + \langle v^2\boldsymbol{F}\cdot\mathbf{r}\rangle_s + \gamma_v v_0\langle(\boldsymbol{F}\cdot\mathbf{r})(\hat{\boldsymbol{u}}\cdot\mathbf{r})\rangle_s + \mu\langle v(\boldsymbol{F}\cdot\mathbf{r})(\boldsymbol{F}\cdot\hat{\boldsymbol{u}})\rangle_s + \mu\boldsymbol{F}_0^2\langle v\hat{\boldsymbol{u}}\cdot\mathbf{r}\rangle_s\right],$$
$$\langle(\boldsymbol{F}\cdot\mathbf{r})^2\rangle_s = \frac{1}{s}\left[2D\boldsymbol{F}_0^2/s + 2\langle v(\boldsymbol{F}\cdot\mathbf{r})(\boldsymbol{F}\cdot\hat{\boldsymbol{u}})\rangle_s + 2\mu\boldsymbol{F}_0^2\langle\boldsymbol{F}\cdot\mathbf{r}\rangle_s\right],$$
$$\langle(\boldsymbol{F}\cdot\mathbf{r})\mathbf{r}^2\rangle_s = \frac{1}{s}\left[2(d+2)D\langle\boldsymbol{F}\cdot\mathbf{r}\rangle_s + 2\langle v(\boldsymbol{F}\cdot\mathbf{r})(\hat{\boldsymbol{u}}\cdot\mathbf{r})\rangle_s + \langle v(\boldsymbol{F}\cdot\hat{\boldsymbol{u}})\mathbf{r}^2\rangle_s\right.$$
$$\left. + 2\mu\langle(\boldsymbol{F}\cdot\mathbf{r})^2\rangle_s + \mu\boldsymbol{F}_0^2\langle\mathbf{r}^2\rangle_s\right].$$

Finally, inverse Laplace transform of Eq. (3.47) leads to $\langle\mathbf{r}^4\rangle(t)$. The final expression is too long to show here. We present the results in graphical form in Fig.(3.10), comparing against direct numerical simulations.

3.7.3 Persistent motion

Here, we calculate the small and large time limit of the fourth order moment in the absence of external force $\boldsymbol{F} = 0$. Further, we analyze the behavior of $\langle\mathbf{r}^4\rangle$ at the short and long time limits. In the short time limit, $\langle\mathbf{r}^4\rangle$ can be expanded around $t = 0$ to obtain,

$$\langle\mathbf{r}^4\rangle = 4d(d+2)D^2t^2 + 4(d+2)Dv_0^2t^3 + \left(v_0^4 - \frac{4(d+2)D}{3}\left((d-1)D_rv_0^2 - 2D_v\right)\right)t^4$$
$$+\frac{1}{3}\left[12D_vv_0^2 - 2(d-1)D_rv_0^4 + (d+2)D\left((d-1)^2D_r^2v_0^2 - 2(d-1)D_rD_v - 6D_v\gamma_v\right)\right]t^5$$
$$+\mathcal{O}(t^6), \tag{3.48}$$

shows that at smallest time $\langle\mathbf{r}^4\rangle \sim t^2$, which crosses over to $\sim t^3$ at $t_I = dD/v_0^2$. A second crossover from $\langle\mathbf{r}^4\rangle \sim t^3$ to $\sim t^4$ may appear at,

$$t_{II} = \frac{12(d+2)Dv_0^2}{3v_0^4 - 4(d+2)D((d-1)D_rv_0^2 - 2D_v)},$$

provided $v_0^4 > 4(d+2)D((d-1)D_r v_0^2 - 2D_v)/3$. In long time limit, $\langle \mathbf{r}^4 \rangle$ leads to,

$$\langle \mathbf{r}^4 \rangle \simeq \frac{4(2+d)\left[(d-1)D_r(D_v + dD\gamma_v((d-1)D_r+\gamma_v)) + \gamma_v((d-1)D_r+\gamma_v)v_0^2\right]^2 t^2}{d(d-1)^2 D_r^2 \gamma_v^2((d-1)D_r+\gamma_v)^2} \tag{3.49}$$

In Fig. (3.10)(a, b), we show $\langle \mathbf{r}^4 \rangle$ as a function of time. It shows a good agreement of analytic predictions for $\langle \mathbf{r}^4 \rangle$ with simulation results. Fig. (3.10)(a) corresponds to the limit $D_r \ll \gamma_v$ and Fig. (3.10)(b) corresponds to the limit $D_r \gg \gamma_v$.

Directed persistent motion

Here, we show the short and long time limit of the fourth order moment of displacement in the presence of an external force $\boldsymbol{F}$. In the small time limit, $\langle \mathbf{r}^4 \rangle$ gives,

$$\begin{aligned}\langle \mathbf{r}^4 \rangle &= 4d(d+2)D^2t^2 + 4(d+2)D\left[v_0^2 + 2v_0\mu(\boldsymbol{F}_0\cdot\hat{\boldsymbol{u}}_0) + \mu^2\boldsymbol{F}_0^2\right]t^3 \\ &+ \left[(v_0^2 + 2v_0\mu(\boldsymbol{F}_0\cdot\hat{\boldsymbol{u}}_0) + \mu^2\boldsymbol{F}_0^2)^2 - 4(d+2)D\left[(d-1)D_r v_0(v_0 + 3\mu(\boldsymbol{F}_0\cdot\hat{\boldsymbol{u}}_0))\right.\right. \\ &\left.\left. -2D_v\right]/3\right]t^4 + \mathcal{O}(t^5).\end{aligned} \tag{3.50}$$

This shows that at shortest times $\langle \mathbf{r}^4 \rangle \sim t^2$, which crosses over to $\sim t^3$ at

$$t_I = dD/\left[v_0^2 + 2v_0\mu(\boldsymbol{F}_0\cdot\hat{\boldsymbol{u}}_0) + \mu^2\boldsymbol{F}_0^2\right].$$

A second crossover from $\langle \mathbf{r}^4 \rangle \sim t^3$ to $\sim t^4$ may appear at,

$$\begin{aligned}t_{II} &= 12(d+2)D\left[v_0^2 + 2v_0\mu(\boldsymbol{F}_0\cdot\hat{\boldsymbol{u}}_0) + \mu^2\boldsymbol{F}_0^2\right]/\left[3(v_0^2 + 2v_0\mu(\boldsymbol{F}_0\cdot\hat{\boldsymbol{u}}_0) + \mu^2\boldsymbol{F}_0^2)^2\right. \\ &\left.-4(d+2)D\left[(d-1)D_r v_0(v_0 + 3\mu(\boldsymbol{F}_0\cdot\hat{\boldsymbol{u}}_0)) - 2D_v\right]\right].\end{aligned}$$

In the long time limit, $\langle \mathbf{r}^4 \rangle$ leads to,

$$\langle \mathbf{r}^4 \rangle \simeq \mu^4\boldsymbol{F}_0^4 t^4. \tag{3.51}$$

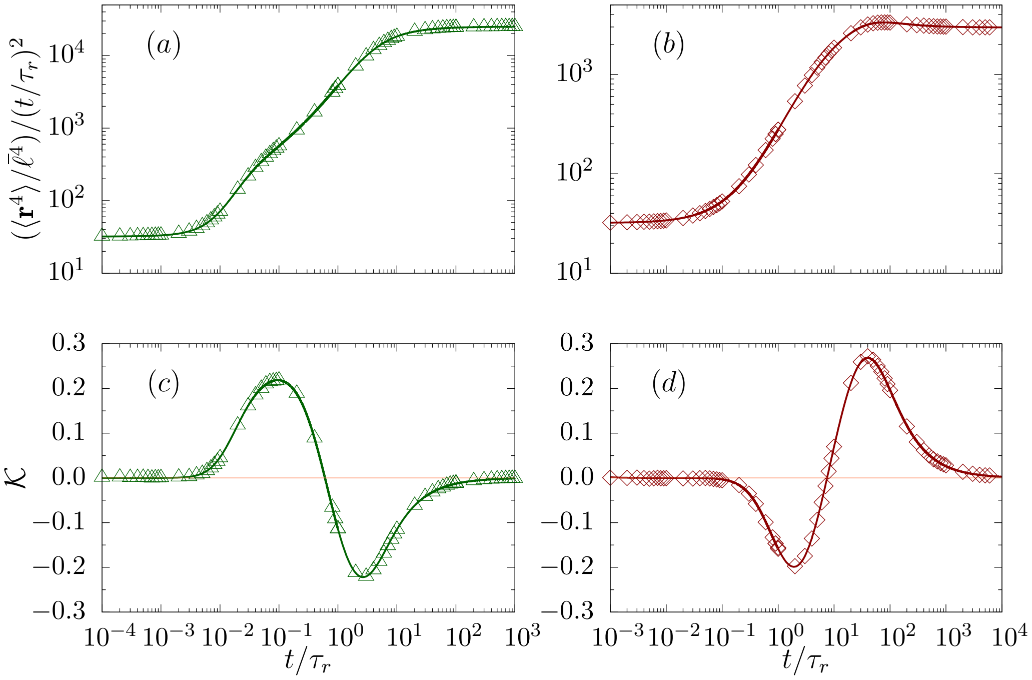

Figure 3.10: (color online) Persistent motion: Plots of $\langle \mathbf{r}^4 \rangle$ (a, b) and Kurtosis $(\mathcal{K})$ (c, d) as a function of time in two dimensions. (a, c) Parameter values used are $\tilde{\gamma_v} = \gamma_v \tau_r = 10^2$, $\tilde{D_v} = D_v \tau_r / \bar{v}^2 = 4 \times 10^4$, and $Pe = v_0/\bar{v} = 7.07$. (b, d) Parameter values used are $\tilde{\gamma_v} = \gamma_v \tau_r = 5 \times 10^{-2}$, $\tilde{D_v} = D_v \tau_r / \bar{v}^2 = 0.25$, and $Pe = v_0/\bar{v} = 3.54$. The points denote simulation results averaged over 10^6 independent trajectories. The solid lines depict analytic results obtained from the inverse Laplace transform of Eq. (3.47). The orange line in (c, d) corresponds to zero kurtosis. Initial conditions used are speed $v_1/\bar{v} = Pe$ and orientation $\hat{\boldsymbol{u}}_0 = \hat{x}$.

In Fig. (3.11)(a), we show $\langle \mathbf{r}^4 \rangle$ as a function of time.

3.7.4 Kurtosis: deviation from Gaussian process

For a Gaussian process with non zero mean, the definition of the fourth-order moment of displacement is,

$$\mu_4 := \langle \mathbf{r}^2 \rangle^2 + \frac{2}{d} \left(\langle \mathbf{r}^2 \rangle^2 - \langle \mathbf{r} \rangle^4 \right). \tag{3.52}$$

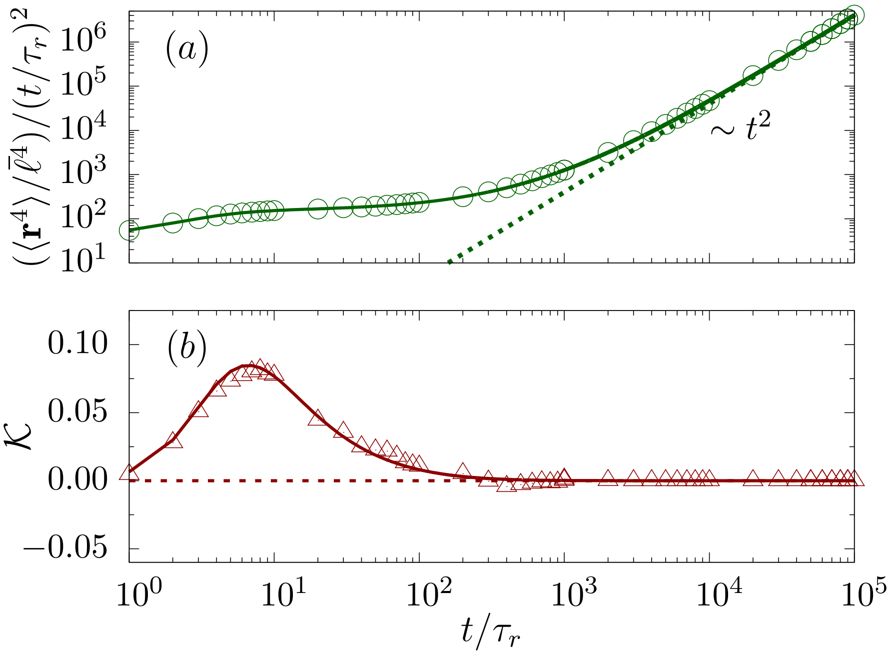

Figure 3.11: (color online) Directed persistent motion: (a) $\langle \mathbf{r}^4\rangle$ and (b) Kurtosis $\mathcal{K}$ as a function of time in 2d at $\tilde{\gamma_v} = \gamma_v\tau_r = 0.5$, $\tilde{D_v} = D_v\tau_r/\bar{v}^2 = 1$, $Pe = v_0/\bar{v} = 1$, and $\tilde{\boldsymbol{F}}_0 = \mu\boldsymbol{F}_0/\bar{v} = 0.01\ \hat{r}$. The solid line in (a) and (b) correspond to the inverse Laplace transform of Eq. (3.47). The dashed line in (a) corresponds to the long-time scaling in Eq. (3.51). The dashed line in (b) is corresponds to $\mathcal{K} = 0$. The initial conditions used are the speed $v_1/\bar{v} = Pe$ and the heading direction $\hat{\boldsymbol{u}}_0 = \hat{x}$.

Thus, deviations from such a Gaussian process is captured by the kurtosis

$$\mathcal{K} = \frac{\langle \mathbf{r}^4\rangle}{\mu_4} - 1. \tag{3.53}$$

Persistent motion

Fig. (3.10)(c,d) shows the kurtosis as a function of time in the absence of external force. A non zero value of the kurtosis indicates deviations of the stochastic process from a possible Gaussian nature. A positive value corresponds to distributions with tails longer than normal distributions, while a negative value corresponds to tail less extreme than the normal distributions. Fig. (3.10)(c) corresponds to $\langle \mathbf{r}^4\rangle$ in Fig. (3.10)(a) in the limit of $D_r \gg \gamma_v$. It shows deviations to positive values at shorter time scales and negative values at longer times. The plot of kurtosis

Fig. (3.10)(d) is corresponding to $\langle \mathbf{r}^4 \rangle$ in Fig. (3.10)(b) in the limit of $D_r \ll \gamma_v$. In contrast to Fig. (3.10)(c), in this parameter regime, the kurtosis shows deviations to negative values at short time that gets into positive values at longer times before returning to Gaussian nature at the longest time scales. As it has been shown in the previous chapter, the orientational fluctuations of the heading direction leads to negative kurtosis in the intermediate times. The positive kurtosis observed here is determined by the speed fluctuation time-scale. In Fig. (3.10)(c) with $\tilde{\gamma_v} \gg 1$ the orientational fluctuation time-scale is longer than the speed fluctuation time-scale. As a result the negative kurtosis appears at a later time and the positive kurtosis at a shorter time. On the other hand, in Fig. (3.10)(c) due to $\tilde{\gamma_v} \ll 1$, the shorter orientational fluctuation time-scale leads to the negative kurtosis at shorter time and positive kurtosis at longer times.

Directed persistent motion

In the presence of a constant external force, we show the behavior of the fourth order moment $\langle \mathbf{r}^4 \rangle$ and kurtosis $\mathcal{K}$ as a function of time in Fig. (3.11). In the figure the points denote simulation results, and the lines depict analytic expressions. In the long time limit, $\langle \mathbf{r}^4 \rangle \sim t^4$, $\langle \mathbf{r} \rangle \sim t$ and $\langle \mathbf{r}^2 \rangle \sim t^2$, thus utilizing Eq. (3.52) and (3.53) one obtains $\mathcal{K} = 0$, as is shown in Fig. (3.11)(b).

3.8 Conclusions

We have studied the dynamics of active Brownian particles with speed fluctuations, in the presence and absence of external directed force. In our model, two independent time scales describe the stochastic change of heading direction and speed. Here we considered the active speed generation using a simple energy pump implemented via an Ornstein-Uhlenbeck process. We have extended the Fokker-Planck equation based method developed in the previous chapter to calculate all the relevant dynamical moments of motion in arbitrary dimensions. To summarize the main results:

1. We calculated the mean-squared displacement $\langle \mathbf{r}^2 \rangle$ starting from the Fokker-Planck approach. We showed how the result can also be derived using the formal solutions of Langevin equations utilizing the auto-correlation function of active speed. Instead, if one uses a time-scale separation assuming a faster relaxation for the active speed utilizing the steady-state limit of this speed correlation function, our results reduce to earlier results obtained in 2d [101, 108]. Moreover, we have calculated the fluctuations of displacement vector, its components along and perpendicular to the initial heading orientation, the fourth moment of the displacement vector, and its kurtosis.
2. We have identified several crossovers in the moments and fluctuations of displacement vectors and analyzed the crossover time-scales using our expressions. The number of crossovers depend on parameter values used and the presence or absence of the external directed force.
3. We have calculated the kurtosis of displacement vector to show the deviations from Gaussian process in intermediate times. For persistent motion, the kurtosis deviates towards a positive value when the speed fluctuation dominates over the orientation fluctuation and a negative value when the orientation fluctuation dominates over the speed fluctuation. Thus, kurtosis show opposite behavior in the limit of $\gamma_v \tau_r \ll 1$ and $\gamma_v \tau_r \gg 1$. In the absence of speed fluctuation, the kurtosis deviates towards the negative values at intermediate times as we showed in Chapter 2.

In this chapter, the stochastic Schienbein-Gruler type mechanism of active speed generation and the associated relaxation times played a crucial role in determining the ABP dynamics. In the following chapter we will consider a different kind of active process where the active speed is associated with an additive Gaussian noise.

3.9 Appendix

3.9.1 Autocorrelation of active speed

Here, we calculate the active speed auto-correlation function directly from the governing Langeving Eq. (3.2). The formal solution of Eq. (3.2) with the initial condition $v(t = 0) = v_1$ is

$$v(t) = v_1\, e^{-\gamma_v t} + \int_0^t \left(\gamma_v v_0 + \sqrt{2D_v}\Lambda(t')\right) e^{-\gamma_v (t-t')}\, dt', \tag{3.54}$$

with $\langle \Lambda(t) \rangle = 0$, and $\langle \Lambda(t)\Lambda(t') \rangle = \delta(t - t')$. In this expression, the integration of the second term gives,

$$I = \int_0^t \gamma_v v_0\, e^{-\gamma_v (t-t')}\, dt' = \gamma_v v_0\, e^{-\gamma_v t} \int_0^t e^{\gamma_v t'}\, dt' = v_0(1 - e^{-\gamma_v t}).$$

This allows us to calculate the instantaneous mean speed

$$\langle v(t) \rangle = v_1 e^{-\gamma_v t} + v_0 \left(1 - e^{-\gamma_v t}\right). \tag{3.55}$$

Thus, the deviation of speed from its mean value

$$\delta v(t) \equiv v(t) - \langle v(t) \rangle = \sqrt{2D_v} e^{-\gamma_v t} \int_0^t \Lambda(t') e^{\gamma_v t'}\, dt'. \tag{3.56}$$

As a result, the speed autocorrelation function of speed fluctuations can be calculated as

$$\langle \delta v(t_1) \delta v(t_2) \rangle = 2D_v e^{-\gamma_v (t_1+t_2)} \int_0^{t_1} dt_1' \int_0^{t_2} dt_2'\, e^{\gamma_v \left(t_1'+t_2'\right)} \delta(t_1' - t_2') \tag{3.57}$$

If $(t_1 > t_2)$, the $\delta(t_1' - t_2')$ restricts the integration over $t_1' = t_2'$ line, then t_1' effectively runs up to t_2.

$$\langle \delta v(t_1) \delta v(t_2) \rangle = \frac{D_v}{\gamma_v} \left[e^{-\gamma_v (t_1-t_2)} - e^{-\gamma_v (t_1+t_2)}\right] \tag{3.58}$$

The steady state correlation may be obtained by, letting $t_1, t_2 \to \infty$ and keeping $t_1 - t_2$ finite,

$$\langle \delta v(\tau) \delta v(0) \rangle = \frac{D_v}{\gamma_v} e^{-\gamma_v \tau} \tag{3.59}$$

where $\tau = t_1 - t_2$. In the steady state limit the instantaneous fluctuation, $\langle \delta v^2(0) \rangle =$

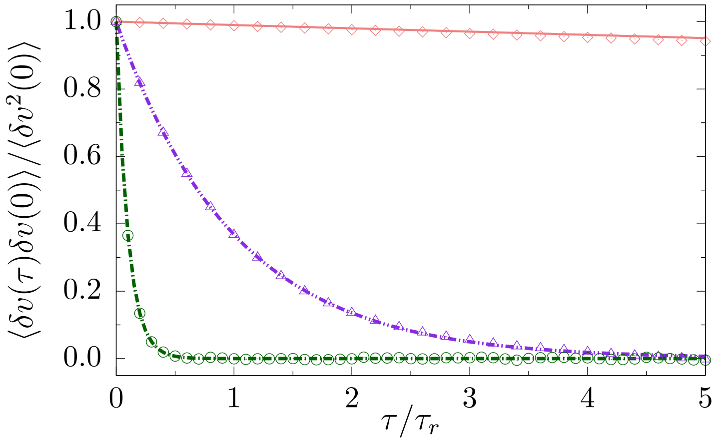

Figure 3.12: (color online) Active speed autocorrelation $\langle\delta v(\tau)\delta v(0)\rangle$ as a function of time τ at $\tilde{D_v} = D_v\tau_r/\bar{v}^2 = 1$, $Pe \equiv v_0/\bar{v} = 1$ for $\tilde{\gamma_v} = \gamma_v\tau_r = 10(\circ), 1(\triangle), 0.01(\diamond)$. The points denote simulation results and the lines correspond to the function $\exp(-\gamma_v\tau)$ calculated in Eq. (3.60). Here $\langle\delta v(\tau)\delta v(0)\rangle = \langle\delta v(\tau)\delta v(0)\rangle/\langle\delta v^2(0)\rangle$ with $\langle\delta v^2(0)\rangle = D_v/\gamma_v$.

D_v/γ_v.

Thus we may write, speed correlation in normalized form,

$$\frac{\langle\delta v(\tau)\delta v(0)\rangle}{\langle\delta v^2(0)\rangle} = e^{-\gamma_v\tau} \tag{3.60}$$

The fluctuation in the speed approach to steady state, letting $t_1 = t_2 \equiv t$,

$$\frac{\langle\delta v^2(t)\rangle}{\langle\delta v^2(0)\rangle} = \left(1 - e^{-2\gamma_v t}\right) \tag{3.61}$$

3.9.2 Steady state probability distribution of speed and its cumulative distribution

The evolution equation of probability distribution of speed $P(v,t)$ derived from the Schienbein-Gruler mechanism [101] of active speed generation as in Eq. (3.2), obeys

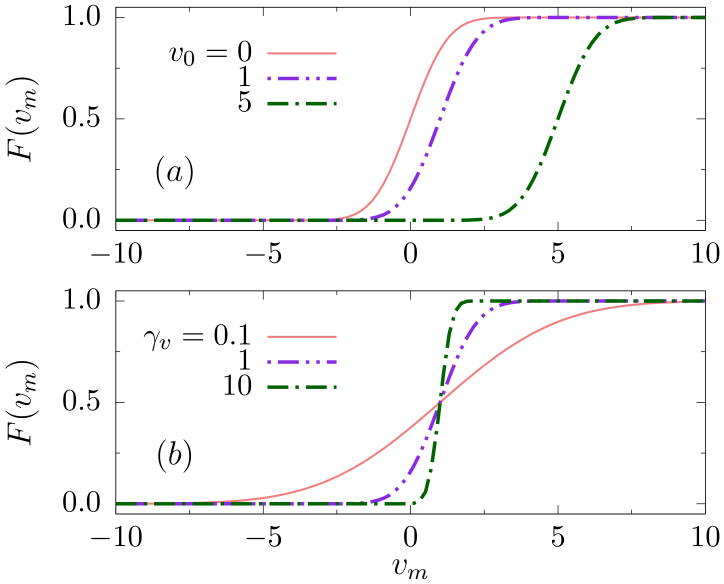

Figure 3.13: (color online) Cumulative distribution function $F(v_m)$ in Eq. (3.65) as a function of v_m at $D_v\tau_r/\bar{v}^2 = 1$. (a) $Pe = 0, 1, 5$ and $\gamma_v\tau_r = 1$. (b) $\gamma_v\tau_r = 0.1, 1, 10$ and $Pe = 1$.

the following Fokker-Planck equation

$$\partial_t P(v,t) = D_v\partial_v^2 P + \gamma_v\partial_v[(v - v_0)P]. \tag{3.62}$$

The normalized steady-state distribution calculated from Eq. (3.62) is Gaussian around the speed v_0,

$$P_s(v) = \left(\frac{\gamma_v}{2\pi D_v}\right)^{1/2} \exp\left(-\frac{\gamma_v}{2D_v}(v - v_0)^2\right) \tag{3.63}$$

In the chemo-kinetic response, the ratio of speed v_0 to the width of the distribution $\sqrt{\gamma_v/2D_v}$ is a control parameter signifying the signal-to-noise ratio [101]. The cumulative distribution function of speed up to a maximum value v_m is

$$F(v_m) = \left(\frac{\gamma_v}{2\pi D_v}\right)^{1/2} \int_{-\infty}^{v_m} dv\ \exp\left(-\frac{\gamma_v}{2D_v}(v - v_0)^2\right). \tag{3.64}$$

The cumulative distribution function can be expressed as

$$F(v_m) = \frac{1}{2}\left[1 + \text{erf}\left(\frac{v_m - v_0}{\sqrt{2D_v/\gamma_v}}\right)\right]. \tag{3.65}$$

In Fig. (3.13), we show the variation of cumulative distribution function for speed with changing $Pe = v_0/\bar{v}$ and $\tilde{\gamma_v} = \gamma_v \tau_r$. The probability of getting negative speed, an effective active speed opposite to the heading direction, decreases with increase of v_0 and γ_v.

4

Active Brownian Particle: active speed associate with an additive Gaussian noise

4.1 Introduction

As we have shown in the last two chapters, self-propelled particles performing persistent motion, even at the single particle level, display a variety of new phenomena [13, 87, 107]. First we considered active Brownian particles with constant active speed. The impact of orientation fluctuations of the active heading direction alone led to several crossovers of displacement fluctuations, anisotropic dynamics and displacement fluctuations with tails of distributions less extreme than normal distributions over intermediate time-scales, before returning to an effective diffusion over long times. As we have shown in the previous chapter, the dynamics gets richer and shows additional crossovers in mean-squared displacement and displays new kinds of non-Gaussian fluctuations over intermediate time-scales as one considers fluctuations in active speed via the Schienbein-Gruler self-propulsion mechanism [15, 101, 108]. In the current chapter, we consider a second kind of active speed generation, taking the continuum limit of a chemical reaction driven self-propulsion in the presence of orientational fluctuations [16]. The Langevin equation describing the dynamics is similar to that of an active Brownian particle (ABP) considered in Chapter 2, with an active speed that has Gaussian fluctuations around a well-defined mean. As in the simple ABP, the heading difection undergoes orientational diffusion leading to a persistent motion.

The outline of the chapter is as follows. In Section-4.2, we describe the Langevin model and derive the corresponding Fokker-Planck equation. Using the Laplace transform technique we present how to calculate any moment of dynamical variables at arbitrary dimensions. In Section-4.3, we present the calculations of the mean squared displacement and displacement fluctuations. In Section-4.4, we demonstrate the anisotropy in displacement fluctuations at short times and analyze their crossovers as time elapses. Next, we calculate the distributions of scalar displacements for different lengths of trajectory in Section-4.5. In Section-4.6, we calculate the fourth moment of displacement and show the deviations from a Gaussian process in terms of its kurtosis. Finally, in Section-4.7, we conclude presenting a summary of results.

4.2 Model

The dynamics of this active particle in d-dimensions is described by its position $\mathbf{r} = (r_1, r_2, \dots, r_d)$ and orientation $\hat{\boldsymbol{u}} = (u_1, u_2, \dots, u_d)$, which is a unit vector in d-dimensions. Let the infinitesimal increment at time t are denoted by $dr_i = r_i(t+dt) - r_i(t)$ and $du_i = u_i(t+dt) - u_i(t)$. In Ito convention, the equation of motion of the ABP with chemically driven self-propulsion is given by [16],

$$dr_i = (v_0\ dt + dB^s)\ u_i + dB_i^t(t), \tag{4.1}$$

$$du_i = (\delta_{ij} - u_i u_j)\, dB_j^r(t) - (d-1) D_r u_i\, dt, \tag{4.2}$$

where the translational noise $\boldsymbol{dB}^t$ due to the heat bath follows a Gaussian distribution with its components obeying $\langle \boldsymbol{dB}_i^t \rangle = 0$ and $\langle dB_i^t dB_j^t \rangle = 2D\delta_{ij}dt$. Within a discrete lattice model in Ref. [16], the active displacement was considered to be associated with the release of a chemical potential. In the continuum limit it led to a deterministic speed v_0 and a Gaussian stochastic component dB^s obeying $\langle dB^s \rangle = 0$ and $\langle dB^s dB^s \rangle = 2D_{\text{ac}}\, dt$. The rotational diffusion is governed by the Gaussian noise dB_i^r with $\langle dB_i^r \rangle = 0$ and $\langle dB_i^r dB_j^r \rangle = 2D_r \delta_{ij}\, dt$.

It is straightforward to perform a direct numerical simulation of Eqs. (4.1) and (4.2) using the Euler-Maruyama integration. The units of time and length are set by $\tau_r = 1/D_r$ and $\bar{\ell} = \sqrt{D/D_r}$, respectively. We express the unit of velocity as $\bar{v} = \bar{\ell}/\tau_r = \sqrt{DD_r}$.

4.2.1 Fokker-Planck equation

Here, we first derive the Fokker-Planck equation from the governing Eqs. (4.1) and (4.2). The average dispalcement can be calculated from Eq. (4.1) as $\langle dr_i \rangle = v_0 u_i dt$. Thus, the drift term is

$$\lim_{dt \to 0} \frac{\langle dr_i \rangle}{dt} = v_0 u_i. \tag{4.3}$$

The diffusive term is given by

$$\lim_{dt \to 0} \frac{\langle dr_i dr_j \rangle}{dt} = 2D_{\text{ac}} u_i u_j + 2D\delta_{ij}, \tag{4.4}$$

The rotational diffusion term was already derived before in Chapter-2. The probability distribution $P(\mathbf{r}, \hat{\boldsymbol{u}}, t)$ of the position $\mathbf{r}$ and the active orientation $\hat{\boldsymbol{u}}$ of the particle follows the Fokker-Planck Eq. [91, 107]

$$\partial_t P(\mathbf{r}, \hat{\boldsymbol{u}}, t) = -\partial_i \left[\lim_{dt \to 0} \frac{\langle dr_i \rangle}{dt} P \right] + \frac{1}{2} \partial_i \partial_j \left[\lim_{dt \to 0} \frac{\langle dr_i dr_j \rangle}{dt} P \right] + D_r \nabla_u^2 P, \tag{4.5}$$

Substituting Eq. (4.3) and Eq. (4.4) in Eq. (4.5), we get,

$$\partial_t P(\mathbf{r}, \hat{\boldsymbol{u}}, t) = D_{\rm ac}(\hat{\boldsymbol{u}} \cdot \nabla)^2 P + D_r \nabla_u^2 P + D\nabla^2 P - v_0\, \hat{\boldsymbol{u}} \cdot \nabla P, \tag{4.6}$$

where ∇ is the d-dimensional Laplacian operator, and ∇_u is the Laplacian in the $(d-1)$ dimensional orientation space.

***Calculation of moments*:** In terms of the Laplace transform $\tilde{P}(\mathbf{r}, \hat{\boldsymbol{u}}, s) = \int_0^\infty dt e^{-st} P(\mathbf{r}, \hat{\boldsymbol{u}}, t)$, the Fokker-Planck equation takes the form,

$$-P(\mathbf{r}, \hat{\boldsymbol{u}}, 0) + s\tilde{P}(\mathbf{r}, \hat{\boldsymbol{u}}, s) = D_{\rm ac}(\hat{\boldsymbol{u}} \cdot \nabla)^2 \tilde{P} + D_r \nabla_u^2 \tilde{P} + D\nabla^2 \tilde{P} - v_0\, \hat{\boldsymbol{u}} \cdot \nabla \tilde{P}.$$

Defining the mean of an observable $\langle \psi \rangle_s = \int d\mathbf{r}\, d\hat{\boldsymbol{u}}\, \psi(\mathbf{r}, \hat{\boldsymbol{u}}) \tilde{P}(\mathbf{r}, \hat{\boldsymbol{u}}, s)$, multiplying the above equation by $\psi(\mathbf{r}, \hat{\boldsymbol{u}})$ and integrating over all possible $(\mathbf{r}, \hat{\boldsymbol{u}})$ we find,

$$-\langle \psi \rangle_0 + s\langle \psi \rangle_s = D_{\rm ac}\langle (\hat{\boldsymbol{u}} \cdot \nabla)^2 \psi \rangle_s + D_r \langle \nabla_u^2 \psi \rangle_s + D\langle \nabla^2 \psi \rangle_s + v_0\, \langle \hat{\boldsymbol{u}} \cdot \nabla \psi \rangle_s, \tag{4.7}$$

where, the initial condition sets $\langle \psi \rangle_0 = \int d\mathbf{r}\, d\hat{\boldsymbol{u}}\, \psi(\mathbf{r}, \hat{\boldsymbol{u}}) P(\mathbf{r}, \hat{\boldsymbol{u}}, 0)$. Without any loss of generality, we consider the initial condition to follow $P(\mathbf{r}, \hat{\boldsymbol{u}}, 0) = \delta(\mathbf{r})\delta(\hat{\boldsymbol{u}} - \hat{\boldsymbol{u}}_0)$. Equation (4.7) can be utilized to compute all the moments of dynamical variables as a function of time.

4.3 Mean squared displacement and displacement fluctuation

In this section, we derive the mean-squared displacement and displacement fluctuation utilizing Eq. (4.7). To illustrate this we first outline the calculation of $\langle \mathbf{r}^2 \rangle(t)$. We set the inital position of the particle at origin. It is easy to see that $\langle \mathbf{r}^2 \rangle_0 = 0$ and $\langle \nabla_u^2 \mathbf{r}^2 \rangle_s = 0$. The average $\langle (\hat{\boldsymbol{u}} \cdot \nabla)^2 \mathbf{r}^2 \rangle_s = 2\langle 1 \rangle_s$ and $\langle \nabla^2 \mathbf{r}^2 \rangle_s = 2d\langle 1 \rangle_s$. Note that $\langle 1 \rangle_s = \int d\mathbf{r} d\hat{\boldsymbol{u}} \tilde{P} = \int d\mathbf{r} d\hat{\boldsymbol{u}} \int_0^\infty dt e^{-st} P = \int_0^\infty dt e^{-st} \{d\mathbf{r} d\hat{\boldsymbol{u}} P\} = \int_0^\infty dt e^{-st} = 1/s$. Further, $\langle \hat{\boldsymbol{u}} \cdot \nabla \mathbf{r}^2 \rangle_s = 2\langle \hat{\boldsymbol{u}} \cdot \mathbf{r} \rangle_s$. Thus Eq. (4.7) leads to $s\langle \mathbf{r}^2 \rangle_s = 2D_{\rm ac}/s +$

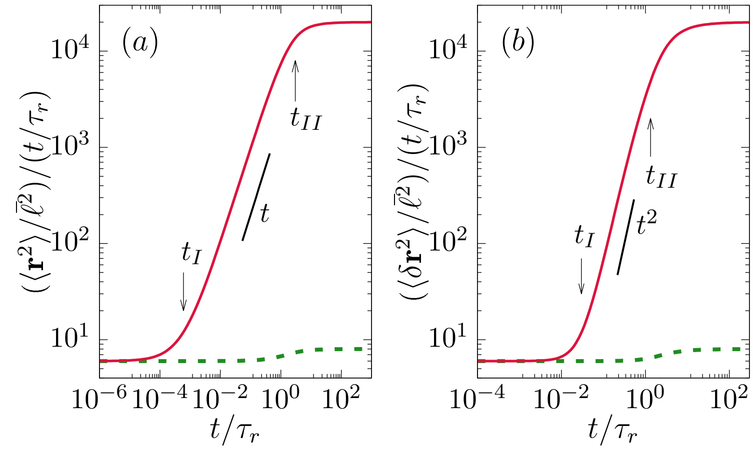

Figure 4.1: (color online) Time dependence of (a) $\langle \mathbf{r}^2\rangle$ in Eq. (4.9) and (b) $\langle \delta\mathbf{r}^2\rangle$ in Eq. (4.13) in $d = 2$ for $Pe = v_0/\bar{v} = 1$ (dashed line), 100 (solid line) with $\tilde{D}_\mathrm{a} = D_\mathrm{ac}\tau_r/\bar{\ell}^2 = 1$. The crossover times for $Pe = 100$ are (a) $t_I \approx 6\times 10^{-4}$ and $t_{II} \approx 3$ and (b) $t_I = 0.03$ and $t_{II} \approx 4/3$.

$2dD/s\, + 2v_0\langle \hat{\boldsymbol{u}}\cdot\mathbf{r}\rangle_s$. To complete the calculation, one needs to evaluate $\langle \hat{\boldsymbol{u}}\cdot\mathbf{r}\rangle_s$ using the same Eq. (4.7). One may proceed like before, utilizing $\nabla_u^2\hat{\boldsymbol{u}} = -(d-1)\hat{\boldsymbol{u}}$, $\langle \hat{\boldsymbol{u}}\cdot\nabla\psi\rangle_s = \langle \hat{\boldsymbol{u}}^2\rangle_s = 1/s$, to get $s\langle \hat{\boldsymbol{u}}\cdot\mathbf{r}\rangle_s = -(d-1)D_r\langle \hat{\boldsymbol{u}}\cdot\mathbf{r}\rangle_s + v_0/s$ to finally obtain $\langle \hat{\boldsymbol{u}}\cdot\mathbf{r}\rangle_s = v_0/[s(s+(d-1)D_r)]$. Thus, finally, plugging this relation in the expression of $\langle \mathbf{r}^2\rangle_s$ one finds

$$\langle \mathbf{r}^2\rangle_s = \frac{2D_\mathrm{ac}}{s^2} + \frac{2dD}{s^2} + \frac{2v_0^2}{s^2(s+(d-1)D_r)}. \tag{4.8}$$

Performing the inverse Laplace transform, this leads to

$$\langle \mathbf{r}^2\rangle = 2d\left(D + \frac{D_\mathrm{ac}}{d} + \frac{v_0^2}{(d-1)dD_r}\right)t - \frac{2v_0^2}{(d-1)^2D_r^2}\left(1 - e^{-(d-1)D_r t}\right). \tag{4.9}$$

As is evident from Eq. (4.9), in the absence of active fluctuations $D_\mathrm{ac} = 0$, the expression of $\langle \mathbf{r}^2\rangle$ agrees with the results for ABP in Chapter-2 and Ref.[107]. In the small time limit ($t \to 0$), $\langle \mathbf{r}^2\rangle$ in Eq. (4.9) leads to

$$\langle \mathbf{r}^2\rangle = 2d(D + \frac{D_\mathrm{ac}}{d})t + v_0^2t^2 - \frac{(d-1)}{3}v_0^2D_rt^3 + \mathcal{O}(t^4),$$

and in the long time limit ($t \to \infty$), $\langle \mathbf{r}^2 \rangle$ in Eq. (4.9) gives

$$\langle \mathbf{r}^2 \rangle = 2d \left(D + \frac{D_{\rm ac}}{d} + \frac{v_0^2}{(d-1)dD_r} \right) t.$$

Thus the mean squared displacement is expected to show crossovers from a diffusive $\langle \mathbf{r}^2 \rangle \sim t$ to ballistic $\langle \mathbf{r}^2 \rangle \sim t^2$ behavior at $t_I \approx 2(dD + D_{\rm ac})/v_0^2$, followed by another ballistic to diffusive scaling at $t_{II} \approx 3/(d-1)D_r$. In Fig. (4.1)($a$), the solid line shows the crossovers from $\langle \mathbf{r}^2 \rangle \sim t$ to $\langle \mathbf{r}^2 \rangle \sim t^2$ finally to $\langle \mathbf{r}^2 \rangle \sim t$ for $\tilde{D}_{\rm a} = 1$ and $Pe = 100$. The corresponding crossover times are $t_I \equiv t_I/\tau_r = 2(2 + \tilde{D}_{\rm a})/Pe^2 \approx 6 \times 10^{-4}$ and $t_{II} \equiv t_{II}/\tau_r \approx 3$.

Comparision with the Model in Chapter 3: Mean squared displacement in Chapter 3 for persistent motion with Schienbein-Gruler mechanism for active speed generation was

$$\begin{aligned} \langle \mathbf{r}^2 \rangle &= 2dDt + \frac{2v_0^2}{(d-1)D_r} \left(t - \frac{1 - e^{-(d-1)D_r t}}{(d-1)D_r} \right) \\ &+ \frac{2D_v}{\gamma_v(\gamma_v + (d-1)D_r)} \left(t - \frac{1 - e^{-(\gamma_v + (d-1)D_r)t}}{\gamma_v + (d-1)D_r} \right) \\ &- \frac{2D_v}{\gamma_v(\gamma_v + (d-1)D_r)} \left[\frac{1 - e^{-2\gamma_v t}}{2\gamma_v} - \frac{e^{-2\gamma_v t} - e^{-(\gamma_v + (d-1)D_r)t}}{\gamma_v - (d-1)D_r} \right]. \end{aligned} \tag{4.10}$$

In the limit of $D_v \to \infty$ and $\gamma_v \to \infty$ while D_v/γ_v^2 finite, Eq. (4.10) leads to

$$\langle \mathbf{r}^2 \rangle = 2d \left(D + \frac{D_v}{d\gamma_v^2} + \frac{v_0^2}{(d-1)dD_r} \right) t - \frac{2v_0^2}{(d-1)^2 D_r^2} \left(1 - e^{-(d-1)D_r t} \right), \tag{4.11}$$

Comparing Eq. (4.11) with Eq. (4.9), we get $D_{\rm ac} = D_v/\gamma_v^2$. In Fig. (4.2), we compare Eq. (4.9) with Eq. (4.10) in the limit of large D_v and large γ_v. In the long time limit $\langle \mathbf{r}^2 \rangle$ shows nice agreement for large Pe in Figures (4.2)(a, b).

***Displacement*:** Using $\psi = \mathbf{r}$, along with the result $\langle \hat{u} \rangle_s = \hat{u}_0/(s + (d-1)D_r)$ allows us to calculate $\langle \mathbf{r} \rangle_s = v_0 \hat{\boldsymbol{u}}_0 / s(s + (d-1)D_r)$ that leads to

$$\langle \mathbf{r} \rangle(t) = \frac{v_0\, \hat{\boldsymbol{u}}_0}{(d-1)D_r} \left(1 - e^{-(d-1)D_r\, t} \right). \tag{4.12}$$

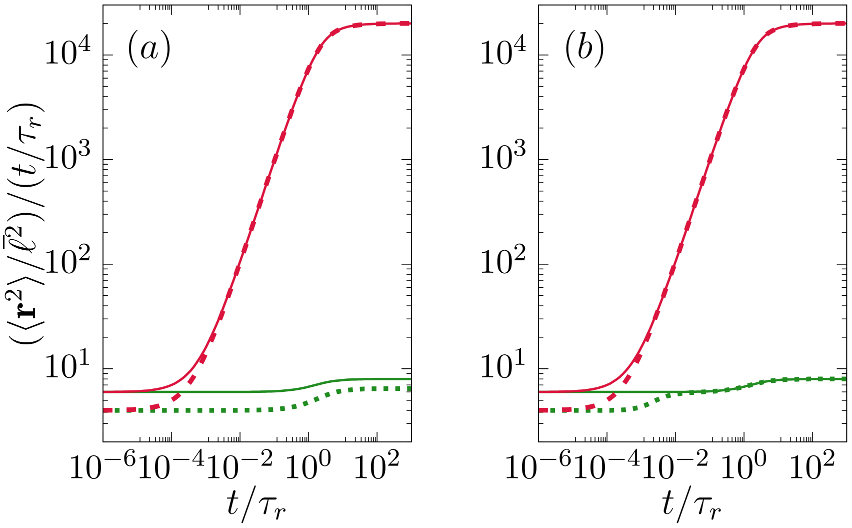

Figure 4.2: (color online) Comparision of $\langle \mathbf{r}^2 \rangle$ in Eq. (4.9) (solid line) with $\langle \mathbf{r}^2 \rangle$ in Eq. (4.10) (dashed line) in two dimensions. Parameter values used are $Pe = v_0/\bar{v} = 1$ (green solid line), 100 (red solid line) with $\tilde{D}_{\rm a} = D_{\rm ac}\tau_r/\bar{\ell}^2 = 1$. We used the conversion of the parameters $(D_v\tau_r/\bar{v}^2)/(\gamma_v^2\tau_r^2) = D_{\rm ac}\tau_r/\bar{\ell}^2$ with $D_v\tau_r/\bar{v}^2 = 0.1$ (a) and 10^6 (b).

The displacement vector saturates to a finite value $v_0/(d-1)D_r$ asymptotically in the direction of initial orientation $\hat{\boldsymbol{u}}_0$.

***Displacement fluctuation*:** One can then calculate the displacement fluctuation $\langle \delta\mathbf{r}^2 \rangle = \langle \mathbf{r}^2 \rangle - \langle \mathbf{r} \rangle^2$ directly to get

$$\langle \delta\mathbf{r}^2 \rangle = 2d\left(D + \frac{D_{\rm ac}}{d} + \frac{v_0^2}{(d-1)dD_r}\right)t - \frac{v_0^2}{(d-1)^2D_r^2}\left(3 - 4e^{-(d-1)D_rt} + e^{-2(d-1)D_rt}\right). \tag{4.13}$$

In the small time limit of $t \to 0$,

$$\langle \delta\mathbf{r}^2 \rangle = 2(dD + D_{\rm ac})t + \frac{2}{3}(d-1)v_0^2D_rt^3 - \frac{1}{2}(d-1)^2v_0^2D_r^2t^4 + \mathcal{O}(t^5).$$

Thus the mean squared displacement is expected to show crossovers from a diffusive $\langle \delta\mathbf{r}^2 \rangle \sim t$ scaling to $\langle \delta\mathbf{r}^2 \rangle \sim t^3$ scaling at $t_I \approx [3(dD + D_{\rm ac})/(d-1)v_0^2D_r]^{1/2}$. This would be followed by another crossover back to diffusive scaling near $t_{II} \approx 4/3(d-1)D_r$. On the other hand, in the high activity regime, one expects a single crossover from $\langle \delta \mathbf{r}^2 \rangle \sim t^3$ to $\langle \delta \mathbf{r}^2 \rangle \sim t$ at $t_{II} \approx 4/3(d-1)D_r$. In Fig. (4.1)(*b*), the solid line shows the crossovers $\langle \delta \mathbf{r}^2 \rangle \sim t$ to $\sim t^3$ finally to $\sim t$ for $\tilde{D}_{\rm a} = 1$ and $Pe = 100$. The crossover times are $t_I \equiv t_I/\tau_r = [3(2+\tilde{D}_{\rm a})/Pe^2]^{1/2} = 0.03$ and $t_{II} \equiv t_{II}/\tau_r = 4/3$.

In the long time limit of $t \to \infty$, $\langle \delta \mathbf{r}^2 \rangle$ in Eq. (4.13) becomes diffusive $\langle \delta \mathbf{r}^2 \rangle = 2dD_{\rm eff}t$ with an effective diffusion constant

$$D_{\rm eff} \;=\; D + \frac{D_{\rm ac}}{d} + \frac{v_0^2}{(d-1)dD_r}. \tag{4.14}$$

Position- orientation cross-correlation **:** The equal time position- orientation cross-correlation

$$\langle \hat{\boldsymbol{u}}.\mathbf{r} \rangle(t) = \frac{v_0}{(d-1)D_r}\left(1 - e^{-(d-1)D_r\, t}\right) \tag{4.15}$$

remains the same as in Chapter 2 [107].

4.4 Components of displacement fluctuation

We assume the initial orientation of activity is towards the x-axis, $\hat{\boldsymbol{u}}_0 = \hat{x}$. Thus $r_\parallel^2 = x^2$ leads to $s\langle r_\parallel^2 \rangle_s = 2D_{\rm ac}\langle u_x^2 \rangle_s + 2D\langle 1 \rangle_s + 2v_0\langle xu_x \rangle_s$. To proceed, we use $\psi = u_x^2$ to find $\langle \psi \rangle_0 = 1$, $(\hat{\boldsymbol{u}} \cdot \nabla)^2 \psi = 0$, $\langle \nabla_u^2 \psi \rangle_s = -2d\langle u_x^2 \rangle_s + 2/s$, $\hat{\boldsymbol{u}} \cdot \nabla \psi = 0$ to get $-1 + s\langle u_x^2 \rangle_s = -2dD_r\langle u_x^2 \rangle_s + 2D_r/s$ gives $\langle u_x^2 \rangle_s = \frac{(s+2D_r)}{s(s+2dD_r)}$. Further, we consider $\psi = xu_x$, giving $\langle \psi \rangle_0 = 0$, $(\hat{\boldsymbol{u}} \cdot \nabla)^2 \psi = 0$, $\nabla_u^2 \psi = -(d-1)xu_x$, $\hat{\boldsymbol{u}} \cdot \nabla \psi = u_x^2$, to get $s\langle xu_x \rangle_s = -(d-1)D_r\langle xu_x \rangle_s + v_0\langle u_x^2 \rangle_s$ leading to $\langle xu_x \rangle_s = \frac{v_0}{s+(d-1)D_r}\langle u_x^2 \rangle_s$. Thus putting together all these relations we obtain

$$\langle r_\parallel^2 \rangle_s = \frac{2D_{\rm ac}(s+2D_r)}{s^2(s+2dD_r)} + \frac{2D}{s^2} + \frac{2v_0^2(s+2D_r)}{s^2(s+(d-1)D_r)(s+2dD_r)} \tag{4.16}$$

Performing the inverse Laplace transform we find,

$$\langle r_\parallel^2\rangle = 2\left(D + \frac{D_{\rm ac}}{d} + \frac{v_0^2}{(d-1)dD_r}\right)t + \frac{(d-1)D_{\rm ac}}{d^2D_r}\left(1-e^{-2dD_rt}\right)$$
$$+\frac{v_0^2}{D_r^2}\left(\frac{(d-1)e^{-2dD_rt}}{d^2(d+1)} + \frac{2(3-d)e^{-(d-1)D_rt}}{(d-1)^2(d+1)} + \frac{d^2-4d+1}{(d-1)^2d^2}\right) \tag{4.17}$$

The relative fluctuation in the initial orientation is $\langle \delta r_\parallel^2\rangle = \langle r_\parallel^2\rangle - \langle r_\parallel\rangle^2$ where the displacement $\langle r_\parallel\rangle = \langle \mathbf{r}\cdot\hat{\boldsymbol{u}}_0\rangle = \frac{v_0}{(d-1)D_r}\left(1-e^{-(d-1)D_r\,t}\right)$.

The fluctuation in the perpendicular component $\langle \delta\mathbf{r}_\perp^2\rangle = \langle \mathbf{r}_\perp^2\rangle$ as the mean displacement perpendicular to the initial orientation $\langle \mathbf{r}_\perp\rangle = 0$. Thus $\langle \delta\mathbf{r}_\perp^2\rangle = \langle \mathbf{r}^2\rangle - \langle r_\parallel^2\rangle$. They are given by

$$\langle \delta r_\parallel^2\rangle = 2\left(D + \frac{D_{\rm ac}}{d} + \frac{v_0^2}{(d-1)dD_r}\right)t + \frac{(d-1)D_{\rm ac}}{d^2D_r}\left(1-e^{-2dD_rt}\right)$$
$$+\frac{v_0^2}{D_r^2}\left(\frac{(d-1)e^{-2dD_rt}}{d^2(d+1)} + \frac{8e^{-(d-1)D_rt}}{(d-1)^2(d+1)} - \frac{e^{-2(d-1)D_rt}}{(d-1)^2} - \frac{4d-1}{(d-1)^2d^2}\right), \tag{4.18}$$

$$\langle \delta\mathbf{r}_\perp^2\rangle = 2(d-1)\left(D + \frac{D_{\rm ac}}{d} + \frac{v_0^2}{(d-1)dD_r}\right)t - \frac{(d-1)D_{\rm ac}}{d^2D_r}\left(1-e^{-2dD_rt}\right)$$
$$+\frac{v_0^2}{D_r^2}\left(\frac{4e^{-(d-1)D_rt}}{d^2-1} - \frac{(d-1)e^{-2dD_rt}}{d^2(d+1)} - \frac{3d-1}{d^2(d-1)}\right). \tag{4.19}$$

In two dimensions: The above results simplifies in two dimensions, setting $d = 2$. In the long time limit, both the components show the same diffusive scaling $\langle r_\parallel^2\rangle, \langle \mathbf{r}_\perp^2\rangle \sim t$. In the small time parallel component $\langle \delta r_\parallel^2\rangle$ in Eq. (4.18) and the normal component $\langle \delta\mathbf{r}_\perp^2\rangle$ in Eq. (4.19) of the displacement fluctuation leads to

$$\langle \delta r_\parallel^2\rangle(t\to 0) = 2(D+D_{\rm ac})t - 2D_{\rm ac}D_rt^2 + \frac{8}{3}D_{\rm ac}D_r^2t^3 + (\frac{1}{3}v_0^2 - \frac{8}{3}D_{\rm ac}D_r)D_r^2t^4$$
$$-(\frac{7}{15}v_0^2 - \frac{32}{15}D_{\rm ac}D_r)D_r^3t^5 + \mathcal{O}(t^6) \tag{4.20}$$

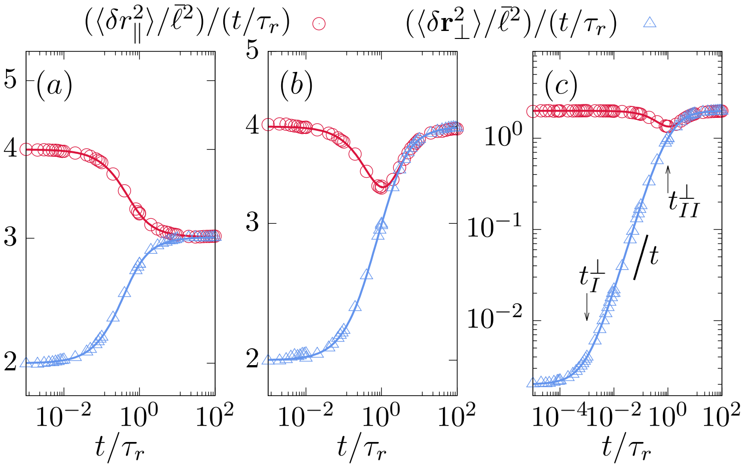

Figure 4.3: (color online) Components of displacement fluctuation in two dimensions for low activity ($Pe^2 \leq \tilde{D}_{\rm a}$). Points denote simulations results and lines depict analytical predictions. The components of displacement fluctuations $\langle\delta r_{\parallel}^2\rangle$ (○, red) and $\langle\delta \mathbf{r}_{\perp}^2\rangle$ (△, blue) correspond to Eq. (4.18) and Eq. (4.19) respectively. The parameter values used for (a) $\tilde{D}_{\rm a} = D_{\rm ac}\tau_r/\bar{\ell}^2 = 1$ and $Pe = v_0\tau_r/\bar{\ell} = 0.1$, (b) $\tilde{D}_{\rm a} = D_{\rm ac}\tau_r/\bar{\ell}^2 = 1$ and $Pe = v_0\tau_r/\bar{\ell} = 1$, (c) $\tilde{D}_{\rm a} = D_{\rm ac}\tau_r/\bar{\ell}^2 = 10^3$ and $Pe = v_0\tau_r/\bar{\ell} = 31.62$. The parallel component shows sub-diffusive behavior as the condition $Pe^2 \leq \tilde{D}_{\rm a}$ holds. (c) The crossover timescales are $t_I^{\perp}/\tau_r = 10^{-3}$, and $t_{II}^{\perp}/\tau_r = 1$.

$$\langle\delta \mathbf{r}_{\perp}^2\rangle(t\to 0) = 2Dt + 2D_{\rm ac}D_r t^2 + (\frac{2}{3}v_0^2 - \frac{8}{3}D_{\rm ac}D_r)D_r t^3 - (\frac{5}{6}v_0^2 - \frac{8}{3}D_{\rm ac}D_r)D_r^2 t^4 + \mathcal{O}(t^5) \tag{4.21}$$

In the absence of speed fluctuation $D_{\rm ac} = 0$, the above result reduces to that of ABPs obtained in Chapter 2 [107]. However, in the presence of Gaussian speed fluctuations, the small time limit gives a diffusive scaling with $\langle\delta r_{\parallel}^2\rangle(t\to 0) \approx 2(D + D_a)t$ and $\langle\delta \mathbf{r}_{\perp}^2\rangle(t\to 0) \approx 2Dt$. In the long time limit again they become diffusive, albeit with different diffusion constants

$$\begin{aligned}
\langle\delta r_{\parallel}^2\rangle(t\to\infty) &= 2\left(D + \frac{D_{\rm ac}}{2} + \frac{v_0^2}{2D_r}\right)t,\\
\langle\delta \mathbf{r}_{\perp}^2\rangle(t\to\infty) &= 2\left(D + \frac{D_{\rm ac}}{2} + \frac{v_0^2}{2D_r}\right)t.
\end{aligned} \tag{4.22}$$

The difference between these diffusion constants can be easily seen from,

$$\begin{aligned}\langle \delta r_{\parallel}^2 \rangle(t \to \infty) - \langle \delta r_{\parallel}^2 \rangle(t \to 0) &= \left(\frac{v_0^2}{D_r} - D_{\rm ac} \right) t \\ \langle \delta \mathbf{r}_{\perp}^2 \rangle(t \to \infty) - \langle \delta \mathbf{r}_{\perp}^2 \rangle(t \to 0) &= \left(\frac{v_0^2}{D_r} + D_{\rm ac} \right) t. \end{aligned} \tag{4.23}$$

Low activity limit $v_0^2 \le D_{\rm ac} D_r$: Equation (4.23) suggests the final diffusivity in $\langle \delta r_{\parallel}^2 \rangle$ is smaller than the initial diffusivity in this limit. Thus one expects $\langle \delta r_{\parallel}^2 \rangle$ to reduce with time to finally saturate to the form in Eq. (4.19). However, the second relation in Eq. (4.23) suggests that the final diffusivity is always positive and $\langle \delta \mathbf{r}_{\perp}^2 \rangle$ transits from initial to final diffusion by increasing monotonically with time. In the Fig. (4.3) we demonstrate these behaviors using a comparison of numerical simulations and analytic expressions. In the Fig. (4.3)(a), parallel component shows diffusive- subdiffusive- diffusive crossovers as $Pe = 0.1$ and $\tilde{D}_{\rm a} = 1$ hold the condition $Pe^2 < \tilde{D}_{\rm a}$. In Fig. (4.3)(b), $\langle \delta r_{\parallel}^2 \rangle$ shows diffusive- subdiffusive- ballistic- diffusive crossovers as $Pe = 1$ and $\tilde{D}_{\rm a} = 1$ obey the condition $Pe^2 = \tilde{D}_{\rm a}$. In Fig. (4.3)(c), $\langle \delta r_{\parallel}^2 \rangle$ shows diffusive- subdiffusive- ballistic- diffusive crossovers as $Pe = 31.62$ and $\tilde{D}_{\rm a} = 10^3$ holds the condition $Pe^2 = \tilde{D}_{\rm a}$. The crossovers $\langle \delta \mathbf{r}_{\perp}^2 \rangle \sim t$ to $\langle \delta \mathbf{r}_{\perp}^2 \rangle \sim t^2$, finally to $\langle \delta \mathbf{r}_{\perp}^2 \rangle \sim t$ may appear when the third term in Eq. (4.21) is negative, $v_0^2 < 4 D_{\rm ac} D_r$. Thus the crossover from $\langle \delta \mathbf{r}_{\perp}^2 \rangle \sim t$ to $\langle \delta \mathbf{r}_{\perp}^2 \rangle \sim t^2$ appears at $t_I^{\perp} = [D/D_{\rm ac}] D_r^{-1}$, followed by another crossover back to $\langle \delta \mathbf{r}_{\perp}^2 \rangle \sim t$ at $t_{II}^{\perp} \approx [3 D_{\rm ac} D_r / (v_0^2 - 4 D_{\rm ac} D_r)] D_r^{-1}$. The crossovers $\langle \delta \mathbf{r}_{\perp}^2 \rangle \sim t$ to $\sim t^2$ to $\sim t$ are shown in Fig. (4.3)(c) for $\tilde{D}_{\rm a} = 10^3$ and $Pe = 31.62$ as the condition $Pe^2 < 4\tilde{D}_{\rm a}$ holds. The crossover times are $t_I^{\perp} \equiv t_I^{\perp}/\tau_r = 1/\tilde{D}_{\rm a} = 10^{-3}$ and $t_{II}^{\perp} \equiv t_{II}^{\perp}/\tau_r \approx [3\tilde{D}_{\rm a}/(Pe^2 - 4\tilde{D}_{\rm a})] = 1$.

High activity limit $v_0^2 > D_{\rm ac} D_r$: In this limit the final diffusivity in $\langle \delta r_{\parallel}^2 \rangle$ is larger than the short time diffusivity. The parallel component $\langle \delta r_{\parallel}^2 \rangle$ first crosses over from $\langle \delta r_{\parallel}^2 \rangle \sim t$ to $\langle \delta r_{\parallel}^2 \rangle \sim t^3$ at $t_I \approx (3(1 + D/D_{\rm ac})/4)^{1/2} D_r^{-1}$ followed by another crossover from $\langle \delta r_{\parallel}^2 \rangle \sim t^3$ to $\langle \delta r_{\parallel}^2 \rangle \sim t^4$ at $t_{II} \approx [8 D_{\rm ac} D_r / (v_0^2 - 8 D_{\rm ac} D_r)] D_r^{-1}$ and finally in the long time a further crossover from $\langle \delta r_{\parallel}^2 \rangle \sim t^3$ to $\langle \delta r_{\parallel}^2 \rangle \sim t$ at

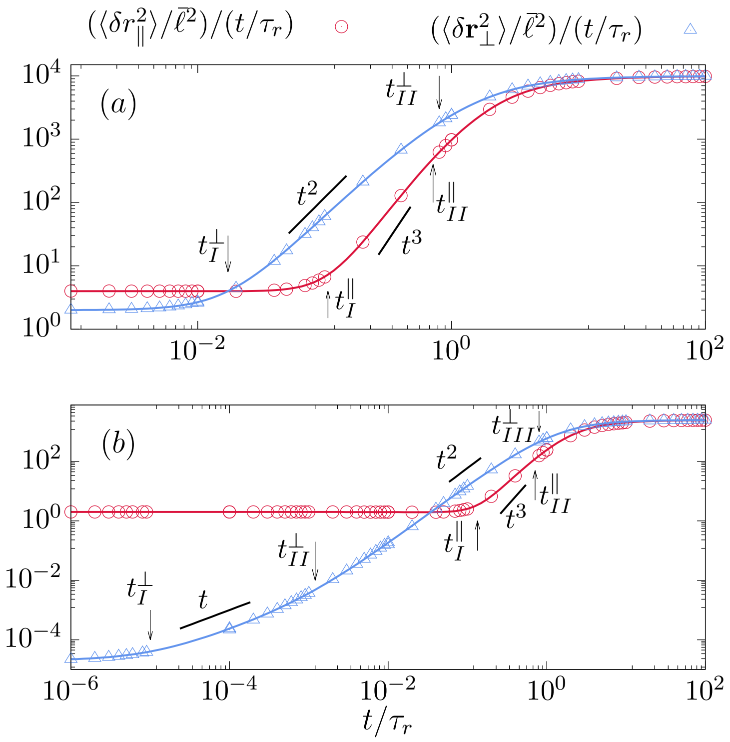

Figure 4.4: (color online) Components of displacement fluctuation in $d = 2$ for high activity $Pe^2 > \tilde{D}_{\rm a}$. The points denote numerical simulations and the lines denote theory. The parallel ($\circ$, red) and perpendicular ($\triangle$, blue) components of displacement fluctuation correspond to Eq. (4.18) and Eq. (4.19) respectively. The parameter values used are (a) $\tilde{D}_{\rm a} = D_{\rm ac}\tau_r/\bar{\ell}^2 = 1$, $Pe = v_0\tau_r/\bar{\ell} = 10^2$ and (b) $\tilde{D}_{\rm a} = D_{\rm ac}\tau_r/\bar{\ell}^2 = 10^5$ and $Pe = v_0\tau_r/\bar{\ell} = 1.58 \times 10^4$. In (a), the crossover times are denoted by $t_I^{\parallel}/\tau_r = 0.11$, $t_{II}^{\parallel}/\tau_r = 0.71$, $t_I^{\perp}/\tau_r = 1.7 \times 10^{-2}$, and $t_{II}^{\perp}/\tau_r = 0.8$. In (b), the crossover times are denoted by $t_I^{\parallel}/\tau_r = 0.13$, $t_{II}^{\parallel}/\tau_r = 0.71$, $t_I^{\perp}/\tau_r = 10^{-5}$, $t_{II}^{\perp}/\tau_r = 1.2 \times 10^{-3}$, and $t_{III}^{\perp}/\tau_r = 0.8$.

$t_{III} \approx [5(v_0^2 - 8D_{\rm ac}D_r)/(7v_0^2 - 32D_{\rm ac}D_r)]D_r^{-1}$ when $t_I < t_{II} < t_{III}$ is satisfied. The crossover times are calculated by comparing different terms in Eq. (4.20). Thus, the condition $t_{III} > t_{II}$ leads to $v_0^2 > ((68 + \sqrt{1744})/5)D_{\rm ac}D_r$ and another condition $t_{II} > t_I$ leads to $v_0^2 < (16(D_{\rm ac}^3/3(D + D_{\rm ac}))^{1/2} + 8D_{\rm ac})D_r$. Even for $D = 0$, the condition $t_{II} > t_I$ leads to $v_0^2 < (16/\sqrt{3} + 8)D_{\rm ac}D_r$, a relation that conflicts with the assumption of $v_0^2 > D_{\rm ac}D_r$. It suggests the $\langle \delta r_\parallel^2 \rangle \sim t^3$ is not possible. Thus, the possible crossovers are $\langle \delta r_\parallel^2 \rangle \sim t$ to $\langle \delta r_\parallel^2 \rangle \sim t^4$, finally to $\langle \delta r_\parallel^2 \rangle \sim t$. The first crossover $\langle \delta r_\parallel^2 \rangle \sim t$ to $\langle \delta r_\parallel^2 \rangle \sim t^4$ can appear at $t_I^{\parallel} = [6(D + D_{\rm ac})/(v_0^2 - 8D_{\rm ac}D_r)]^{1/3}$ and the second crossover $\langle \delta r_\parallel^2 \rangle \sim t^4$ to $\langle \delta r_\parallel^2 \rangle \sim t$ can appear at $t_{II}^{\parallel} = t_{III} = [5(v_0^2 - 8D_{\rm ac}D_r)/(7v_0^2 - 32D_{\rm ac}D_r)]D_r^{-1}$. In Fig. (4.4), we show the crossovers $\langle \delta r_\parallel^2 \rangle \sim t$

to $\sim t^4$ finally to $\sim t$. The crossover times in Fig. (4.4)(a) for $\tilde{D}_{\rm a} = 1$ and $Pe = 10^2$ are $t_I^{\parallel} \equiv t_I^{\parallel}/\tau_r = [6(1+\tilde{D}_{\rm a})/(Pe^2-8)]^{1/3} \approx 0.11$ and $t_{II}^{\parallel} = t_{II}^{\parallel}/\tau_r = [5(Pe^2 - 8\tilde{D}_{\rm a})/(7Pe^2 - 32\tilde{D}_{\rm a})] \approx 0.71$. Similarly, the crossover times in Fig. (4.4)(b) for $\tilde{D}_{\rm a} = 10^5$ and $Pe = 1.58 \times 10^4$ are $t_I^{\parallel} \equiv t_I^{\parallel}/\tau_r \approx 0.13$ and $t_{II}^{\parallel} = t_{II}^{\parallel}/\tau_r \approx 0.71$.

One can separately analyze the expression of $\langle \delta \mathbf{r}_\perp^2 \rangle$ to identify a first crossover from $\langle \delta \mathbf{r}_\perp^2 \rangle \sim t$ to $\langle \delta \mathbf{r}_\perp^2 \rangle \sim t^2$ at $t_I^\perp = [D/D_{\rm ac}]D_r^{-1}$ followed by another crossover from $\langle \delta \mathbf{r}_\perp^2 \rangle \sim t^2$ to $\langle \delta \mathbf{r}_\perp^2 \rangle \sim t^3$ at $t_{II}^\perp \approx 3D_{\rm ac}/(v_0^2 - 4D_{\rm ac}D_r)$, provided $v_0^2 > 4D_{\rm ac}D_r$. At $t_{III}^\perp = [4(v_0^2 - 4D_{\rm ac}D_r)/(5v_0^2 - 16D_{\rm ac}D_r)]D_r^{-1}$ a third crossover back to $\langle \delta \mathbf{r}_\perp^2 \rangle \sim t$ is expected.

Another possible scenario of crossovers is the following: (i) from $\langle \delta \mathbf{r}_\perp^2 \rangle \sim t$ to $\langle \delta \mathbf{r}_\perp^2 \rangle \sim t^3$ at $t_I^{\perp\prime} = [3DD_r/(v_0^2 - 4D_{\rm ac}D_r)]^{1/2}D_r^{-1}$ with condition $v_0^2 > 4D_{\rm ac}D_r + 3D_{\rm ac}^2 D_r/D$ ($t_{II}^\perp < t_I^\perp$), (ii) back to $\langle \delta \mathbf{r}_\perp^2 \rangle \sim t$ at $t_{III}^\perp = [4(v_0^2 - 4D_{\rm ac}D_r)/(5v_0^2 - 16D_{\rm ac}D_r)]D_r^{-1}$ with condition $v_0^2 > [(47+\sqrt{417})/8]D_{\rm ac}D_r(t_{II}^\perp < t_{III}^\perp)$. Moreover, $t_{III} > t_I$ leads to the condition $v_0^2 > 16(D - D_{\rm ac})D_{\rm ac}D_r/(5D - 4D_{\rm ac})$. The crossovers $\langle \delta \mathbf{r}_\perp^2 \rangle \sim t$ to $\sim t^3$ and finally to $\sim t$ are shown in Fig. (4.4)(a) for $\tilde{D}_{\rm a} = 1$, $Pe = 10^2$. The crossover times are $t_I^\perp \equiv t_I^\perp/\tau_r = [3/(Pe^2 - 4\tilde{D}_{\rm a})]^{1/2} = 1.7 \times 10^{-2}$, $t_{II}^\perp \equiv t_{II}^\perp/\tau_r = [4(Pe^2 - 4\tilde{D}_{\rm a})/(5Pe^2 - 16\tilde{D}_{\rm a})] = 0.8$

Full crossovers are $\langle \delta \mathbf{r}_\perp^2 \rangle \sim t$ to $\langle \delta \mathbf{r}_\perp^2 \rangle \sim t^2$ at $t_I^\perp = [D/D_{\rm ac}]D_r^{-1}$ with condition $v_0^2 < 4D_{\rm ac}D_r + 3D_{\rm ac}^2 D_r/D$ ($t_{II}^\perp > t_I^\perp$) to $\langle \delta \mathbf{r}_\perp^2 \rangle \sim t^3$ at $t_{II}^\perp = 3D_{\rm ac}/(v_0^2 - 4D_{\rm ac}D_r)$ with condition $v_0^2 > [(47+\sqrt{417})/8]D_{\rm ac}D_r(t_{III}^\perp > t_{II}^\perp)$ to $\langle \delta \mathbf{r}_\perp^2 \rangle \sim t$ with condition $v_0^2 > 4D_{\rm ac}D_r$ at $t_{III}^\perp = [4(v_0^2 - 4D_{\rm ac}D_r)/(5v_0^2 - 16D_{\rm ac}D_r)]D_r^{-1}$. It shows in Fig. (4.4)(b) for $\tilde{D}_{\rm a} = 10^5$ and $Pe = 1.58 \times 10^4$. The crossover times are $t_I^\perp \equiv t_I^\perp/\tau_r = 1/\tilde{D}_{\rm a} = 10^{-5}$, $t_{II}^\perp \equiv t_{II}^\perp/\tau_r = 3\tilde{D}_{\rm a}/(Pe^2 - 4\tilde{D}_{\rm a}) \approx 1.2 \times 10^{-3}$ and $t_{III}^\perp \equiv t_{III}^\perp/\tau_r = 4(Pe^2 - 4\tilde{D}_{\rm a})/(5Pe^2 - 16\tilde{D}_{\rm a}) \approx 0.8$.

4.5 Displacement distribution

The transition in the dynamical crossovers realises via displacement distributions at different length of the trajectories $L = v_0 t/\bar{\ell}$. In Fig. (4.5) we plot the distri-

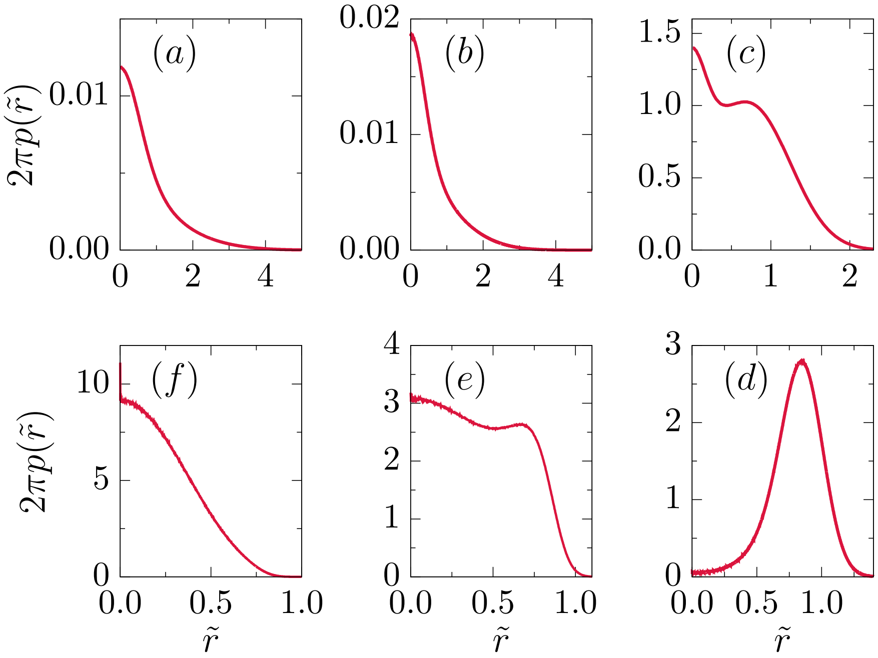

Figure 4.5: (color online) Probability distribution of displacement $2\pi p(\tilde{r})$ at $Pe = v_0\tau_r/\bar{\ell} = 31.6$ and $\tilde{D_{\text{ac}}} = D_{\text{ac}}\tau_r/\bar{\ell}^2 = 10$ over different time-segments expressed as $L = v_0 t/\bar{\ell} = 0.32$ (a), 0.63 (b), 3.16 (c), 31.62 (d), 126.49 (e), and 316.23 (f). Here $\tilde{r} = r/L$.

bution functions $p(\tilde{r})$ of the scaled separation $\tilde{r} = r/L$ at $Pe = v_0\tau_r/\bar{\ell} = 31.6$ and $\tilde{D_{\text{ac}}} = D_{\text{ac}}\tau_r/\bar{\ell}^2 = 10$. Note that here Pe gives a dimensionless measure of persistence length of the trajectories. For the small length of the trajectories, the displacement distributions in Fig. (4.5)(a, b) shows a Gaussian-like profile for the length of the trajectories $L = 0.32$ (a) and 0.63 (b). It is due to the combined effect of the uncorrelated Gaussian active noise in speed and the thermal translational noise. It transforms to a distribution characterizing strongly extended trajectories in Fig. (4.5)(d) at $L = 31.62$, via an intermediate regime of clear bimodality shown in Fig. (4.5)(c) at $L = 3.16$. Here the ratio of length of the trajectories to the persistence length is $L/Pe = 0.1$. This bimodality is maintained by the fluctuation in active speed. At long times $L = 316.23$ the distribution returns to Gaussian profile as in Fig. (4.5)(f) via again pronounced bimodality shown in Fig. (4.5)(e) for $L = 126.49$ corresponding to $L/Pe = 4$. This bimodality is maintained by the orientational fluctuations as in the ABPs of Chapter-2 [93, 107].

4.6 Fourth moment and kurtosis

In this section, we calculate the fourth moment of displacement and use it to show the deviations from Gaussian process using the kurtosis. We use Eq. (4.7) as for calculations of other moments to compute $\langle \mathbf{r}^4 \rangle$. The fourth oder moment in Laplace space can be expressed as

$$\begin{aligned}\langle \mathbf{r}^4 \rangle_s &= 8[D_{\mathrm{ac}} + (d+2)D](D_{\mathrm{ac}} + dD)\frac{1}{s^3} + \frac{16 D_{\mathrm{ac}}(D_{\mathrm{ac}} + D)}{s^2(s + 2dD_r)} + \frac{32 D_{\mathrm{ac}}(D_{\mathrm{ac}} + D)D_r}{s^3(s+2dD_r)} \\ &+ \frac{8D_{\mathrm{ac}} v_0^2(5s + 2(d-1)D_r)}{s^3(s+(d-1)D_r)^2} + \frac{32 D_{\mathrm{ac}} v_0^2 (s + 2D_r)}{s^3(s+(d-1)D_r)(s+2dD_r)} \\ &+ \frac{8Dv_0^2(d+2)(3s+2(d-1)D_r)}{s^3(s+(d-1)D_r)^2} + \frac{8v_0^4(3s+2(d+2)D_r)}{s^3(s+(d-1)D_r)^2(s+2dD_r)}. \end{aligned} \tag{4.24}$$

The calculation involves the following main steps,

$$\begin{aligned} &s\langle \mathbf{r}^4\rangle_s = 4D_{\mathrm{ac}}(\langle \mathbf{r}^2\rangle_s + 2\langle(\hat{\boldsymbol{u}}\cdot\mathbf{r})^2\rangle_s) + 4(d+2)D\langle \mathbf{r}^2\rangle_s + 4v_0\langle(\hat{\boldsymbol{u}}\cdot\mathbf{r})\mathbf{r}^2\rangle_s, \\ &s\langle \hat{\boldsymbol{u}}\cdot\mathbf{r}\rangle_s = -(d-1)D_r\langle \hat{\boldsymbol{u}}\cdot\mathbf{r}\rangle_s + v_0\langle 1\rangle_s, \\ &s\langle(\hat{\boldsymbol{u}}\cdot\mathbf{r})^2\rangle_s = 2D_{\mathrm{ac}}\langle 1\rangle_s + 2D_r\langle r^2\rangle_s - 2dD_r\langle(\hat{\boldsymbol{u}}\cdot\mathbf{r})^2\rangle_s + 2D\langle 1\rangle_s + 2v_0\langle \hat{\boldsymbol{u}}\cdot\mathbf{r}\rangle_s, \\ &s\langle(\hat{\boldsymbol{u}}\cdot\mathbf{r})\mathbf{r}^2\rangle_s = 6D_{\mathrm{ac}}\langle \hat{\boldsymbol{u}}\cdot\mathbf{r}\rangle_s - (d-1)D_r\langle(\hat{\boldsymbol{u}}\cdot\mathbf{r})\mathbf{r}^2\rangle_s + (4+2d)D\langle \hat{\boldsymbol{u}}\cdot\mathbf{r}\rangle_s + v_0\langle \mathbf{r}^2\rangle_s \\ &+ 2v_0\langle(\hat{\boldsymbol{u}}\cdot\mathbf{r})^2\rangle_s. \end{aligned}$$

where $\langle \mathbf{r}^2 \rangle_s$ in Eq. (4.8) is already evaluated. Performing the inverse Laplace transform, we obtain the time evolution of fourth moment,

$$
\begin{aligned}
&\langle \mathbf{r}^4 \rangle(t) = 4[D_{\text{ac}} + (d+2)D](D_{\text{ac}} + dD)t^2 \\
&+ 16D_{\text{ac}}(D_{\text{ac}} + D)\left[\frac{t}{2dD_r} - \frac{1}{(2dD_r)^2}\left(1 - e^{-2dD_r t}\right)\right] \\
&+ 32D_{\text{ac}}(D_{\text{ac}} + dD)D_r\left[\frac{t^2}{4dD_r} - \frac{t}{(2dD_r)^2} + \frac{1}{(2dD_r)^3}\left(1 - e^{-2dD_r t}\right)\right] \\
&+ 8D_{\text{ac}}v_0^2\left[\frac{t^2}{(d-1)D_r} + \frac{t}{(d-1)^2D_r^2} + \frac{3te^{-(d-1)D_r t}}{(d-1)^2D_r^2} - \frac{4}{(d-1)^3D_r^3}\left(1 - e^{-(d-1)D_r t}\right)\right] \\
&+ 32D_{\text{ac}}v_0^2\left[\frac{t^2}{2(d-1)dD_r} + \frac{(d^2-4d+1)t}{2(d-1)^2d^2D_r^2} + \frac{-3d^3+11d^2-5d+1}{4(d-1)^3d^3D_r^3}\right] \\
&+ 32D_{\text{ac}}v_0^2\left[\frac{(d-3)e^{-(d-1)D_r t}}{(d-1)^3(d+1)D_r^3} - \frac{(d-1)e^{-2dD_r t}}{4d^3(d+1)D_r^3}\right] \\
&- \frac{8\left(d^2v_0^4 + 10dv_0^4 + 25v_0^4\right)e^{-(d-1)D_r t}}{(d-1)^4(d+1)^2D_r^4} + \frac{4\left(d^3v_0^4 + 23d^2v_0^4 - 7dv_0^4 + v_0^4\right)}{(d-1)^4d^3D_r^4}
\end{aligned}
$$

$$
\begin{aligned}
&+\frac{8te^{-(d-1)D_r t}\left(d^3DD_rv_0^2+2d^2DD_rv_0^2-dDD_rv_0^2+dv_0^4-2DD_rv_0^2-7v_0^4\right)}{(d-1)^3(d+1)D_r^3}\\
&+\frac{4t^2\left(d^5D^2D_r^2-3d^3D^2D_r^2+2d^3DD_rv_0^2+2d^2D^2D_r^2+2d^2DD_rv_0^2-4dDD_rv_0^2+dv_0^4+2v_0^4\right)}{(d-1)^2dD_r^2}\\
&-\frac{8t\left(d^4DD_rv_0^2+d^3DD_rv_0^2-2d^2DD_rv_0^2+d^2v_0^4+6dv_0^4-v_0^4\right)}{(d-1)^3d^2D_r^3}. \qquad (4.25)
\end{aligned}
$$

For $D_{\text{ac}} = 0$ this agrees with the fourth moment for ABPs in [107]. In two dimensions, using $d = 2$, the relation simplifies to,

$$
\begin{aligned}
\langle \mathbf{r}^4(t)\rangle &= 4\left(D_{\text{ac}}+4D\right)\left(D_{\text{ac}}+2D\right)t^2+16D_{\text{ac}}(D_{\text{ac}}+D)\left[\frac{t}{4D_r}-\frac{1}{(4D_r)^2}\left(1-e^{-4D_rt}\right)\right]\\
&+32D_{\text{ac}}(D_{\text{ac}}+2D)D_r\left[\frac{t^2}{8D_r}-\frac{t}{(4D_r)^2}+\frac{1}{(4D_r)^3}\left(1-e^{-4D_rt}\right)\right]\\
&+8D_{\text{ac}}v_0^2\left[\frac{t^2}{D_r}+\frac{t}{D_r^2}+\frac{3te^{-D_rt}}{D_r^2}-\frac{4}{D_r^3}\left(1-e^{-D_rt}\right)\right]\\
&+32D_{\text{ac}}v_0^2\left[\frac{t^2}{4D_r}-\frac{3t}{8D_r^2}+\frac{11}{32D_r^3}\left(1-\frac{32}{33}e^{-D_rt}-\frac{1}{33}e^{-4D_rt}\right)\right]\\
&+\frac{8te^{-D_rt}\left(12DD_rv_0^2-5v_0^4\right)}{3D_r^3}-\frac{2t\left(16DD_rv_0^2+15v_0^4\right)}{D_r^3}\\
&+\frac{v_0^4e^{-4D_rt}}{18D_r^4}-\frac{392v_0^4e^{-D_rt}}{9D_r^4}+\frac{87v_0^4}{2D_r^4}. \qquad (4.26)
\end{aligned}
$$

In the long time limit, $t \to \infty$, the first term in the above expression dominates to give,

$$
\langle \mathbf{r}^4(t)\rangle(t\to\infty) \approx 8\left[\left(D_{\text{ac}}+2D\right)^2+\frac{2D_{\text{ac}}v_0^2}{D_r}\right]t^2 \qquad (4.27)
$$

In the small time limit of $t \to 0$, the expansion leads to,

$$
\begin{aligned}
\langle \mathbf{r}^4(t)\rangle &= (12D_{\text{ac}}^2+32D_{\text{ac}}D+32D^2)t^2+\left[4(3D_{\text{ac}}+4D)v_0^2-\frac{16}{3}D_{\text{ac}}^2D_r\right]t^3\\
&+\left(v_0^4+\frac{16D_{\text{ac}}^2D_r^2}{3}-\frac{16}{3}DD_rv_0^2-\frac{20}{3}D_{\text{ac}}D_rv_0^2\right)t^4\\
&-\left(\frac{2}{3}v_0^4D_r+\frac{64D_{\text{ac}}^2D_r^3}{15}-\frac{4DD_r^2v_0^2}{3}-\frac{11D_{\text{ac}}D_r^2v_0^2}{3}\right)t^5+\mathcal{O}(t^6). \qquad (4.28)
\end{aligned}
$$

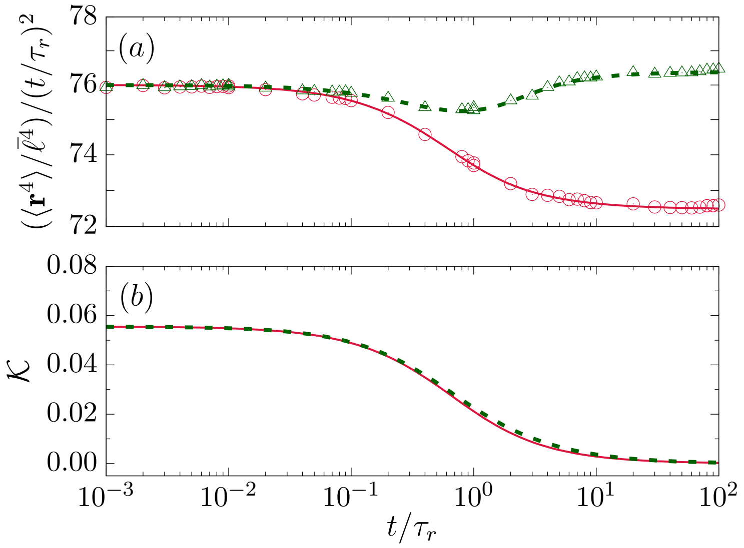

Figure 4.6: (color online) (*a*) Fourth moment and (*b*) kurtosis of displacement as a function of time in $d = 2$ at $\tilde{D}_{\rm a} = 1$. Points denote numerical simulations and lines denoted theory. (*a*) Two crossovers at $Pe = 0.1$ (red ∘): $\langle \mathbf{r}^4\rangle \sim t^2$ to $\sim t^\alpha$ with $\alpha < 2$ to $\sim t^2$. Three crossovers at $Pe = 0.3$ (green △): $\langle \mathbf{r}^4\rangle \sim t^2$ to $\sim t^\alpha$ with $\alpha < 2$ to $\sim t^\alpha$ with $\alpha > 2$ to a final $\sim t^2$. (*c*) Kurtosis as a function of time corresponding to (*a*). (*b*) Kurtosis as a function of time corresponding to $Pe = 0.1$ (red solid line) and $Pe = 0.3$ (green dashed line).

Low activity limit: The difference between the small and long time fourth order moment gives

$$\langle \mathbf{r}^4\rangle(t \to \infty) - \langle \mathbf{r}^4\rangle(t \to 0) = \frac{4D_{\rm ac}}{D_r}\left(4v_0^2 - D_{\rm ac}D_r\right)t^2. \tag{4.29}$$

The fourth moment shows crossovers from $\langle \mathbf{r}^4(t)\rangle \sim t^2$ to $\langle \mathbf{r}^4(t)\rangle \sim t^\alpha$ with $\alpha < 2$, finally to $\langle \mathbf{r}^4(t)\rangle \sim t^2$ behavior provided $v_0^2 < D_{\rm ac}D/4$ dominated by the flucttutaion in the speed. And the condition to get the ballistic behavior in the intermediate time regime is $v_0^2 \geq D_{\rm ac}D/4$ dominated by the speed. In the Fig. (4.6)(*a*), we show the $\langle \mathbf{r}^4(t)\rangle \sim t^\alpha$ behavior in the intermediate time regime. The solid line at $Pe = 0.1$ and $\tilde{D}_{\rm a} = 1$ in Fig. (4.6)(*a*) shows the crossovers from $\langle \mathbf{r}^4(t)\rangle \sim t^2$ to $\langle \mathbf{r}^4(t)\rangle \sim t^\alpha$ with $\alpha < 2$, finally to $\langle \mathbf{r}^4(t)\rangle \sim t^2$ as the condition $Pe^2 < \tilde{D}_{\rm a}/4$ holds. The dashed line, $Pe = 0.3$ and $\tilde{D}_{\rm a} = 1$ in Fig. (4.6)(*a*) shows the crossovers from $\langle \mathbf{r}^4(t)\rangle \sim t^2$ to $\langle \mathbf{r}^4(t)\rangle \sim t^{<2}$ to $\langle \mathbf{r}^4(t)\rangle \sim t^{>2}$, finally to $\langle \mathbf{r}^4(t)\rangle \sim t^2$ as the condition $Pe^2 > \tilde{D}_{\rm a}/4$ holds.

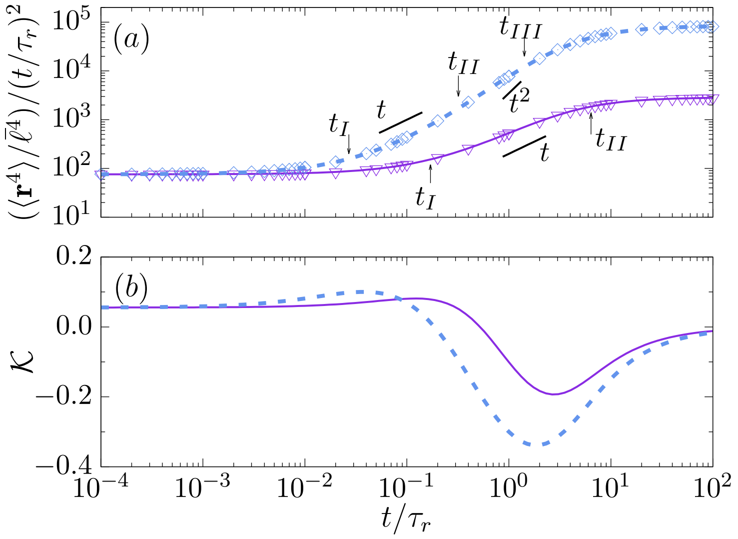

Figure 4.7: (color online) (a) Fourth moment and (b) kurtosis of displacement as a function of time in $d = 2$ at $\tilde{D}_{\rm a} = 1$. (a) Two crossovers at $Pe = v_0\tau_r/\bar{\ell} = 4$ ($\triangledown$) at $t_I \approx 0.17$ and $t_{II} \approx 6.38$. Three crossovers at $Pe = v_0\tau_r/\bar{\ell} = 10$ ($\diamond$) at $t_I \approx 0.027$, $t_{II} \approx 0.32$, and $t_{III} \approx 1.42$. (b) Kurtosis as a function of time at $Pe = 4$ (solid line) and $Pe = 10$ (dashed line).

High activity limit: The small time expansion shows that at smallest time $\langle \mathbf{r}^4(t)\rangle \sim t^2$ which crosses over to $\langle \mathbf{r}^4(t)\rangle \sim t^3$ at $t_I = 3(3D_{\rm ac}^2{+}8D(D_{\rm ac}{+}D))/[3(3D_{\rm ac}{+}4D)v_0^2 - 4D_{\rm ac}^2 D_r]$ provided $v_0^2 > 4D_{\rm ac}^2 D_r/[3(3D_{\rm ac} + 4D)]$.

Further crossovers depend on the activity : In Fig. (4.7)(a) solid line corresponds to $\tilde{D}_{\rm a} = 1$ and $Pe = 4$ shows a first crossover from $\langle \mathbf{r}^4(t)\rangle \sim t^2$ to $\sim t^3$ that appears at $t_I \equiv t_I/\tau_r = 3(3\tilde{D}_{\rm a}^2 + 8(1 + \tilde{D}_{\rm a}))/[3(3\tilde{D}_{\rm a} + 4)Pe^2 - 4\tilde{D}_{\rm a}^2] \approx 0.17$. The second crossover from $\langle \mathbf{r}^4(t)\rangle \sim t^3$ to $\sim t^2$ appears at $t_{II} \equiv t_{II}/\tau_r = 4[3(3\tilde{D}_{\rm a} + 4)Pe^2 - 4\tilde{D}_{\rm a}^2]/[3Pe^4 + 16\tilde{D}_{\rm a}^2 - 4(4 + 5\tilde{D}_{\rm a})Pe^2] \approx 6.38$ as the condition $t_{III} \equiv t_{III}/\tau_r = 5[3Pe^4 + 16\tilde{D}_{\rm a}^2 - 4(4 + 5\tilde{D}_{\rm a})Pe^2]/[10Pe^4 + 64\tilde{D}_{\rm a}^2 - 5(4 + 11\tilde{D}_{\rm a})Pe^2] \approx 0.73 < t_{II}$ is satisfied.

In Fig. (4.7)(a) dashed line, $\tilde{D}_{\rm a} = 1$ and $Pe = 10$ shows first crossover from $\langle \mathbf{r}^4(t)\rangle \sim t^2$ to $\sim t^3$ that appears at $t_I \equiv t_I/\tau_r = 3(3\tilde{D}_{\rm a}^2 + 8(1 + \tilde{D}_{\rm a}))/[3(3\tilde{D}_{\rm a} + 4)Pe^2 - 4\tilde{D}_{\rm a}^2] \approx 0.027$. The second crossover from $\langle \mathbf{r}^4(t)\rangle \sim t^3$ to $\sim t^4$ appears at $t_{II} \equiv t_{II}/\tau_r = 4[3(3\tilde{D}_{\rm a} + 4)Pe^2 - 4\tilde{D}_{\rm a}^2]/[3Pe^4 + 16\tilde{D}_{\rm a}^2 - 4(4 + 5\tilde{D}_{\rm a})Pe^2] \approx 0.32$. The final crossover $\langle \mathbf{r}^4(t)\rangle \sim t^4$ to $\sim t^2$ appears at $t_{III} \equiv t_{III}/\tau_r = 5[3Pe^4 + 16\tilde{D}_{\rm a}^2 -$

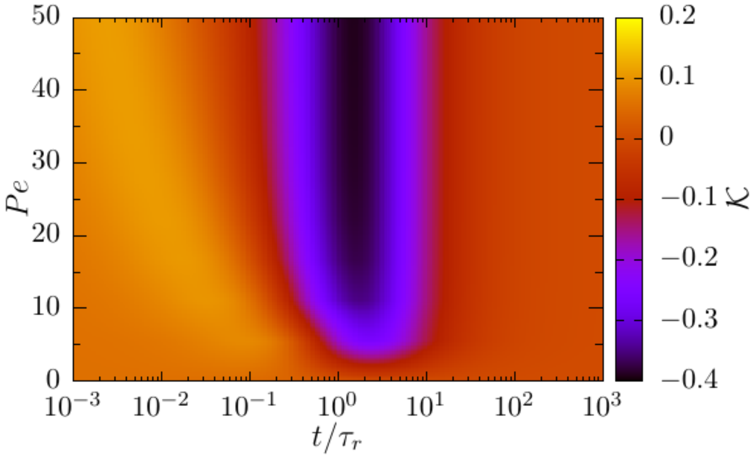

Figure 4.8: (color online) Deviation from Gaussian nature: A heat map of kurtosis $\mathcal{K}$ for different Pe and time t in $d = 2$ at $\tilde{D}_{\mathrm{a}} = 1$.

$4(4 + 5\tilde{D}_{\mathrm{a}})Pe^2]/[10Pe^4 + 64\tilde{D}_{\mathrm{a}}^2 - 5(4 + 11\tilde{D}_{\mathrm{a}})Pe^2] \approx 1.42$.

Calculation of Kurtosis and deviations from Gaussian nature: For the quantitative study of the active particle models and their comparison with the experimental realizations, we calculate kurtosis as a parameter to show the deviation from Gaussian behavior. The fourth moment of a general Gaussian process obeys

$$\mu_4 = \langle \mathbf{r}^2 \rangle^2 + \frac{2}{d} \left(\langle \mathbf{r}^2 \rangle^2 - \langle \mathbf{r} \rangle^4 \right). \tag{4.30}$$

In Eq. (4.25) we have already computed $\langle \mathbf{r}^4 \rangle(t)$ in d-dimensions for our model ABP with chemically driven self-propulsion. It is then straightforward to evaluate the kurtosis in d-dimensions defined as

$$\mathcal{K} = \frac{\langle \mathbf{r}^4 \rangle}{\mu_4} - 1. \tag{4.31}$$

We show the variation of kurtosis as a function of time in Fig. 4.6(b) and Fig. 4.7(b). The deviation from the Gaussian process shows positive kurtosis in the small-time regime due to the speed fluctuation. Fig. 4.6(b) at low Pe shows that positive kurtosis at small time directly goes to a vanishing kurtosis in the long time limit. In Fig. 4.7(b), at a relatively high Pe value, the deviation from the Gaussian process goes from small-time positive kurtosis to intermediate time negative kurtosis to a long time zero kurtosis. At the intermediate time, non-zero negative kurtosis emerges due to the persistence of active motion. For all activity, the kurtosis asymptotically goes to zero at long time. In Fig. (4.8), we show a heat map of kurtosis as a function of time for speed ranges from 0 to 50.

It is interesting to note here that the models of self-propulsion that we studied are aimed to provide reasonable description of experiments on various self-propelled agents. Sometimes the simple Gaussian mechanism of active Ornstein-Uhlenbeck process (AOUP) is invoked to analyze such experiments. Our study clearly indicates that active Brownian particles with speed and orientational fluctuations will show deviations from such a Gaussian process in the intermediate time regime. A comparison of our predictions with experiments then can illustrate to what extent simple processes like AOUP suffice to describe such experimental results.

4.7 Conclusions

We have studied the dynamics of active Brownian particles where active speed is associated with additive Gaussian noise. We observed that the crossovers observed in mean squared displacement and displacement fluctuation are similar to ABPs without speed fluctuations [107] in Chapter 2. We compared the mean squared displacement obtained for this model with that of Chapter 3. For fast speed relaxation $\gamma_v \to \infty$ and large speed fluctuations $D_v \to \infty$ mean squared displacement in Schienbein-Gruler model in Chapter 3 reduces to the results in the current chapter. In the long time limit, the behavior is similar if one identifies $D_{\rm ac} = D_v/\gamma_v^2$. We observed anisotropy in the components of the displacement fluctuation. For low activity limit, $\langle \delta r_{\parallel}^2 \rangle$ shows subdiffusive behavior in the intermediate timescale while $\langle \delta r_{\perp}^2 \rangle$ shows there a ballistic behavior. For high activity limits, both the components of displacement fluctuation exhibit ballistic behavior in the intermediate time scales. The displacement distribution undergoes a transition from Gaussian to extended trajectories back to Gaussian via two intermediate bimodal regimes.

The two bimodalities are characterized by speed fluctuations and persistence. Further, we calculated the fourth moment of displacement and the deviation from the Gaussian process in the intermediate time regime. It is interesting to note that the active Ornstein-Uhlenbeck process is sometimes invoked to study active particles. The non-Gaussian behavior described here can be utilized to identify differences of active particle behavior from such Gaussian processes.

5

Filament- motor proteins system under loading

5.1 Introduction

In the previous chapters, we investigated the three models of active particles and showed rich physics at the single-particle level. In this chapter, we extend our study to motor proteins that collectively drive a rod-like filament. Cytoskeletal filaments and associated motor proteins (MP) stabilize the structure of the cell and determine its dynamics [22, 48]. MP attaches to a filament via an active non-equilibrium process hydrolyzing ATP. The cross-linking MPs extending towards one end of the polar filament can shear filament pairs against each other. Within a living cell, the filaments form a meshwork, in which each filament encounters forces due to its surrounding [49–51]. This force majorly comes from active processes [41]. Recent studies showed that entropic force effects like depletion and diffusible passive cross-linkers lead to a significant sliding on overlapping filaments [56, 110–112]. The gliding motion of filaments on motor proteins assay uses to study the dynamics of cytoskeletal filaments outside the living cell. The competition between opposing groups of MPs can lead to spontaneous oscillations in gliding assays [60]. Filament motion under cooperative MPs and position-dependent load that could arise from passive cross-linkers or harmonic trap showed emergence of stable limit cycle oscillations [56–59]. Similar spontaneous oscillations observe in many contexts in cell biology [64, 65], e.g., sarcomere oscillations, mitotic spindle oscillations, and chromosome oscillations [66–69].

Using mean-field theory and stochastic simulations, we consider the motion of a filament in a gliding assay in the presence of an external force. As has been shown recently, the depletion potential in filament bundles can change from a linear to harmonic form with an increase in filament number [110]. We consider an external force that could be constant or be a function of filament position. The filament on MP assay under constant loading shows a dynamical crossover from stable to unstable phase. Whereas, in the presence of an elastic loading, the filament shows limit cycle oscillations when the number of MPs is large than a critical value [57, 67]. We show how the onset of spontaneous oscillations depends on the MP activity in terms of its extension rate and detachment force, which can be tuned, e.g., by changing ATP concentration [113–115]. We present a linear stability analysis of mean-field equations to find phase diagrams showing linearly stable and unstable phases, separated from stable and unstable spirals. We compare this with numerical solutions of the non-linear equations. The boundary between linear instability and spiral with instability disappears once nonlinearities consider, and the whole region shows stable limit cycle oscillations. We show how a critical number of MPs required to get the onset of spontaneous oscillatory behavior depends on the stiffness of the elastic load acting on the filament. This property might utilize by cells to sense the stiffness of the extra-cellular matrix. The mean-field phase diagrams constitute our first main result. We present a derivation of the mean-field equations for bound MPs using the probability of bound and unbound MPs. In this way, we can identify the limitations in the approximation involved in the two approaches. However, the complete numerical simulation of the model, distinguishing the individual MPs and incorporating the stochastic nature of the dynamics, shows good agreement with the mean-field prediction of the supercritical Hopf bifurcation boundary identifying the onset of spontaneous oscillations. It is our second main result. Deep inside the oscillatory phase, the dynamics show a behavior typical of relaxation oscillators. The predictions of stable oscillatory behavior obtained from the mean-field equations show good agreement with the stochastic simulations. In our analysis, we use parameter values corresponding to microtubule and kinesin motor proteins. It allowed our predictions amenable to direct experimental verification.

The chapter organizes as follows. In Section-5.2 we present our model. The linear stability analysis and its comparison with solutions of non-linear mean-field equations present in Section-5.3. Next, we present the derivation of the mean number of attached MPs using the Fokker-Planck approach in Section-5.4. In Section-5.5, we describe a detailed stochastic simulation method of our model and compare the results with the Fokker-Planck mean-field approach. Finally, we conclude by summarizing the main results in Section-5.6.

5.2 Model

We consider a gliding assay set up (Fig. (5.1)) in which the *tail end* of the MPs are attached irreversibly to a coverslip. The MPs are assumed to be active harmonic linkers having stiffness k_m. The *head end* of MPs can attach to a segment of rigid filament floating on the assay within a cutoff range r_c with a rate ω_a in a diffusion-limited manner. The maximum number of MPs that can attach to the filament of length L is $N = L\,\phi_{MP}$, where ϕ_{MP} is the linear density of MPs attached to the substrate. The attached head of each MP extends along the filament in a directed fashion, from negative to positive end of the filament. This active extension requires energy consumption from ATP hydrolysis that brings the system out of equilibrium. The rate of extension in i-th MP denotes an active velocity v_m^i. It depends on the load force $f_l^i = k_m y^i$ exerted on the MP due to the extension y^i itself. We consider

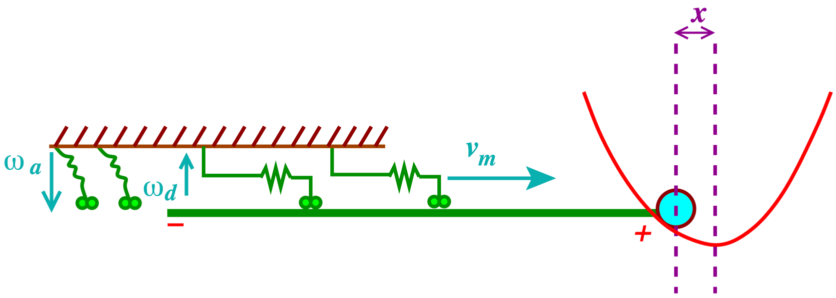

Figure 5.1: (color online) Schematic diagram of the model where a motile MT filament is attached with a harmonic trap of stiffness constant K_T. When attached, kinesin walks along the filament towards right with a velocity v_m, pulling the filament towards left. Figure is adapted from Subhadip Ghosh's thesis.

a piece-wise linear relation [60, 116]

$$v_m^i(f_l^i) = \begin{cases} v_0 & \text{for} \quad f_l^i \leq 0 \\ v_0\left(1 - \frac{f_l^i}{f_s}\right) & \text{for} \quad 0 < f_l^i \leq f_b,\ f_b > f_s \\ -v_{back} & \text{for} \quad f_l^i > f_b \end{cases} \tag{5.1}$$

where f_s denotes the stall force and v_0 stands for the intrinsic MP velocity. For a load force beyond stall, $f_l \geq f_b > f_s$, the velocity saturates to an extremely small negative value v_{back} [60, 116], while supportive loads do not affect the intrinsic MP motion. Assuming the MPs to be forming slip bonds, the load dependent detachment rate is expressed as $\omega_{\rm off} = \omega_d \exp(|f_l^i|/f_d)$. The attachment detachment ratio breaks detailed balance.

All the parameters v_0, ω_a, ω_d, f_s, and f_d characterizing MPs are potentially functions of the ATP concentration in the ambient fluid. An assumption of Michaelis-Menten kinetics of ATP hydrolysis used to describe the ATP dependence of v_0 for kinesin, where v_0 increases linearly for small ATP concentrations to eventually saturate [114, 117]. Previous analysis of kinesin run-lengths demonstrated the ATP dependence of f_d [56, 114]. A change in v_0 leads to various interesting dynamical regimes. We return to this point later in the chapter.

The overdamped dynamics of the filament position x determine by the mechanical force balance,

$$\gamma_f \dot{x} = F_m + F_e \tag{5.2}$$

where the left hand side corresponds to the friction force characterized by γ_f and associated to the relative motion of the filament $\dot{x} := dx/dt$ with respect to the substrate. The n_m number of attached motor proteins exert a total force $F_m = -\sum_{i=1}^{n_m} f_l^i$, and F_e denotes the external loading that acts against the drive of the MPs. The filament motion can in turn drag the attached MPs along with it, such that the extension of i-th MP is given by

$$\dot{y}^i = v_m^i(f_l^i) + \dot{x}. \tag{5.3}$$

5.3 Mean field theory

In this section, we first present a mean-field description of the model. We utilize it to obtain linear stability predictions for dynamical phases and phase transitions presence of external loading on the filament. Numerical solutions of the non-linear mean-field equations use to compare with the linear stability results.

We assume all the MPs to be equivalent within the mean-field approximation, and describe them using the same average extension $y = (1/n_m) \sum_{i=1}^{n_m} y^i$, where n_m denotes the number of attached MPs. To express the equations in a dimensionless form we use the energy scale set by $k_B T$, the time scale ω_d^{-1}, and the length scale $l_0 = \sqrt{k_B T/\gamma_f \omega_d}$. The unit of force is set by $f = \sqrt{k_B T \gamma_f \omega_d}$. Within mean field approximation, the dynamics is described by three coupled non-linear differential equations for dimensionless forms of filament position $\tilde{x} = x/l_0$, mean extension of

MPs $\tilde{y} = y/l_0$, and the attached fraction of MPs $\tilde{n}_m = n_m/N$,

$$\begin{aligned}
\frac{d\tilde{x}}{d\tau} &= \tilde{F}_e - N\tilde{n}_m\tilde{k}_m\tilde{y}, \\
\frac{d\tilde{y}}{d\tau} &= \tilde{v}_0\left(1 - \frac{\tilde{k}_m\tilde{y}}{\tilde{f}_s}\right) + \frac{d\tilde{x}}{d\tau}, \\
\frac{d\tilde{n}_m}{d\tau} &= (1-\tilde{n}_m)\tilde{\omega} - \tilde{n}_m \exp\left[\frac{\tilde{k}_m\tilde{y}}{\tilde{f}_d}\right].
\end{aligned} \tag{5.4}$$

In the above equations we used the dimensionless time $\tau = t\omega_d$, spring constant of MPs $\tilde{k}_m = k_m l_0/f$, attachment ratio $\tilde{\omega} = \omega_a/\omega_d$, stall force $\tilde{f}_s = f_s/f$, and detachment force $\tilde{f}_d = f_d/f$. In the presence of an external load acting against directed MPs, the mean MP extension remains positive. This allows us to express the mean detachment rate as $\omega_{\text{off}} = \omega_d \exp(k_m y/f_d)$. We return to this point in Section-5.4.

In numerical estimates throughout this chapter, we use parameter values typical of microtubule-kinesin assays shown in Table-5.1. These values set the unit of length $l_0 = \sqrt{k_B T/\gamma_f \omega_d} = 33\,\text{nm}$, force $f = k_B T/l_0 = 0.125\,\text{pN}$, and velocity $v = l_0\omega_d = 33\,\text{nm/s}$. In the following, we first perform a linear stability analysis of Eq. (5.4) using a constant loading $\tilde{F}_e$.

Table 5.1: Parameters: Two values of v_0 and f_d correspond to ATP concentrations of $5\,\mu$M and $2\,$mM respectively.

Definition	Parameters	Values
active velocity	v_0	0.006, 0.8μm/s [114, 118]
stall force	f_s	7.5 pN [116, 118]
back velocity	v_{back}	0.02μm/s [116]
detachment force	f_d	1.8, 2.4 pN [56]
attachment rate	ω_a	5, 20/s [114, 119, 120]
detachment rate	ω_d	1/s [118]
motor stiffness	k_m	1.7 pN/nm [56] [1], 0.3 pN/nm [122]
MT viscous friction	γ_f	893 k_BT-s/μm^2 [112]

5.3.1 Constant loading

The fixed points of the system of equations is obtained by setting all the time derivatives of Eq. (5.4) to zero to obtain,

$$\tilde{k}_m \tilde{y}_0 = \tilde{f}_s,\ \tilde{n}_m^0 = \tilde{\omega}/[\tilde{\omega} + \exp(\tilde{f}_s/\tilde{f}_d)] = \tilde{F}_e/N\tilde{f}_s, \tag{5.5}$$

The last relation determines the loading $\tilde{F}_e$ corresponding to the fixed point of a system of N MPs characterized by attachment ratio $\tilde{\omega}$, stall force $\tilde{f}_s$ and detachment force $\tilde{f}_d$. In the absence of position dependence of the external force, the fixed point is $\tilde{x}$- independent. Its stability can be analyzed considering the evolution $d|\psi\rangle/d\tau = \boldsymbol{a}\ |\psi\rangle$ of a small perturbation $|\psi\rangle = (\delta\tilde{x}, \delta\tilde{y}, \delta\tilde{n}_m)$, where $\boldsymbol{a}$ denotes the stability matrix with elements

$$\begin{aligned}
&a_{11} = 0, a_{12} = -\tilde{k}_m N \tilde{n}_m^0, a_{13} = -\tilde{f}_s N, a_{21} = 0,\\
&a_{22} = -\left(\tilde{\mu} + \tilde{k}_m N \tilde{n}_m^0\right), a_{23} = a_{13},\ a_{31} = 0,\\
&a_{32} = -(\tilde{k}_m/\tilde{f}_d)\tilde{\omega}(1 - \tilde{n}_m^0), a_{33} = -\tilde{\omega}/\tilde{n}_m^0,
\end{aligned}$$

where $\tilde{\mu} := \tilde{v}_0/\tilde{y}_0$. Diagonalizing the stability matrix $\boldsymbol{a}$ gives the characteristic equation $\lambda(\lambda^2 + p\lambda + q) = 0$ with solutions $\lambda_1 = 0$, and the other two eigenvalues given by $\lambda_\pm = (1/2)[-p \pm \sqrt{p^2 - 4q}]$. Here $p = -(a_{22} + a_{33}) > 0$ always, and

$$q = (a_{22}a_{33} - a_{13}a_{32}) \tag{5.6}$$

may change sign, thereby controlling the stability of the fixed point. In this case, the smaller eigenvalue λ_- remains negative, λ_+ can become positive when q changes sign from positive to negative. Thus $q = 0$ line denotes the boundary between stable and unstable fixed points. This phase boundary is shown in Fig. (5.2).

The filament moves in a direction opposite to the extension of MPs. Thus, it maintains the force balance in a stable phase. In the unstable phase, the extension of MPs cannot stabilize the filament position, which slides in the direction of extension

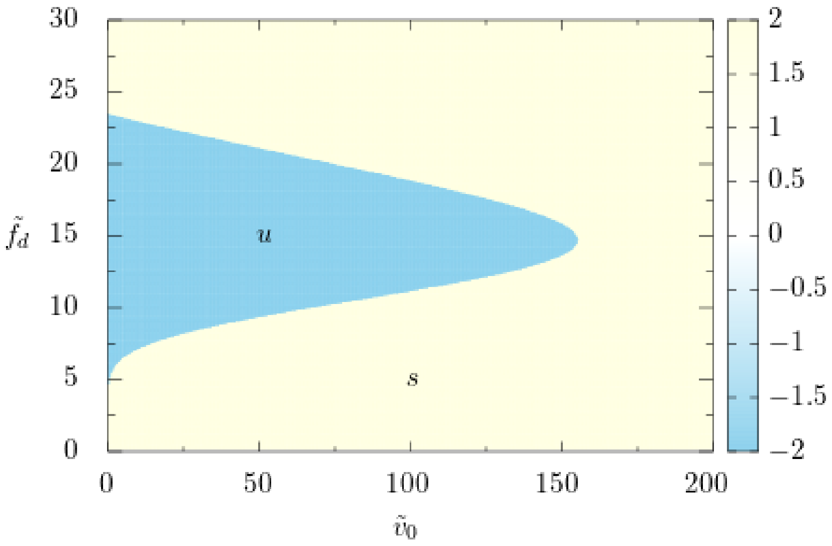

Figure 5.2: (color online) Phase diagram under constant loading in $\tilde{v}_0 - \tilde{f}_d$ plane shown using the heat map of the quantity q defined in Eq. (5.6). We use parameter values typical of a microtubule- kinesin system, $\tilde{k}_m = 450\,(k_m = 1.7\,\text{pN/nm})$, $\tilde{f}_s = 60$, $\tilde{\omega} = 20$ and use $N = 5$ number of MPs. The color-box shows the mapping of q-values to the color code. The light blue (yellow) region denotes unstable (stable) phase under perturbation.

of the attached MPs. However, since the discriminant $p^2 - 4q = (a_{22} - a_{33})^2 + 4a_{13}a_{32} > 0$, the quadratic equation does not support any imaginary part in the eigenvalues. Thus oscillatory behavior, stable or unstable, is ruled out. Under constant external loading, the filament driven by MPs cannot sustain oscillations.

5.3.2 Elastic loading

For elastic loading $\tilde{F}_e = -\tilde{K}_T \tilde{x}$. It might generate on the filament by trapping one of its ends by a laser tweezer or atomic force microscope tip. As in the previous case, we perform a linear stability analysis. The fixed points of the mean-field dynamics are given by

$$\tilde{k}_m \tilde{y}_0 = \tilde{f}_s,\ \tilde{n}_m^0 = \tilde{\omega}/[\tilde{\omega} + \exp(\tilde{f}_s/\tilde{f}_d)],\ \tilde{x}_0 = -\frac{\tilde{n}_m^0 N \tilde{f}_s}{\tilde{K}_T}.$$

The small perturbations around the fixed point $|\psi\rangle = (\delta\tilde{x}, \delta\tilde{y}, \delta\tilde{n}_m)$ evolves with $d|\psi\rangle/d\tau = \boldsymbol{a'}\ |\psi\rangle$ where the elements of the stability matrix $\boldsymbol{a'}$ are given by

$$
\begin{aligned}
& a'_{11} = -\tilde{K}_T, a'_{12} = -\tilde{k}_m \tilde{n}^0_m\, N, a'_{13} = -\tilde{f}_s N, \\
& a'_{21} = a'_{11}, a'_{22} = -(\tilde{\mu} + \tilde{k}_m N \tilde{n}^0_m), a'_{23} = a'_{13}, \\
& a'_{31} = 0, a'_{32} = -(\tilde{k}_m/\tilde{f}_d)\tilde{\omega}(1 - \tilde{n}^0_m), a'_{33} = -\tilde{\omega}/\tilde{n}^0_m,
\end{aligned}
$$

where, as before, $\tilde{\mu} := \tilde{v}_0/\tilde{y}_0$. In the case of constant loading, the matrix element a_{11} was zero, reducing one eigenvalue to zero. The other two eigenvalues were determined by a quadratic equation. However, for elastic loading, $a'_{11} \neq 0$ and the eigenvalues are given by the full cubic equation

$$
\lambda^3 + A\lambda^2 + B\lambda + C = 0 \tag{5.7}
$$

In terms of different matrix elements $A = -\mathrm{Tr}(\boldsymbol{a'})$, $B = \frac{1}{2}\left(a_{ii}a_{jj} - a_{ij}a_{ji}\right)$ where we implied summation over repeated indices, and $C = -\det(\boldsymbol{a'})$. They can be expressed as

$$
\begin{aligned}
& A = \tilde{\mu} + \tilde{K}_T + \tilde{\omega}/\tilde{n}^0_m + \tilde{n}^0_m \tilde{k}_m\, N \\
& B = \tilde{\mu}\tilde{K}_T + \frac{\tilde{\omega}}{\tilde{n}^0_m}(\tilde{\mu} + \tilde{K}_T) + \tilde{k}_m \tilde{\omega} \left[1 - \frac{\tilde{f}_s}{\tilde{f}_d}(1 - \tilde{n}^0_m)\right] N \\
& C = \tilde{\mu}\tilde{K}_T\, \tilde{\omega}/\tilde{n}^0_m.
\end{aligned} \tag{5.8}
$$

Properties of these coefficients determine the existence of different phases and the dynamical behavior of the system. A cubic polynomial has eight possible combinations of real and complex roots. Here A is positive definite, C is positive semi-definite, while B can change its sign. These strong restrictions eliminate four combinations for roots to the cubic polynomial $\lambda_{1,2,3}$. The remaining four combinations characterize the four different phases in the system. The possible combinations are as follows: (i) All three eigenvalues $\lambda_{1,2,3}$ are real negative, characterizing a *linearly stable* (s) phase. (ii) λ_1 is real negative, but $\lambda_{2,3}$ are real positive characterizing a *linearly unstable* (u) phase. (iii) λ_1 is real negative. On the other hand $\lambda_{2,3}$ are complex conjugate pairs with negative real part, $\lambda_{2,3} = -\alpha \pm i\beta$, characterizing a decaying oscillation of perturbations in *stable spiral* (ss) phase. (iv) λ_1 is real negative though $\lambda_{2,3}$ are complex conjugates with positive real part. $\lambda_{2,3} = \alpha \pm i\beta$ with $\alpha > 0$ denotes oscillations with growing amplitude in *unstable spiral* (us) phase.

Phase transitions

(a) *Phase boundary between linearly (un) stable and (un) stable spiral phase:*

The complex conjugate roots disappear as the minimum of the polynomial $p(\lambda) = \lambda^3 + A\lambda^2 + B\lambda$ touches the line $p(\lambda) = -C$, corresponding to two degenerate eigenvalues. The minimum of $p(\lambda)$ is at $\lambda_m = -\frac{A}{3} + \frac{1}{3}\sqrt{A^2 - 3B}$. This condition lead to the phase boundary,

$$C = \left[\frac{A}{3} + \frac{2}{3}\sqrt{A^2 - 3B}\right]\left[-\frac{A}{3} + \frac{1}{3}\sqrt{A^2 - 3B}\right]^2 \tag{5.9}$$

For $B \geq 0$, the boundary is between linear stable (s) and stable spiral (ss) phases. On the the hand, for $B < 0$, it denotes the boundary between unstable spiral (us) and linearly unstable (u) phases.

(b) Phase boundary between stable spiral and unstable spiral phases:

As the sign of the real part α of complex conjugate roots $\lambda_{2,3} = \alpha \pm i\beta$ changes from negative to positive the system becomes unstable and start to oscillate. This transition is captured by setting $\alpha = 0$. This leads to the condition

$$C - AB = 0 \tag{5.10}$$

The growing amplitudes of oscillations in us phase predicted by linear stability analysis gets stabilized by non-linearities into stable limit cycle oscillations, as we show later in Section-5.4 using Fokker-Planck equations and Section-5.5 using stochastic simulations. This denotes a supercritical Hopf bifurcation to a stable limit cycle, e.g., at a critical number of MPs N^* (Fig. (5.3)(a)). The expression of N^* can be obtained by solving Eq. (5.10), a quadratic equation in terms of N^*. Note that in the absence of elastic loading $K_T = 0$ the polynomial coefficient $C = 0$. As a result Eq. (5.10) cannot be satisfied, and the Hopf bifurcation disappears.

At the supercritical Hopf bifurcation, the imaginary part of the eigenvalue $\beta = \sqrt{B}$, so that the MP- filament system shows oscillations with a frequency $f_\omega = \sqrt{B}/2\pi$. Clearly, the frequency of oscillations f_ω depends on the number of MPs, ATP-dependent activity of MPs determined by active velocity, attachment detachment rates, stall force, and detachment force, apart from the effective elastic constant of the external loading force.

Phase diagrams

Using Eqs. (5.9) and (5.10) we present two phase diagrams showing the transitions between the above mentioned phases in Fig. (5.3)(a, b). We use parameter values corresponding to kinesin-microtubule assays (Table-5.1).

In Fig. (5.3)(a), we show the phase diagram in number of MPs N- and attachment ratio $\tilde{\omega}$ plane. This indicates the requirement of a threshold number of MPs N^* to get sustained oscillations in the us phase. In addition, sustained oscillations depend on the activity in the system, parametrized in terms of attachment-detachment ratio $\tilde{\omega}$, active velocity $\tilde{v}_0$ and the detachment force $\tilde{f}_d$. The lines in the plot show phase boundaries obtained from linear stability analysis, using Eqs. (5.9) and (5.10). The boundary between ss and us phase appears via a supercritical Hopf bifurcation. The full non-linear dynamics corresponding to Eq. (5.4) show decaying oscillations in ss phase ($\triangle$), and limit cycle oscillations ($\bigcirc$) in the region denoted by us and u. Clearly, once the non-linearities are considered, the boundary between us and u phase become irrelevant, the whole region inside the us boundary shows limit cycle oscillations.

In Fig. (5.3)(b) we further characterize these dynamical phase transitions in terms the of detachment force $\tilde{f}_d$ and active velocity $\tilde{v}_0$. As before, the linear sta-

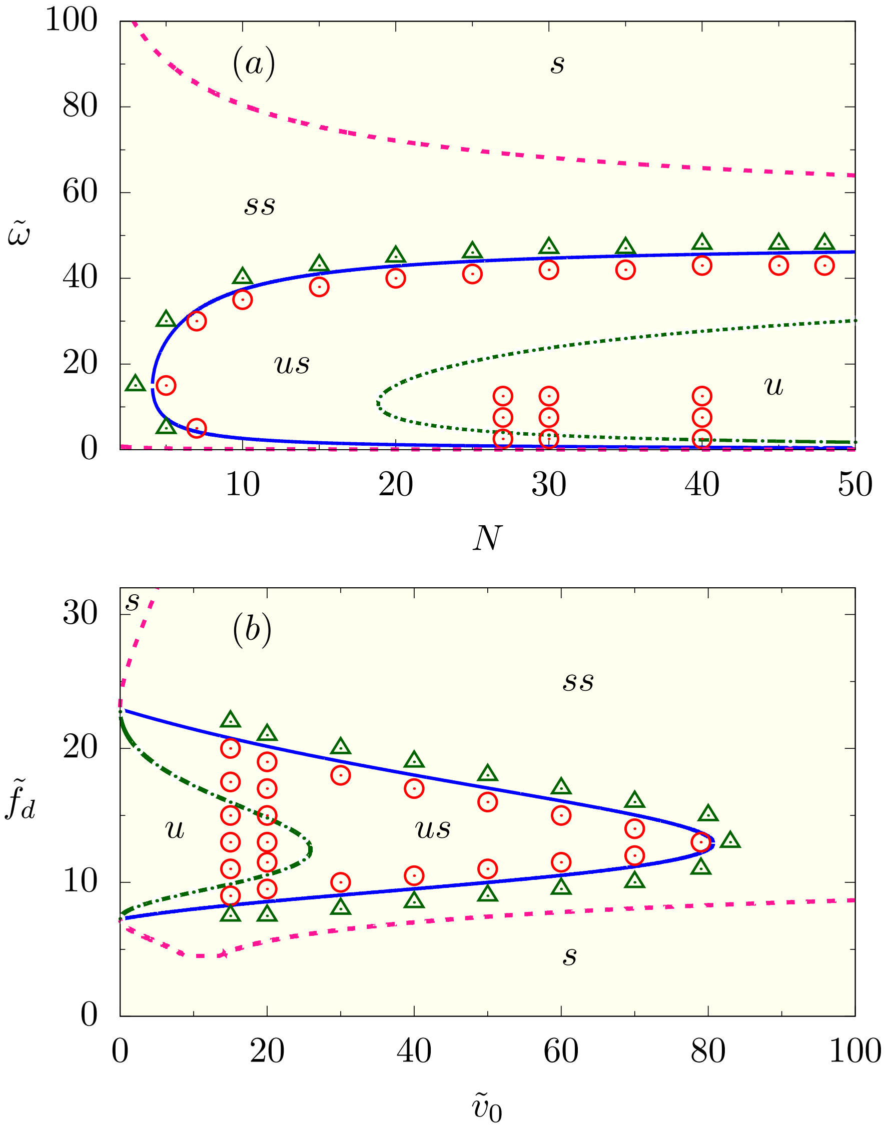

Figure 5.3: Phase diagram for filament in MP assay under elastic loading in $N - \tilde{\omega}$ plane, with $\tilde{k}_m = 450$, $\tilde{v}_0 = 24.24$, $\tilde{f}_s = 60$, $\tilde{f}_d = 19.2$, $\tilde{K}_T = 83$ kept fixed. The lines denote the linear stability phase boundaries between linearly stable (s), stable spiral (ss), unstable spiral (us), and linearly unstable (u) phases. The points denoted by △ and ○ indicate decaying oscillations and limit cycle oscillations, respectively, corresponding to the full non-linear dynamics in Eq. (5.4). Phase diagram for filament in MP assay under harmonic trap in $\tilde{v}_0 - \tilde{f}_d$ plane, keeping $\tilde{k}_m = 450$, $\tilde{\omega} = 20$, $\tilde{f}_s = 60$, $N = 5$ and $\tilde{K}_T = 83$ fixed.

bility analysis shows boundaries between s, ss, us and u phases. The consideration of non-linearities shows that the whole region of us and u display limit cycle oscillations. The stable limit cycle phase appears from a stable spiral via a supercritical Hopf bifurcation. This transition will be explored in further detail in Section-5.5

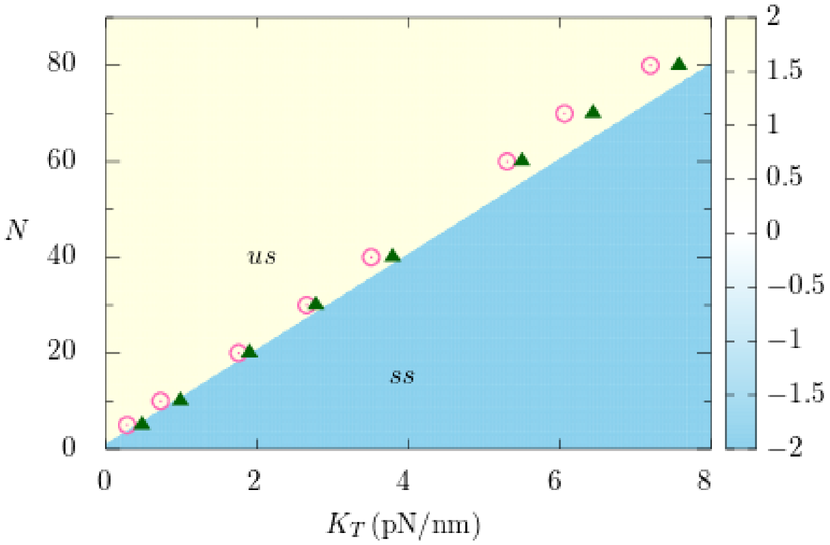

Figure 5.4: The linear stability phase boundary between the stable spiral (blue: ss) and unstable spiral (yellow: us) phase in the plane of elastic loading stiffness K_T and MP number N is shown using the heat map of $C - AB$ in Eq. (5.10). The color box shows the mapping for the values of the function. Parameters used correspond to kinesin-microtubule assay, keeping $\tilde{k}_m = 450$, $\tilde{\omega} = 20$, $\tilde{f}_s = 60$, $\tilde{f}_d = 19.2$, $\tilde{v}_0 = 24.24$ fixed. The points denoted by $\triangle$ and $\bigcirc$ indicate decaying oscillations (ss) and stable limit cycle oscillations (us), respectively, corresponding to the full non-linear dynamics shown in Eq. (5.4). Here we express K_T in units of pN/nm.

using numerical simulations of the stochastic dynamics governing the MPs and filament. Note that the phase boundaries between ss and s in Fig. (5.3)(a, b) are inconsequential, as both the phases are stable in long time limit.

In Fig. (5.4), we show how the onset of stable limit cycle oscillations (us) depends on the number of MPs N recruited for a given rigidity K_T of the elastic loading. The plot uses parameter values corresponding to microtubule-kinesin MP assay, at an ATP concentration of 2 mM. The minimum number of MPs required for the onset of spontaneous oscillations increases with the stiffness K_T of the substrate. While the particular calculations are performed for microtubule-kinesin system, the physical mechanism is equally applicable for acto-myosin systems. Our simple setup has a parallel in the rigidity sensing by cells, where contractile acto-myosin system couples to the extra-cellular matrix (ECM) via an adhesion complex consisting of alpha-actinin and integrin [123, 124]. The range of K_T values used in Fig. (5.4) belongs to the range of rigidities of sub-micron elastomeric pillars used in cell spreading experiments [124]. The cell may utilize an increase of processive myosin bundles, required for the onset of oscillations (tugging), as a strategy to sense the ECM stiffness [124, 125]. In fact, larger multifilament assemblies of myosin is noted near more rigid substrate [124].

The parameter values used in the above phase diagrams correspond to a gliding assay of microtubule on kinesin MPs (Table-5.1). The elastic loading on the filament can be applied by optical tweezers or atomic force microscopes [57, 122, 126]. In Fig. $(5.3)(a, b)$, we used a value of dimensionless stiffness $\tilde{K}_T$ that corresponds to $0.3\,\mathrm{pN/nm}$. While the location of phase boundaries depends on $\tilde{K}_T$, the qualitative features remain unaltered. In the limit of extremely small $\tilde{K}_T$, however, the harmonic trap can act like a constant loading, as was shown in Ref. [127]. Within the cell, our study has relevance for the relative sliding motion of filaments where the loading might be provided by other cellular components, or the filament bending [67], and may have implications for rigidity sensing by cells [123, 124]. We considered length stabilized filaments, which are typically used in gliding assay experiments, thus disregarding the possible effects of active polymerization depolymerization of filaments in living cells [22].

5.4 Fokker-Planck approach to mean field

In this section, we present a Fokker-Planck description, derive the mean-field equations, and discuss its limitations. Finally, we perform detailed numerical simulations of the full stochastic model and compare the results with mean-field predictions.

Having established the phase diagrams using mean field equations and linear stability analysis, in this section we use a Fokker-Planck approach [67] involving the probability distributions $P_{a,d}(y, t)$ of attached and detached fractions of MPs to derive and analyze the mean field equations. The distribution functions obey the normalization $\int_{-\infty}^{\infty}(P_a + P_d)\,dy = 1$, and evolve as

$$\begin{aligned} \partial_t P_a + \partial_y J_a &= \omega_a P_d - \omega_d P_a \\ \partial_t P_d + \partial_y J_d &= -\omega_a P_d + \omega_d P_a, \end{aligned} \tag{5.11}$$

where, the probability currents

$$\begin{aligned} J_a &= \dot{y} P_a(y,t) - D_a\,\partial_y P_a(y,t) \\ J_d &= -\nu y P_d(y,t) - D_d\,\partial_y P_d(y,t). \end{aligned} \tag{5.12}$$

Here D_a, D_d are the diffusion coefficient of attached and detached MPs, respectively, and ν is the relaxation rate of the extension for the detached MPs.

As the typical relaxation rate is much faster than the attachment rate, $\nu \gg \omega_a$, one can assume the detached MPs relaxes immediately to equilibrium distribution,

$$P_d(y,t) = \tilde{n}_d(t)\,A\exp\left(-\frac{k_m y^2}{2k_B T}\right) \tag{5.13}$$

with normalization $A = (k_m/2\pi k_B T)^{1/2}$. As a result, the fraction of detached MPs $\tilde{n}_d(t) = \int_{-\infty}^{\infty} dy P_d(y,t)$. This is related to the fraction of attached MPs $\tilde{n}_m(t) = \int_{-\infty}^{\infty} dy P_a(y,t)$ via the conservation of total probability $\tilde{n}_m(t) = 1 - \tilde{n}_d(t)$. Integrating the first equation of Eq. (5.11) we get

$$\frac{d\tilde{n}_m}{dt} = (1-\tilde{n}_m)\omega_a - \langle \omega_d(y)\rangle \tilde{n}_m \tag{5.14}$$

where $\langle \omega_d(y)\rangle := \int_{-\infty}^{\infty} dy P_a(y,t)\omega_d(y) / \int_{-\infty}^{\infty} dy P_a(y,t)$. Using the expression for slip bond $\omega_d(y) = \omega_d \exp(k_m|y|/f_d)$ leads to

$$\frac{d\tilde{n}_m}{dt} = (1-\tilde{n}_m)\omega_a - \omega_d \langle e^{k_m|y|/f_d}\rangle \tilde{n}_m \tag{5.15}$$

By Jensen's inequality $\langle e^{k_m|y|/f_d}\rangle \geq e^{k_m\bar{y}/f_d}$ with $\bar{y} = \langle |y| \rangle$ denoting the mean extension in the attached state. Thus the actual relaxation $d\tilde{n}_m/dt$ is slower than

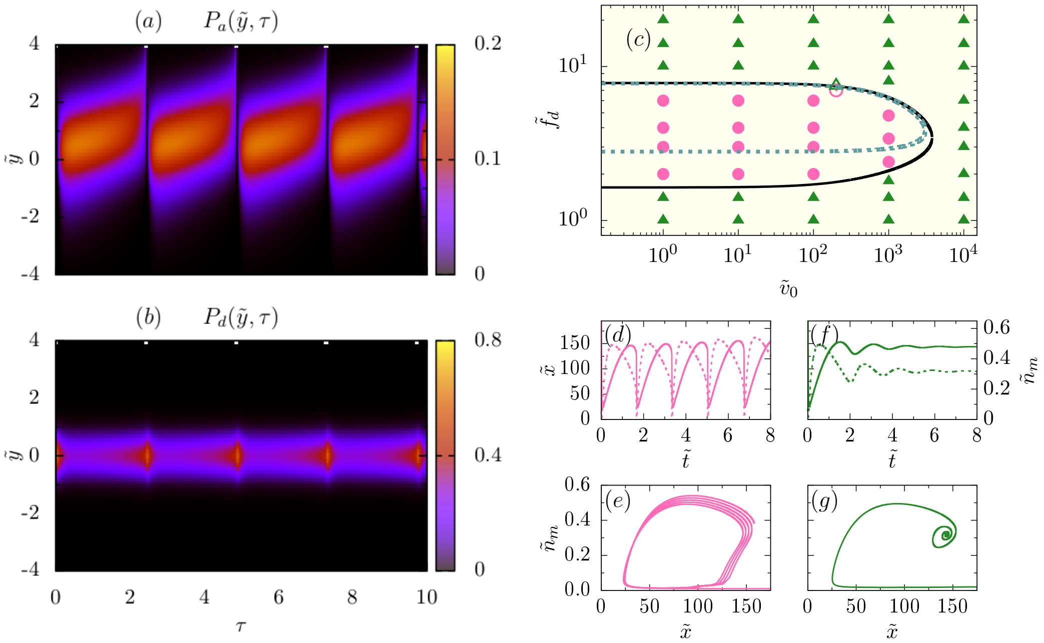

Figure 5.5: (color online) (a, b) Kymographs show the time evolution of the probability distributions of MPs with extension $\tilde{y}$: (a) in the attached state (P_a), and (b) in the detached state (P_d). The color-box describes the values of probability distributions. The relaxation dynamics are determined by dimensionless diffusion constants $\tilde{D}_a = 15.6$, $\tilde{D}_d = 17.4$, and the relaxation rate $\tilde{\nu} = 80$. Other parameter values used are $\tilde{v}_0 = 50$, $\tilde{f}_d = 4$, $\tilde{k}_m = 4.57$, $\tilde{\omega} = 5$, $\tilde{f}_s = 14.29$, $N = 160$ and $\tilde{K}_T = 4.57$. (c) Phase diagram for harmonically trapped microtubule-kinesin assay in $\tilde{v}_0$-$\tilde{f}_d$ plane, at fixed $\tilde{k}_m = 4.57$, $\tilde{\omega} = 5$, $\tilde{f}_s = 14.29$, $N = 160$ and $\tilde{K}_T = 4.57$. The points denote the two phases characterized by decaying oscillations ($\triangle$) and stable limit cycle oscillations ($\bigcirc$) obtained from numerical simulations. The solid black line identifies the boundary of supercritical Hopf-bifurcation predicted by Eq. (5.10). (d, e) Dynamics corresponding to open $\circ$. (d) Time series of $\tilde{x}$ (solid line) and $\tilde{n}_m$ (dashed line). (e) Unstable limit cycle corresponding to time series of growing oscillation in (d). (f, g) Dynamics corresponding to open $\triangle$. (d) Time series of $\tilde{x}$ (solid line) and $\tilde{n}_m$ (dashed line). (e) Stable limit cycle corresponding to time series of decaying oscillation in (f).

that assumed in Eq. (5.4).

The active extension and relaxation dynamics in terms of $P_{a,d}(y, t)$ is shown in Fig. (5.5) by numerically integrating the Fokker-Planck Eqs. (Eqs. (5.11) and (5.12)) along with the evolution of filament position x (Eq. (5.2)), and mean extension of MPs following

$$\dot{y} = v_m(y) + \dot{x}. \tag{5.16}$$

In the above equation the piecewise linear form of v_m is used from Eq. (5.1) replacing the load force $f_l = k_m y$. In Eq. (5.2), at this point, we use $F_m = -k_m \sum_{i=1}^{n_m} y^i = -k_m \int_{-\infty}^{\infty} dy\, y\, P_a(y,t)$. This reduces Eq. (5.2) to

$$\gamma_f \dot{x} = -K_T x - k_m \int_{-\infty}^{\infty} dy\, y\, P_a(y,t). \tag{5.17}$$

In plotting this graph we used $D_d = k_B T/\gamma_f$, $D_a < D_d$, and $\nu = k_m/\gamma_f$. The last choice maintains $\nu \gg \omega_a$. The parameters used correspond to kinesin-microtubule system (Table-(5.1)). Here the unit of length is chosen to be $l_0 = 8\,\mathrm{nm}$, the dimer-size of microtubules [22]. The unit of force is $f = k_B T/l_0 = 0.525\,\mathrm{pN}$, and time is $\omega_d^{-1} = 1\,\mathrm{s}$. As before, we express dimensionless extensions $\tilde{y} = y/l_0$, $\tilde{x} = x/l_0$ and dimensionless time $\tau = \omega_d t$.

Here, $\gamma_f = 893\ k_B T\text{-}s\text{-}\mu\mathrm{m}^{-2} = 3.75\ \mathrm{pN\text{-}s\text{-}}\mu\mathrm{m}^{-1}$, in dimensionless unit $\tilde{\gamma}_f = 0.057$. Thus, we re-define linear stability coefficients A, B, and C,

$$\begin{aligned}
A &= \tilde{\mu} + \frac{\tilde{K}_T}{\tilde{\gamma}_f} + \frac{\tilde{\omega}}{\tilde{n}_m^0} + \frac{\tilde{n}_m^0 \tilde{k}_m N}{\tilde{\gamma}_f} \\
B &= \frac{\tilde{\mu}\tilde{K}_T}{\tilde{\gamma}_f} + \frac{\tilde{\omega}}{\tilde{n}_m^0}\left(\tilde{\mu} + \frac{\tilde{K}_T}{\tilde{\gamma}_f}\right) + \frac{\tilde{k}_m \tilde{\omega}}{\tilde{\gamma}_f}\left[1 - \frac{\tilde{f}_s}{\tilde{f}_d}(1 - \tilde{n}_m^0)\right] N \\
C &= \frac{\tilde{\mu}\tilde{K}_T \tilde{\omega}}{\tilde{\gamma}_f \tilde{n}_m^0}.
\end{aligned} \tag{5.18}$$

Due to the directed nature of the MP extension and the loading acting against MPs on an average, the mean extension $\tilde{y}$ of the attached fraction remains positive (Fig. (5.5)(a)), a fact used in replacing $\exp(k_m|\tilde{y}|/f_d)$ by $\exp(k_m\tilde{y}/f_d)$ in the mean field description of Eq. (5.4). As Fig. (5.5)(a) shows in terms of the evolution of $P_a(\tilde{y},\tau)$, the mean extension grows slowly up to a maximum, before relaxing back rapidly to zero in a time periodic manner. This is a characteristic of relaxation oscillators [128]. With detachment of one MP, the shared load on other attached MPs increases, increasing the effective rate of detachment. This mediates an avalanche of MP detachment leading to the rapid relaxation. Once relaxed, MPs reattaches, maintaining oscillations. The avalanche in detachments lead to an associated rapid

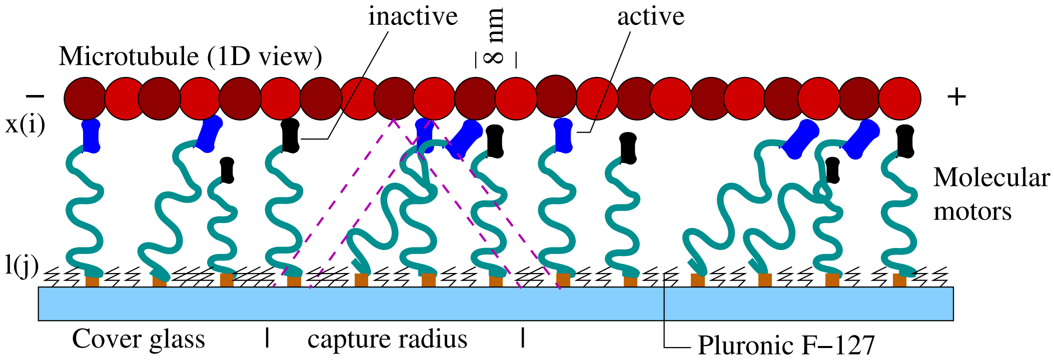

Figure 5.6: (color online) Schematic representation of Microtubule-kinesin motors. Motile microtubule filament attaches with a harmonic trap of stiffness constant K_T. The attached active kinesin represent in blue head walks along the filament towards the right with a velocity v_m, pulling the filament towards the left. Pluronic F-127 used for surface blocking.

increase in $P_d(\tilde{y},\tau)$ (Fig. (5.5)(b)). Note that the distribution $P_d(\tilde{y},\tau)$ maintains a maximum at $\tilde{y} = 0$, and is always symmetric around $\tilde{y} = 0$, vindicating the simplification used in Eq. (5.13).

Performing the numerical integration over a range of activity $\tilde{v}_0$ and detachment force $\tilde{f}_d$ we obtain the phase diagram in Fig. (5.5)(c). It shows two phases, one is characterized by decaying oscillations corresponding to stability ($\triangle$), and the other displays stable limit cycle oscillations ($\bigcirc$). The phase boundary obtained from numerical integration shows good agreement with analytic result, Eq. (5.10).

5.5 Stochastic simulation

In this section, we describe the stochastic simulation method of our model. We compare the simulation results with the numerical integration of Fokker-Planck equations.

We perform a stochastic simulation of the MP-filament model described in Section-5.2. The schematic diagram of the stochastic simulation method present in Fig. (5.6). We consider a kinesin-microtubule system with the microtubule held in its positive end using a harmonic trap of strength K_T. Myosin- F-actin with the

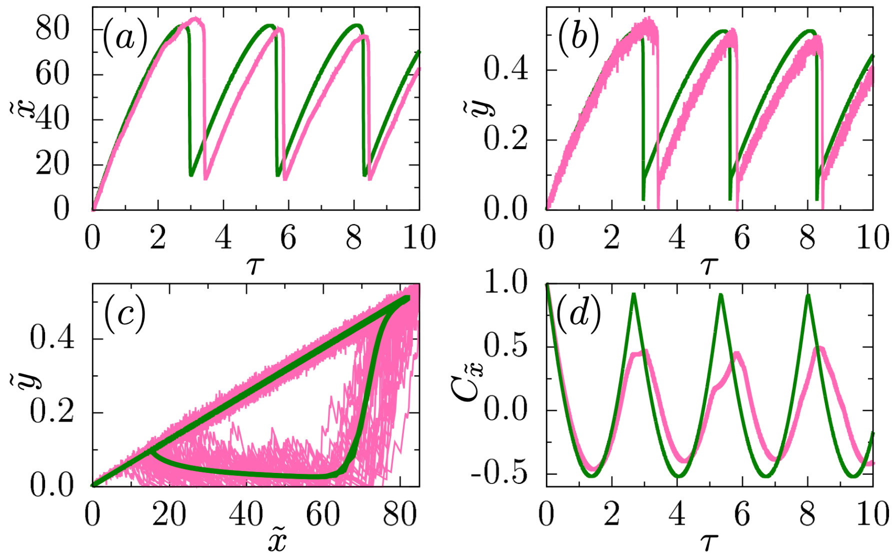

Figure 5.7: (color online) Time evolutions of (a) microtubule displacement $\tilde{x}(\tau)$, and (b) mean kinsein extension $\tilde{y}(\tau)$. (c) A parametric plot of $\tilde{x}(\tau)$ and $\tilde{y}(\tau)$ shows stable limit cycle. (d) Correlation function of microtubule displacement $C_{\tilde{x}}(\tau)$ in the time-periodic steady state. The red (green) lines in all these figures correspond to numerical simulations (solutions to the Fokker-Planck based mean field equations). We used $\tilde{v}_0 = 50$, $\tilde{f}_d = 4$. All other parameter values are the same as in Fig. (5.5)(c).

F-actin held by an elastic load provided by a laser tweezer was considered before in the experiment, Ref. [57]. We model the microtubule as a connected rigid string of $\sigma = 8$ nm segments. In this section, we use $l_0 = \sigma$ as the unit of length, which sets the unit of force $f = k_B T / l_0 = 0.525\,\mathrm{pN}$. We still use the unit of time $\omega_d^{-1} = 1\,\mathrm{s}$. The i-th kinesin can attach to a microtubule segment within the cutoff or capture radius(Fig. (5.6)) $r_c/l_0 = 1.0$ stochastically with rate ω_a. When attached, the MP extends towards the plus(minus) end of the microtubule stochastically with a rate of v_m/l_0 with $v_m > 0$($v_m < 0$). The instantaneous load force on the i-th MP is $f_l^i = k_m y^i$, expressed in terms of the extension $y^i(t)$. We use Eq. (5.1) for the load dependence of the extension rate. The MPs detach from the filament stochastically with the rate $\omega_d \exp(k_m |y^i| / f_d)$. Thermal fluctuation of micotubule considered as Gaussian noise with diffusion constant of microtubule $D_{MT} = k_B T / \gamma_f \sim 10^{-3} \mu\mathrm{m}^2$ sec^{-1}. Thus, the time evolution of filament position in Eq. (5.2) with thermal fluctuation integrates numerically using Euler-Maruyama integration. We simulate a large number of MPs $N = 160$ to compare with mean-field results.

The dynamics deep inside the stable limit cycle phase is illustrated in Fig. (5.7), using results from numerical simulations. We plot the evolutions of filament position $\tilde{x}(\tau)$ and mean extension of kinesins $\tilde{y}(\tau)$ deep inside the limit cycle phase ($\tilde{v}_0 = 50$, $\tilde{f}_d = 4$). They show anharmonic oscillations with a well defined periodicity (Fig. (5.7)(*a*,*b*)). The slow extension (increase in $\tilde{x}$) followed by rapid relaxation is a typical relaxation oscillator behavior [128]. Here MP detachment avalanches the rapid relaxation. When presented as a parametric plot in $\tilde{x}$-$\tilde{y}$ plane, they clearly show a stable limit cycle, although with a spread in the trajectories due to their inherent stochastic nature (Fig. (5.7)(*c*)). Similar spread has been observed in *in vitro* experiments [57]. The limit cycle oscillations are independent of initial conditions. Using the time series in Fig. (5.7)(*a*), we obtain the two-time correlation function of the microtubule displacement $C_{\tilde{x}}(\tau) = \langle \tilde{\delta} x(\tau) \tilde{\delta} x(\tilde{0}) \rangle / \langle \tilde{\delta} x^2(\tilde{0}) \rangle$ where $\delta x = x - \langle x \rangle$ is measured in the time-periodic steady state shows in Fig. (5.7)(*d*).

We compare the simulation results with the Fokker Planck description developed in the previous subsection. For that we use the equation for $P_a(\tilde{y}, \tau)$ using Eqs. (5.11), (5.12) and the expression of $P_d(\tilde{y}, \tau)$ from Eq. (5.13). To determine $\tilde{n}_d(\tau) = 1 - \tilde{n}_m(\tau)$ we use Eq. (5.15). These equations are solved numerically along with Eq. (5.16) and (5.17). The comparisons are displayed in Fig. (5.7), and show semi-quantitative agreement.

5.6 Conclusions

We have studied the dynamics of a cytoskeletal filament in a motor protein (MP) assay under external loading. We used a mean-field description along with linear stability analysis to determine various phase boundaries. Under constant loading, the system shows a transition from stable to unstable behavior. The over-damped active system under harmonic loading displays an emergence of spontaneous oscillations via a supercritical Hopf bifurcation. In linear stability analysis, this appears as a boundary between a stable and unstable spiral phase. The non-linearities make the boundary between unstable spiral and linear instability irrelevant, with the system showing stable limit cycle oscillations in both of them. The increase in the critical number of MPs required at the onset of stable limit cycle oscillations with an increase in the stiffness of elastic loading may be utilized by spreading cells for sensing the stiffness of the extra-cellular matrix. Using a Fokker-Planck description, we analyzed the limitations of the mean-field equations used. Finally, we performed numerical simulations involving stochastic dynamics of individual MPs and the filament. The resulting phase diagram shows good agreement with the mean-field prediction. While the stochastic dynamics display a characteristic spread of trajectories, they reproduce the limit cycle behavior in an average sense. We obtained a semi-quantitative agreement between the mean-field prediction for time evolution with stochastic trajectories. In our numerical analysis, we used parameters corresponding to the microtubule-kinesin system. Our method is equally applicable to other filament-MP systems, e.g., filamentous actin-myosin. The quantitative results presented here are amenable to direct experimental verifications in gliding assay setups of microtubule and kinesin molecules. The parameter values used in Fig. (5.7) correspond to kinesin extension rate $0.4\,\mu$m/s, and a detachment force 2 pN.

We used a trapping potential of strength $K_T = 0.3\,\mathrm{pN/nm}$, which can control in experiments [57, 122, 126]. The amplitude and frequency of oscillations of the microtubule in the limit cycle phase shown in Fig. (5.7) correspond to $0.4\,\mu$m and 0.5 Hz, respectively. On the other hand, for MPs, while the frequency remains around 0.5 Hz, the amplitude of oscillation is $\sim 4\,\mathrm{nm}$.

In the next chapter, we consider the semiflexibility of the filaments. We study the statistical mechanics of a semiflexible filament driven by motor proteins assay in two dimensions.

6

Semiflexible filament in a gliding assay

6.1 Introduction

The cytoskeleton in living cells consists of semiflexible filaments like F-actins and microtubules, and motor proteins (MPs) [22, 48]. The MPs hydrolyse ATP to undergo binding, unbinding cycles and move in a directional manner along the associated filaments [5, 52, 53]. On cross-linked filaments of cytoskeleton, the active chemical cycle of MPs generate mechanical stress to maintain the cell structure and dynamics [39, 55]. The MPs drive energy flux at the smallest length scales of the system, typical of active matter [2, 29, 54]. This breaks the detailed balance, and the equilibrium fluctuation- dissipation relation.

The *in vitro* molecular motor assays are often used to derive direct physical understanding of the active properties of filaments and MPs [17, 18, 61, 129]. The motility assay setup with actin filaments or microtubules floating on top of an immobilized MP- bed, showed fascinating dynamical behaviors, e.g., spiral formation, collective gliding and swirling [19–21, 61, 63]. For spiral formation of microtubules on kinesin assay [19, 61], a microtubule- specific theory has been recently developed [62]. However, similar behavior has been observed in other active polymer studies [130–135].

In this chapter we consider a detailed theoretical model of a two- dimensional motility assay, and study the change in shape and size of an extensible semiflexible polymer driven by MPs. In our model, the MPs are immobilized by attachment of their *tails* to a substrate, while the *head* domains undergo active attachment- detachment with the filament, and drive the filament by performing active extension. The detachment and extension rates are assumed to be load dependent in a manner consistent with established MP models [67, 114]. Most of the current studies which attempt to understand the static and dynamic properties of a filament in the presence of activity, either consider the polymers as made up active monomers with a constant velocity in the tangential direction or introduce activity via an active noise term [130–144]. However, two-fold effect of MPs on the conformational and dynamical properties of a semiflexible filament are profound and therefore need explicit consideration [106, 117, 145].

We perform extensive numerical simulations to study the polymer in motility assay, and use phenomenological arguments to illustrate several findings. We obtain a *first order* conformational transition from open chain to spiral as a function of the MP activity, which has two main aspects: (i) the rate of extension, and (ii) the turnover – given by the ratio of attachment- detachment rates. The transition is characterized by the coexistence of the open and spiral phases. Obtaining the resultant phase diagram is the first main contribution of this chapter. It shows a remarkable reentrance from open chain to spiral to open chain with increasing activity. The spirals are characterized by their turning number. An approximate data-collapse of the non- monotonic variations of the mean squared turning number with active extension for different turnovers leads to a scaling function. This is supported by a torque- balance argument, which also describes the phase boundary. This is our second main contribution. The distribution function of the end- to- end separation shows bi-stability capturing the coexistence between open and spiral states. We use radius of gyration tensor to determine the instantaneous size, shape, and effective orientation of the polymer. Accompanied by the reentrance transition, the polymer size, and shape- asymmetry show non-monotonic variations with activity. The non- monotonic variation in size shows qualitative difference with respect to that of polymers in active bath [132]. We study the steady state dynamics using the two- time autocorrelation functions. The dynamics of turning number, size and shape of the polymer depend on the conformational changes. Their autocorrelations reveal double- exponential decay at phase- coexistence, corresponding to the relaxation within a state, and slow transition between the states. The correlation time shows non-monotonic variation with a maximum at an intermediate rate of MP extension. This is our third main result. The autocorrelation function of the instantaneous orientation of the polymer conformation shows an overall single time-scale decay, and oscillations related to the rotation of the spirals at higher activity. The corresponding correlation time decreases with MP extension rate as a power-law.

The plan of the chapter is as follows. In Section-6.2 we present the detailed model of the motility assay and the extensible semiflexible polymer. In Section-6.3 we demonstrate the spiral formation, rotation and breaking with the help of turning number. Using its probability distribution, in Section-6.4, we demonstrate a first order phase transition from open chain to spiral with increasing activity. The phase diagram is presented in Section-6.5. In Section-6.6 we discuss an approximate scaling form of the turning number fluctuations. In Section-6.7 the end- to- end distribution function, the change in polymers size, and shape is discussed. This is followed by a discussion of the polymer dynamics in terms of autocorrelation functions of turning number, polymer size, shape, and orientation in Section-6.8. Finally, we conclude in Section-6.9 summarizing our main results.

6.2 Model and simulation

6.2.1 Model

We consider an extensible semi-flexible polymer of N-beads with monomer positions $\mathbf{r}_1$, $\mathbf{r}_2$, $\ldots, \mathbf{r}_N$. The chain is described by both stretching and bending energy terms. The bond vectors $\mathbf{b}_i = \mathbf{r}_{i+1} - \mathbf{r}_i$ are defined for $i = 1, 2, \ldots, N-1$ and are oriented along the local tangents $\hat{t}_i = \mathbf{b}_i/|\mathbf{b}_i|$. The connectivity of the chain is maintained by the stretching- energy

$$\mathcal{E}_s = \sum_{i=1}^{N-1} \frac{A}{2r_0} \left[\mathbf{b}_i - r_0 \hat{t}_i\right]^2, \tag{6.1}$$

characterized by the bond- stiffness A and the equilibrium bond- length r_0. The bending rigidity κ of the semiflexible filament leads to a bending energy cost between the consecutive tangent vectors,

$$\mathcal{E}_b = \sum_{i=1}^{N-2} \frac{\kappa}{2r_0} \left[\hat{t}_{i+1} - \hat{t}_i\right]^2. \tag{6.2}$$

The self-avoidance of the filament is implemented through a short-ranged Weeks-Chandler-Anderson repulsion between all the non-bonded pairs of beads i and j,

$$\begin{aligned} \mathcal{E}_{\rm WCA} &= 4[(\sigma/r_{ij})^{12} - (\sigma/r_{ij})^6 + 1/4] \text{ if } r_{ij} < 2^{1/6}\sigma \\ &= 0, \text{ otherwise.} \end{aligned} \tag{6.3}$$

Thus the full polymer model is described by the energy cost $\mathcal{E} = \mathcal{E}_s + \mathcal{E}_b + \mathcal{E}_{\rm WCA}$. The energy and length scales are set by ϵ and σ respectively. The corresponding microscopic time scale is $\tau_0 = \sigma\sqrt{m/\epsilon}$.

In the motility assay setup, the polymer is placed on a substrate of MPs (Fig. (6.1)). The MPs are assumed to be immobilized by attachment of their *tails* irreversibly to the substrate at positions $\mathbf{r}_0^i = (x_0^i, y_0^i)$ placed on a two dimensional square lattice with a uniform density ρ. The *heads* of MPs can attach to the nearest bead of

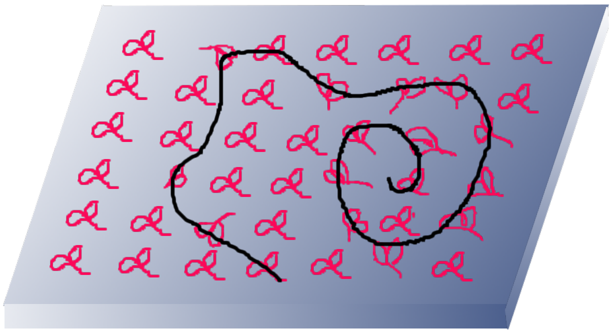

Figure 6.1: (color online) A schematic diagram of the system showing a polymer floating on the motility assay. The *tails* of MPs are attached irreversibly on a square grid. The *head* domains can attach to the filament, when any segment of it comes within the capture radius. The active extension of the attached *head* along the filament generates force in the opposite direction. The MP *stalk* is modeled as a harmonic spring.

the polymer within a capture radius r_c through a diffusion limited process which is implemented by a constant attachment-rate $\omega_{\rm on}$. The stalks of the MPs are modeled as elastic linkers of stiffness k_m. The extension $\Delta\mathbf{r}$ of a MP in the attached state generates an elastic force $\mathbf{f}_l = -k_m\Delta\mathbf{r}$ on the segment of the filament it is attached to. This extension can be due to two processes: (i) the attached head may be dragged by the filament, and (ii) it can move actively over the filament towards one of its ends. The attached head moves along the bonds. Thus its instantaneous location can be anywhere between the beads. The MP- extension generates a force $\mathbf{f}_l$, which is divided between the beads forming the bond on which the MP- head is located. This is done using the lever rule, and depends on the relative separation of the MP- head with respect to the polymer beads. The nearer the MP is to a specific bead, the larger is the share of the force on it. For example, attached kinesins (dyeneins) move along the microtubule towards its positive (negative) end. The active velocity is known to decrease with resistive load, and can be modeled as [114, 117]

$$v_t^a(f_t) = \frac{v_0}{1 + d_0 \exp(f_t/f_s)}, \tag{6.4}$$

where $f_t = -\mathbf{f}_l.\hat{t}$, $d_0 = 0.01$ and f_s is the stall force. Here v_0 denotes the velocity of free MP. The actual extension $\Delta\mathbf{r}$, and as a result f_t on different MP is different. It depends on the time spent in the attached state, which in turn depends on the stochastic detachment rate

$$\omega_{\rm off} = \omega_0 \exp(f_l/f_d), \tag{6.5}$$

where ω_0 is the bare off rate, $f_l = |\mathbf{f}_l|$ and f_d sets the scale of the detachment force. The ratio $\omega_{\rm on} : \omega_{\rm off}$ does not obey detailed balance. The net force imparted by MPs depend on the processivity $\Omega(f_l) = \omega_{\rm on}/(\omega_{\rm on} + \omega_0 \exp(f_l/f_d)\,)$.

6.2.2 Simulation

We perform molecular dynamics simulations of the polymer using beads of unit mass $m = 1$, in the presence of a Langevin heat bath of isotropic friction per bead $\gamma = 1/\tau_0$ keeping the temperature constant at $k_BT = 1.0\,\epsilon$. We use bond- stiffness $A = 100\,\epsilon/\sigma$ for the $N = 64$ bead chain.

In equilibrium worm-like-chain, the ratio of the contour length $L = (N-1)r_0$ to persistence length $\lambda = 2\kappa/[(d-1)k_BT]$, the rigidity parameter $u = L/\lambda$, determines whether the filament behaves like a rigid rod or a flexible polymer [93, 94]. The end-to-end distribution of worm-like-chain shows Gaussian chain behavior with a single maximum at zero- separation at $u \approx 10$, and a rigid-rod behavior with a single peak near full extension of the chain at $u \approx 1$. In the semiflexible regime of u =3 to 4, the free energy shows a characteristic double minimum corresponding to the coexistence of both the rigid rod and flexible chain behaviors. To probe this regime, we choose $\kappa/r_0k_BT = 9.46$ corresponding to $u = 3.33$. Unless stated otherwise, we choose the equilibrium bond-length $r_0 = 1.0\,\sigma$. At this point it is important to note that the typical size of individual MPs are three to four orders of magnitude smaller than the typical length of polymers used in motility assay setups. Incorporating this large length scale separation makes the numerical simulations prohibitively expensive. We use a capture radius $r_c = 0.5\,\sigma$, and MP density $\rho = 3.8\,\sigma^{-2}$ in our simulations. To avoid introduction of further energy scales, we use $k_m = A/\sigma$. To maintain active forces larger than thermal fluctuations, we use $f_s = 2\,k_BT/\sigma$, $f_d =$

f_s. The dynamics of the active system is characterized by the dimensionless ratio of attachment and detachment rates $\omega_{\rm on}/\omega_0$, and a dimensionless Péclet number $Pe = v_0 L/D_t$ expressed as a ratio of convective and diffusive transport of the filament. Using translational diffusion coefficient of polymer $D_t = D/(L/r_0)$ with $D = k_B T/\gamma$, one obtains $Pe = v_0 L^2/D r_0$.

This expression, along with the rigidity parameter $u = L/\lambda$, give the flexure number $Pe\, u = v_0 L^3 (d-1)/2\kappa r_0$, which plays crucial role in determining buckling instability, and spiral formation in active polymers [63, 131, 136]. The characteristic time for the filament to diffuse over its contour length L is $\tau = L^3\gamma/4 r_0 k_B T$. We use this as a unit of time in expressing the time-scales in simulation results. The numerical integrations are performed using δt adjusted for numerical stability. The presence of turnover reduces the effective active force imparted on the chain, as MPs detach under longer extension. As a result, the smallest δt required in these simulations is $1.6 \times 10^{-8}\,\tau$, larger than that was necessary for active polymer simulations [131]. The results are presented here from simulations over 2×10^9 steps, discarding the first 10^9 steps to ensure steady state measurements.

6.3 Spiral formation, rotation and breaking

Beyond a minimum on- off ratio $\omega_{\rm on}/\omega_0$, and activity Pe, the polymer spontaneously starts to get into spiral structures. The nature of the spiral can be quantified in terms of the turning number [146], $\psi_i = (1/2\pi)\sum_{j=1}^{i-1}[\theta_{j+1} - \theta_j]$ where θ_j is defined by $\hat{t}_j = (\cos\theta_j, \sin\theta_j)$, and $[\theta_{j+1} - \theta_j]$ gives the angle increment between consecutive bonds. Thus turning number ψ_N with $i = N$ measures the (real) number of turns the chain takes between its two ends. For a straight chain $\psi_N = 0$, and for a chain forming a single anticlockwise (clockwise) loop $\psi_N = 1\,(\psi_N = -1)$. Larger values of ψ_N correspond to more than one turn forming the spiral. In Fig. (6.2) we show a typical time series of ψ_N, along with three representative conformations corresponding to $\psi_N \approx 0$ and a turning number $\psi_N \approx \pm 3$. In Fig. (6.3)(a), we show the snapshots of the semiflexible polymer in the dynamics of the spiral formation.

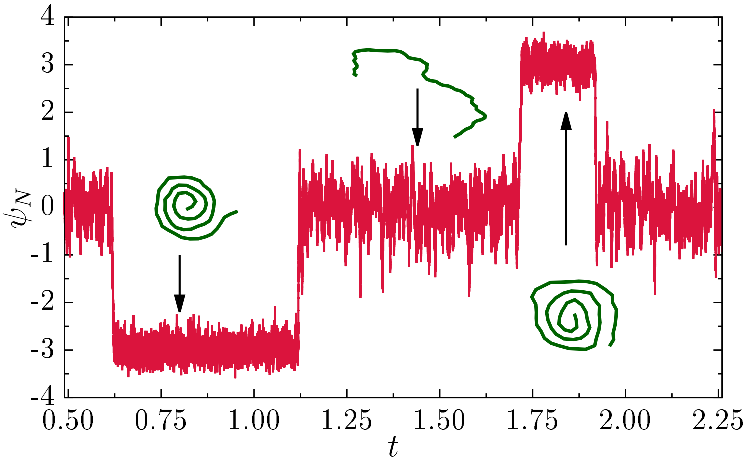

Figure 6.2: (color online) Time evolution of the turning number ψ_N at $Pe = 10^5$ and the ratio $\omega_{\text{on}}/\omega_0 = 1$. Time t is expressed in the unit of τ. The plot shows stochastic switching between three states, an open state with $\psi_N \approx 0$, and two spiral states with $\psi_N \approx \pm 3$. Representative polymer configurations corresponding to the three states are shown at three time instances indicated by arrows.

(*a*) Spiral formation

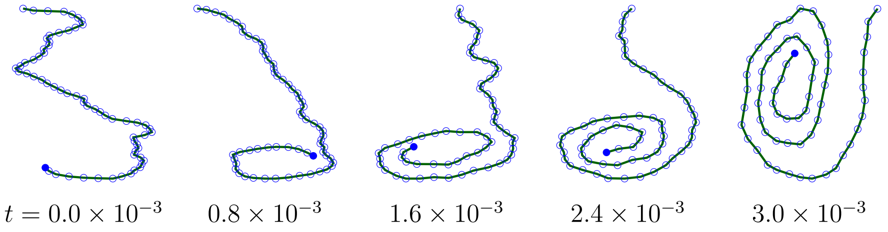

(*b*) Spiral breaking

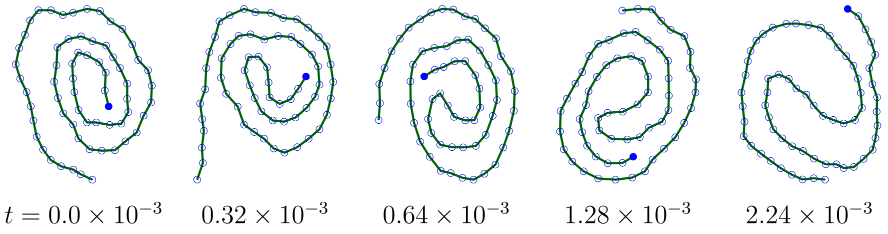

Figure 6.3: (color online) Typical configurations of the (*a*) formation and (*b*) breaking of the spiral at $Pe = 10^5$ and the ratio $\omega_{\text{on}}/\omega_0 = 1$. Time t is expressed in the unit of τ. The solid point indicate the head of the spiral.

In Fig. (6.3)(*b*), we show the snapshots of the semiflexible polymer in the dynamics of the spiral breaking. In Fig. (6.4), we show the snapshots of the semiflexible polymer in the dynamics of the spiral rotation.

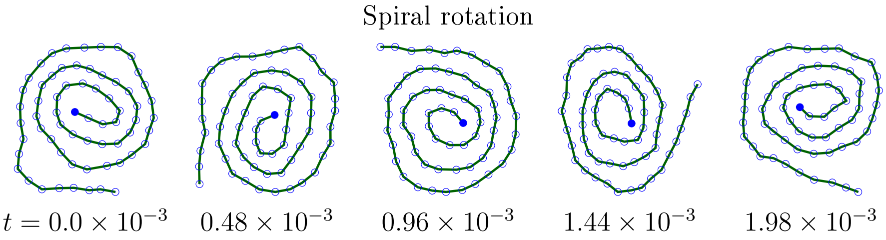

Figure 6.4: (color online) Typical configurations of the rotation of the spiral at $Pe = 10^5$ and the ratio $\omega_{\rm on}/\omega_0 = 1$. Time t is expressed in the unit of τ. The solid point indicate the head of the spiral.

6.4 First order phase transition : open chain to spiral

In Fig. (6.5)(a) we show the steady state probability distributions of the turn number $p(\psi_N)$ at different values of Pe, corresponding to a fixed on- off ratio $\omega_{\rm on}/\omega_0 = 1$. At small Pe we find a unimodal distribution with the maximum located at $\psi_N = 0$ corresponding to open chains. With increasing the activity to $Pe = 0.2 \times 10^5$ two other metastable maxima appear in $p(\psi_N)$ near $\psi_N = \pm 1.8$, positioned symmetrically around the central peak at $\psi_N = 0$, which remains the global maximum. Appearance of such metastable states across a phase transition is a characteristic of a first order transition. As we increase Pe, the heights of the maxima corresponding to spiral grow. Near $Pe = 0.67 \times 10^5$, all the three maxima of $p(\psi_N)$ becomes equally probable, identifying the *binodal point* of the first order phase transition from the open- chain to spiral. The increase in the probability of the spiral states, characterized by the rise of height of the two non-zero ψ_N maxima, continue up to $Pe = 1.19 \times 10^5$. This indicates further (de-) stabilization of the (open) spiral state. A remarkable non-monotonic feature is observed with further increase in Pe. For larger Pe, the non-zero ψ_N- peaks corresponding to the spiral states start to reduce in height with respect to the peak at $\psi_N = 0$. Again near $Pe = 1.58 \times 10^5$, all three maxima attain the same height, indicating a *binodal* corresponding to the *reentrant transition* back from spiral to open chain state. At larger Pe, the heights of the non-zero ψ_N peaks keep diminishing with increasing Pe values. Despite this non-monotonic nature of the stability of open and spiral states, it should be noted that, all through, the positions of the peaks at non-zero turning number ψ_N consistently

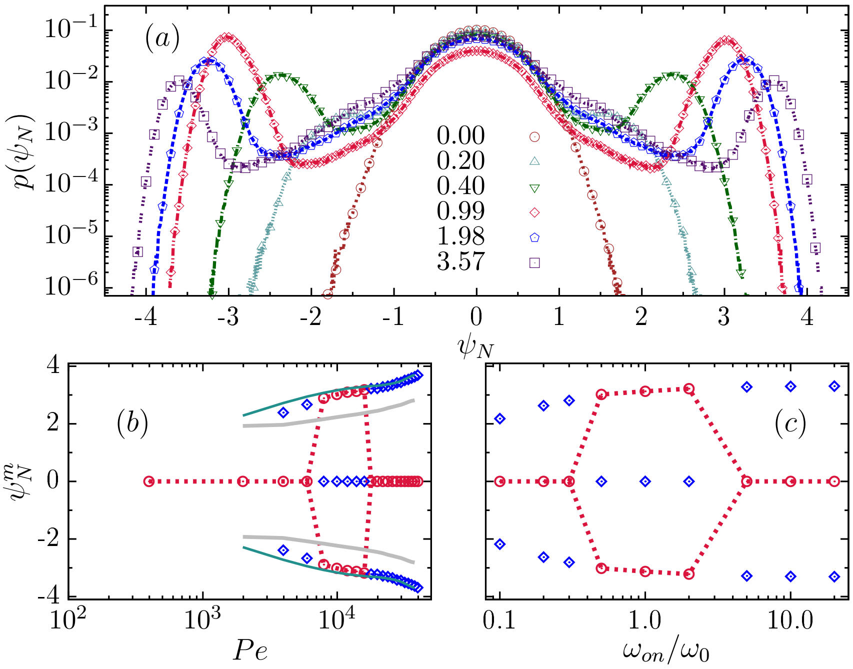

Figure 6.5: (color online) (a) Probability distribution functions of turn number $p(\psi_N)$ for different $Pe = \tilde{Pe} \times 10^5$ where values of $\tilde{Pe}$ are denoted in the figure legend, at a fixed ratio $\omega_{on}/\omega_0 = 1$. The triple- maxima characterize the coexistence in transition from open chains to spirals. The dependence of the stable (global) (red ○) and metastable (blue ◇) maxima of $p(\psi_N)$ are shown as a function of Pe at $\omega_{\text{on}}/\omega_0 = 1$ in (b), and as a function of $\omega_{\text{on}}/\omega_0$ at $Pe = 1.39 \times 10^5$ in (c). In (b), the green lines show the plot of $\pm(|u_4|/2u_6)^{1/2}$, and the grey lines show the plot of $\pm(u_2/2u_4)^{1/2}$, where u_2, u_4 and u_6 are defined by Eq. (6.6).

increases to larger amplitudes of $\pm\psi_N$ as Pe increases. Thus, while the probability of spirals at $Pe > 1.58 \times 10^5$ gets smaller with increasing Pe, when formed, the spirals at higher Pe consistently display higher turning numbers.

We analyzed all such probability distributions within a range of $0 \leq Pe \leq 3.97 \times 10^5$, and attachment- detachment ratios $0.1 \leq \omega_{\text{on}}/\omega_0 \leq 20$ using the locations and heights of the peak positions of $p(\psi_N)$. In Fig. (6.5)(b), we show using ○ (red), the ψ_N^m values corresponding to the stable phase, i.e., the peak position(s) of the global maximum (maxima) in $p(\psi_N)$. Points denoted by ◇ (blue) show the peak positions corresponding to the metastable state(s), having peak heights smaller than the global maximum. The dotted lines are guide to eye showing the variation of the global maximum with increasing Pe, which displays the open- to predominantly spiral- to predominantly open transition as expected from the probability distributions. Note that the coexistence points, symmetric about the central peak (points corresponding to $\psi_N^m = 0$) mark the familiar coexistence curves (binodal) in a first order phase transition. The various transitions are the unique non-equilibrium features of the motility assay set up. Similar non-equilibrium features are observed when ψ_N^ms is plotted as a function of the ratio $\omega_{\text{on}}/\omega_0$ at a constant Pe (Fig. (6.5)(c)).

From the probability distribution of ψ_N, and using an effective *equilibrium*- like approximation $p(\psi_N) \sim \exp[-\mathcal{F}(\psi_N)]$ we can write

$$\mathcal{F}(\psi_N) = \frac{1}{2}u_2\psi_N^2 - u_4\psi_N^4 + u_6\psi_N^6, \tag{6.6}$$

apart from an additive constant. Such a fitting with Fig. (6.5)(a) allows us to obtain the values of u_2, u_4 and u_6 as a function of Pe and $\omega_{\text{on}}/\omega_0$ ratio. It is straightforward to show [147] that along the first order line described by $\partial\mathcal{F}/\partial\psi_N = 0$ and $\mathcal{F} = 0$, the turn number obeys the relation $\psi_N = \pm(|u_4|/2u_6)^{1/2}$. This shows good agreement with simulation results (Fig. (6.5)(b)). Moreover, the spinodal lines, obeying $\partial\mathcal{F}/\partial\psi_N = 0$ and $\partial^2\mathcal{F}/\partial\psi_N^2 = 0$, are given by $\psi_N = \pm(u_2/2u_4)^{1/2}$, and are shown by the grey lines in Fig. (6.5)(b).

6.5 Phase diagram : reentrant transition

In Fig. (6.6), we plot the phase diagram in the $\omega_{\text{on}}/\omega_0$ - Pe plane characterizing the *open* and *spiral* states and their stability. The symbol △ denotes the region where the *open* chain is the only phase possible, with the distribution $p(\psi_N)$ showing a single maximum at $\psi_N = 0$. The regions denoted by □ indicates coexistence of the stable *open chain*, with a metastable *spiral* phase. In the region denoted by ○ in the phase diagram, it is the *spiral* state which is stable, but in coexistence with a metastable *open* state. The two boundaries between the ○ and □ in Fig. (6.6) identify the two *binodal* lines of the first- order transition. Along them, both the open and the spiral states are equally probable. The presence of these two binodal lines characterize the reentrant nature of the first order conformational transition

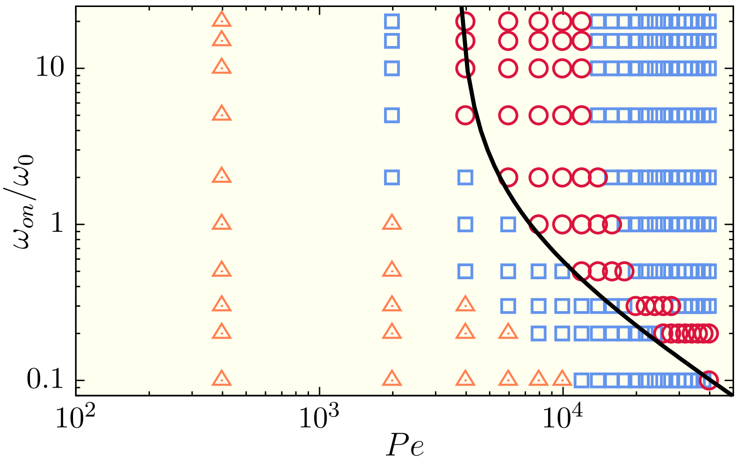

Figure 6.6: (color online) Phase diagram calculated from probability distribution of turn number $p(\psi_N)$. The data points denoted by green $\triangle$ denotes a stable open chain state, in the complete absence of spirals. The blue $\square$ points denote stable open chains in the presence of metastable spirals. The red $\bigcirc$ denotes stable spirals coexisting with metastable open chains. The boundaries between $\square$ and $\bigcirc$ denote the binodals where open chains and spirals are equally probable. The solid line capturing one such phase boundary is a plot of the function $\omega_{\text{on}}/\omega_0 = \alpha/(Pe - \alpha)$ where $\alpha = 3.67 \times 10^4$ (see Section-(6.6)).

of the polymer.

The phase diagram clearly brings out the importance of the attachment-detachment kinetics of the MPs. At a fixed $\omega_{\text{on}}/\omega_0$, the polymer goes from a stable open chain to stable spiral to stable open chain reentrant transition with increase in Pe. At higher attachment-detachment ratios, $\omega_{\text{on}}/\omega_0 > 2$ for the parameters in our simulations, the region of stable spiral states $0.4 \times 10^5 \leq Pe \leq 1.19 \times 10^5$, is independent of the $\omega_{\text{on}}/\omega_0$ ratio. At lower $\omega_{\text{on}}/\omega_0$, the region where the spiral state is the stable state of the polymer appears at progressively larger Pe values. Also the single maxima region, corresponding to only an open chain conformation, persists for higher values of Pe at low $\omega_{\text{on}}/\omega_0$.

Active polymers showed formation of spirals at activity larger than the onset of buckling instability [131]. However, this did not show the re-entrance behavior we find. Our detailed modeling of the MP- bed allowed us to clearly characterize the impact of the MP turnover, revealing the dependence on the $\omega_{\text{on}}/\omega_0$ ratio. This remained outside the scope of the active polymer model.

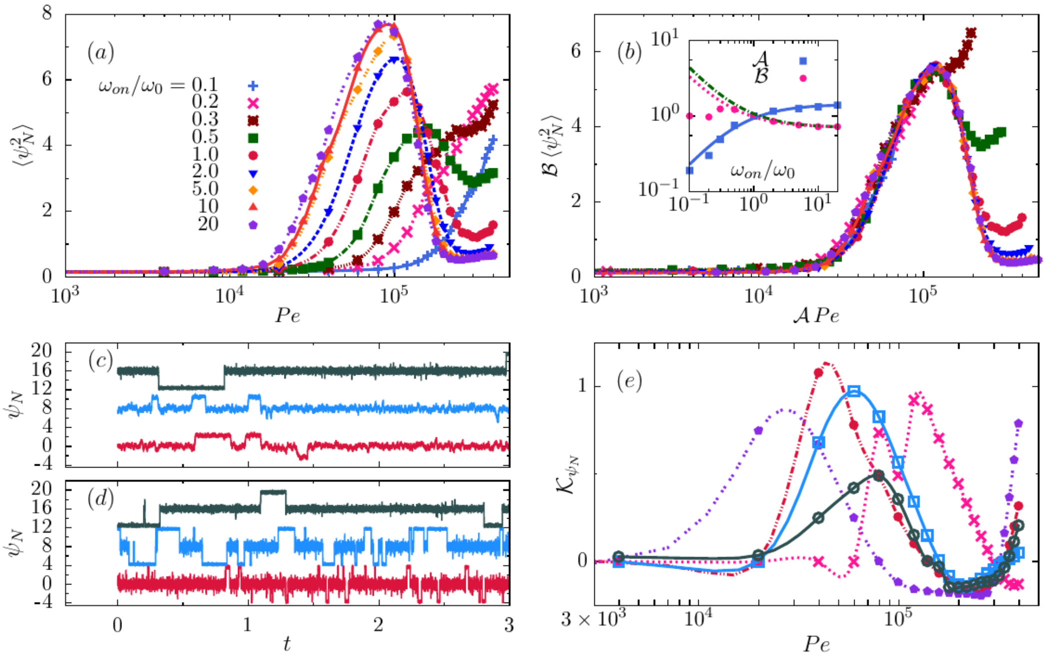

Figure 6.7: (color online) (a) The steady state turning number fluctuation $\langle\psi_N^2\rangle$ as a function of Pe at different values of $\omega_{\rm on}/\omega_0$ ratios denoted in the figure legend. (b) Approximate data collapse of different plots in (a) by using scale factors $\mathcal{A}$, $\mathcal{B}$. Inset: The dependence of $\mathcal{A}$ and $\mathcal{B}$ on $q = \omega_{\rm on}/\omega_0$. The solid line $\Omega_f = 1.42\,q/(0.52 + q)$ shows a fit to the data for $\mathcal{A}$. The dotted line shows a fit $(0.37 + q)/1.41\,q$ to the data for $\mathcal{B}$ in the regime $q > 0.3$. The dash- dotted line is a plot of $1/\Omega_f$. Comparison of time series of ψ_N for bond lengths $r_0 = 1.0\sigma$ (red), 0.75σ (blue) and 0.5σ (green) are shown at $Pe = 3.97\times10^4$ (c) and $Pe = 3.97\times10^5$ (d). Time t is expressed in the unit of τ. The data for $r_0 = 0.75\,\sigma$ and $0.5\,\sigma$ are shifted upwards by 8 and 16 for better visibility. (e) Kurtosis $\mathcal{K}_{\psi_N}$ of turning number ψ_N plotted at $\omega_{\rm on}/\omega_0 = 0.2$, 1.0, 20 with data shown by the same symbols as in (a). The open □ and ○ denote data at $\omega_{\rm on}/\omega_0 = 1.0$ for $r_0 = 0.75\,\sigma$ and $0.5\,\sigma$ respectively.

6.6 Turn number fluctuations

In this section we consider the first two moments of the $p(\psi_N)$ distributions. This is due to the fact that, with respect to the full distributions, moments are easier quantities to determine from experiments. The chiral symmetry in the system $p(-\psi_N) = p(\psi_N)$ ensures that, all through, $\langle\psi_N\rangle = 0$. The quantitative measure of the effective turn number is given by the root- mean square fluctuation $\langle\psi_N^2\rangle^{1/2}$. Fig. (6.7)$(a)$ shows the non-monotonic variation of $\langle\psi_N^2\rangle$ with Pe at fixed $\omega_{\rm on}/\omega_0$ ratios, corresponding to the reentrant transition. Re-scaling of Pe and $\langle\psi_N^2\rangle$ leads to an approximate data collapse as shown in Fig. (6.7)(b). We can extract a functional dependence of the scale factors $\mathcal{A}$, $\mathcal{B}$ on the ratio $q = \omega_{\rm on}/\omega_0$ as $\mathcal{A} \approx \Omega_f(q)$ and $\mathcal{B} \approx 1/\Omega_f(q)$ (see inset of Fig. (6.7)(b)). $\Omega_f(q)$ has the form of a bare processivity, $\Omega(f_l = 0) = \omega_{\rm on}/(\omega_{\rm on} + \omega_0) = q/(1+q)$. The data- collapse suggests a functional dependence

$$\langle \psi_N^2(q, Pe) \rangle \approx \Omega_f(q) \mathcal{G}[\Omega_f(q)\, Pe]. \tag{6.7}$$

A spiral with radius R has a turn number $\psi_N = L/2\pi R$. The shape can be maintained via a torque balance $FR^2 = \kappa/R$, where F denotes the MP force per unit length. This force depends f_l, the force exerted due to active extension of MPs, the linear density of MPs $\sqrt{\rho}$, and their processivity (f_l). The mean of the active force f_l is denoted here by $f_a \approx \gamma v_0$. Thus the net active force per unit length $F := \sqrt{\rho} f_a (f_a)$. This leads to the following activity dependence of turning number

$$\psi_N^2 \sim \mathcal{G}_1((f_a), f_a). \tag{6.8}$$

Noting that $Pe \sim f_a$, Eq. (6.8) is related to but cannot fully capture the scaling form in Eq. (6.7). The reason lies in the fact that the polymer switches between the spiral and open state, and $\langle \psi_N^2 \rangle$ is averaged over the probability distribution spanning both the states.

The onset of spiral requires $\psi_N^2 > 1$, i.e., $F > F_c = \kappa(2\pi/L)^3$. Thus the phase boundary denoting this is given by $F := f_a(f_a) = F_c$. In the limit of load- independent detachment rate, with $f_a \sim Pe$, the equality $f_a(f_a) = F_c$ leads to a dimensionless form $qPe/(1+q) = \alpha$, where $q = \omega_{\rm on}/\omega_0$, and α denotes a dimensionless constant proportional to F_c. This can be simplified to the hyperbolic relation

$$\omega_{\rm on}/\omega_0 = \alpha/(Pe - \alpha). \tag{6.9}$$

In the phase diagram Fig. (6.6), the solid line is a plot of this function with $\alpha = 3.67 \times 10^4$, and approximately captures the phase boundary of the onset of spiral phase.

As it has been pointed out earlier [131, 140], the modulation of potential energy along the chain due to WCA repulsion from polymer beads costs energy to slide chain segments past each other. The resultant increase in sliding friction can increase the lifetime of spirals. To examine this we consider chains of the same contour length L but smaller bond lengths $r_0 = 0.75\,\sigma$ and $0.5\,\sigma$ having smoother potential profiles along the chain. In Fig. (6.7)(c) and (d) we show a comparison between their time series of turning number ψ_N at two activities, $Pe = 3.97 \times 10^4$, 3.97×10^5, keeping $\omega_{\rm on}/\omega_0 = 1$. We find formation of spirals in all the cases. As expected, the life-time of spirals corresponding to all the different phases decreases with reduction of r_0/σ, smoothening the polymer. For each r_0/σ, however, the time-scale shows non-monotonic variation with Pe (Section-6.8.3). A quantitative analysis of the time-scales are presented in Fig. (6.15) of Section-6.8.3.

In Fig. (6.7)(e) we show variation of kurtosis $\mathcal{K}_{\psi_N} = [\langle \psi_N^4 \rangle / 3\langle \psi_N^2 \rangle^2 - 1]$ with Pe for three different r_0/σ ratios calculated at $\omega_{\rm on}/\omega_0 = 1$. It also shows $\mathcal{K}_{\psi_N}(Pe)$ for $\omega_{\rm on}/\omega_0 = 0.2,\ 20.0$ using the chain with bond length $r_0 = 1.0\,\sigma$. To reduce statistical uncertainties we calculated kurtosis over several initial conditions such that the distribution of ψ_N gets symmetric and restricting analysis to the spiral states [131]. At small Pe we find $\mathcal{K}_{\psi_N} = 0$, consistent with the Gaussian distribution. As the spirals start to appear $\langle \psi_N^4 \rangle$ increases, increasing $\mathcal{K}_{\psi_N}$. At higher Pe, as the spirals stabilize, the second cumulant $\langle \psi_N^2 \rangle$ start to dominate reducing $\mathcal{K}_{\psi_N}$ from a maximum to eventually $\mathcal{K}_{\psi_N}$ reach a minimum. Finally at further higher Pe, the kurtosis increases again corresponding to the re-entrance.

The kurtosis $\mathcal{K}_{\psi_N}$ calculated for three different values of $r_0/\sigma = 1.0$, 0.75, 0.5 at $\omega_{\rm on}/\omega_0 = 1$ in Fig. (6.7)(e) display similar non-monotonic behavior, but the peak of the curves shift towards larger Pe for smaller r_0/σ. For example, the peak position of $\mathcal{K}_{\psi_N}$ shifts from $Pe = 4.4 \times 10^4$ at $r_0/\sigma = 1.0$ to $Pe = 6.0 \times 10^4$ at $r_0/\sigma = 0.75$ and to $Pe = 7.9 \times 10^4$ at $r_0/\sigma = 0.5$. Such a shift can be understood by noticing that the reduction in r_0/σ increases the bending rigidity κ of the filament. As has been pointed out before Eq. (6.9), the active force F_c needed for the onset of spiral increases linearly with κ. Thus spiral formation at smaller r_0/σ requires higher Pe.

[1]

6.7 Size and shape

Associated with the active open to spiral transition, the polymer undergoes significant change in its size and shape. In this section we clearly demonstrate these transformations with the help of (*i*) the end- to- end separation, and (*ii*) the radius of gyration tensor.

6.7.1 End- to- end separation

In Fig. (6.8)(*a*) we show the probability distribution of the scaled end- to- end separation $\tilde{r}_e = r_e/\langle L\rangle$ of the polymer for different Pe at a fixed $\omega_{\rm on}/\omega_0$, where $\langle L\rangle$ denotes the mean contour length. The distribution function $p(\tilde{r}_e)$ is normalized to $\int_0^1 d\tilde{r}_e\, 2\pi\tilde{r}_e\, p(\tilde{r}_e) = 1$. At $Pe = 0$, it shows a single maximum at $\tilde{r} \approx 0.8$ corresponding to rigid- rod like configurations. This points to a relatively large effective bending rigidity of the filament [106]. Note that $Pe = 0$ does not imply an equilibrium passive polymer, because of the active attachment- detachment of the MPs with $\omega_{\rm on}/\omega_0 \neq 0$. With increasing Pe, the distribution changes qualitatively. At $Pe = 0.2 \times 10^5$, a new maximum appears near $\tilde{r} \approx 0.15$. This bimodality corresponds to coexistence of rod-like shapes with folded polymers, a behaviour that appears even before the chain starts to form spirals. At further higher activity, $Pe \geq 0.4 \times 10^5$, as the probability of spiral- state increases, the small $\tilde{r}_e$ maximum shifts to smaller values, and their corresponding probability increases up to $Pe = 1.19 \times 10^5$. At even higher Pe, the spiral state starts to become less stable, as has been discussed in Section-6.4. Associated with that, the height of the small $\tilde{r}_e$ maximum in $p(\tilde{r}_e)$ decreases. This non-monotonic behaviour is clearly observable in Fig. (6.8)(*a*). The peak at small $\tilde{r}_e$ increases with increasing activity in the range

---

[1] The availability of more attachment points of MPs for a filament with smaller r_0/σ, within our model, could increase the imparted active force on the filament. However, this effect would shift the $\mathcal{K}_{\psi_N}$ graphs to smaller Pe, unlike what we observe in Fig. (6.7)(*e*).

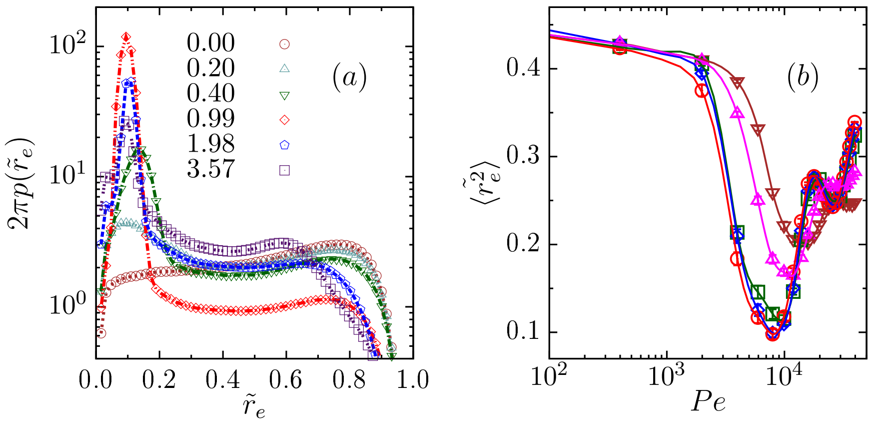

Figure 6.8: (color online) (a) End-to-end distribution functions $2\pi p(\tilde{r}_e)$ for $Pe = \tilde{P}e \times 10^5$ with $\tilde{P}e$ values shown in the figure legend, at a fixed $\omega_{\text{on}}/\omega_0 = 1$. ($b$) Mean squared end- to- end separation $\langle \tilde{r}_e^2 \rangle$ as a function of Pe for $\omega_{on}/\omega_0 = 0.5\,(\triangledown)$, $1\,(\triangle)$, $5\,(\square)$, $10\,(\Diamond)$, $20\,(\bigcirc)$. Error bars are smaller than the symbol size. The lines through data are guides to eye.

of $Pe \times 10^{-5} = 0.2$ to 1. At higher activity, $Pe \times 10^{-5} = 0.99$, 1.98, 3.57, this peak-height decreases.

In Fig. (6.8)(b), we show the non-monotonic variation of the second moment of the end- to- end distribution $\langle \tilde{r}_e^2 \rangle$ with Pe, for different $\omega_{\text{on}}/\omega_0$. For all $\omega_{\text{on}}/\omega_0$, $\langle \tilde{r}_e^2 \rangle$ initially decreases from the value at $Pe = 0$ as the polymer starts folding and getting into predominantly spiral states. As Pe is increased further, $\langle \tilde{r}_e^2 \rangle$ starts increasing since the stability of spiral states decrease. At small $\omega_{\text{on}}/\omega_0$, $\langle \tilde{r}_e^2 \rangle$ shows eventual saturation with Pe. However, for larger $\omega_{\text{on}}/\omega_0$, the curve shows a further non monotonic behavior with an asymptotic increase in $\langle \tilde{r}_e^2 \rangle$ at higher values of $Pe > 2.58 \times 10^5$. Note that a non-monotonic variation of $\langle \tilde{r}_e^2 \rangle$ with Pe was observed earlier in polymers in active bath [132]. The main difference of that result with our model is, for $\omega_{\text{on}}/\omega_0 \geq 5$ we find two minima in the $\langle \tilde{r}_e^2 \rangle$ versus Pe curve instead of the single minimum in Ref. [132], before the asymptotic increase. The size variation is associated with the persistence length of the filament discussed in the next section.

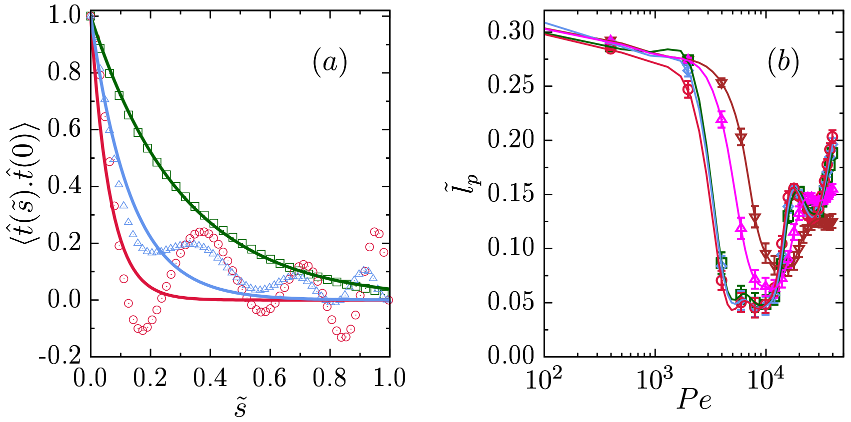

Figure 6.9: (color online) Persistence length. (a) Tangent-tangent correlation function for $Pe \times 10^{-5} = 0(\square)$, $0.99(\bigcirc)$, $1.98(\triangle)$ and $\omega_{on}/\omega_0 = 1$. The points denote the simulation results, and the solid lines represent the fitting functions $\exp(-\tilde{s}/\tilde{l}_p)$. (b) Variation of the effective persistence length $\tilde{l}_p$ with Pe at $\omega_{\rm on}/\omega_0 = 0.5\,(\triangledown)$, $1\,(\triangle)$, $5\,(\square)$, $10\,(\diamond)$, $20\,(\bigcirc)$. The lines through data are guides to eye. At equilibrium, the chain has persistence length $\tilde{l}_p \approx 0.3$, close to the values at $Pe = 0$.

6.7.2 Effective persistence length

The effective persistence length can be quantified in terms of the correlation function between local tangents $\langle \hat{t}(s)\cdot\hat{t}(0) \rangle$ at contour positions separated by s. For the worm-like- chain the correlation shows a single- exponential decay $\langle \hat{t}(s)\cdot\hat{t}(0) \rangle = \exp(-s/\lambda)$ defining the persistence length λ. The semiflexible polymer under the motility assay drive shows non- trivial tangent correlations (Fig. (6.9)(a)). The oscillations in the decaying correlation at higher Pe is associated with the formation of the spiral configurations. However, the initial decay in correlation can be fitted to a single exponential form $\exp(-s/l_p)$ to capture the effective persistence length l_p. In Fig. (6.9)(a) the contour lengths s are expressed as $\tilde{s} = s/\langle L \rangle$, where $\langle L \rangle$ is the mean chain- length. The scaled effective persistence lengths $\tilde{l}_p = l_p/\langle L \rangle$ are plotted as a function of Pe, at fixed $\omega_{\rm on}/\omega_0$ ratios in Fig. (6.9)(b). The variation of $\tilde{l}_p$ shows non-monotonic change with Pe, and follows the variation of the mean squared end-to- end separation $\langle \tilde{r}_e^2 \rangle$ plotted in Fig. (6.8)(b).

6.7.3 Radius of gyration tensor

The size and shape of the polymer configurations can be extracted from analyzing the radius of gyration matrix

$$S = \frac{1}{N}\begin{pmatrix} \sum_i (x_i - x_{cm})^2 & \sum_i (x_i - x_{cm})(y_i - y_{cm}) \\ \sum_i (x_i - x_{cm})(y_i - y_{cm}) & \sum_i (y_i - y_{cm})^2 \end{pmatrix} \tag{6.10}$$

where (x_i, y_i) denotes the position vector of the i-th bead, and (x_{cm}, y_{cm}) denotes the center of mass coordinate of the instantaneous polymer configuration. The two eigenvalues $\tilde{\lambda}_+$ and $\tilde{\lambda}_-$ of $S/\langle L\rangle^2$ describe the instantaneous configuration of the polymer as an elliptical shape, with $\tilde{\lambda}_+$ and $\tilde{\lambda}_-$ denoting the square of lengths along the semi-major and semi-minor axes whose orientations are determined by the eigenvectors.

Here we show the probability distributions of the eigenvalues of the radius of gyration matrix, $p(\lambda_\pm)$. In Fig. (6.10)(a), (b) we show these distribution functions

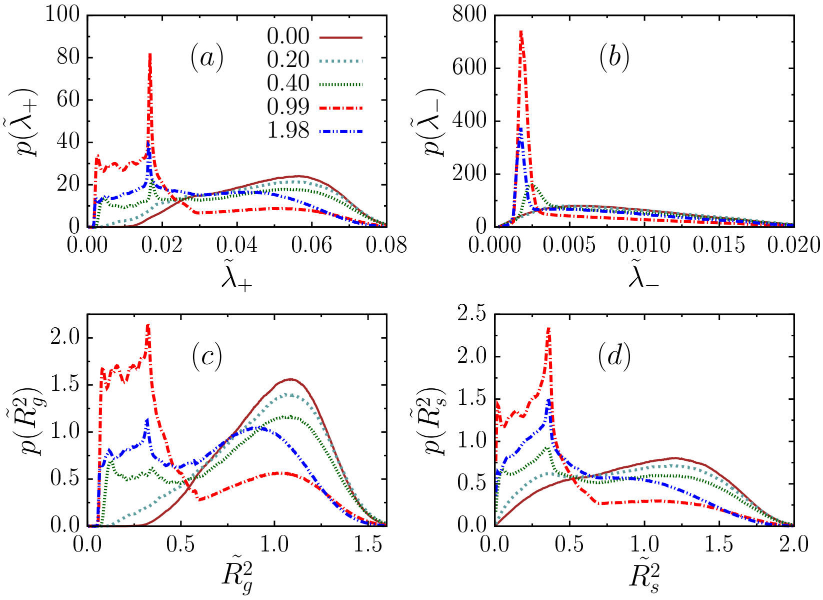

Figure 6.10: (color online) Probability distributions of the eignevalues (a) $\tilde{\lambda}_+$, and (b) $\tilde{\lambda}_-$, (c) size $\tilde{R}_g^2$, and (d) shape $\tilde{R}_s^2$ are shown. All the distribution functions are obtained at $\omega_{\text{on}}/\omega_0 = 1$, and the different graphs in (a)–(d) correspond to the $Pe = \tilde{Pe} \times 10^5$ with $\tilde{Pe}$- values indicated in the legend of (a).

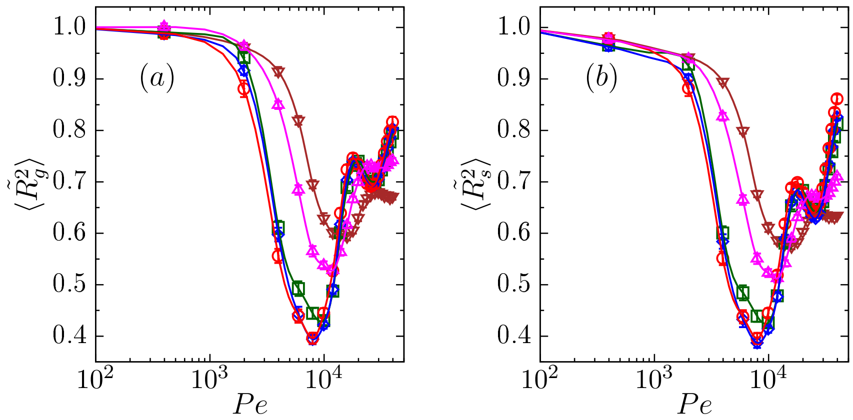

Figure 6.11: (color online) Radius of Gyration. Fig. (a), (b) shows the variation of size $\langle \tilde{R}_g^2 \rangle$ and shape $\langle \tilde{R}_s^2 \rangle$ with standard error as a function of Pe at different $\omega_{on}/\omega_0 = 0.5$ (brown ▽), 1 (pink △) 5 (green □), 10 (blue ◇), 20 (red ○) respectively.

evaluated for various Pe and a fixed turnover $\omega_{\rm on}/\omega_0 = 1$. Clearly, at the onset of instability towards formation of spirals both the distributions $p(\tilde{\lambda}_\pm)$ start to show emergence of a very sharp delta- function like peak. This corresponds to a typical size and shape of the configurations forming spiral. This feature is further quantified in the distribution functions of the relative size and shape variables $\tilde{R}_g^2$ and $\tilde{R}_s^2$ shown in Fig. (6.10)(c), (d).

A measure of effective size of the polymer is given by $R_g^2 = \tilde{\lambda}_+ + \tilde{\lambda}_-$. The difference between the eigenvalues denotes its shape $R_s^2 = \tilde{\lambda}_+ - \tilde{\lambda}_-$, with $R_s^2 = 0$ for a symmetric circular shape. In Fig. (6.11) we show variations of the scaled size $\langle \tilde{R}_g^2 \rangle = \langle R_g^2 \rangle / \langle R_g^2 \rangle_{Pe=0}$ and shape $\langle \tilde{R}_s^2 \rangle = \langle R_s^2 \rangle / \langle R_s^2 \rangle_{Pe=0}$ with Pe. As expected, the variation of $\langle \tilde{R}_g^2 \rangle$ follows the same non-monotonic variation as the other measure of size $\langle \tilde{r}_e^2 \rangle$ shown in Fig. (6.8). Remarkably, the shape of the polymer $\langle \tilde{R}_s^2 \rangle$ follows the same qualitative dependence on Pe at all $\omega_{\rm on}/\omega_0$ ratios.

6.8 Dynamics

Associated with the re- entrant phase transition, the conformational dynamics displays a non-monotonic variation of the characteristic time- scales with MP activity. In this section, we study the two- time autocorrelation functions corresponding to

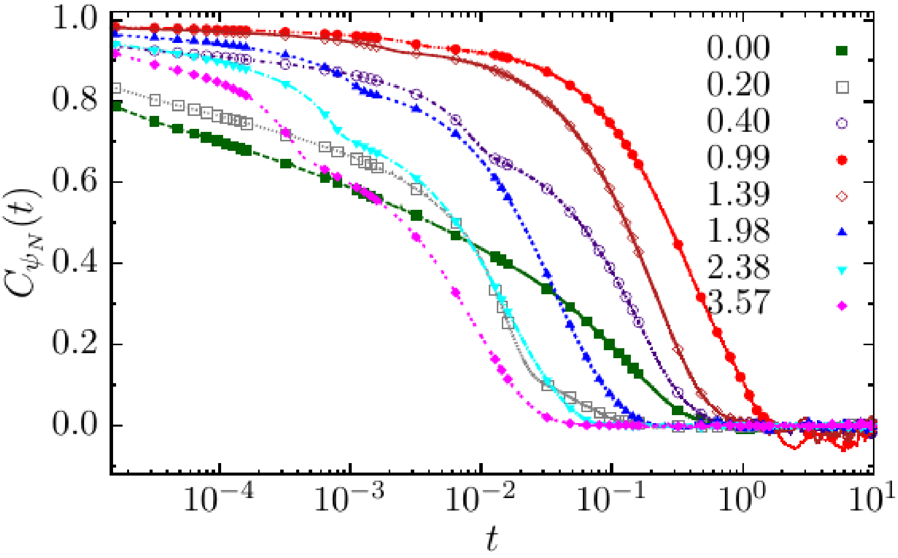

Figure 6.12: (color online) Two time autocorrelation function $C_{\psi_N}(t) = \langle\psi_N(t)\psi_N(0)\rangle/\langle\psi_N^2(0)\rangle$ evaluated at different $Pe = \tilde{Pe} \times 10^5$ with $\tilde{Pe}$ shown in the figure-legend keeping the on- off ratio $\omega_{\text{on}}/\omega_0 = 1$ constant. Time t is expressed in the unit of τ.

the turning number, the radius of gyration, and the polymer shape as defined above. The overall orientation, described by the eigenvector corresponding to the larger eigenvalue of the radius of gyration tensor, does not involve conformational relaxation. As a result, its dynamics gets faster monotonically with increasing activity.

6.8.1 Dynamics of turning number

In Fig. (6.12) we show the two- time autocorrelation function of the turning number, $C_{\psi_N}(t) = \langle\psi_N(t)\psi_N(0)\rangle/\langle\psi_N^2(0)\rangle$ at different Pe values keeping the ratio $\omega_{\text{on}}/\omega_0 = 1$ constant. In using this definition it is noted that $\langle\psi_N(t)\rangle = 0$ by symmetry, thus the fluctuation $\delta\psi_N = \psi_N$. For $Pe \leq 0.2 \times 10^5$, the chain stays in the open state corresponding to the unimodal distribution in $p(\psi_N)$ with the maximum at $\psi_N = 0$. The stochastic relaxation within this state gives rise to the single- exponential decay observed in Fig. (6.12). At the phase coexistence, a new mechanism corresponding to the switching between the open and spiral states can lead to a crossover of the correlation to a second exponential decay. In Fig. (6.12) we observe such a double exponential for $Pe \geq 0.4 \times 10^5$. The crossover between the two exponentials gets imperceptibly shallow between $Pe = 10^5$ and 2×10^5, as the overall faster dynamics due to larger Pe, makes the switching between states easier. As we increase Pe further, the increasing number of turns of the polymer increases the distance between the open and spiral peaks in the space of ψ_N. Switching between states becomes prohibitively expensive which makes the crossovers sharper again.

6.8.2 Dynamics of size, shape, and orientation

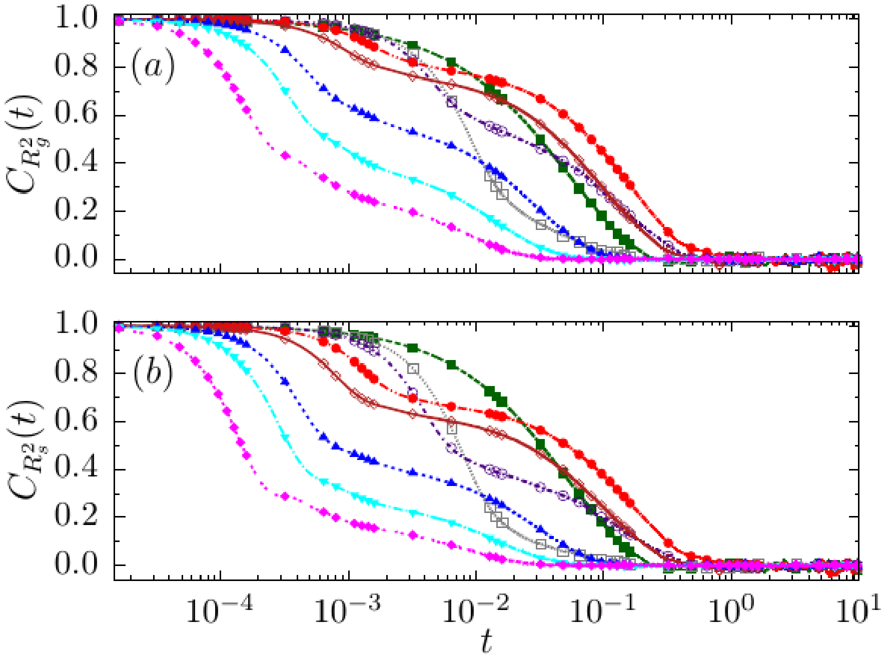

Figure 6.13: (color online) Two- time correlation functions of (a) R_g^2, and (b) R_s^2 at various $Pe = \tilde{Pe} \times 10^5$ with $\tilde{Pe}$-values indicated in the legend, keeping $\omega_{\rm on}/\omega_0 = 1$ fixed. Time t is expressed in the unit of τ. The points are same as in Fig. (6.12)

The dynamics of the size, shape, and overall orientation of the polymer can be determined by analyzing the time- series of the eigenvalues of the radius of gyration tensor, and the eigen- vector $\hat{\boldsymbol{u}}$ corresponding to the larger eigenvalue λ_+. We use the correlation functions $C_{R_g^2}(t) = \langle \delta R_g^2(t) \delta R_g^2(0) \rangle / \langle \delta R_g^4 \rangle$, $C_{R_s^2}(t) = \langle \delta R_s^2(t) \delta R_s^2(0) \rangle / \langle \delta R_s^4 \rangle$, and $C_{\hat{\boldsymbol{u}}}(t) = \langle \hat{\boldsymbol{u}}(t) \cdot \hat{\boldsymbol{u}}(0) \rangle$. The fluctuations $\delta R_{g,s}^2(t) = R_{g,s}^2(t) - \langle R_{g,s}^2(t) \rangle$. The correlation functions are plotted in Fig. (6.13). The size and shape correlations display double- exponential decay at $Pe \geq 0.4 \times 10^5$, as in the turning number correlation function in Fig. (6.12). This is because of the close relation between the size, shape and the turning number, all of which depend on the polymer conformation. However, the dynamics of the overall orientation of the polymer captured by $\hat{\boldsymbol{u}}$, is not related to internal structural relaxation. Thus it shows single exponential decay of the correlation, describing an orientational diffusion at $Pe \leq 0.2 \times 10^5$. Once the spirals are formed they start to rotate under the active drive. As a result, the orientation $\hat{\boldsymbol{u}}$ also rotates. This is captured by the oscillations in $C_{\hat{\boldsymbol{u}}}(t)$ at $Pe \gtrsim 0.4 \times 10^5$. As can be easily seen from Fig. (6.14), the frequency of rotation increases and the amplitude of oscillation in $C_{\hat{\boldsymbol{u}}}(t)$ decreases with increasing Pe.

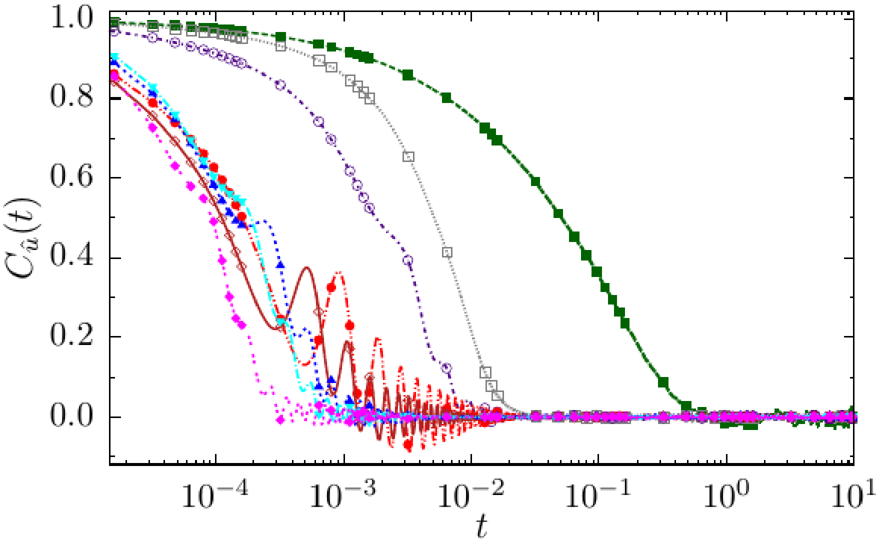

Figure 6.14: (color online) Two- time correlation functions of eigen- vector $\hat{\boldsymbol{u}}$ at various $Pe = \tilde{Pe} \times 10^5$ with $\tilde{Pe}$-values indicated in the legend, keeping $\omega_{\text{on}}/\omega_0 = 1$ fixed. Time t is expressed in the unit of τ. The points are same as in Fig. (6.12)

6.8.3 Time scales

The correlation time τ_c is the time scale at which the autocorrelation function touches zero for the first time. In Fig. (6.15)(a) we show the dependence of τ_c on Pe keeping $\omega_{\text{on}}/\omega_0 = 1$. τ_c corresponding to the orientational correlation function $C_{\hat{\boldsymbol{u}}}(t)$ decreases monotonically with increasing Pe. This can be understood by noticing that the overall orientational dynamics does not involve internal conformational relaxation of the polymer. It is thus controlled by the active time scale $D/v_0^2 \sim 1/Pe^2$, and decreases monotonically with increasing Pe (Fig. (6.15)(a)).

On the other hand, the value of τ_c corresponding to $C_{\psi_N}(t)$, $C_{R_g^2}(t)$ and $C_{R_s^2}(t)$ is controlled by two competing effects. The enhanced activity at higher Pe is expected to make the dynamics faster. On the other hand, as the system undergoes phase transition, the slow switching between states can slowdown the overall dynamics. This competition leads to a non-monotonic variation of τ_c with a maximum reached at $Pe = 10^5$ (Fig. (6.15)(a)). The maximum in τ_c is associated with the dominance of spirals in the dynamics. The correlation time τ_c for a smoothened chain of $r_0/\sigma = 0.75$ shows a similar non-monotonic variation (Appendix-6.10.2), however, with smaller τ_c values than the chain with $r_0/\sigma = 1.0$, due to a reduced sliding friction.

At this point, it is instructive to focus on τ_c corresponding to $C_{\psi_N}(t)$. Note that at $Pe = 10^5$, where the maximum of $\tau_c = 1.3 \times 10^5\,\tau$ is observed (Fig. (6.15)(a)), the simulation results for the mean dwell times at the open and spiral states are $\tau_o = 1.3 \times 10^4\,\tau$ and $\tau_s = 2.5 \times 10^4\,\tau$, respectively. Using an assumption of a dichotomous Markov process, they lead to an estimate of the correlation time [148] $\tau_e = \tau_o\tau_s/(\tau_o + \tau_s) \approx 10^4\,\tau < \tau_c = 1.3 \times 10^5\,\tau$. Such a difference is not unexpected as the actual dynamics is not really a dichotomous process, and involves other mechanisms, e.g, a gradual transition between the open and spiral states.

In the following we attempt to obtain estimates of τ_o and τ_s using a relaxation dynamics corresponding to the effective free energy $\mathcal{F}(\psi_N)$ in Eq. (6.6). For notational simplicity, we replace ψ_N by ψ in the rest of this section. The non-conserved dynamics is given by [147]

$$\partial\psi/\partial t = -M\left[\partial\mathcal{F}/\partial\psi\right] + \sqrt{2k_BT_eM}\,\Lambda(t), \tag{6.11}$$

where T_e plays the role of an effective temperature, M a mobility and $\Lambda(t)$ is a univariate and uncorrelated Gaussian random noise. The triple- minima of the *free energy* are at $\psi = 0$ and $\psi_m = \pm(u_4/3u_6)^{1/2}\left[1 + (1 - 3u_2u_6/2u_4^2)^{1/2}\right]^{1/2}$,

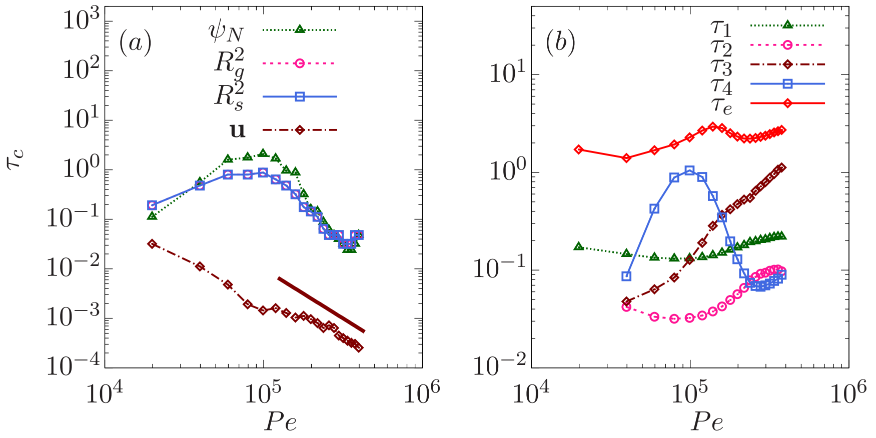

Figure 6.15: (color online) (a) Variation of correlation time τ_c (in the unit of τ) with Pe at $\omega_{\text{on}}/\omega_0 = 1$, obtained for ψ_N, R_g^2, R_s^2, and $\hat{\boldsymbol{u}}$. The brown solid line denotes the scaling form $1/Pe^2$. (b) Time scales calculated at $\omega_{\text{on}}/\omega_0 = 1$ using the expressions from the approximate non-conserved dynamics Eq. (6.11).

while the double maxima are at $\psi_M = \pm(u_4/3u_6)^{1/2}\left[1-(1-3u_2u_6/2u_4^2)^{1/2}\right]^{1/2}$. Disregarding the mobility M in the absence of an independent measure, the relaxation time scales at the minima of $\mathcal{F}$, are given by $[\partial^2\mathcal{F}/\partial\psi^2]^{-1}_{\psi=0,\psi_m}$. The relaxation around $\psi = 0$ leads to the inverse time-scale $\tau_1^{-1} \sim \omega_1 = u_2$, and that around $\psi = \psi_m$ gives $\tau_2^{-1} \sim \omega_2 = u_2 - (4u_4^2/u_6)\left[1+(1-3u_2u_6/2u_4^2)^{1/2}\right] + (30u_4^2/9u_6)\left[1+(1-3u_2u_6/2u_4^2)^{1/2}\right]^2$. The expressions for τ_1 and τ_2 at $\omega_{\text{on}}/\omega_0 = 1$ are plotted in Fig. (6.15)(b). Further, we calculate the Kramer's escape times [148] for barrier crossing: τ_3 from $\psi = 0$, and τ_4 from $\psi = \psi_m$. These are $\tau_3 \sim (\omega_1|\omega_M|)^{-1}\exp[\mathcal{F}(\psi_M) - \mathcal{F}(0)]$, and $\tau_4 \sim (\omega_2|\omega_M|)^{-1}\exp[\mathcal{F}(\psi_M) - \mathcal{F}(\psi_m)]$, where

$$\begin{aligned}\omega_M = u_2 - (4u_4^2/u_6)\left[1-(1-3u_2u_6/2u_4^2)^{1/2}\right] \\ +(30u_4^2/9u_6)\left[1-(1-3u_2u_6/2u_4^2)^{1/2}\right]^2 \qquad (6.12)\end{aligned}$$

(see Fig. (6.15)(b)). It is interesting to note that, among these time scales, only τ_4, the time- scale determining the rate of exiting the spiral state, has a non-monotonic variation with Pe, and dominates the overall behavior. The above analysis allows us to express the two effective dwell times as $\tau_o = (\tau_1 + \tau_3)$ and $\tau_s = (\tau_2 + \tau_4)$. The estimate $\tau_e = \tau_o\tau_s/(\tau_o + \tau_s)$ is plotted in Fig. (6.15)(b) with a multiplicative shift by 10 for better visibility. This shows a non-monotonic variation, with a small maximum at an intermediate Pe, a behavior that is qualitatively similar to the dependence of correlation times corresponding to ψ_N, R_g^2 and R_s^2 with Pe (Fig. (6.15)(a)).

The main caveat to the above analysis is Eq. (6.11) obeys the equilibrium fluctuation- dissipation relation, and is not strictly valid as a description for active systems. Further, even within an effective equilibrium interpretation, the Kramer's theory of barrier crossing is subject to modification when interpreted for transition rates between multiple minima of a free energy profile.

6.9 Conclusions

We considered a detailed model of motility assay consisting of an extensible semiflexible filament driven by motor proteins (MP) immobilized on a substrate. The numerical simulations showed a reentrant first order transition from open chain to spirals with changing activity. This transition is characterized by the presence of metastable maxima in the probability distribution of turning number. We obtained the phase- diagram in the Pe-$\omega_{\text{on}}/\omega_0$ plane, which clearly brings out the importance of attachment- detachment kinematics of the MPs. At a constant $\omega_{\text{on}}/\omega_0$, the polymer shows reentrance transition from open chain to spiral to open chain with increasing Pe. With lowering of $\omega_{\text{on}}/\omega_0$, the phase boundary shifts progressively to higher Pe, following a hyperbolic relation derived from a local torque balance.

The reentrant transition is associated with non-monotonic variations of the polymer size, shape and fluctuations in turning number $\langle\psi_N^2\rangle$ with Pe. The data collapse of the $\langle\psi_N^2\rangle$ versus Pe curves at different $\omega_{\text{on}}/\omega_0$ led to a scaling relation, which could approximately be captured by the torque balance argument that describes the phase boundary. The coexistence of open chain and spirals is preceded by a coexistence of open and folded chains captured by the bimodality in the distribution of end- to-end separation.

Our detailed analysis of the dynamics showed a double- exponential decay in the autocorrelation function of size, shape and turning number. The corresponding correlation times showed a non-monotonic variation with Pe, with a maximum due to the dominance of spirals. We developed an approximate description of the correlation time in terms of a dichotomous process between the open and spiral states. Using an effective free energy description of the phase transition and non-conserved relaxation dynamics, we obtained expressions for the dwell times in the two states, giving an estimate of the correlation time. This showed a non-monotonic variation with Pe, albeit with relatively small variations. The two-time autocorrelation of the polymer orientation, on the other hand, showed a single exponential decay, with characteristic oscillations associated with the rotation of spirals. The orientational dynamics does not depend on the conformational relaxation, and the corresponding correlation time decreases with activity as $1/Pe^2$.

Our detailed modeling of MPs allowed us to explicitly identify dependence of the polymer properties on both the active velocity of MPs v_0, and the attachment-detachment kinematics fixed by the ratio $\omega_{\rm on}/\omega_0$. Together, they characterize the MP activity and depend on the ambient ATP concentration. Our predictions are amenable to direct experimental verifications in *in vitro* motility assays. For example, we can estimate the correlation time for turning number and polymer extension of a filament driven by motor proteins. The viscosity in the cell is around 100 times that of water $\eta_w = 0.001\,\text{pN-s}/\mu\text{m}^2$ [22]. Assuming a similar viscosity in the motility assay, one gets $\eta = 100\,\eta_w = 0.1\,\text{pN-s}/\mu\text{m}^2$. The corresponding viscous damping over a bond-length σ is $\gamma = 3\pi\eta\sigma$. The activity of MPs can be changed by changing the ambient ATP concentration. For example, for kinesins, the active velocity v_0 varies from $0.01\,\mu\text{m/s}$ to $1\,\mu\text{m/s}$, as the ATP concentration is increased from $1\,\mu\text{M}$ to $1\,\text{mM}$ [114]. This corresponds to $Pe = \gamma v_0 L^2/k_B T\sigma = 3\pi\eta v_0 L^2/k_B T$. At room temperature $k_B T = 4.2\times10^{-3}\text{pN-}\mu\text{m}$. A filament of length $10\,\mu\text{m}$ experiences $Pe \approx 2\times10^4$. Using the unit of time $\tau = \gamma L^3/4\sigma k_B T = 3\pi\eta L^3/4k_B T \approx 15.6$ hours, the estimated correlation time for turning number, radius of gyration and end-to-end separation of the filament $\sim 0.1\,\tau$ translates to about 1.5 hours. Our qualitative predictions for transitions between open chain to spiral, and the non-monotonic variations of the polymer size and shape with changing v_0 can be tested by controlling ATP concentration in the motility assays.

In the next chapter, we approach the cytoskeletal filaments and motor proteins using active hydrodynamics.

6.10 Appendix

6.10.1 Equilibrium persistence

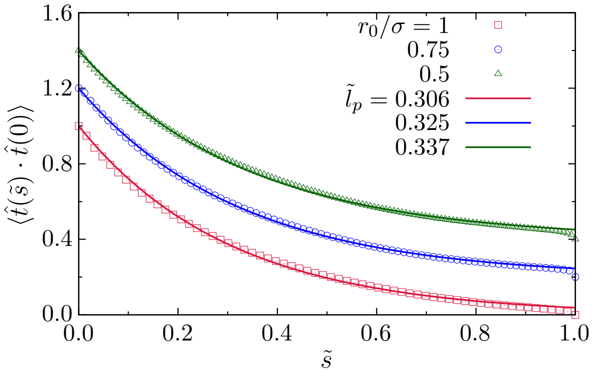

Figure 6.16: (color online) Increase in equilibrium persistence length due to reduction of bond length r_0 with respect to the WCA length scale σ. Tangent-tangent correlation functions $\langle \hat{t}(\tilde{s}) \cdot \hat{t}(0) \rangle$ as a function of $\tilde{s} = s/L$ are shown at three values of $r_0/\sigma = 1, 0.75, 0.5$. The lines denote the exponential decay of correlation as $\exp(-\tilde{s}/\tilde{l}_p)$, with corresponding persistence length $\tilde{l}_p$ denoted in the figure legend. Plots for $r_0/\sigma = 0.75, 0.5$ are shifted upwards by 0.2 and 0.4 for better visibility.

The presence of WCA repulsion between non-bonded beads changes the equilibrium properties of the chain with respect to an ideal semiflexible polymer. At short length scale it increases the effective persistence length. This can be seen from Fig. (6.16), where we plotted the tangent-tangent correlation $\langle \hat{t}(\tilde{s}) \cdot \hat{t}(0) \rangle$ with $\tilde{s} = s/L$ denoting relative contour-wise separation between bonds. Smoothening of the potential profile along the chain, reducing bond length r_0 with respect to the WCA size σ, leads to enhanced repulsion between neighboring bonds. This adds to the energy cost to transverse fluctuations, thereby increasing the effective

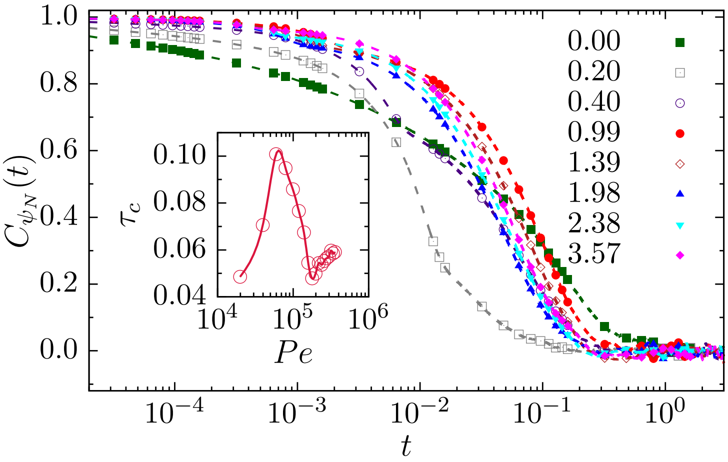

Figure 6.17: (color online) Two time correlation functions of turning number $C_{\psi_N}(t)$ for a smoothened polymer with $r_0/\sigma = 0.75$ calculated at $\omega_{\text{on}}/\omega_0 = 1$ and various activity $Pe = \tilde{P}e \times 10^5$ with $\tilde{P}e$-values denoted in the figure legend. The inset shows a non-monotonic variation of the corresponding correlation times with Pe.

persistence length $\tilde{l}_p$ defined as $\langle \hat{t}(\tilde{s}) \cdot \hat{t}(0) \rangle \approx \exp(-\tilde{s}/\tilde{l}_p)$. The increase in $\tilde{l}_p$ with r_0/σ is shown in Fig. (6.16). In fact, for longer chains, at large contour separations with respect to the persistence length, the effect of self-avoidance dominates over bending rigidity. It leads to the Flory scaling $\langle r^2(s) \rangle \sim s^{2\nu}$, which corresponds to a power-law decay in the correlation $\langle \hat{t}(s) \cdot \hat{t}(0) \rangle \sim s^{-(2-2\nu)}$ at long contour separations. In an intermediate $\tilde{s}$, the correlation function crosses over from exponential to power-law decay.

6.10.2 Correlation time in smoothened polymer

Here we compute the correlation function of turning number $C_{\psi_N}(t) = \langle \psi_N(t)\psi_N(0) \rangle / \langle \psi_N^2(0) \rangle$ for the smoothened chain with $r_0/\sigma = 0.75$ (Fig. (6.17)) at different values of Pe keeping the attachment- detachment ratio $\omega_{\text{on}}/\omega_0 = 1$ fixed. To keep the chain length unchanged with respect to the chain with $r_0/\sigma = 1.0$, we use $N = 85$ beads. The correlation times τ_c are determined by identifying where $C_{\psi_N}(t)$ touches zero. The plot of correlation time in the inset of Fig. (6.17) shows a non-monotonic variation similar to Fig. (6.15)(a), while the actual values of τ_c remains smaller than the chain with $r_0/\sigma = 1.0$.

7

Pattern formation in active fluids: uniform and stress- dependent turnover

7.1 Introduction

The cell cortex is an actin and myosin rich layer of cytoplasm on the inner face of cell membrane regulating the cell behavior. In most eukaryotic cells it consists of a network of cross-linked filamentous actin (F-actin), myosin II mini-filaments, actin binding proteins, membrane anchors, and other regulatory proteins [48]. It generates active mechanical stress forming self-organized patterns that govern crucial mechanical and dynamical properties of animal cells [39, 70]. It was recognized early on that changes in morphology is determined by the coupling between chemical and mechanical states in cells and tissues [73]. The generation of active mechanical forces utilizing ATP and associated active advection can lead to spatial pattern formation in cells [23]. Such pattern formation, spontaneous oscillation, pulsation, propagation of stress waves were observed and studied in several contexts [57, 75–78]. The changing morphology of cells and tissues utilize regulation of active force generation and transmission [71, 72]. Actomyosin pulsations, waves, and wavy protrusions of cell membranes are found in migrating cells [149–153].

In the actomyosin cortex, F-actin network undergoes active contraction due to cross-linked myosins [78, 150, 154]. Such contraction can generate active flow. Depending on the local state, myosins can detach from the actin network relieving the stress build up. In the current chapter, we consider a coarse-grained theory to study the resultant pattern formation and dynamics. We develop a framework where we consider the fraction of the system in which myosins actively contract the actomyosin as the active component. The other regions where myosins are detached from F-actins, the actomyosin is considered to be a passive component. As a whole, we consider the actomyosin as a two component fluid with active and passive components undergoing turnover between them. Over a short time scale, the actomyosin behaves like an elastomeric mesh. However, over time-scales longer than the network reorganization time, attachment-detachment of cross-linkers can fluidize the actomyosin complex. We consider the actomyosin as an active fluid with turnover between its effective passive and active components. For simplicity, we use an isotropic active fluid model [23, 74]. In the simplest picture, the turnover rates can be assumed to be uniform. In this chapter, we also consider a possible stress-dependent turnover. The possibility of strain-rate dependent turnover is considered separately in the following chapter.

The chapter is organized as follows. In Section-7.2, we present the model and governing equations for the two-component active fluids with turnover. In Section-7.3, we demonstrate the linear stability analysis of governing equations. We identify the different phases allowed within the linear stability analysis. In Section-7.4, we describe the results for uniform turnover rates. In Section-7.5, we discuss the stress-dependent turnover. Finally, we conclude the chapter in Section-7.6.

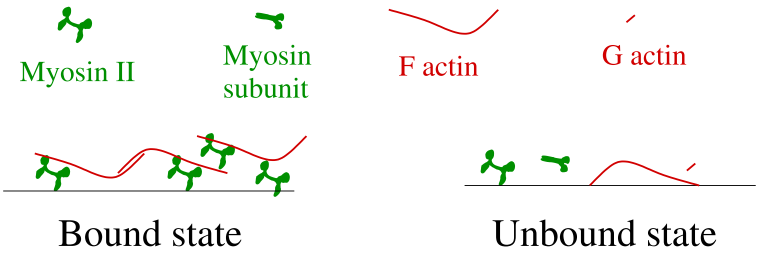

Figure 7.1: (Color online) Schematic representation of actomyosin complex: Bound state and unbound state. Bound state : Myosin II attached F-actin and Unbound state : Myosin II and F-actin in detached state. The diagram also indicates myosin subunits, and globular actins (G-actin).

7.2 Hydrodynamic description of model

In this section we describe the actomyosin layer as an active viscous fluid. We build up a hydrodynamic description of the active fluid with turnover between its components. We consider a minimal phenomenological description. The main elements of the actomyosin complex is shown in the schematic diagram of Fig. (7.1). It consists of a cross-linked F-actin network and myosin minifilaments which can bind to this network. The main elements of the theory are: (a) The actomyosin complex consisting of myosin-II mini-filaments attached to the actin network considered as bound or active fraction of actomyosin. (b) The detached actomyosin complex which is consists of myosin-II mini-filaments detached from actin-network, G-actin monomers, myosin subunits. This is considered passive not able to generate the contractile stress. The actomyosin network is immersed in a highly viscous cytosol and undergo dynamics on a dissipative substrate. A hydrodynamic force balance in the over-damped limit gives the estimate of flow.

A perpendicular projection of the thin actomyosin layer along a cell-membrane can be described as a quasi-one dimensional system [23]. We consider a two component fluid with bound and unbound actomyosin concentrations $C_b(x,t)$ and $C_u(x,t)$ undergoing drift, diffusion and turnover following

$$\partial_t C_b = -\partial_x (v\ C_b) + D_b \partial_x^2 C_b - \omega_{\text{off}}\ C_b + \omega_{on}\ C_u, \tag{7.1}$$

$$\partial_t C_u = -\partial_x (v\ C_u) + D_u \partial_x^2 C_u + \omega_{\text{off}}\ C_b - \omega_{on}\ C_u. \tag{7.2}$$

In the above equations $D_{b,u}$ denotes the diffusivities of the bound and unbound) fractions. In the last two terms $\omega_{\text{off, on}}$ describe the turnover. The drift current $v(x,t)$ is governed by the force balance relation

$$\eta \partial_x^2 v - \partial_x P + \partial_x \sigma_a = \gamma v. \tag{7.3}$$

Note that within the one-dimensionally projected description the fluid behaves as compressible, as it can flow out in the plane parallel to the membrane. Thus η describes that effective bulk viscosity. The passive stress of the fluid can be described in terms of the pressure P. The last term in the above equation, σ_a denotes the active stress. The dynamics is considered to take place in the presence of a friction due to the membrane described by the frictional drag γ.

The pressure due to the passive unbound fraction $C_u(x,t)$ can be described as

$$P = \xi_p f(C_u). \tag{7.4}$$

Assumption of the ideal gas law requires $\xi_p = k_B T$ and $f(C_u) = C_u$. The active stress arises from the force exerted by attached myosins [37]. Assuming isotropy, one can express the active stress as

$$\sigma_a = \xi_a (\Delta\mu)_0 f(C_b), \tag{7.5}$$

where, ξ_a is the strength of activity and $(\Delta\mu)_0$ represents the change in chemical potential due to the hydrolysis of adenosine-tri-phosphate (ATP). Here $\xi_a > 0$ (< 0) describes a contractile (extensile) stress generation. Since an active contractile stress arises due to the bound myosin mini-filaments [23, 155–159], the stress is assumed to be function of the bound actomyosin concentration. The active stress saturates at large enough concentrations [160]. Thus, we consider a hyperbolic function $f(C_b) = C_b/(1 + C_b)$.

The turnover between the active and passive fraction consists of attachment-detachment events of individual molecular motors. The detachment rate of individual motor proteins are known depend on the load force acting on them [67]. In the coarse-grained theory the turnover rates may depend on the local stress $\sigma(x,t)$ or strain-rate $\dot{\epsilon} = \partial_x v(x,t)$. We consider a diffusion limited attachment described by a constant ω_{on}, and a Hill form for $\omega_{\text{off}} = \omega_0 \exp(\sigma/\sigma_0)$ or $\omega_{\text{off}} = \omega_0 \exp(\dot{\epsilon}/\nu)$.

7.3 Dimensionless equations and linear stability analysis

In this section we non- dimensionalize the evolution governed by Eq.s (7.1), (7.2), and (7.3) and describe the linear stability analysis.

7.3.1 Dimensionless equations

The unit of length is set by the hydrodynamic length scale $l = \sqrt{\eta/\gamma}$. We set the unit of time using the diffusion time scale of the bound fraction $\tau = l^2/D_b$. We recast the governing equations (7.1), (7.2), and (7.3) in a dimensionless form by renaming $x/l \to x$, $t/\tau \to t$, $C_b l \to C_b$, $C_u l \to C_u$, $v\tau/l \to v$ and $D_u/D_b \to D$, $\omega_0 \tau \to \omega_0$, $\omega_{on}\tau \to \omega_{on}$, $\alpha/\tau \to \alpha$. Thus, in the dimensionless form the evolution can be expressed as

$$\partial_t C_b = -\partial_x(v\ C_b) + \partial_x^2 C_b - \omega_{\text{off}}\ C_b + \omega_{on}\ C_u, \tag{7.6}$$

$$\partial_t C_u = -\partial_x(v\ C_u) + D\partial_x^2 C_u + \omega_{\text{off}}\ C_b - \omega_{on}\ C_u, \tag{7.7}$$

$$\partial_x^2 v - \xi\ \partial_x f(C_u) + Pe\ \partial_x f(C_b) = v, \tag{7.8}$$

where $\xi = \xi_p/\gamma D_b$ denotes the strength of passive pressure and the Péclet number $Pe = \xi_a(\Delta\mu)_0/\gamma D_b$ denotes activity in terms of the ratio of diffusive time scale $\tau = l^2/D_b$ and advective time scale $\tau_a = \eta/\xi_a(\Delta\mu)_0$.

Dimensionless form of rates: (a) The dimensionless form of the stress dependent off-rate is $\omega_{\text{off}} = \omega_0 \exp[\alpha\sigma]$ where $\alpha = \eta/\sigma_0\tau$ is a dimensionless constant and $\sigma = \partial_x v + Pef(C_b) - \xi f(C_u)$ is the dimensionless stress. (b) The dimensionless form of strain rate dependent off rate is $\omega_{\text{off}} = \omega_0 \exp(\alpha\partial_x v)$ where $\alpha = 1/\tau\nu$ is a dimensionless constant and $\partial_x v$ is a dimensionless strain rate. We investigate the effect of strain-rate-dependent turnover in the next chapter. In this chapter, we discuss the stress-dependent turnover of the two-component active fluids. However, for clarity and simplicity, we begin our discussion using a uniform off-rate.

The total concentration $C_{t0} = C_{b0}(t) + C_{u0}(t)$ is a conserved field in the sense $\int dx C_{t0}(x)$ integrated over the whole space is constant. We perform direct numerical integration of the dimensionless coupled equations (8.5), (8.6), and (8.7) using the IMEX scheme (MCNAB algorithm) with periodic boundary conditions [161]. The details of the scheme is discussed in Appendix-7.7.1.

7.3.2 Linear stability analysis

The homogeneous steady state is described by $v = 0$ and concentrations C_{b0} and C_{u0}. We linearize the equations for small deviations around this steady state: $v \sim \delta v_0 e^{\lambda t} e^{iqx}$ and $C_{b(u)} - C_{b0(u0)} \sim \delta C_{b0(u0)} e^{\lambda t} e^{iqx}$ with wave vector q and growth rate λ. The spatial Fourier-amplitude of the velocity field can be expressed as

$$\delta v_0 = \frac{iq}{1+q^2} \left[Pe\delta C_{b0} f_{C_b} - \xi \delta C_{u0} f_{C_u} \right], \tag{7.9}$$

where $f_{C_b} = \partial_{C_b} f(C_b)|_{C_b = C_{b0}} = 1/(1+C_{b0})^2$ and $f_{C_u} = \partial_{C_u} f(C_u)|_{C_u = C_{u0}} = 1$. The equations governing the concentration evolution leads to $\lambda(\delta C_{b0}, \delta C_{u0}) = \Omega(\delta C_{b0}, \delta C_{u0})$. The properties of the dynamics can be analyzed diagonalizing the 2×2 linear stability matrix Ω. This gives eigenvalues $\lambda = (tr \pm \sqrt{tr^2 - 4\,det})/2$, where tr and *det* denote the trace and determinant of the matrix Ω, respectively. The parameter regimes of $tr < 0$ and $det > 0$ denote stable homogeneous state. The eigenvalues show non-zero imaginary part if $det > tr^2/4$. The homogeneous state undergoes pulsating instability at $tr = 0$ for $det > 0$. At $det > 0$ regime, the pulsating state transforms into inhomogeneous pattern as the linear instability line $tr = 2\sqrt{det}$ is crossed by increasing tr. On the other hand, the whole region of $det < 0$ is linearly unstable with respect to the homogeneous state, leading to pattern formation.

7.4 Uniform turnover

In this section, we investigate the active fluids with uniform turnover. We describe the linear stability analysis and explore the phase diagram in the ω_{on}-Pe plane for constant off-rate ω_0.

7.4.1 In the absence of pressure

In the limit of high activity $Pe \gg \xi$, the pressure term in Eq. (8.7) can be neglected. We investigate the pattern formation and phase diagram in ω_{on}-Pe.

Linear stability analysis

In the absence of pressure Eq. (7.9) reduces to $\delta v_0 = iq\left[Pe\delta C_{b0} f_{C_b}\right]/(1+q^2)$. Linear analysis of C_b and C_u evolution Eq. (8.5) and (8.6) around a small perturbation of the form $C_{b(u)} - C_{b0(u0)} \sim \delta C_{b0(u0)} e^{\lambda t} e^{iqx}$ and using the linearised form of δv_0 leads to the linear stability matrix Ω,

$$\Omega = -q^2 \begin{pmatrix} 1 - \frac{Pe}{1+q^2} C_{b0} f_{C_b} & 0 \\ -\frac{Pe}{1+q^2} C_{u0} f_{C_b} & D \end{pmatrix} + \begin{pmatrix} -\omega_0 & \omega_{\text{on}} \\ \omega_0 & -\omega_{\text{on}} \end{pmatrix}, \tag{7.10}$$

The eigen values of the linear stability matrix Ω in Eq. (7.10) are $\lambda = (tr \pm \sqrt{\Delta})/2$ where tr is the trace of the linear stbility matrix and $\Delta = tr^2 - 4\ det$ is the

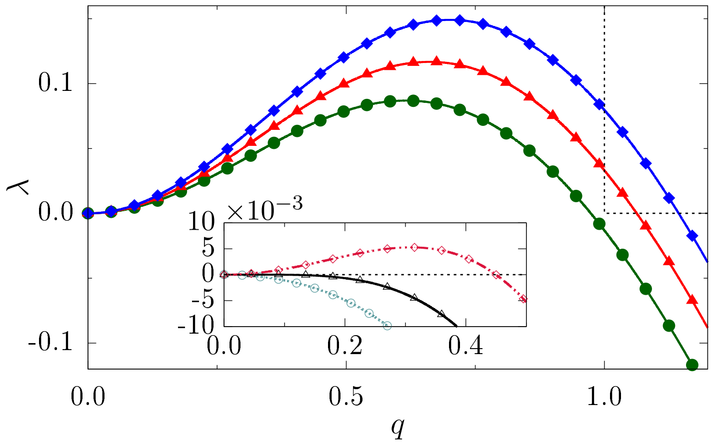

Figure 7.2: (Color online) Two component active fluids system with uniform turnover in the absence of pressure $\xi = 0$. Plot of the maximum eigen value $\lambda_{max} = (tr + \sqrt{\Delta})/2$ of the linear stability matrix in Eq. (7.10) as a function of q with Péclet numbers $Pe = 5.0(\bigcirc)$, $5.5(\triangle)$, $6.0(\diamond)$. Inset: The first zero crossing of maximum eigen value (λ) is shown for $Pe = 2.0(\bigcirc)$, $2.5(\triangle)$, $3.0(\diamond)$. In a system of size $L = 2\pi$, the minimum possible q mode that influences the system is $q = 2\pi/L = 1$. This suggests that the uniform state in such a system at $Pe = 5.0$ will be linearly stable – see the region inside the black dashed line in the main figure covering the region of $\lambda > 0$ and $q \geq 1$. With increasing system size L, smaller q-modes can appear. The parameter values used are $D = 0.1$, $\omega_0 = 1$, $\omega_{on} = 1$, $C_{t0} = 1$.

discriminant of the linear stability matrix in Eq. (7.10) where *det* is determinant of the linear stbility matrix in Eq. (7.10). In case of $\Delta > 0$, maximum eigen value of the linear stability matrix is $\lambda_{max} = (tr + \sqrt{\Delta})/2 = 0$ determines the boundary between linearly stable to linearly unstable regimes. In case of $\Delta < 0$, the trace $tr = 0$ of the linear stability matrix in Eq. (7.10) determines the phase boundary between stable spiral and unstable spiral.

The trace of the linear stability matrix in Eq. (7.10),

$$tr = -q^2(1 + D) + \frac{q^2}{1 + q^2} Pe C_{b0} f_{C_b} - (\omega_0 + \omega_{on}) \tag{7.11}$$

It switches sign from negative to a positive value with increasing of contractile

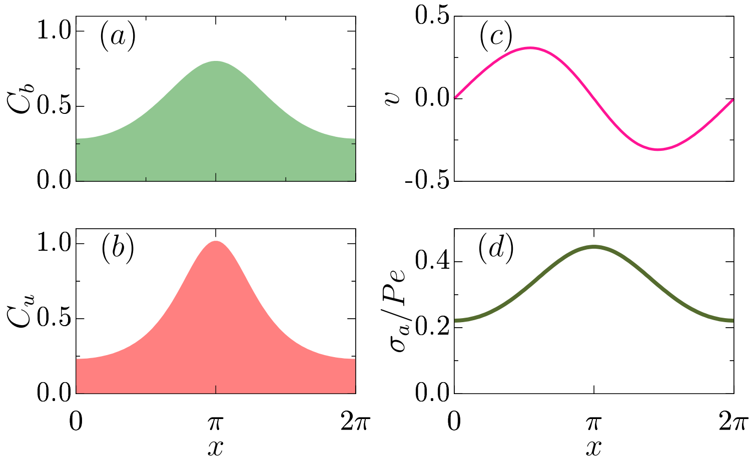

Figure 7.3: (Color online) Two component active fluid with uniform turnover in the absence of pressure $\xi = 0$. The system size is $L = 2\pi$. (a) shows a non-uniform pattern of bound concentrations $C_b(x)$. (b) shows a non-uniform pattern of unbound concentrations $C_u(x)$. (c) corresponding to the velocity profile $v(x)$ and (d) represents the active stress $\sigma_a(x)$. The parameter values are $D = 0.1$, $\omega_0 = 1$, $\omega_{on} = 1$, $C_{t0} = 1$ and $Pe = 5.5$.

activity Pe. The discriminant of the linear stability matrix in Eq. (7.10) is

$$\begin{aligned}\Delta = &\left[-q^2\left(1+D\right) + \frac{q^2}{1+q^2} Pe C_{b0} f_{C_b} - \left(\omega_0 + \omega_{on}\right)\right]^2 \\ &+ 4\,\omega_{on}\left(\frac{q^2}{1+q^2} Pe C_{u0} f_{C_b} + \omega_0\right). \end{aligned} \tag{7.12}$$

The condition to get an imaginary part in the eigen values is $\Delta < 0$. In case of contractile active fluids the activity parameter Pe is always positive. Thus, the discriminant Δ in Eq. (7.12) is always positive leading states that could be either linearly stable or linearly unstable.

Fig. (7.2)(a) shows the variation of maximum eigen value of linear stability matrix in Eq. (7.10) with mode number q for two component active fluids system with uniform turnover rate. Inset of Fig. (7.2) shows the minimum amount of activity Pe required for the onset of instability.

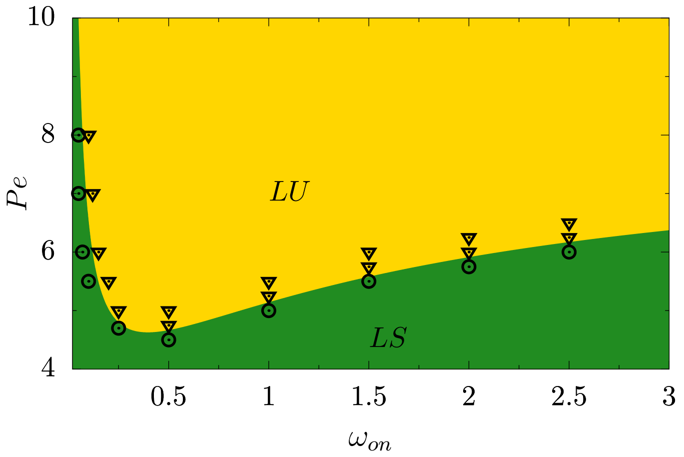

Figure 7.4: (Color online) Phase diagram for the two component active fluid with uniform turnover and pressure $\xi = 0$ for system size $L = 2\pi$ in one dimension. The linearly stable (LS) regime represents $\lambda_{max} < 0$ and linearly unstable (LU) regime represents $\lambda_{max} > 0$. The phase boundary corresponds to $\lambda_{max} = 0$ where $\lambda_{max} = (tr+\sqrt{\Delta})/2$ where tr is given by Eq. (7.11) and Δ is given by Eq. (7.12). The points denote results from direct numerical integrations of Eq. (8.5), (8.6), and (8.7). The symbols denote homogeneous steady state (○) fluid pattern and inhomogeneous pattern formation (▽). The growing modes within linearly stability analysis corresponding to the linearly unstable regime (LU) regime stabilizes by the non-linearities in the equations forming steady patterns. The parameter values used are $D = 0.1$, $\omega_0 = 1$, $C_{t0} = 1$.

Patterns and phase diagram

We solve the dimensionless governing Eqs. (8.5), (8.6), and (8.7) numerically, for a periodic system of size $L = 2\pi$ in one dimension. Fig. (7.3)(a) shows a non-uniform fluid pattern of bound concentrations C_b. Fig. (7.3)(b) shows a non-uniform fluid pattern of unbound concentrations C_u. Fig. (7.3)(c) corresponding to velocity $v(x)$ and Fig. 7.3(d) represents the active stress $\sigma_a(x)$. Fig. (7.4) shows the corresponding phase diagram in the ω_{on}-Pe plane. It clearly shows that a minimum activity Pe is required for pattern formation. The transition from homogenous state to pattern formation shows an interesting re-entrant behavior with ω_{on} rate leading to a homogeneous to pattern forming to homogeneous state with increasing ω_{on}.

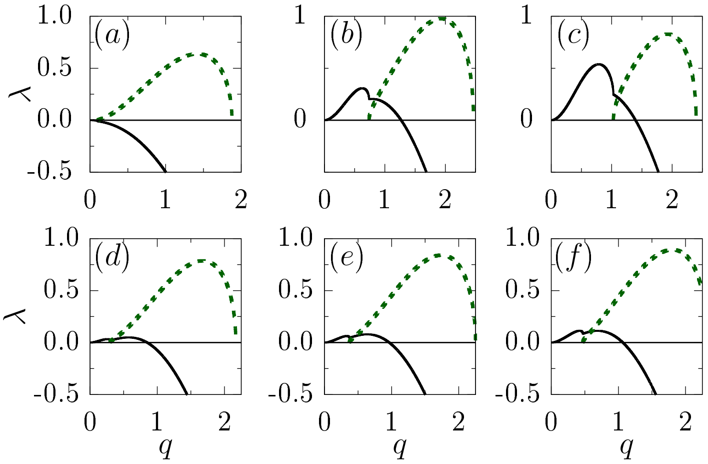

Figure 7.5: (Color online) Two component active fluids system with uniform turnover in the presence of pressure $\xi = 1$. Plot of the real part(black solid line) and imaginary part(blue dashed line) of the maximum eigen value $\lambda_{max} = (tr + \sqrt{\Delta})/2 \equiv \lambda_{Re} + i\lambda_{Im}$ of the linear stability matrix Ω in Eq. (7.13) as a function of mode number q. Fig. (a), (b), and (c): $Pe = 15$, $\omega_{on} = 0.001$ (a), 0.011 (b), and 0.021 (c). Fig. (d), (e), and (f): $\omega_{on} = 0.01$, $Pe = 11$ (d), 12 (e), and 13 (f). The parameter values are $D = 0.1$, $\omega_0 = 0.01$, $C_{t0} = 1$.

7.4.2 In the presence of pressure

Here, we investigate the two-component active fluids with uniform turnover in the presence of pressure, $\xi \neq 0$. We describe the linear stability analysis and explore the phase diagram in the ω_{on}-Pe plane.

Linear stability analysis

The linear stability matrix in this case becomes

$$\Omega = -q^2 \begin{pmatrix} 1 & 0 \\ 0 & D \end{pmatrix} + \frac{q^2}{1+q^2} \begin{pmatrix} Pe\, C_{b0} f_{C_b} & -\xi C_{b0} f_{C_u} \\ Pe\, C_{u0} f_{C_b} & -\xi C_{u0} f_{C_u} \end{pmatrix} + \begin{pmatrix} -\omega_0 & \omega_{on} \\ \omega_0 & -\omega_{on} \end{pmatrix}. \quad (7.13)$$

The eigen-values are are $\lambda = (tr \pm \sqrt{\Delta})/2$ where tr is the trace and $\Delta = tr^2 - 4det$ is the discriminant of Ω. For $\Delta < 0$, the trace $tr = 0$ of the linear stability matrix in Eq. (7.13) determines the phase boundary between the stable spiral and unstable spiral phase. In case of $\Delta > 0$, the maximum eigen-value of the linear stability matrix is $\lambda_{max} = (tr + \sqrt{\Delta})/2$. Here $\lambda_{max} = 0$ determines the boundary between the linearly stable and linearly unstable phases.

The trace tr of the linear stability matrix in Eq. (7.13),

$$tr = -q^2(1+D) + \frac{q^2}{1+q^2}\left[Pe\, C_{b0} f_{C_b} - \xi C_{u0} f_{C_u}\right] - (\omega_0 + \omega_{on}). \tag{7.14}$$

Trace of the linear stability matrix switches sign from negative to a positive value with increasing contractile activity Pe. Thus, it leads to oscillatory instability when discriminant $\Delta < 0$. In the hydrodynamic limit the trace in Eq. (7.14) simplifies to $tr_{q\to 0} = -(\omega_0 + \omega_{on})$. Thus, there is no instability in the hydrodynamic limit. Now, we calculate discriminant Δ of the linear stability matrix in Eq. (7.13),

$$\begin{aligned}\Delta = &\left[-q^2\left(1+D\right) + \tfrac{q^2}{1+q^2}\left(Pe\, C_{b0} f_{C_b} - \xi C_{b0} f_{C_u}\right) - \left(\omega_0 + \omega_{on}\right)\right]^2 \\ &+4\left(-\tfrac{q^2}{1+q^2}\xi C_{b0} f_{C_u} + \omega_{on}\right)\left(\tfrac{q^2}{1+q^2} Pe C_{u0} f_{C_b} + \omega_0\right).\end{aligned} \tag{7.15}$$

The condition to get imginary part in the eigen values is $\Delta < 0$. The first term of the discriminant in Eq. (7.15) is always poisitive. In the absence of pressure $\xi = 0$, the discriminant Δ in Eq. (7.15) is always positive. And, the second term of the discriminant in Eq. (7.15) switches sign from positive to a negative value when $\xi > (1+q^2)\omega_{on}/q^2 C_{b0} f_{C_u}$. Thus discriminant Δ in Eq. (7.15) may switch the sign from a positive to a negative value in the presence of pressure.

Steady state results: phase diagram, patterns, pulsation

In Fig. (7.6) we show the phase diagram obtained from the above analysis and direct numerical integration of Eq. (7.14). This shows three phases, homogeneous steady state, localized pulsation, and steady state pattern formation. Fig. (7.7) and Fig. (7.8) show space-time plot of bound, unbound concentrations, and the velocity profile. Fig. (7.7) shows localized pulsation of the non-uniform fluid pattern. Here, the bound and unbound concentrations show same phase pulsation. The peak of bound concentration emerges at the same spatial location as the peak of the unbound concentration. On the other hand, Fig. (7.8) displays local structure in

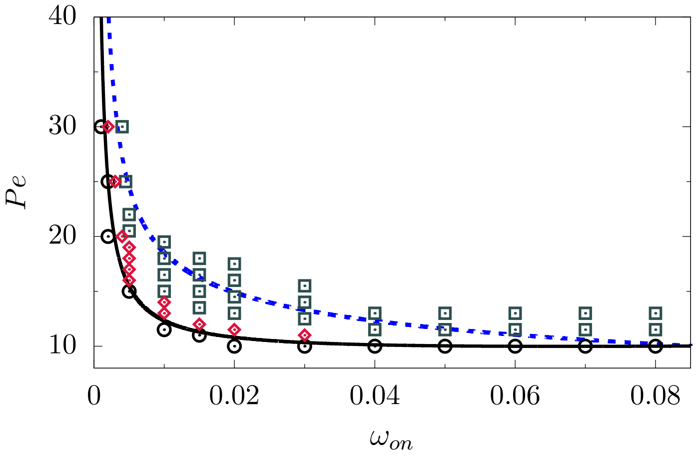

Figure 7.6: (Color online) Phase diagram of the two component active fluid with uniform turnover in the presence of pressure $\xi = 1$, for system size $L = 2\pi$ in one dimension. The black solid line corresponds to $tr = 0$ in Eq. (7.14), and the dashed blue line corresponds to $\Delta = 0$ and $tr > 0$ in Eq. (7.15). The regime between these two lines represents the unstable spiral phase. The points denote numerical integrations of Eq. (8.5), (8.6), and (8.7). The symbols denote regimes of homogenous steady state (○), localized pulsation (◇), and inhomogeneous steady state pattern (□). The parameter values used are $D = 0.1$, $\omega_0 = 0.01$, $C_{t0} = 1$.

the stationary pattern forming phase.

Average bound, unbound concentrations, and flow velocity : The spatial average quantity of a function $f(x,t)$ defined as $S_f(t) = \frac{1}{2\pi}\int_{x=0}^{L} dx\ f(x,t)$. We numerically investigate the spatial average of $C_b(x,t)$, $C_u(x,t)$ and $v(x,t)$. The sptial average of bound and unbound concentration becomes $S_{C_b}(t) = C_{b0}$, $S_{C_u}(t) = C_{u0}$ respectively. The mean flow velocity $S_v(t) = 0$. Thus, there is no overall directed flow in active fluids with uniform turnover.

7.5 Stress-dependent turnover

In this section, we investigate the active fluids with stress-dependent turnover. We describe the linear stability analysis and explore the phase diagram in the ω_{on}-Pe plane. The concentration fields C_b and C_u are coupled through advection and stress-dependent turnover. The spatially homogeneous steady-state solutions of the governing equations are $C_{u0} = (\omega_0^{\text{eff}}/\omega_{\text{on}})C_{b0}$ where $\omega_0^{\text{eff}} = \omega_0 \exp[\alpha(Pef(C_{b0}) -$

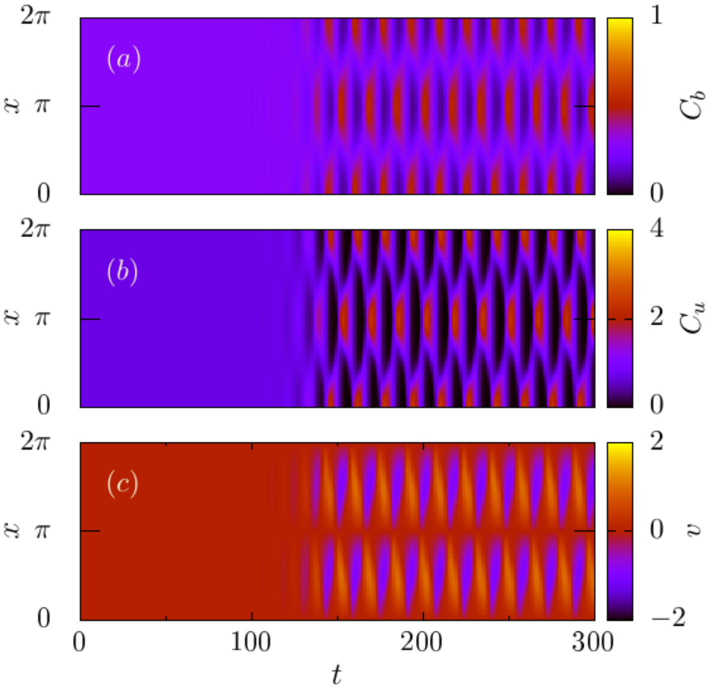

Figure 7.7: (Color online) Evolution of the relevant fields (*a*) $C_b(x,t)$, (*b*) $C_u(x,t)$, and (*c*) $v(x,t)$ for the two component active fluid with uniform turnover in the presence of pressure $\xi = 1$. The parameter values are $D = 0.1$, $\omega_0 = 0.01$, $C_{t0} = 1$, $\omega_{\rm on} = 0.004$, $Pe = 20$ correspond to the localized pulsatory patterns. The initial homogeneous state starts to show pulsations ear $t = 150$.

$\xi f(C_{u0}))]$ and $v = 0$. The total concentration is $C_{t0} = C_{b0} + C_{u0}$. Thus, the steady state solution for C_{b0} leads to the condition,

$$C_{t0} - C_{b0} = \frac{\omega_0 C_{b0}}{\omega_{on}} \exp[\alpha(Pef(C_{b0}) - \xi f(C_{t0} - C_{b0}))]. \tag{7.16}$$

This self-consistent equation is solved for particular parameter values to obtain the homogeneous steady state values of C_b and hence $C_u = C_{t0} - C_b$ in Fig. (7.9).

The procedure of linear stability analysis of C_b and C_u evolution using a small perturbation of the form $C_{b(u)} - C_{b0(u0)} \sim \delta C_{b0(u0)} e^{\lambda t} e^{iqx}$ and Eq. (7.9) leads to the

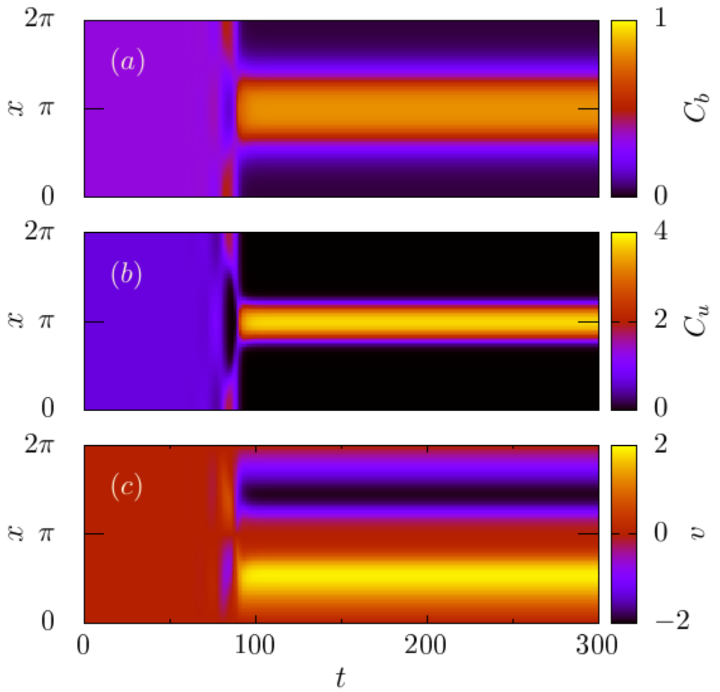

Figure 7.8: (Color online) Evolution of the relevant fields (a) $C_b(x,t)$, (b) $C_u(x,t)$, and (c) $v(x,t)$ for the two component active fluid with uniform turnover in the presence of pressure $\xi = 1$. The parameter values $D = 0.1$, $\omega_0 = 0.01$, $C_{t0} = 1$, $\omega_{on} = 0.005$, $Pe = 20$ correspond to stationary pattern formation. The initial homogeneous state starts to form pattern near $t = 100$.

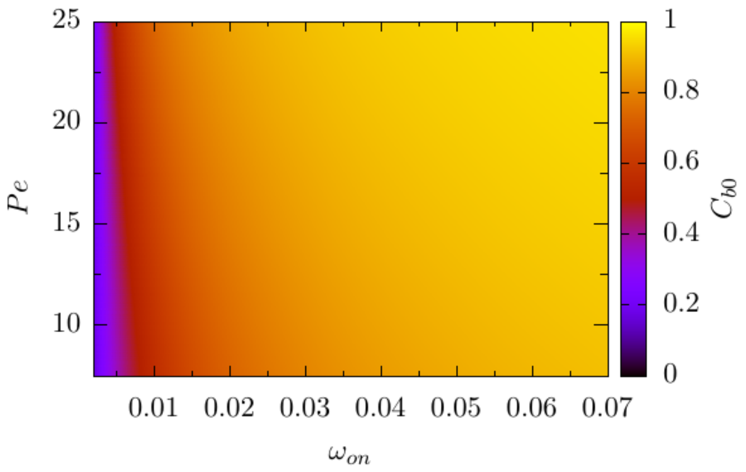

Figure 7.9: (Color online) Two component active fluids system with stress-dependent turnover in the presence of pressure $\xi = 1$. The steady state solution of bound concentration C_{b0} is shown as a function of ω_{on} and Pe. We numerically solved the self-consistent Eq. (7.16) for parameter values $D = 0.1$, $\alpha = -0.1$ $\omega_0 = 0.01$, $C_{t0} = 1$.

linear stability matrix Ω,

$$\Omega = -q^2 \begin{pmatrix} 1 & 0 \\ 0 & D \end{pmatrix} + \frac{q^2}{1+q^2} \begin{pmatrix} Pe\ C_{b0} f_{C_b} & -\xi\ C_{b0} f_{C_u} \\ Pe\ C_{u0} f_{C_b} & -\xi\ C_{u0} f_{C_u} \end{pmatrix}$$

$$+ \frac{\alpha\ \omega_0^{\text{eff}} C_{b0}}{1+q^2} \begin{pmatrix} -Pe\ f_{C_b} & \xi\ f_{C_u} \\ Pe\ f_{C_b} & -\xi\ f_{C_u} \end{pmatrix} + \begin{pmatrix} -\omega_0^{\text{eff}} & \omega_{on} \\ \omega_0^{\text{eff}} & -\omega_{on} \end{pmatrix} \tag{7.17}$$

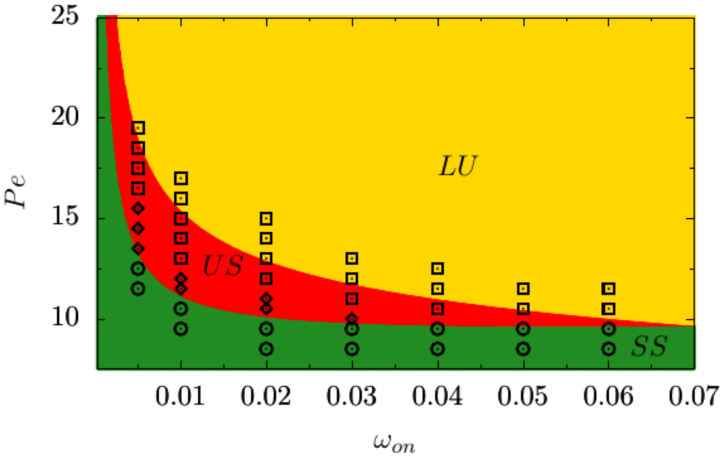

Figure 7.10: (Color online) Phase diagram of the two component active fluid with stress-dependent turnover in the presence of pressure $\xi = 1$, for system size $L = 2\pi$ in one dimension. The different color shades correspond to predictions of three different states from linear stability analysis: stable spiral (green SS), unstable spiral (red US), linearly unstable (yellow LU). The symbols denote phase behaviors obtained from direct numerical integration of Eq. (8.5), (8.6), and (8.7). The symbols denote regimes of pattern formation (□), localized pulsation (◇), and homogeneous fluid (○). The parameter values used are $D = 0.1$, $\alpha = -0.1$ $\omega_0 = 0.01$, $C_{t0} = 1$.

The homogeneous state undergoes an instability when the real part of the greater eigenvalue or trace of the linear stability matrix $tr(q) > 0$. The condition for growing oscillatory instability is $tr^2 < 4\ det$. Assuming $tr^2 < 4\ det$, the trace of the linear stability matrix determines the phase boundary between steady-state homogeneous patterns and pulsatory patterns. The real eigen value of the linear stbility becomes $\lambda_{Re} = tr(q)$ and the imaginary part of the eigen value is $\lambda_{Im} \equiv \sqrt{-(tr^2 - 4\,det)}$. When $tr^2 \geq 4\ det$, real eigen value of the linear stability matrix is $\lambda_{Re} \equiv \lambda_{max} = (tr + \sqrt{tr^2 - 4\,det})/2$ and $\lambda_{Im} = 0$.

The trace of the linear stability matrix in Eq. (7.17) is

$$\begin{aligned} tr(q) = -q^2(1+D) + \tfrac{q^2}{1+q^2}\left[Pe\ C_{b0} f_{C_b} - \xi\ C_{u0} f_{C_u}\right] \\ -\tfrac{\alpha\ \omega_0^{\text{eff}} C_{b0}}{1+q^2}\left[Pe\ f_{C_b} + \xi\ f_{C_u}\right] - (\omega_0^{\text{eff}} + \omega_{on}), \end{aligned} \tag{7.18}$$

In the hydrodynamic limit of $q \to 0$, the trace leads to, $tr_{q\to 0} = -\alpha\,\omega_0^{\text{eff}} C_{b0}\left[Pe\ f_{C_b} + \xi\ f_{C_u}\right] - (\omega_0^{\text{eff}} + \omega_{on})$. Moreover, the determinant in this hydrodynamic limit is $det_{q\to 0} = 0$ leading to the discriminant $\Delta = tr$. Thus the maximum eigen-value is $\lambda_{q\to 0} = tr_{q\to 0}$.

Fig. (7.10) shows the phase diagram in ω_{on}-Pe plane. It show three linear-stability regimes: stable spiral (SS), unstable spiral (US), and linearly unstable (LU). Direct numerical solutions of Eq. (8.5), (8.6), and (8.7) show that they correspond to homogeneous fluid (SS), localized pulsation (US), and stationary pattern formation (LU). Thus, stress-dependent turnover shows same qualitative phase behavior as in the case of uniform turnover.

7.6 Conclusions

We have studied the two-component active fluids with turnover. *First*, we have studied the pattern formation in the presence of the uniform turnover rate. *Second*, we have studied the effect of stress-dependent turnover.

1. *Uniform turnover*: In the absence of pressure, we showed onset of pattern formation in the ω_{on}-Pe plane with increasing Pe. The phase diagram showed a re-entrant transition along the ω_{on} axis. The local variation of active stress generates a contractile flow and, as a result, the pattern formation.
2. *Uniform turnover*: In the presence of pressure, using the phase diagram in the ω_{on}-Pe plane we showed that apart from the homogeneous state and pattern formation, the system sustains localized pulsation over an intermediate regime of Pe and ω_{on}. The interplay of active contractile stress and pressure allows such pulsatory fluid pattern.
3. *Stress-dependent turnover*: The phase diagram in the presence of stress dependent turnover shows same qualitative behavior as in the previous case, displaying homogeneous steady state, pulsatory patterns, and stationary pattern formation.

In the next Chapter, we study the two-component active fluid in the presence of strain-rate dependent turnover.

7.7 Appendix

7.7.1 Implicit-Explicit (IMEX) Scheme: MCNAB method

We solved the governing equations using the Modified Crank-Nicolson, Adams-Bashforth (MCNAB) method [161]. Here, we outline the discretization of advection-diffusion equation,

$$\partial_t f(x,t) = \partial_x^2 f(x,t) - \partial_x[v(x,t)f(x,t)] + S(x,t), \tag{7.19}$$

where $S(x,t)$ is the source term.

The time derivative can be discretized as

$$\partial_t f(x,t) = \frac{f(x,t+dt) - f(x,t)}{dt}. \tag{7.20}$$

The diffusion term is discretized using the Crank-Nicolson method,

$$\begin{aligned}
&\partial_x^2 f(x,t) = \frac{9}{16}\frac{f(x+dx,t+dt) + f(x-dx,t+dt) - 2f(x,t+dt)}{dx^2} \\
&+ \frac{3}{8}\frac{f(x+dx,t) + f(x-dx,t) - 2f(x,t)}{dx^2} \\
&+ \frac{1}{16}\frac{f(x+dx,t-dt) + f(x-dx,t-dt) - 2f(x,t-dt)}{dx^2}
\end{aligned}$$

The advection term is discretized in modified Adams-Bashforth manner, to give

$$\begin{aligned}
&\partial_x[v(x,t)f(x,t)] = \frac{3}{2}\partial_x[v(x,t)f(x,t)] - \frac{1}{2}\partial_x[v(x,t-dt)f(x,t-dt)] \\
&= \frac{3}{2}\left[v(x,t)\frac{f(x+dx,t) - f(x-dx,t)}{2\ dx} + f(x,t)\frac{v(x+dx,t) - v(x-dx,t)}{2\ dx}\right] \\
&- \frac{1}{2}\left[v(x,t-dt)\frac{f(x+dx,t-dt) - f(x-dx,t-dt)}{2\ dx}\right. \\
&\left. + f(x,t-dt)\frac{v(x+dx,t-dt) - v(x-dx,t-dt)}{2\ dx}\right]
\end{aligned}$$

The IMEX method require additional memory storage of $f(x,t-dt)$. We descritized $C_b(x,t)$, $C_u(x,t)$ and $v(x,t)$ in the similar method of discritization $f(x,t)$.

Stress-dependent turnover : The source term,

$$S(x,t) = -\omega_0 e^{\alpha\sigma(x,t)} C_b(x,t) + \omega_{on} C_u(x,t).$$

The source term is discretized in explicit method,

$$\begin{aligned}
S(x,t) &= \frac{3}{2} S(x,t) - \frac{1}{2} S(x,t-dt) \\
&= \frac{3}{2} \left[-\omega_0 e^{\alpha\sigma(x,t)} C_b(x,t) + \omega_{on} C_u(x,t) \right] \\
&- \frac{1}{2} \left[-\omega_0 e^{\alpha\sigma(x,t-dt)} C_b(x,t-dt) + \omega_{on} C_u(x,t-dt) \right]
\end{aligned}$$

Strain-rate dependent turnover: This will be used in the next chapter. The source term is

$$S(x,t) = -\omega_0 e^{\alpha \partial_x v(x,t)} C_b(x,t) + \omega_{on} C_u(x,t).$$

As there is no second-order derivative in x, thus we discretize the source term in explicit method,

$$\begin{aligned}
S(x,t) &= \frac{3}{2} S(x,t) - \frac{1}{2} S(x,t-dt) \\
&= \frac{3}{2} \left[-\omega_0 \exp\left(\alpha \frac{v(x+dx,t) - v(x-dx,t)}{2\ dx} \right) C_b(x,t) + \omega_{on} C_u(x,t) \right] \\
&- \frac{1}{2} \left[-\omega_0 \exp\left(\alpha \frac{v(x+dx,t-dt) - v(x-dx,t-dt)}{2\ dx} \right) C_b(x,t-dt) \right. \\
&\left. + \omega_{on} C_u(x,t-dt) \right] \qquad (7.21)
\end{aligned}$$

The presence of $f(x, t+dt)$ in the diffusion allows one to treat the problem as in linear algebra involving a tridiagonal matrix. We use the Thomas algorithm to solve the tridiagonal matrix system efficiently. The dt value used in numerical integration ranges from $dt = 10^{-4}$ to $dt = 10^{-6}$ depending on the required numerical stability of the system.

8

Contractile active fluids with strain-rate-dependent turnover

8.1 Introduction

In the previous chapter, we have discussed two-component active fluids with uniform turnover and stress-dependent turnover. In this chapter, we consider the case of strain-rate dependent turnover. The spatiotemporal regulation of actomyosin network plays crucial role in numerous biological contexts. Examples include development of embryos, morphogenesis in epithelial cells [162, 163]. The coupling between chemical process of active stress generation and mechanical response in terms of resultant flow can lead to pattern formation [23]. Pulsatory patterns can form in a two-component system of fast diffusing species up-regulateing the active stress and slow diffusing species down regulating it [74]. Actomyosin modeled as an active elastomers with turnover showed emergence of spontaneous oscillations [75, 164, 165].

The actomyosin networks undergo assembly and disassembly [78]. The non-muscle myosin-II proteins can produce contractile stress on the network in their attached state. They themselves undergo attachment- detachment cycles relieving the local stress build up. As in the previous chapter, here we consider the actomyosin system as a two-component active fluid undergoing turnover between a passive to active contractile state. The passive state may emerge due to either myosin-detachment from the network or the disassembly of the network itself. The passive to active transition is assumed to be controlled by a constant rate parameter. We consider a strain-rate dependent off-rate from the active to passive state, such that it increases under local extension of the active fluid, as a positive strain-rate takes different parts of the network away from each other.

The chapter is organized as follows. We present the model and governing equations for the two-component contractile active fluid with strain-rate dependent turnover in Section-8.2. In Section-8.3, we present a linear stability analysis, and identify the various phases. In Section-8.4, we present the phase diagram and associated dynamics with the help of numerical integration and analytical results. Finally, we conclude presenting a summary in Section-8.5.

8.2 Model

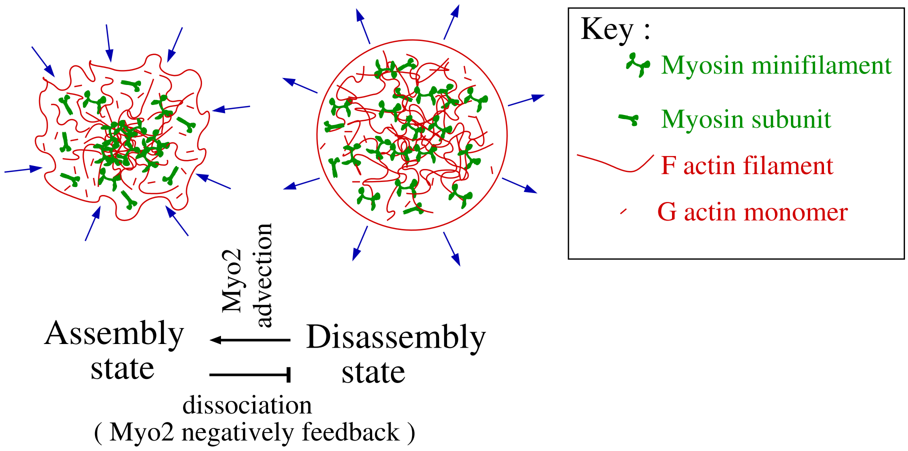

Figure 8.1: (Color online) Pulsed contractility in actomyosin. Myosin II *contractility*-induced advection leads to the actomyosin assembly state. Negative feedback via strain-rate from the myosin II reduces (enhances) the off-rate at the center (edges) of the assembly state [27].

We present a description of the actomyosin layer as a two-component active fluid.

We build up a hydrodynamic description with turnover between its components. We consider a minimal phenomenological description (Fig.8.1). In the active state with myosin motor cross-linking, the actomyosin undergoes active contractile stress. On the other hand, detachment rate of myosin motors decreases under such contraction providing a positive feedback. When myosins detach, the network relaxes and in expanded networks the detachment rate also increases. The myosin-bound active network is described by the bound concentration $C_b(x,t)$, and the passive unbound fraction has the concentration $C_u(x,t)$. We consider an overall conservation such that $\int^L dx[C_b + C_u]$ is a constant. The evolution of the concentrations is described by

$$\partial_t C_b = -\partial_x(vC_b) + D_b\partial_x^2 C_b - \omega_{off}C_b + \omega_{on}C_u, \tag{8.1}$$

$$\partial_t C_u = -\partial_x(vC_u) + D_u\partial_x^2 C_u + \omega_{off}C_b - \omega_{on}C_u, \tag{8.2}$$

$$\eta\partial_x^2 v + \partial_x\sigma_a = \gamma v, \tag{8.3}$$

where, the last equation determines the flow velocity obtained from a force-balance condition involving the friction coefficient γ describing the drag due to the substrate. Here, we consider the passive pressure to be zero, i.e., negligible with respect to the active stress,

$$\sigma_a = \xi_a(\Delta\mu)_0 f(C_b). \tag{8.4}$$

The active stress arises from the force exerted by the motor proteins (MP) attached to the filaments[37]. Here, for simplicity, we consider an isotropic active stress generation [23]. ξ_a is the strength of the activity with $\xi_a > 0$ corresponding to a contractile stress. $(\Delta\mu)_0$ represents the change in chemical potential due to the hydrolysis of adenosine-tri-phosphate (ATP). The local strain rate $\dot{\epsilon} = \partial_x v$. We consider here an off-rate obeying the Hill form $\omega_{\text{off}} = \omega_0\exp(\dot{\epsilon}/\nu)$ where ν is a parameter with the dimension of a frequency. For $\nu > 0$, the off-rate increases with extensile strain $\dot{\epsilon} > 0$.

We recast the governing Eqs. (8.1)-(8.3) in dimensionless form by letting $x/l \to x$, $t/\tau \to t$, $C_b l \to C_b$, $C_u l \to C_u$, $v\tau/l \to v$ and $D_u/D_b \to D$, $\omega_0\tau \to \omega_0$, $\omega_{on}\tau \to \omega_{on}$, $\nu\tau \to \alpha^{-1}$ where l is the hydrodynamic length scale $l = \sqrt{\eta/\gamma}$ and $\tau = l^2/D_b$ is the diffusion time scale of the bound fraction. The dimensionless form of governing equations are

$$\partial_t C_b = -\partial_x(vC_b) + \partial_x^2 C_b - \omega_0 e^{\alpha\partial_x v}\, C_b + \omega_{on} C_u, \tag{8.5}$$

$$\partial_t C_u = -\partial_x(vC_u) + D\partial_x^2 C_u + \omega_0 e^{\alpha\partial_x v}\, C_b - \omega_{on} C_u, \tag{8.6}$$

$$\partial_x^2 v + Pe\partial_x f(C_b) = v, \tag{8.7}$$

where Peclet number $Pe = \xi_a(\Delta\mu)_0/\gamma D_b$ is the ratio of the diffusive time scale $\tau = l^2/D_b$ to advection time scale $\tau_a = \eta/\xi_a(\Delta\mu)_0$.

The active contractile stress arises from the binding of myosin mini-filaments[23, 155–159]. Thus, bound actomyosin concentration controls the contraction. The contraction saturates at large active concentrations[160]. Thus, the isotropic active stress is chosen to have a hyperbolic form $f(C_b) = C_b/(1 + C_b)$.

The dimensionless coupled Eqs. (8.5)-(8.7) can be numerically solved using the IMEX scheme (MCNAB algorithm) with periodic boundary conditions, as outlined in the appendix of the previous chapter [161]. We study the emergent structure and dynamics as a function of Pe and ω_{on}.

8.3 Linear Stability Analysis

The concentration fields C_b and C_u are coupled through advection and viscous strain field dependent turnover. The spatially homogeneous steady-state solutions of the governing equations are $C_{u0} = (\omega_0/\omega_{on})C_{b0}$, $v = 0$. The bound (C_b) and unbound (C_u) actomyosin concentrations are not individually conserved fields because of their inter-conversion, but the total concentration $C_t(x,t) = C_b(x,t) + C_u(x,t)$ is,

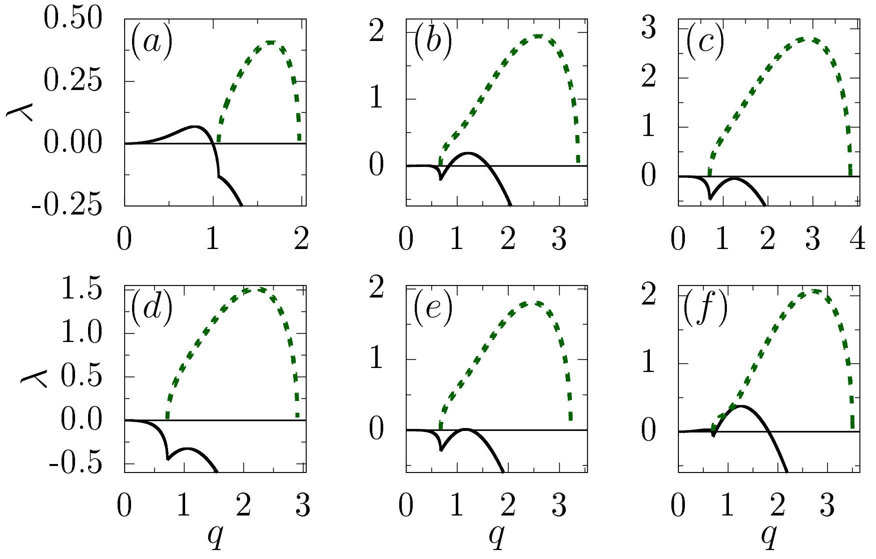

Figure 8.2: (Color online) Plots of the real (solid line) and imaginary (dashed line) parts of the maximum eigen-value of the linear stability matrix as a function of wave number q for the two component active fluid with strain-rate dependent turnover in one dimension. The parameter values are $D = 0.1$, $\omega_0 = 1$, $\alpha = 10$, $C_{t0} = 1$. (a, b, c) $Pe = 2.75$, $\omega_{on} = 0.25(a),\ 1.00(b),\ 1.75(c)$. (d, e, f) $\omega_{on} = 1.0$, $Pe = 2.0(d),\ 2.5(e),\ 3.0(f)$.

obeying $\frac{1}{L}\int_0^L C_t(x,t)\,dx = \text{constant}$.

First, we linearize the force-balance condition for a small perturbation $v \sim \delta v_0 e^{\lambda t} e^{iqx}$ with wave vector q and growth rate λ. The spatial Fourier-amplitude of the velocity field reads

$$\delta v_0 = \frac{iq}{1+q^2} Pe \delta C_{b0} f_{C_b}, \tag{8.8}$$

where $f_{C_b} = \partial_{C_b} f|_{C_b = C_{b0}}$. Furthermore, the linear stability analysis of C_b and C_u evolution equation for small perturbations $C_{b(u)} - C_{b0(u0)} \sim \delta C_{b0(u0)} e^{\lambda t} e^{iqx}$ lead to the linearized form $\lambda(\delta C_{b0}, \delta C_{u0}) = \Omega(\delta C_{b0}, \delta C_{u0})$. The linear stability matrix Ω,

$$\Omega = -q^2 \begin{pmatrix} 1 - \frac{Pe}{1+q^2}\left(1 + \alpha\omega_0\right) C_{b0} f_{C_b} & 0 \\ -\frac{Pe}{1+q^2}\left(C_{u0} - \alpha\omega_0 C_{b0}\right) f_{C_b} & D \end{pmatrix} + \begin{pmatrix} -\omega_0 & \omega_{on} \\ \omega_0 & -\omega_{on} \end{pmatrix}. \tag{8.9}$$

This 2×2 linear stability matrix Ω leads to the following possibilities. The eigen-values of the matrix, $\lambda = (tr \pm \sqrt{tr^2 - 4\,det})/2$, where tr and det denote the trace and determinant of the matrix Ω, respectively. The parameter regime of $tr < 0$

and $det > 0$ denote stable homogeneous state. The eigenvalues have non-zero imaginary part if $det > tr^2/4$. The homogeneous state undergoes pulsating instability at $tr = 0$ with $det > 0$. In the $det > 0$ region, the pulsating state transforms into stationary pattern formation as the linear instability line $tr = 2\sqrt{det}$ is crossed by increasing tr. On the other hand, the whole region of $det < 0$ is linearly unstable for homogeneous state, leading to pattern formation.

In the hydrodynamic limit of $q \to 0$, non zero eigen-value $\lambda = -(\omega_0 + \omega_{on})$ corresponds to a fast relaxation for deviations from the homogeneous state (C_{b0}, C_{u0}). The trace of the linear stability matrix is

$$tr(q) = -q^2 \left(A - \frac{B}{1+q^2} \right) - (\omega_0 + \omega_{on}), \tag{8.10}$$

where, $A = 1 + D$ and $B = Pe(1 + \alpha\omega_0) C_{b0} f_{C_b}$. Thus, homogeneous state undergoes an instability when the real part of the larger eigenvalue is positive, in other words the trace of the linear stability matrix $tr(q) > 0$. To get the growing oscillatory instability that gives the steady-state pulsations, Ω must obey the condition $tr^2 < 4\ det$.

When $tr^2 < 4\ det$, the trace of Ω determines the phase boundary between the homogeneous steady-state and pulsatory patterns. The real part of the eigen-value of Ω becomes $\lambda_{Re} = tr(q)$ and the imaginary part $\lambda_{Im} \equiv \sqrt{-(tr^2 - 4\, det)}$. When $tr^2 \geq 4\ det$, the real part of the eigen-value is $\lambda_{Re} \equiv \lambda_{max} = (tr + \sqrt{tr^2 - 4\, det})/2$ and $\lambda_{Im} = 0$.

The choice $\alpha \neq 0$ keeps the off-rate strain-rate dependent and a growing function of local extension. The element $\Omega_{12} = \omega_{on}$ in the linear stability matrix in Eq. (8.9). The other non-diagonal element of the linear stability matrix in Eq. (8.9) is $\Omega_{21} = \omega_0 + q^2 Pe\, (C_{u0} - \alpha\omega_0 C_{b0})\, f_{C_b}/(1+q^2)$. Thus, Ω_{21} can become negative only when $\alpha > C_{u0}/\omega_0 C_{b0} = 1/\omega_{on}$. The critical condition for switching the sign of the second term of Ω_{21} to negative is $\alpha\omega_{on} > 1$.

In the case of $tr^2 \leq 4\ det$, the growth rate is maximum when $\partial_q tr|_{q=q_{\max}} = 0$, at

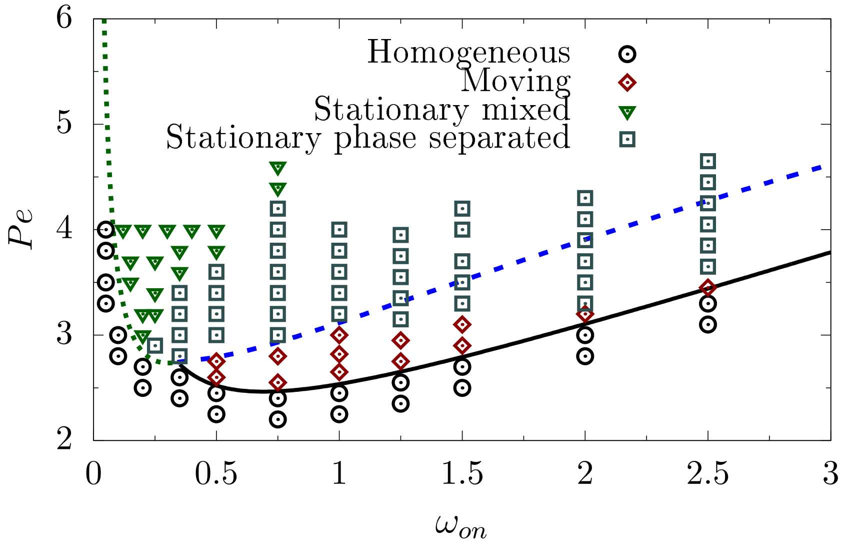

Figure 8.3: (Color online) Phase diagram in ω_{on}-Pe plane for two component active fluids with strain-rate-dependent turnover in one dimension. The lines correspond to phase boundaries calculated from the linear stability matrix(Ω) represents in Eq. (8.9). The solid black line is the plot of the $tr = 0$. The dashed blue line corresponds to $tr^2 - 4\ det = 0$ with the condition $tr > 0$ and the dashed green line corresponds to $det = 0$ with the condition $tr < 0$. The points denote numerical results: homogenous steady-state (○), moving phase-separated pattern(◇), stationary mixed pattern(▽), and stationary phase-separated pattern(□). The moving pattern is shown in Fig. (8.4). The stationary mixed and phase-separated patterns are shown in Fig. (8.6). The parameter values used in this plot are $L = 2\pi$, $D = 0.1$, $\omega_0 = 1$, $\alpha = 10$, $C_{t0} = 1$.

the wave number $q_{\max} = (\sqrt{B/A} - 1)^{1/2}$. The real part of the eigen-value goes to zero at $tr(q_c) = 0$. The threshold q value of the positive growth rate is $q_{\max} = q_c$ with $q_c = [(\omega_0 + \omega_{on})/(1 + D)]^{1/4}$.

Using the value of q_c in Eq. (8.10), setting $tr(q_c) = 0$, enables us to write the parametric dispersion relation in a mode independent way,

$$Pe_c = \frac{1 + q_c^2}{(1 + \alpha\omega_0)C_{b0} f_{C_b}} \left[1 + D + \frac{\omega_0 + \omega_{on}}{q_c^2} \right]. \tag{8.11}$$

Thus, the condition for emergence of unstable spiral is $Pe \geq Pe_c$ where Pe_c in Eq. (8.11) is the critical Peclet number. The frequency of oscillation in the unstable spiral regime is,

$$f = \sqrt{-(tr(q_c)^2 - 4\ det(q_c))}, \tag{8.12}$$

and the time period of such oscillations is $T = 2\pi/f$.

In a periodic system of size L, the relevant wave numbers are $q_m = 2m\pi/L$ with $m = 0, \pm 1, \pm 2, \dots$. We find that the mode q_1 becomes unstable first as Pe and ω_{on} increases. In Fig. (8.2), we plot the real part and imaginary part of the maxium eigen value with $D = 0.1$, $\omega_0 = 1$, $\alpha = 10$, $C_{t0} = 1$. Fig. (8.2)(a)–(c) shows the variation of eigen values as a function of q with different ω_{on} for constant Pe. Fig. (8.2)(d)–(f) shows the variation for constant ω_{on}. In the case of system size $L = 2\pi$, $q_1 = 2\pi/L = 1$. In Fig. (8.2)(a, b, c) λ_{Im} is presented in the range $q \geq 1$. In Fig. (8.2)(a), λ_{Re} remains close to zero at $q = 1$ for $Pe = 2.75$ and $\omega_{on} = 0.25$. This is the transition point from stable spiral to unstable spiral. In Fig. (8.2)(b), λ_{Re} is positive at $q \geq 1$ for $Pe = 2.75$ and $\omega_{on} = 1$. Thus, linear stability shows the onset of the unstable spiral. In Fig. (8.2)(c), λ_{Re} is zero for $Pe = 2.75$ and $\omega_{on} = 1.75$, identifying the transition point between unstable spiral and stable spiral. It clearly indicates towards a reentrant transition from stable spiral to unstable spiral and back to stable spiral. Fig. (8.2)(d, e, f) suggests the transition from stable spiral to unstable spiral with increasing Pe. Further increase of Pe leads to the transition from unstable spiral to linearly unstable state that leads to pattern formation due to non-linearities in the system (the blue dashed line in Fig. 8.3).

8.4 Phase diagram

We numerically solve the governing dimensionless Eqs. (8.5)-(8.7) in one dimensional periodic domain of size $L = 2\pi$ with $D = 0.1$, $\omega_0 = 1$. See Appendix-8.6.1 for a discussion on parameter values. Here, we study the dynamical phases in the long-time limit giving results independent of the initial conditions. In Fig. (8.3), we present a phase diagram in ω_{on}-Pe plane. The lines in Fig. (8.3) represents the phase boundaries obtained from linear stability matrix in Eq. (8.9). The solid black line corresponds to $tr = 0$ representing the phase boundary between the stable spiral and unstable spiral phases. The dashed green line corresponds to $det = 0$ with the condition $tr < 0$ representing the phase boundary between the linearly stable

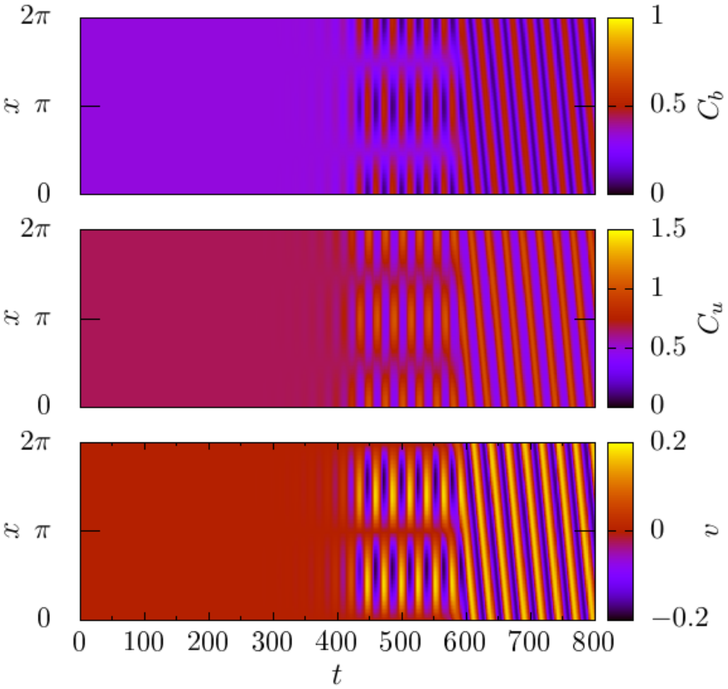

Figure 8.4: (Color online) Moving pattern. Kymogrsph shows the time evolution of C_a, C_p and v for two component active fluids with strain-rate-dependent turnover in one dimension. The parameter values are $L = 2\pi$, $D = 0.1$, $\omega_0 = 1$, $\omega_{on} = 0.5$, $Pe = 2.6$, $C_{t0} = 1$.

and linearly unstable phases. The dashed blue line corresponds to $tr^2 - 4\ det = 0$ with the condition $tr > 0$ representing the phase boundary between the unstable spiral and linearly unstable phases.

The linear stability analysis predicts the existence of the unstable spiral. In this regime, we observe pulsatory patterns from direct numerical integration of the non-linear equations. The non-linearities stabilizes the growth of modes corresponding to the unstable spiral phase, generating steady-state pulsatory patterns. In the linearly unstable regime of the stability analysis, numerical results show stationary pattern formation, as the growth of the unstable modes are stabilized by non-linearities.

The non-linear effect dominates more in the regime of high on-rate, leading to a significant difference between the predictions of the phase boundary of the unstable spiral and linearly stable phase and numerically obtained phase boundary separating the moving or pulsatory and pattern forming phases. For constant Pe, we observe re-entrant transition between the homogeneous state, to pattern formation, and back to homogenous state with increasing ω_{on}, at a fixed Pe, e.g., at $Pe = 3$ in Fig. (8.3). In particular, the phase diagram shows three different kinds of re-entrant transitions with increasing ω_{on}: (*i*) For $Pe \approx 2.75$, re-entrance from homogeneous state to moving pattern to homogenous state. (*ii*) For $Pe \approx 3$, re-entrance from homogenous state to stationary pattern to moving pattern to homogeneous state transition. (*iii*) For $Pe > 3$ re-entrance from homogeneos state to stationary co-localized pattern to stationary pattern with shifted maxima of $C_b(x)$ and $C_u(x)$ to homogenous state.

In the following we discuss the instabilities of pulsation, moving patterns and stationary pattern.

Pulsation and moving patterns: We show the onset of pulsation and moving patterns using the time evolutions of the bound concentration $C_b(x,t)$, unbound concentration $C_u(x,t)$, and fluid velocity field $v(x,t)$ in Fig. (8.4), starting from a homogeneous initial condition. We observe phase-separated pulsatory patterns for $400 \lesssim t \lesssim 600$. Near $t \approx 600$, this pulsatory pattern starts to show emergence of a steady non-uniform shape moving with a constant flow velocity. In the absence of any external field breaking the right-left symmetry, this spontaneous flow is equally likely to go in either direction. The chosen direction, in the absence of stochastic forces, depends on the initial perturbation but the flow speed itself is robust and depends only on the control parameters like Pe and ω_{on}.

To investigate quantitatively the pattern forming phases, we calculate the spatial average of bound concentration, unbound concentration, and velocity as a function of time. For this purpose we use the spatial average of a function $f(x,t)$ defined as $S_f(t) = \frac{1}{L}\int_0^L dx \;\; f(x,t)$. We numerically investigate the spatial averages of $C_b(x,t)$, $C_u(x,t)$ and $v(x,t)$. Fig. (8.5)(a) shows the oscillations in average bound (S_b) and unbound (S_u) concentrations in the pulsatory regime $400 \lesssim t \lesssim 600$. The average velocity S_v in the pulsatory regime is zero. We observe emergence of a non-zero constant mean velocity S_v at $t > 600$ in Fig. (8.5)(a). In this steady-state regime the oscillations in average bound and unbound concentrations disappear.

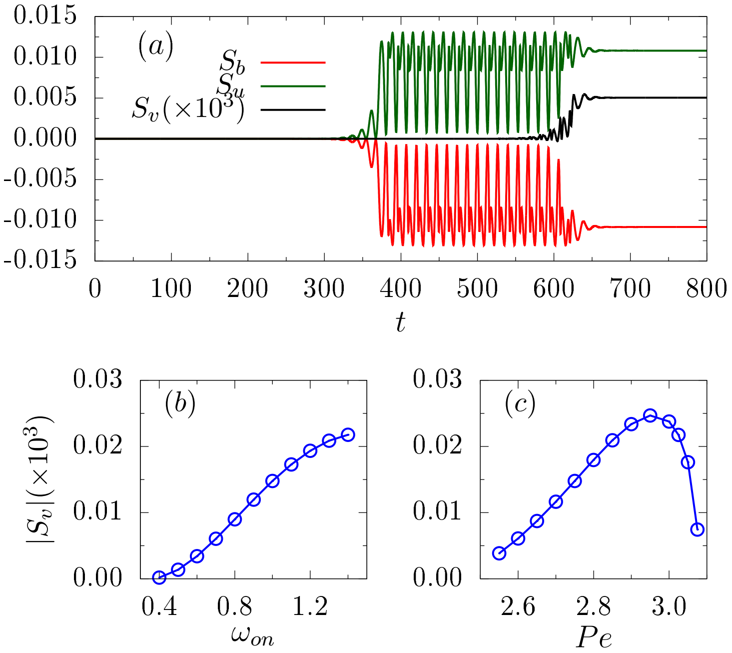

Figure 8.5: (Color online) (a) Time evolution of S_b, S_u and S_v for two component active fluids with strain-rate-dependent turnover in one dimension. Here $S_b \equiv S_b - C_{b0}$ and $S_u \equiv S_u - C_{u0}$ where $C_{b0} = \omega_{on} C_{t0}/(\omega_0 + \omega_{on})$ and $C_{u0} = C_{t0} - C_{b0}$. The parameter values are $D = 0.1$, $\omega_0 = 1$, $\omega_{on} = 0.5$, $Pe = 2.6$, $q = 1$, $C_{t0} = 1$. (b) Average flow velocity($|S_v|$) as a function of ω_{on} for Pe =2.75. (c) Average flow velocity($|S_v|$) as a function of Pe for $\omega_{on} = 1$. (b, c) The parameter values are $L = 2\pi$, $D = 0.1$, $\omega_0 = 1$, $C_{t0} = 1$.

The fields C_b and C_u maintain their shape and propagates with a constant velocity as in a solitary wave packet. We call this phase as moving pattern. In Fig. (4)(c), the dimensionless propagation velocity is $v_{max} \sim 0.2$, which, when translated into dimensional form, gives $v_{max} \sim 0.12\ \mu\text{m s}^{-1}$, a number which belongs to the same approximate range of actomyosin flow velocities observed in different contexts, e.g., in Drosophila germband extension [150].

Average flow velocity: In the absence of any explicit symmetry breaking, both the directions of the spontaneous flow is equally likely. Thus we use the modulus of the spontaneous flow velocity $|S_v|$ as a measure of the flow and plot it in Fig. (8.5)(b, c).

They show the flow velocity as a function of (b) ω_{on} and (c) Pe. It increases with ω_{on} and shows a tendency of saturation. With Pe, the flow velocity reaches a well-defined maximum near $Pe = 3$. Thus it is clear that reaching a maximum velocity requires a subtle balance between the active contractility and turnover which the

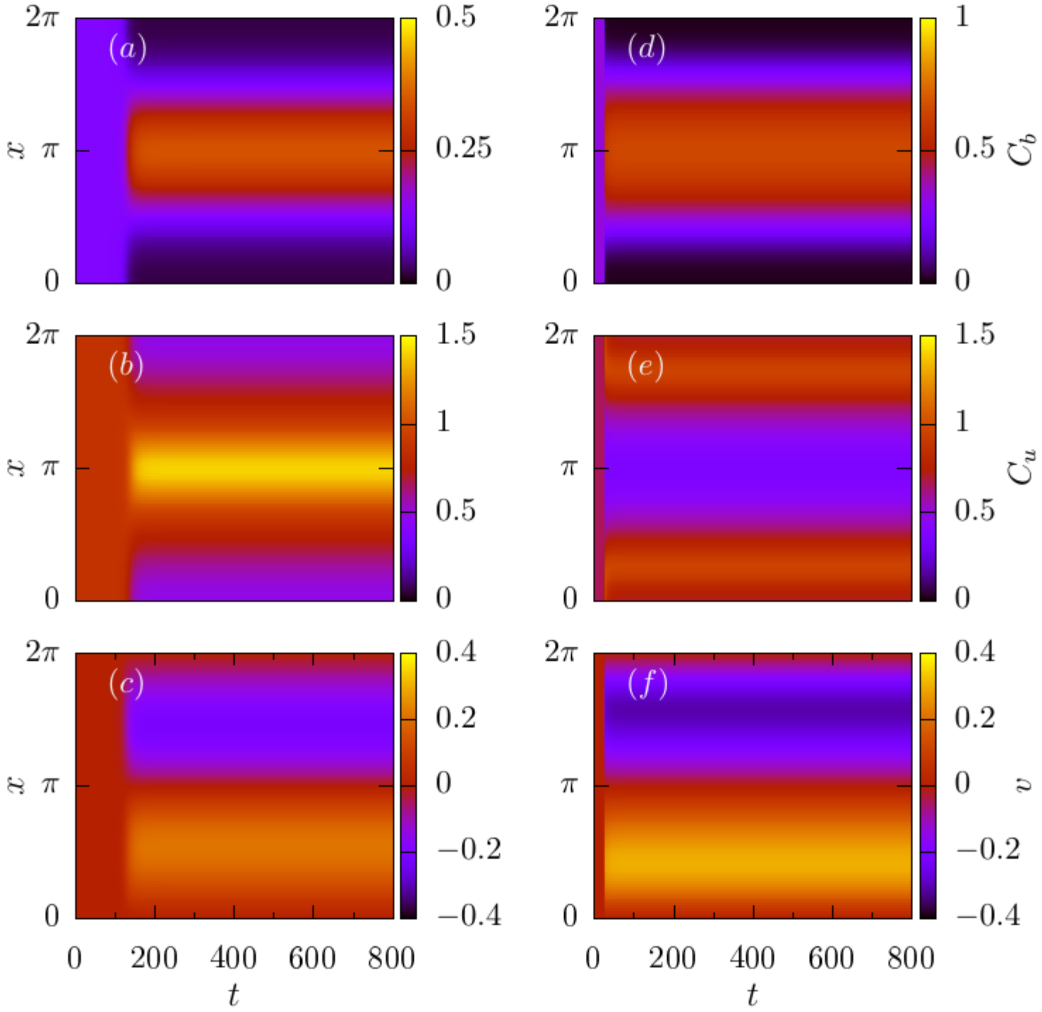

Figure 8.6: (Color online) Kymogrsph shows the time evolution of C_a, C_p and v for two component active fluids with strain-rate-dependent turnover in one dimension with $L = 2\pi$, $D = 0.1$, $\omega_0 = 1$, $C_{t0} = 1$. (a, b, c) Stationary (mixed) pattern. The parameter values are $\omega_{on} = 0.15$, $Pe = 3.5$. (d, e, f) Stationary phase-separated pattern. The parameter values are $\omega_{on} = 0.5$, $Pe = 3$.

living cell may use as control parameters.

Stationary pattern: This model shows two kinds of stationary patterns, the details of which are illustrated in Fig. (8.6) using $L = 2\pi$, $D = 0.1$, $\omega_0 = 1$, $C_{t0} = 1$: (i) Fig. (8.6)(a, b, c) show stationary mixed patterns at $\omega_{on} = 0.15$ and $Pe = 3.5$. Fig. (8.6)(a) and Fig. (8.6)(b) display kymographs of bound and unbound concentrations respectively. On the other hand, Fig. (8.6)(c) shows the kymograph of the fluid velocity. It is clearly seen that the peaks of the bound and

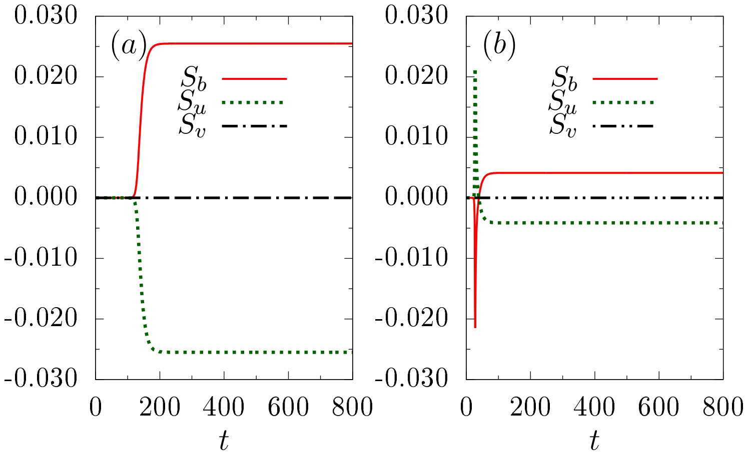

Figure 8.7: (Color online) Time evolution of S_b, S_u and S_v for two component active fluids with strain-rate-dependent turnover in one dimension with $L = 2\pi$, $D = 0.1$, $\omega_0 = 1$, $C_{t0} = 1$. Here $S_b \equiv S_b - C_{b0}$ and $S_u \equiv S_u - C_{u0}$ where $C_{b0} = \omega_{on} C_{t0}/(\omega_0 + \omega_{on})$ and $C_{u0} = C_{t0} - C_{b0}$. The parameter values corresponds to (a) stationary (mixed) pattern with $\omega_{on} = 0.15$ and $Pe = 3.5$ and (b) stationary phase-separated pattern with $\omega_{on} = 0.5$ and $Pe = 3$.

unobound concentrations appear at the same spatial location. Thus, we call this kind of pattern as mixed stationary pattern. (ii) Fig. (8.6)(d, e, f) show stationary phase-separated patterns at $\omega_{on} = 0.5$ and $Pe = 3$. Fig. (8.6)(a) and Fig. (8.6)(b) display kymographs of bound and unbound concentrations, respectively. Further, Fig. (8.6)(c) shows the kymograph of fluid velocity. Here, the peaks of the bound and unbound concentrations appear at different spatial locations suggesting a phase-separation between them. We denote this kind of patterns as stationary phase-separated pattern. Thus with changing parameter the possibility of a steady state phase separation is observed.

We find stationary mixed patterns for low on-rates ω_{on} and stationary phase-separated patterns for relatively high on-rates ω_{on}, at a constant Pe, as shown in Fig. (8.3). In the case of a low on-rate, the average bound concentration is much smaller as $C_{b0} = C_{t0}\ \omega_{on}/(\omega_{on} + \omega_0)$. The low diffusivity of C_b with respect to C_u maintains the phase separation at large ω_{on} rate, while at small ω_{on} rates they get enough opportunity to mix. The phase diagram shows stationary mixed patterns for low contractility Pe and stationary phase-separated patterns for higher contractility for a constant ω_{on}, as is shown in Fig. (8.3).

In Fig. (8.7) we plot the average bound and unbound concentrations, and the flow velocity as a function of time corresponding to Fig. (8.6). The average flow velocity remains zero throughout the time evolution associated with the stationary behavior of the patterns.

8.5 Conclusions

We have studied the two-component active fluids with strain-rate-dependent turnover. We numerically investigated the dynamics and observed three pattern forming regimes along with the homogenous state in ω_{on}-Pe plane. The pattern forming phases show stationary phase-separated and stationary mixed patterns, and moving non-uniform pattern. The onset of the moving pattern phase starting from an homogenous initial state first shows formation of localized pulsatory patterns in the intermediate time regime. This subsequently transforms to the moving pattern in long times. The peaks of the bound and unbound concentrations appear at different positions locations indicating phase-separation as the pattern moves. The stationary patterns appear in two forms, stationary pattern where the bound and unbound fractions remain mixed with their peaks appearing at the same location. In the phase-separated pattern, the peaks of bound and unbound concentrations remain spatially separated. While our predictions are amenable to direct experimental verifications using cytoskeletal extracts, they may have implications for pattern formation in cells and growing tissues.

8.6 Appendix

8.6.1 Physical parameters

Active contratile stress strength $\xi_a(\Delta\mu)_0/\gamma \sim 25.4 \pm 9.2\ \mu\text{m}^2\ \text{s}^{-1}$ [166] for *C. elegans* where $\xi_a(\Delta\mu)_0$ denotes isotropic active stress generated through ATP consumption of myosin, positive for contraction and dependent on the change in chemical potential associated with ATP hydrolysis $(\Delta\mu)_0$. And γ is a friction coefficient that describes frictional interactions between the cortex and its surrounding cytosol and membrane. The flow velocity of actomyosin $v \sim 0.08$ μm s^{-1} [150]. We use the hydrodynamic length scale corresponding to the *C. elegans* cortex $l \approx 14\,\mu$m [166]. The timescale value is $\tau = 24$ s [166].

Table 8.1: We list the physical parameter values used in our analysis.

Definition	Parameters	Values
Viscosity of actomyosin cortex	η	$\sim 10^4$ pN s μm^{-2}[167]
Frictional coefficient	$\gamma(= \eta/l^2)$	~ 51 pN s μm^{-4}
Bound diffusion constant	$D_b(= l^2/\tau)$	~ 8 μm^2 s^{-1}
Unbound diffusion constant	D_u	0.9 ± 0.2 μm^2 s^{-1} [168]
On rate	ω_{on}	~ 0.2 s^{-1}
Bare off rate	ω_0	$\sim 0.2 \pm 0.08$ s^{-1}[78]
Isotropic active contraction	$\xi_a(\Delta\mu)_0/\gamma$	$\sim 25.4 \pm 9.2$ μm^2 s^{-1}[166] $\sim 0 - 100$ μm^2 s^{-1}[169]

Table 8.2: We estimate various scaled parameter values and ranges using Table-8.1. We list all the scaled parameters here.

Definition	Scaled parameters	Scaled values
Diffusivity ratio	$D(= D_u/D_b)$	~ 0.1
On rate	$\omega_{on}(= \omega_{on}\tau)$	~ 4.8
Bare off rate	$\omega_0(= \omega_0\tau)$	~ 4.8
Turnover timescale	$\alpha(= \alpha/\tau)$	$1, 3$ [77]
Active contraction	$Pe(= \xi_a(\Delta\mu)_0/\gamma D_b)$	$\sim 1.97 - 4.27$, $0 - 15$

9

Discussions

In the first part of this thesis, we have presented three models of the active Brownian particle (ABP). We started our exploration using ABPs that are considered to self-propel with a constant speed in a heading direction, which undergoes stochastic reorientation. We showed a mapping of the path probabilities of the trajectories to a semiflexible polymer model. Using a Laplace transform of the governing Fokker-Planck equation of the active Brownian particle, we described a direct method to derive exact expressions for all the moments of the relevant dynamical variables in arbitrary dimensions.

We then considered the stochasticity in active speed as well. We first used a model of speed generation via an active Ornstein-Uhlenbeck process [15]. We extended the technique of Laplace transforming Fokker-Planck equations to calculate all the time-dependent moments of dynamical variables in arbitrary dimensions. We considered a second model incorporating speed fluctuations in terms of an additive Gaussian noise due to a chemical process generating the active speed [16]. We again calculated all the time-dependent dynamical moments in arbitrary dimensions using the governing Fokker-Planck equations. These studies showed several ballistic-diffusive crossovers and non-trivial changes in displacement distributions.

In the second part of the thesis, we studied polymers driven by a molecular motor assay. *First*, we presented the dynamics of a rigid filament under motor-protein drive. We modeled motor proteins as active extensible harmonic linkers with load-dependent rates of extension and detachment from the polymer. Under constant external loading, the system shows a transition from a stable configuration to instability towards detachment of the filament from the motor proteins. Under external elastic loading, we found emergence of limit cycle oscillations via a supercritical Hopf bifurcation with a change of activity and the number of motor proteins. Numerical simulations for large number of motor proteins showed good agreement with mean-field predictions.

The cytoskeletal filaments are semiflexible polymers. Thus we presented a study of semiflexible polymers driven by a motor proteins assay. The conformations of the filament undergo a first-order phase transition from open-chain to spiral. It showed a reentrant transition in both the active extension and the turnover, defined as the ratio of attachment-detachment rates. The size and shape of the polymer changed non-monotonically as the phase transition proceeded. The relevant autocorrelation functions displayed a double-exponential decay, and the correlation times show a maximum at intermediate activity.

In the third part of the thesis, we presented studies of active pattern formation and dynamics in this system using a coarse-grained hydrodynamic formulation. We have studied a two-component active fluid undergoing advection-diffusion and turnover in the presence of stress-dependent flow. We first considered the simplest case of constant turnover between the active and passive fractions. Depending on the Péclet number and on-off rates, the system remained either in a homogeneous steady state or exhibited stationary pattern formation. The maximum densities of the two components appear at the same spatial locations. The incorporation of extensile pressure due to the passive component led to pulsatory pattern formation. In modeling the stress and strain-rate dependent turnover, we assumed that the off-rate describing the transition from active cross-linked to passive unbound state increases (decreases) with the local extension (compaction). The phase behavior for stress-dependent off-rate remains qualitatively the same as in the case of constant turnover. However, in the case of strain-rate dependent turnover, we observed qualitatively new features. Depending on the bare on-rate and Péclet number, the system showed transitions from a homogeneous steady-state to spatial pattern formations in the presence or absence of a steady-state flow. The steady-state patterns showed two different possibilities – (i) the maxima of active and passive densities co-appear in space; (ii) they segregate spatially.

One-line summary: We have presented an extensive study of active matter: from active particles to semiflexible filaments driven by molecular motors to a two-component active fluid model of the cytoskeletal complex.

REFERENCES

[1] F. Schweitzer, *Browning Agents and Active Particles*, *Springer Series in Synergetics* (Springer Berlin Heidelberg, Berlin, Heidelberg, 2007).

[2] M. C. Marchetti, J. F. Joanny, S. Ramaswamy, T. B. Liverpool, J. Prost, M. Rao, and R. A. Simha, Reviews of Modern Physics **85**, 1143 (2013).

[3] C. Bechinger, R. Di Leonardo, H. Löwen, C. Reichhardt, G. Volpe, and G. Volpe, Reviews of Modern Physics **88**, 045006 (2016).

[4] T. Vicsek and A. Zafeiris, Physics Reports **517**, 71 (2012).

[5] F. Jülicher, A. Ajdari, and J. Prost, Reviews of Modern Physics **69**, 1269 (1997).

[6] T. D. Frank, Physical Review E **72**, 011112 (2005).

[7] F. Jülicher, K. Kruse, J. Prost, and J. F. Joanny, Physics Reports **449**, 3 (2007).

[8] S. Das, G. Gompper, and R. G. Winkler, New Journal of Physics **20**, 015001 (2018).

[9] F. J. Sevilla and L. A. Gómez Nava, Physical Review E **90**, 22130 (2014).

[10] F. J. Sevilla and M. Sandoval, Physical Review E **91**, 052150 (2015).

[11] F. J. Sevilla, Physical Review E **94**, 062120 (2016).

[12] C. Kurzthaler and T. Franosch, Soft Matter **14**, 2682 (2018).

[13] U. Basu, S. N. Majumdar, A. Rosso, and G. Schehr, Physical Review E **100**, 062116 (2019).

[14] A. Dhar, A. Kundu, S. N. Majumdar, S. Sabhapandit, and G. Schehr, Physical Review E **99**, 032132 (2019).

[15] M. Schienbein and H. Gruler, Bulletin of Mathematical Biology **55**, 585 (1993).

[16] P. Pietzonka and U. Seifert, Journal of Physics A: Mathematical and Theoretical **51**, 01LT01 (2018).

[17] S. J. Kron and J. A. Spudich, Proceedings of the National Academy of Sciences of the United States of America **83**, 6272 (1986).

[18] J. Howard, A. J. Hudspeth, and R. D. Vale, Nature **342**, 154 (1989).

[19] L. Bourdieu, T. Duke, M. B. Elowitz, D. A. Winkelmann, S. Leibler, and A. Libchaber, Physical Review Letters **75**, 176 (1995).

[20] V. Schaller, C. Weber, C. Semmrich, E. Frey, and A. R. Bausch, Nature **467**, 73 (2010).

[21] Y. Sumino, K. H. Nagai, Y. Shitaka, D. Tanaka, K. Yoshikawa, H. Chaté, and K. Oiwa, Nature **483**, 448 (2012).

[22] J. Howard, Physics Today **55**, 63 (2002).

[23] J. S. Bois, F. Jülicher, and S. W. Grill, Physical Review Letters **106**, 028103 (2011).

[24] F. Jülicher, S. W. Grill, and G. Salbreux, Reports on Progress in Physics **81**, 076601 (2018).

[25] R. J. Archer, A. J. Parnell, A. I. Campbell, J. R. Howse, and S. J. Ebbens, Advanced Science **5**, 1700528 (2018).

[26] L. Farhadi, C. Fermino Do Rosario, E. P. Debold, A. Baskaran, and J. L. Ross, Frontiers in Physics **6**, 75 (2018).

[27] P. Agarwal and R. Zaidel-Bar, Trends in Cell Biology **29**, 150 (2019).

[28] S. Ramaswamy, Annual Review of Condensed Matter Physics **1**, 323 (2010).

[29] T. Vicsek and A. Zafeiris, Collective motion, 2012.

[30] P. Romanczuk, M. Bär, W. Ebeling, B. Lindner, and L. Schimansky-Geier, European Physical Journal: Special Topics **202**, 1 (2012).

[31] R. J. Löffler, M. M. Hanczyc, and J. Gorecki, Physical Chemistry Chemical Physics **21**, 24852 (2019).

[32] Y. Koyano, N. J. Suematsu, and H. Kitahata, Physical Review E **99**, 1 (2019).

[33] R. D. Astumian and P. Hänggi, Physics Today **55**, 33 (2002).

[34] P. Reimann, Physics Report **361**, 57 (2002).

[35] J. Howard, Physics Today **55**, 63 (2002).

[36] N. J. Carter and R. A. Cross, Nature **435**, 308 (2005).

[37] K. Kruse, J. F. Joanny, F. Jülicher, J. Prost, and K. Sekimoto, European Physical Journal E **16**, 5 (2005).

[38] C. P. Brangwynne, G. H. Koenderink, F. C. MacKintosh, and D. A. Weitz, Physical Review Letters **100**, 118104 (2008).

[39] D. A. Fletcher and R. D. Mullins, Nature **463**, 485 (2010).

[40] S. X. Sun, S. Walcott, and C. W. Wolgemuth, Current Biology **20**, R649 (2010).

[41] M. Braun, Z. Lansky, F. Hilitski, Z. Dogic, and S. Diez, BioEssays **38**, 474 (2016).

[42] D. Selmeczi, S. Mosler, P. H. Hagedorn, N. B. Larsen, and H. Flyvbjerg, Biophysical Journal **89**, 912 (2005).

[43] D. Selmeczi, L. Li, L. I. Pedersen, S. F. Nrrelykke, P. H. Hagedorn, S. Mosler, N. B. Larsen, E. C. Cox, and H. Flyvbjerg, European Physical Journal: Special Topics **157**, 1 (2008).

[44] H. U. Bödeker, C. Beta, T. D. Frank, and E. Bodenschatz, EPL (Europhysics Letters) **90**, 28005 (2010).

[45] W.-C. Guo, B.-Q. Ai, and L. He, (2020).

[46] H. S. Niwa, Journal of Theoretical Biology **171**, 123 (1994).

[47] B. Alberts, D. Bray, K. Hopkin, A. Johnson, J. Lewis, M. Raff, K. Roberts, and P. Walter, *Essential Cell Biology*, Fourth Edition (Garland Science, Taylor and Francis Group) .

[48] B. Alberts, D. Bray, K. Hopkins, A. Johnson, J. Lewis, M. Raff, K. Roberts, and P. Walter, *Garland Science* (Garland Science, USA, 2014), p. 728.

[49] K. A. Jansen, D. M. Donato, H. E. Balcioglu, T. Schmidt, E. H. Danen, and G. H. Koenderink, Biochimica et Biophysica Acta - Molecular Cell Research **1853**, 3043 (2015).

[50] G. H. Koenderink, Z. Dogic, F. Nakamura, P. M. Bendix, F. C. MacKintosh, J. H. Hartwig, T. P. Stossel, and D. A. Weitz, Proceedings of the National Academy of Sciences of the United States of America **106**, 15192 (2009).

[51] M. L. Gardel, J. H. Shin, F. C. MacKintosh, L. Mahadevan, P. Matsudaira, and D. A. Weitz, Science **304**, 1301 (2004).

[52] R. D. Vale, Cell **112**, 467 (2003).

[53] D. Chowdhury, Biophysical Journal **104**, 2331 (2013).

[54] D. Needleman and Z. Dogic, Nature Reviews Materials **2**, 17048 (2017).

[55] F. Jülicher, S. W. Grill, and G. Salbreux, Reports on Progress in Physics **81**, 076601 (2018).

[56] S. Ghosh, V. N. Pradeep, S. Muhuri, I. Pagonabarraga, and D. Chaudhuri, Soft Matter **13**, 7129 (2017).

[57] P. Y. Plaçais, M. Balland, T. Guérin, J. F. Joanny, and P. Martin, Physical Review Letters **103**, 1 (2009).

[58] F. Jülicher, A. Ajdari, and J. Prost, Reviews of Modern Physics **69**, 1269 (1997).

[59] F. Jülicher and J. Prost, Physical Review Letters **78**, 4510 (1997).

[60] C. Leduc, N. Pavin, F. Jülicher, and S. Diez, Physical Review Letters **105**, 128103 (2010).

[61] L. A. Amos and W. B. Amos, Journal of Cell Science **98**, 95 (1991).

[62] F. Ziebert, H. Mohrbach, and I. M. Kulić, Physical Review Letters **114**, 148101 (2015).

[63] K. Sekimoto, N. Mori, K. Tawada, and Y. Y. Toyoshima, Physical Review Letters **75**, 172 (1995).

[64] K. Kruse and F. Jülicher, Current Opinion in Cell Biology **17**, 20 (2005).

[65] C. Beta and K. Kruse, Annual Review of Condensed Matter Physics **8**, 239 (2017).

[66] S. Günther and K. Kruse, New Journal of Physics **9**, 417 (2007).

[67] S. W. Grill, K. Kruse, and F. Jülicher, Physical Review Letters **94**, 108104 (2005).

[68] O. Campàs and P. Sens, Physical Review Letters **97**, 1 (2006).

[69] Y. Chikashige, D. Q. Ding, H. Funabiki, T. Haraguchi, S. Mashiko, M. Yanagida, and Y. Hiraoka, Science **264**, 270 (1994).

[70] P. Gross, K. V. Kumar, and S. W. Grill, Annual Review of Biophysics **46**, 337 (2017).

[71] T. Lecuit, P. F. Lenne, and E. Munro, Annual Review of Cell and Developmental Biology **27**, 157 (2011).

[72] N. Masatoshi, S. R. Naganathan, F. Jülicher, and S. W. Grill, eLife **6**, (2017).

[73] A. M. Turing, Bulletin of Mathematical Biology **52**, 153 (1990).

[74] K. V. Kumar, J. S. Bois, F. Jülicher, and S. W. Grill, Physical Review Letters **112**, 208101 (2014).

[75] K. Dierkes, A. Sumi, J. Solon, and G. Salbreux, Physical Review Letters **113**, 148102 (2014).

[76] S. Banerjee, K. J. Utuje, and M. C. Marchetti, Physical Review Letters **114**, 228101 (2015).

[77] D. S. Banerjee, A. Munjal, T. Lecuit, and M. Rao, Nature Communications **8**, 1 (2017).

[78] A. Munjal, J. M. Philippe, E. Munro, and T. Lecuit, Nature **524**, 351 (2015).

[79] J. R. Howse, R. A. Jones, A. J. Ryan, T. Gough, R. Vafabakhsh, and R. Golestanian, Physical Review Letters **99**, 048102 (2007).

[80] J. Palacci, C. Cottin-Bizonne, C. Ybert, and L. Bocquet, Physical Review Letters **105**, 088304 (2010).

[81] M. E. Cates and J. Tailleur, Epl **101**, 20010 (2013).

[82] É. Fodor, C. Nardini, M. E. Cates, J. Tailleur, P. Visco, and F. Van Wijland, Physical Review Letters **117**, 038103 (2016).

[83] C. Kurzthaler, S. Leitmann, and T. Franosch, Scientific Reports **6**, 36702 (2016).

[84] C. G. Wagner, M. F. Hagan, and A. Baskaran, Journal of Statistical Mechanics: Theory and Experiment **2017**, 43203 (2017).

[85] A. Pototsky and H. Stark, Epl **98**, 50004 (2012).

[86] A. Duzgun and J. V. Selinger, Physical Review E **97**, 32606 (2018).

[87] U. Basu, S. N. Majumdar, A. Rosso, and G. Schehr, Physical Review E **98**, 1 (2018).

[88] K. Malakar, V. Jemseena, A. Kundu, K. Vijay Kumar, S. Sabhapandit, S. N. Majumdar, S. Redner, and A. Dhar, Journal of Statistical Mechanics: Theory and Experiment **2018**, 043215 (2018).

[89] T. Demaerel and C. Maes, Physical Review E **97**, 32604 (2018).

[90] K. Malakar, A. Das, A. Kundu, K. V. Kumar, and A. Dhar, Physical Review E **101**, 022610 (2020).

[91] J. J. Hermans and R. Ullman, Physica **18**, 951 (1952).

[92] H. E. Daniels, Proceedings of the Royal Society of Edinburgh. Section A. Mathematical and Physical Sciences **63**, 290 (1959).

[93] A. Dhar and D. Chaudhuri, Physical Review Letters **89**, 065502/1 (2002).

[94] D. Chaudhuri, Physical Review E **75**, 021803 (2007).

[95] P. Castro-Villarreal and J. E. Ramírez, Physical Review E **100**, 012503 (2019).

[96] M. Doi and S. F. Edwards, *The Theory of Polymer Dynamics*, (Clarendon Press, Oxford, 1986) .

[97] M. van den Berg and J. T. Lewis, Bulletin of the London Mathematical Society **17**, 144 (1985).

[98] N. Ikeda, S. Watanabe, M. Fukushima, and H. Kunita, Ito's Stochastic Calculus and Probability Theory (1996).

[99] H. C. Berg and D. A. Brown, Nature **239**, 500 (1972).

[100] C. A. Condat, J. Jäckle, and S. A. Menchón, Physical Review E **72**, (2005).

[101] M. Schienbein, K. Franke, and H. Gruler, Physical Review E **49**, 5462 (1994).

[102] R. J. Petrie, A. D. Doyle, and K. M. Yamada, Nature Reviews Molecular Cell Biology **10**, 538 (2009).

[103] M. Zhao, Seminars in Cell and Developmental Biology **20**, 674 (2009).

[104] G. S. Redner, M. F. Hagan, and A. Baskaran, Physical Review Letters **110**, 055701 (2013).

[105] Y. Fily, A. Baskaran, and M. F. Hagan, Soft Matter **10**, 5609 (2014).

[106] N. Gupta, A. Chaudhuri, and D. Chaudhuri, Physical Review E **99**, 042405 (2019).

[107] A. Shee, A. Dhar, and D. Chaudhuri, Soft Matter **16**, 4776 (2020).

[108] F. Peruani and L. G. Morelli, Physical Review Letters **99**, 010602 (2007).

[109] D. Chaudhuri and A. Dhar, Journal of Statistical Mechanics: Theory and Experiment **013207**, 013207 (2021).

[110] J. Schnauß, T. Golde, C. Schuldt, B. U. Schmidt, M. Glaser, D. Strehle, T. Händler, C. Heussinger, and J. A. Käs, Physical Review Letters **116**, 108102 (2016).

[111] S. Walcott and S. X. Sun, Physical Review E **82**, 050901 (2010).

[112] Z. Lansky, M. Braun, A. Lüdecke, M. Schlierf, P. R. Ten Wolde, M. E. Janson, and S. Diez, Cell **160**, 1159 (2015).

[113] M. P. Sheetz and J. A. Spudich, Cell Motility **3**, 485 (1983).

[114] M. J. Schnitzer, K. Visscher, and S. M. Block, Nature Cell Biology **2**, 718 (2000).

[115] D. Mizuno, C. Tardin, C. F. Schmidt, and F. C. MacKintosh, Science **315**, 370 (2007).

[116] N. J. Carter and R. A. Cross, Nature **435**, 308 (2005).

[117] A. Chaudhuri and D. Chaudhuri, Soft Matter **12**, 2157 (2016).

[118] S. M. Block, C. L. Asbury, J. W. Shaevitz, and M. J. Lang, Proceedings of the National Academy of Sciences of the United States of America **100**, 2351 (2003).

[119] L. Scharrel, R. Ma, R. Schneider, F. Jülicher, and S. Diez, Biophysical Journal **107**, 365 (2014).

[120] C. Leduc, O. Campàs, K. B. Zeldovich, A. Roux, P. Jolimaitre, L. Bourel-Bonnet, B. Goud, J. F. Joanny, P. Bassereau, and J. Prost, Proceedings of the National Academy of Sciences of the United States of America **101**, 17096 (2004).

[121] M. Dogterom, J. W. Kerssemakers, G. Romet-Lemonne, and M. E. Janson, Current Opinion in Cell Biology **17**, 67 (2005).

[122] K. Kawaguchi and S. Ishiwata, Science **291**, 667 (2001).

[123] H. Wolfenson, G. Meacci, S. Liu, M. R. Stachowiak, T. Iskratsch, S. Ghassemi, P. Roca-Cusachs, B. O'Shaughnessy, J. Hone, and M. P. Sheetz, Nature Cell Biology **18**, 33 (2016).

[124] J. Lohner, J. F. Rupprecht, J. Hu, N. Mandriota, M. Saxena, D. P. de Araujo, J. Hone, O. Sahin, J. Prost, and M. P. Sheetz, Nature Physics **15**, 689 (2019).

[125] S. V. Plotnikov, A. M. Pasapera, B. Sabass, and C. M. Waterman, Cell **151**, 1513 (2012).

[126] J. J. Keya, D. Inoue, Y. Suzuki, T. Kozai, D. Ishikuro, N. Kodera, T. Uchihashi, A. M. R. Kabir, M. Endo, K. Sada, and A. Kakugo, Scientific Reports **7**, 6166 (2017).

[127] H. J. Kreuzer and S. H. Payne, Physical Review E **63**, 0219061 (2001).

[128] D. S. Shafer, *SIAM Review* (Westview Press, Boulder, 1995), No. 2, pp. 280–281.

[129] R. D. Vale, C. M. Coppin, F. Malik, F. J. Kull, and R. A. Milligan, Tubulin GTP hydrolysis influences the structure, mechanical properties, and kinesin-driven transport of microtubules, 1994.

[130] H. Jiang and Z. Hou, Soft Matter **10**, 1012 (2014).

[131] R. E. Isele-Holder, J. Elgeti, and G. Gompper, Soft Matter **11**, 7181 (2015).

[132] T. Eisenstecken, G. Gompper, and R. G. Winkler, Polymers **8**, 37 (2016).

[133] R. G. Winkler, J. Elgeti, and G. Gompper, Journal of the Physical Society of Japan **86**, 101014 (2017).

[134] Y. Man and E. Kanso, Soft Matter **15**, 5163 (2019).

[135] R. G. Winkler and G. Gompper, Journal of Chemical Physics **153**, 37 (2020).

[136] R. Chelakkot, A. Gopinath, L. Mahadevan, and M. F. Hagan, Journal of the Royal Society Interface **11**, 20130884 (2014).

[137] A. Ghosh and N. S. Gov, Biophysical Journal **107**, 1065 (2014).

[138] J. Shin, A. G. Cherstvy, W. K. Kim, and R. Metzler, New Journal of Physics **17**, 113008 (2015).

[139] G. De Canio, E. Lauga, and R. E. Goldstein, Journal of the Royal Society Interface **14**, 20170491 (2017).

[140] Ö. Duman, R. E. Isele-Holder, J. Elgeti, and G. Gompper, Soft Matter **14**, 4483 (2018).

[141] K. R. Prathyusha, S. Henkes, and R. Sknepnek, Physical Review E **97**, 022606 (2018).

[142] Z. Mokhtari and A. Zippelius, Physical Review Letters **123**, 028001 (2019).

[143] M. S. Peterson, M. F. Hagan, and A. Baskaran, Journal of Statistical Mechanics: Theory and Experiment **2020**, 13216 (2020).

[144] S. K. Anand and S. P. Singh, Physical Review E **101**, 030501 (2020).

[145] M. Foglino, E. Locatelli, C. A. Brackley, D. Michieletto, C. N. Likos, and D. Marenduzzo, Soft Matter **15**, 5995 (2019).

[146] S. G. Krantz, *Handbook of Complex Variables* (Birkhäuser Boston, Boston, MA, 1999).

[147] P. M. Chaikin and T. C. Lubensky, *Principles of Condensed Matter Physics* (Cambridge University Press, Cambridge, 1995).

[148] P. C. Schmidt, Berichte der Bunsengesellschaft für physikalische Chemie **89**, 721 (1985).

[149] J. Allard and A. Mogilner, Traveling waves in actin dynamics and cell motility, 2013.

[150] M. Rauzi, P. F. Lenne, and T. Lecuit, Nature **468**, 1110 (2010).

[151] S. Saravanan, C. Meghana, and M. Narasimha, Molecular Biology of the Cell **24**, 2350 (2013).

[152] Y. Yang and M. Wu, Philosophical Transactions of the Royal Society B: Biological Sciences **373**, (2018).

[153] W. M. McFadden, P. M. McCall, M. L. Gardel, and E. M. Munro, PLoS Computational Biology **13**, (2017).

[154] M. Roh-Johnson, G. Shemer, C. D. Higgins, J. H. McClellan, A. D. Werts, U. S. Tulu, L. Gao, E. Betzig, D. P. Kiehart, and B. Goldstein, Science **335**, 1232 (2012).

[155] I. Linsmeier, S. Banerjee, P. W. Oakes, W. Jung, T. Kim, and M. P. Murrell, Nature Communications **7**, (2016).

[156] S. Yabunaka and P. Marcq, Emergence of epithelial cell density waves, 2017.

[157] S. K. Wu, G. A. Gomez, M. Michael, S. Verma, H. L. Cox, J. G. Lefevre, R. G. Parton, N. A. Hamilton, Z. Neufeld, and A. S. Yap, Nature Cell Biology **16**, 167 (2014).

[158] A. C. Martin, M. Gelbart, R. Fernandez-Gonzalez, M. Kaschube, and E. F. Wieschaus, Journal of Cell Biology **188**, 735 (2010).

[159] R. Levayer and T. Lecuit, Developmental Cell **26**, 162 (2013).

[160] T. Moore, S. K. Wu, M. Michael, A. S. Yap, G. A. Gomez, and Z. Neufeld, Biophysical Journal **107**, 2652 (2014).

[161] U. M. Ascher, S. J. Ruuth, and B. T. R. Wetton, SIAM, Vol. 32, No. 3, pp. 797–823 (1995).

[162] J. S. Coravos, F. M. Mason, and A. C. Martin, Trends in Cell Biology **27**, 276 (2017).

[163] J. Michaux, F. Robin, W. McFadden, and E. Munro, Journal of Cell Biology **12**, 4230 (2018).

[164] S. Banerjee, T. B. Liverpool, and M. C. Marchetti, Epl **96**, 58004 (2011).

[165] D. S. Banerjee, A. Munjal, T. Lecuit, and M. Rao, Nature Communications **8**, 1121 (2017).

[166] A. Saha, M. Nishikawa, M. Behrndt, C. P. Heisenberg, F. Jülicher, and S. W. Grill, Biophysical Journal **110**, 1421 (2016).

[167] C. Simon, R. Kusters, V. Caorsi, A. Allard, M. Abou-Ghali, J. Manzi, A. Di Cicco, D. Lévy, M. Lenz, J. F. Joanny, C. Campillo, J. Plastino, P. Sens, and C. Sykes, Nat. Phys. **15**, 602 (2019).

[168] Z. Petrášek, C. Hoege, A. Mashaghi, T. Ohrt, A. A. Hyman, and P. Schwille, Biophysical Journal **95**, 5476 (2008).

[169] M. F. Staddon, E. Munro, and S. Banerjee, bioRxiv 2021.02.22.432369 (2021).